Lanthanide Organometallic Complexes: Synthesis and Applications in Single-Molecule Magnetism

Richard Collins

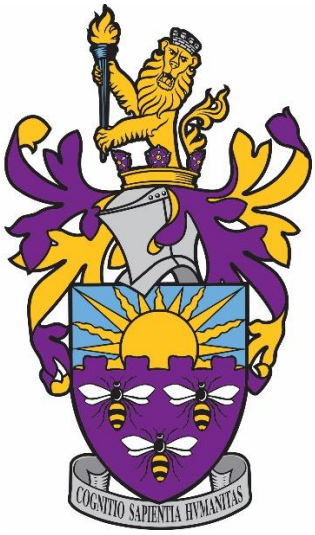

Department of Chemistry, School of Natural Sciences

The University of Manchester

A thesis submitted to the University of Manchester for the degree of Doctor of Philosophy in the Faculty of Science and Engineering

2021

Table of Contents

Word Count: 31385

Abstract

Single-molecule magnets (SMMs) are a classification of molecular nanomagnets which can display slow relaxation of magnetisation. This is manifested in magnetic properties that are not reliant upon the cooperative interactions across domains of spins. This thesis aims to synthesise and characterise lanthanide organometallic complexes and to investigate the resultant magnetic properties.

4f/3d isocarbonyl complexes have previously been shown to display single-molecule magnet behaviour with large energy barriers to reversal of magnetisation, as a result of cooperative effects between the two individual metal centres facilitated by the isocarbonyl link. Isocarbonyl bridging ligands present an opportunity to explore the structural and electronic effects of bridging systems in relation to SMMs, as polymetallic complexes may provide higher blocking temperatures and energy barriers. Here, research is focused on utilising the heavier d-block metal tungsten, in combination with 4f elements to investigate the effect on both the structural and magnetic properties in order to expand on the understanding of isocarbonyl SMMs.

The development of easily handled lanthanide organometallic building blocks, based around the 10π-aromatic-8-membered cyclooctatetraene dianion ($[COT]^{2-}$), for future SMM design are also synthesised and their solid-state properties characterised. Though K_2COT and some COT ligated species can be extremely air sensitive and pyrophoric, the materials reported in this thesis showed no pyrophoricity and a reduced, but not dispelled, air sensitivity relative to previously reported work. The separated-ion pairs are subjected to investigations of their

magnetic properties, which is informative for future efforts to synthesise $[COT]^{2-}$-based SMMs.

The second example of lanthanide inverse-sandwich pentalene complexes are synthesised and their solid-state structures are investigated, alongside computational analysis that demonstrates the change in direction of the principle magnetic axis. The precursor complexes are also characterised structurally and magnetically, to afford further insight into the effects of the ligands upon magnetic properties.

Common Terms and Abbreviations

Ln	Lanthanide
An	Actinide
SMMs	Single-Molecule Magnets
SIMs	Single-Ion Magnets
SCM	Single-Chain Magnets
REE	Rare Earth Element
TM	Transition metal
E_i	Ionisation energy
An	Actinides
SOC	Spin-orbit coupling
MOFs	Metal-organic frameworks
hfac	Hexafluoroacetylacetone
CF	Crystal Field
Pyr	Pyridine
RS	Russel-Saunders
HASB	Hard Acid Soft Base
Pn^{TIPS}	Bis(triisopropylsilyl)pentalene
$[COT]^{2-}$	Cyclooctatetraenyl
Cp	Cyclopentadienyl
THF	Tetrahydrofuran
Pyr	Pyridine
ac	Alternating current
dc	Direct current
SC-XRD	Single-crystal X-ray Diffraction
DSP	3,4-dimethyl-2,5-bis(trimethylsilyl)phospholyl)
T_B	Blocking temperature
TM	Transition metal
ZFS	Zero field splitting
Pc	Phthalocyanine

KD	Kramers Doublet
QTM	Quantum tunnelling mechanism
TA-QTM	Thermally assisted quantum tunnelling mechanism
^{i}Pr	Iso-propyl
CCDC	Cambridge crystallographic data centre
BArF	Tetrakis[3,5-bis(trifluoromethyl)phenyl]borate
Cp^{ttt}	Tri-(tert-butyl)cyclopentadienyl
Cp*	Pentamethylcyclopentadienyl
U_{eff}	Effective energy barrier

Declaration

No portion of the work referred to in the thesis has been submitted in support of an application for another degree or qualification of this or any other university or other institute of learning

Copyright Statement

Acknowledgements

I have to begin by giving thanks to the whole Layfield research group, past and present. They have been key to my growth as a chemist and as a person. Away from my bench, they have been essential to me maintaining my sanity throughout the five years I was a member. I feel honoured to have met and worked with such a diverse range of people, hailing from many different parts of the world. It has been a privilege to work with all of you.

Thanks to Professor Richard A. Layfield, my supervisor, for granting me the opportunity to undertake my Ph.D. in his group.

I would like to pay special thanks to Dr. Ben Day who was instrumental in my learning of actually performing a synthetic reaction in the lab and saved me a lot of headaches and scars. His knowledge of X-ray crystallography was and, still is, extremely impressive, one of the fastest solvers I ever saw. Also, his ability to joke around and have fun only furthered his approachability and likability.

Dr Maria-Jose Ojea Heras deserves thanks, both for her great personality and also her patience in taking me through magnetic data work up techniques. I will always enjoy the memories of Firenze, ICOMC 2018.

Thanks go to my parents, through nurturing my desire to study as well as all the support (particularly financial!) throughout my time at university. I will finally be done with “school”, as they often call it.

Many thanks go to my very good friends, Jonny Barlow and Pippa Sellers, for helping me to assimilate into living in the South. Also, thanks to them for just generally being lovely people and for all the great times we’ve spent together. Thanks also to Audra “Maverick” Taylor for being a great friend for many years, always backing me and providing me with chocolatey goods and silly stories, thanks Maverick.

Even though I have managed to write a thesis, trying to adequately articulate how grateful I am to Rhiannon Jones is the hardest thing to put into words. Though my initial impression when meeting her at the very beginning of my Ph.D. was later shown to be completely incorrect, she has never held it against me, instead I just

have to explain it to people. Over many years, numerous cities, countless hours on trains, lock-downs and more, she has been a constant comfort to me. Her incredible tenacity, exuberance and commitment to tackling new problems has been inspiring and has helped to remind me of why I wanted to pursue a Ph.D.. I cannot describe how much I owe to her for all her help and I can only hope that I can one day repay the immense debt.

Thanks to everyone else who through the many years of being a student have been my friends, put up with my incessant talking of chemistry, helped me stay sane and made sure I had some fun.

Chapter 1:
Introduction

1.1 Introduction

This chapter is separated into four parts, which provide introductory information into the work presented herein. The first section shall provide a general overview on single-molecule magnetism. The second is an introduction to lanthanide single-molecule magnetism (SMM). The third is a focus on utilisation of cyclopentadienyl ligands in SMMs. The final section will consider cyclooctatetraenyl ligand based SMMs, comparing their application and success with cyclopentadienyl systems.

1.2 Single-Molecule Magnets

Single-molecule magnets (SMMs) are a class of coordination compounds which display magnetic bistability as a result of the electronic structures of individual molecules.[1]. This property of retained magnetisation can be demonstrated by the magnetic hysteresis. By contrast, the magnetic properties displayed by classical bulk ferromagnets, such as hard-disk drives which are commonly made from cobalt alloys, is a result of domains of spins involving upwards of 10^9 atoms.[2] Whereas classic bulk ferromagnets display hysteresis to room temperature and above, SMMs only display hysteresis at cryogenic temperatures, clearly languishing behind in terms of working temperatures. Currently, the highest temperature that an SMM retains magnetisation is 80 K, with the hysteresis measured at a scan rate of 25 Oe s^{-1}.[3] The highest temperature at which the ability to display hysteresis is retained is known as the blocking temperature, T_B. Generally, a high T_B is associated with a high energy barrier to magnetic relaxation, U_{eff}/k_BT.

Since the seminal work of Sessoli *et al.* in 1993 introduced single-molecule magnetism, the challenge has to push the both energy barriers and blocking temperatures higher.[4] The realisation of room temperature SMMs has the potential to result in ultra-dense data storage devices.[5] The field of molecular magnetism has developed greatly over the prevailing three decades, moving from transition-metal (TM) coordination complexes, then came lanthanide coordination complexes in 2003 and finally the introduction of organometallic complexes.[3,4,6,7]

For ten years, transition metal complexes represented the entirety of the SMM field. Great synthetic strides have been made to increase the number of spin carriers in a molecule in a bid to increase the effective energy barrier (Equation 1.1). It was hoped that by creating molecules with high ferromagnetic coupling that anisotropy, the directional preference of the primary magnetic axis, could be maximised. A simple method to compliment the simple formula.

$$U_{eff} = |D| \cdot S^2$$

$$U_{eff} = |D| \cdot \left(S^2 - \frac{1}{4}\right)$$

Equation 1.1: Maximum theoretical U_{eff}/k_BT for transition metal SMMs, D is the axial zero-field splitting parameter. Top = systems with integer spins, bottom = systems with half-integer spins, S = total spin. [8]

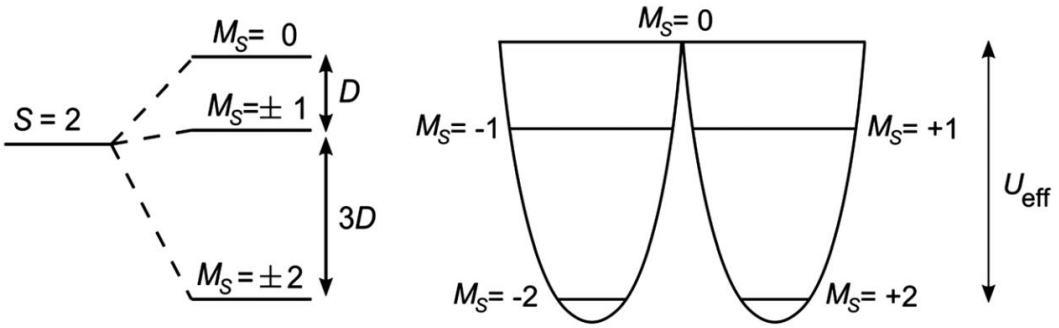

Figure 1.1: (Left) splitting of an S = 2 state into its constituent M_S levels, induced by negative axial ZFS, (right) the resulting double-well. Figure taken from reference 8.

However, studies cast doubt over the method of maximising S, noting that the increasing total spin was not leading to similar increases in U_{eff}/k_BT. With larger number of spin carriers came the difficult task of maintaining the parallel anisotropy within the molecule.[9] Thus, a larger S came at the price of a lower value for the ZFS parameter, D. Rather, Neese and Pantazis suggested that "….more effort should be

directed in understanding the parameters involved in maximizing the anisotropy of small, perhaps even mononuclear, molecules".[10]

The field of single-molecule magnetism began with a focus entirely devoted to molecules based around the transition metals (d-block). The field started with the manganese(III)/manganese(IV) cage-complex $[Mn_{12}O_{12}(OAc)_{16}(H_2O)_4]$, originally synthesised by Lis, which was measured by Sessoli *et al.* and demonstrated magnetic hysteresis properties as a result of a spin ground state of $S = 10$.[4] Subsequently, the first few years saw the domination of polymetallic complexes based on 3d metals.[11] As the field was new, there was no clear direction to move synthetically and so early deviations included substitution of the carboxylate ligands by reacting with a large excess of a different carboxylic acid, utilisation of nitrates and sulfonates and a plethora of other modifications.

Eventually, a goal of increasing the number of manganese atoms in a single ring was targeted and in 2004 Christou *et al.* published a "Giant Single-Molecule Magnet" with a ring of $\{Mn_{84}\}$ (**1.11$_{Mn}$**, Figure 1.1).[12] Even with the impressive number of metal centres, this complex displayed a $U_{eff}/k_BT = 12.1$ cm^{-1}. The low energy barrier can be explained through the problem outlined earlier, that when there is a large number of spins there is a difficulty in controlling the direction of the individual anisotropies to be parallel.

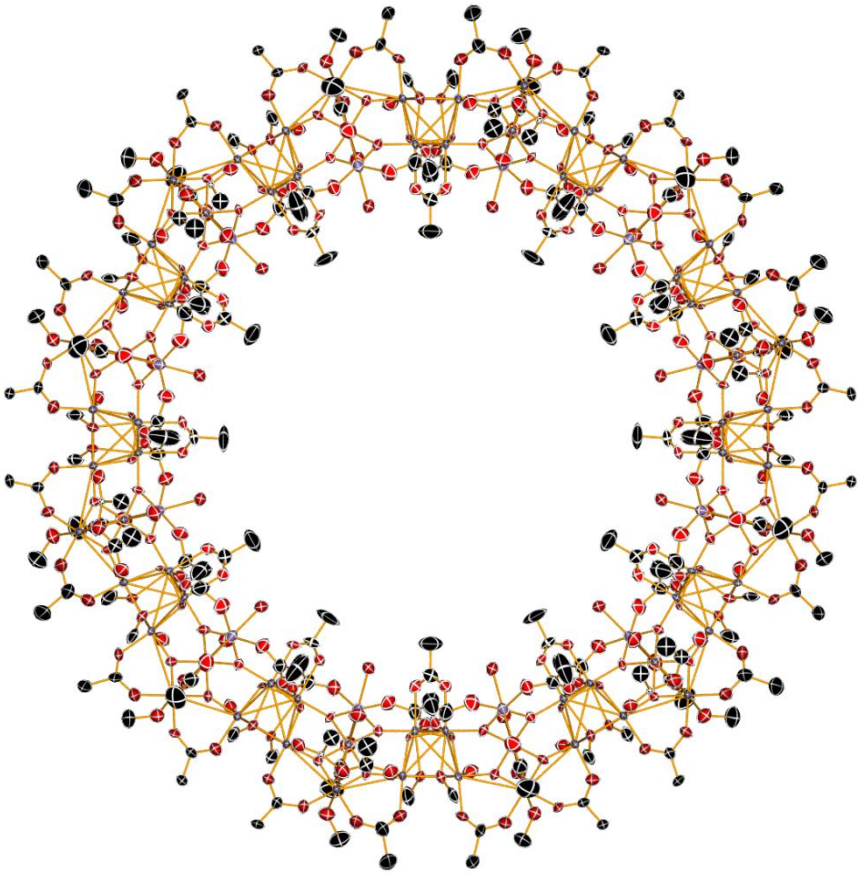

Figure 1.2: Thermal ellipsoid representation of the molecular structures of **1.11$_{Mn}$** ([$Mn_{84}O_{72}(O_2CMe)_{78}(OMe)_{24}$, hydrogen atoms omitted for clarity, displacement ellipsoids set at the 50 % probability level, carbon = black, oxygen = red, manganese = purple).[12]

After continued efforts with manganese-based SMMs failed to realise high (> 300 K) blocking temperatures, the field investigated the properties of other metals within the d-block. Iron(III) complexes became the next target, partly as a result of the large spin state it possesses.[13] A notable example is the relatively small tetranuclear iron(III) complex reported by Sorace *et al.* (**1.12$_{Fe}$** Figure 1.3).[14] This complex displayed an energy barrier of U_{eff}/k_BT = 2.33 cm^{-1}. Though this energy barrier is lower than that of **1.11$_{Mn}$**, the complex did display Ising type anisotropy and the small size allowed for a thorough characterisation of the zero-field splitting thus expanding

the understanding of how the interactions between metal centres affected the magnetic properties.[12]

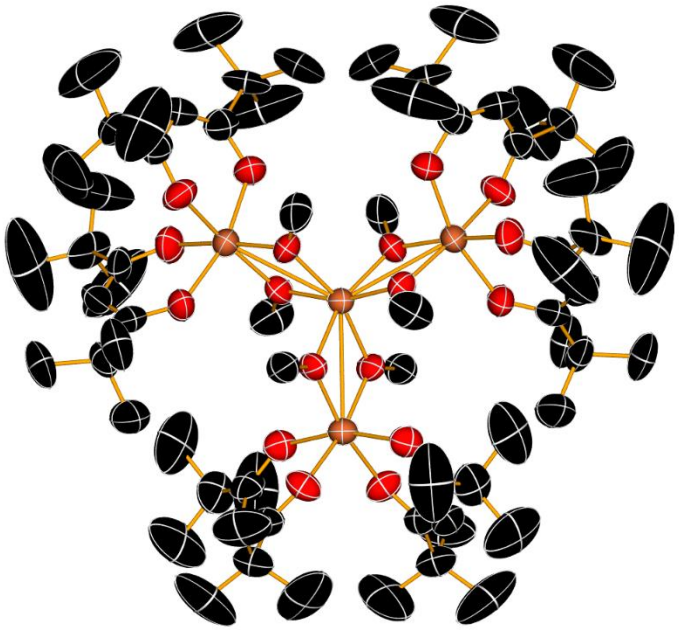

Figure 1.3: Thermal ellipsoid representation of the molecular structures of **1.12$_{Fe}$** [$Fe_4(OCH_3)_4(dpm)_4$-$(HOCH_3)_4$], Hdpm = dipivaloylmethane, hydrogen atoms omitted for clarity, displacement ellipsoids set at the 50 % probability level, carbon = black, oxygen = red, iron = orange).[14]

The synthesis of a hexanuclear cobalt(II) complex by Murrie *et al.* in 2003 (**1.13$_{Co}$**, Figure 1.4) contains a cubane [Co_4O_4] central structure. Investigations elucidated a total spin value of S = 3 for this complex and the authors suggested a ferromagnetic coupling between the cobalt(II) metals.[15] This complex was the second Co-based SMM to be reported demonstrates the care taken to understand the features of the Mn and Fe based SMMs before explorations were made further around the Periodic Table. This SMM displayed an energy barrier of U_{eff}/k_BT = 18 cm^{-1}.[15] Comparing to **1.11$_{Mn}$**, this shows an increased energy barrier with far less metal atoms in the molecule and thus the suitability of cobalt in the field of SMMs.

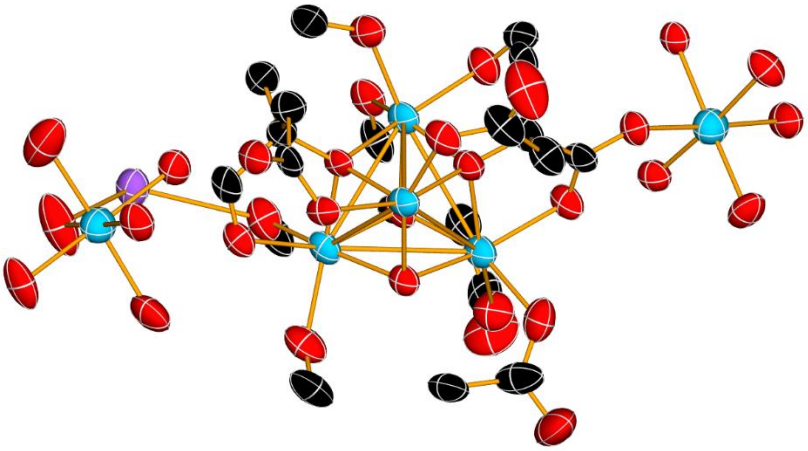

Figure 1.4: Thermal ellipsoid representation of the molecular structure of the anionic segment of **1.13$_{Co}$** $[(NMe_4)_3Na\text{-}\{Co_4(cit)_4[Co(H_2O)_5]_2\}]\cdot_{11}H_2O$, cit^{4-}= $[C(O^-)(CO_2^-)(CH_2CO_2^-)_2]$, hydrogen atoms omitted for clarity, displacement ellipsoids set at the 50 % probability level, carbon = black, oxygen = red, cobalt = blue, sodium = purple).[15]

The three SMMs described thus far are only a small selection of the many molecules synthesised and characterised in the field. They serve to highlight the different directions that the community has explored over the past 30 years and to contextualise the work reported in this thesis. Without this bank of prevailing work, there would be a great dearth of knowledge on the intricacies which dictate the exhibited properties of SMMs.

The rise of molecular magnetism in chemistry has caused a shift away from the idea that magnetism is only a tool for diagnostics and towards a desire for furthering the fundamental understanding of magnetism within molecules.[5] SMMs have allowed for quantum effects to be observed in mesoscopic sized materials, greatly furthering the understanding of these phenomena.[5] It is behaviour such as this, the potential

applications in data storage, in spintronics, in materials generally, that has contributed to the vast interest devoted to SMMs over the past few decades.[16,17]

1.3 Lanthanide Single-Molecule Magnets

The 4f elements, or the lanthanides, exhibit unique physical and chemical properties compared to other metals. The lanthanides possess some of the largest magnetic moment values, along with very high anisotropy, of the entire Periodic Table and so are very well suited for the development of SMMs.[18–20]

The initial foray into lanthanide based SMMs came from the pivotal work of Ishikawa *et al.* in 2003.[6] Magnetic studies on the bis-phthalocyanine complexes of the lanthanides $[Pc_2Ln]^-$, (Pc = phthalocyanine, Ln = Nd, Tb, Dy, Ho, Er, Tm, Yb, **1.14$_{Ln}$**, Figure 1.5) revealed that the terbium and the dysprosium analogues displayed slow magnetisation relaxation. The energy barriers to such relaxation were reported as 230 and 28 $cm^{-1,}$ respectively, and showed temperature ranges which exceeded any seen in TM-cluster based SMMs.[6]

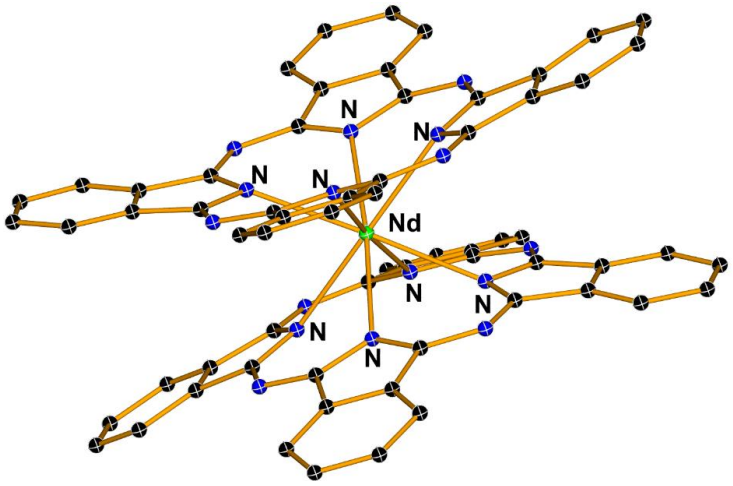

Figure 1.5: Thermal ellipsoid representations of the molecular structures of **1.14$_{Nd}$** (hydrogen atoms omitted for clarity, displacement ellipsoids set at the 50 % probability level). [6]

This work demonstrated the feasibility of harnessing the strong, unquenched spin-orbit coupling seen in lanthanide complexes to engender high energy barriers to the relaxation of magnetisation.

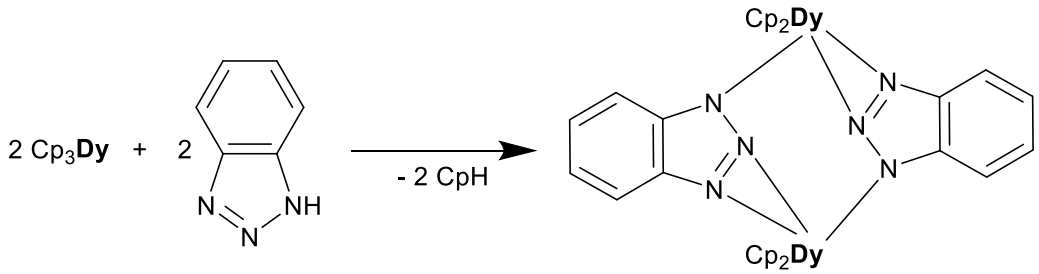

Scheme 1.1: Synthetic route to bridged bimetallic SMM **1.15$_{Dy}$**.[7]

The first organometallic SMM was reported in 2010 by Layfield *et al.* demonstrated that a didysprosium benzotriazole bridged molecule (**1.15$_{Dy}$**, [{$Cp_2Dy(\mu\text{-bta})\}_2$], (bta=1*H*-1,2,3-benzotriazole, Figure 1.6) displayed an energy barrier of U_{eff}/k_BT = 31.9 ± 1.7 cm^{-1}.[7] This work demonstrated how organometallic chemistry allowed for a control over the coordination sphere of the metal, thus allowed control over the magnetic axes and the nuclearity of the synthesised complexes. No blocking temperature was reported. The molecule was synthesised by protonolysis of a tricyclopentadienyl dysprosium precursor (Scheme 1.1).

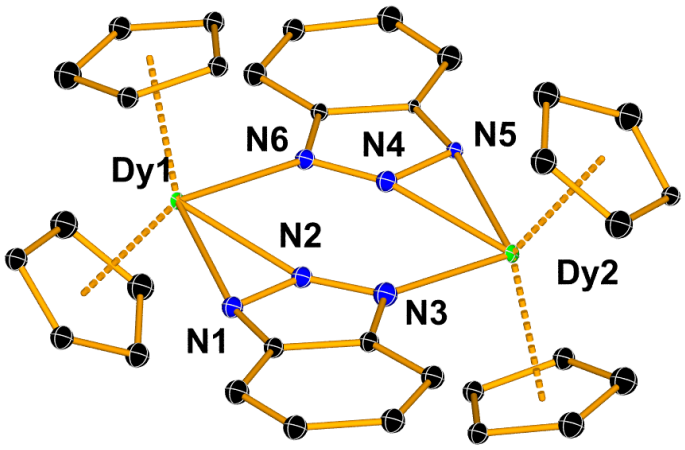

Figure 1.6: Thermal ellipsoid representations of the molecular structure of **1.15$_{Dy}$** (hydrogen atoms omitted for clarity, displacement ellipsoids set at the 50 % probability level).[7]

Shortly thereafter, Rinehart and Long utilised a report by Sievers in 1982 which outlined the asphericity of the 4*f* shells for the lanthanides in the +3 oxidation state.[21] The work by Sievers allowed for a visual representation of the charge density and the shape it takes for a given Ln^{3+} ion is shown in Figure 1.6.[22] It can be seen that for a particular lanthanide, the shape of the electron density varies with the m_J state. In the design of SMMs, primary consideration is given to the highest value of m_J which corresponds to the ground state as defined using the Russell-Saunders (RS) coupling scheme. The RS coupling scheme is commonly employed when discussing the ground states, even though the RS method is only accurate when describing a free ion in the gaseous state. The wide application is due to the simplicity alongside the qualitative information it provides.

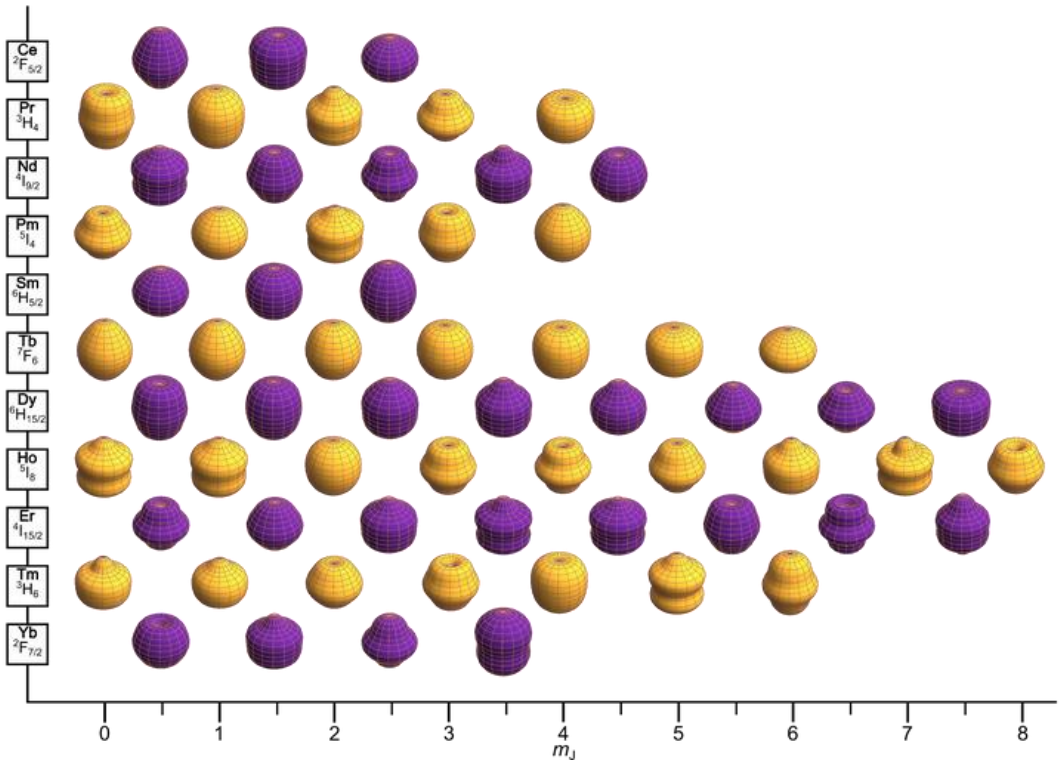

Figure 1.7: Angular dependence of the total 4f charge density for the m_J states of the Ln^{3+} ions in the gaseous state and the shape they take. Purple represents Ln^{3+} ions with integer ground state terms and gold represents ions with half integer ground state terms. [21,22]

Thus, for the elements such as terbium and dysprosium, the charge density takes a shape where the *x*- and *y*-projections are elongated and the *z*-projections is compressed compared against the purely spherical nature of the ground state, isotropic, gadolinium. This is termed oblate. In direct opposition, when the *x*- and *y*-projections are compressed and the *z*-projection is elongated, as is the case for erbium and holmium, the shape is denoted as prolate.[21] The shapes pictorially represent the average distribution of the charge density at different m_J states.

Herein lies the simplicity of the design requirements set forth by Rinehart and Long when constructing an SMM from the 4f elements, namely that an oblate-shaped ground state necessitates the maximisation of crystal field (CF) effects in the axial plane. For a prolate-shaped charge density distribution, maximisation in the

equatorial plane is crucial for the realisation of a high functioning Ln-SMM. This would lead to the anisotropic character of the lanthanide ion being increased by being "squashed". By maximising the LF in the correct orientation, the relevant *g*-tensors – which is describes the Zeeman splitting of the Kramers' doublets - of different m_J states of the lanthanide can be stabilised. This then leads to higher values of U_{eff}/k_BT and higher blocking temperatures.

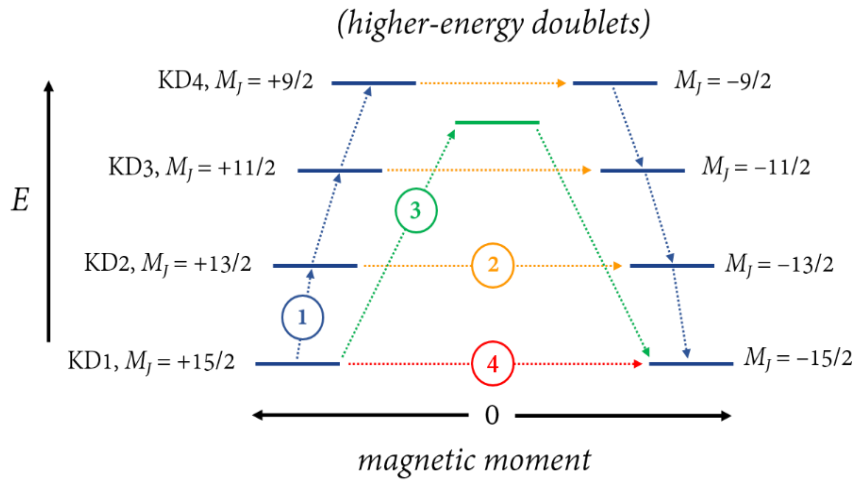

Figure 1.8: Possible relaxation mechanisms for magnetisation of a system where the maximum m_J = ±15/2. 1 = Orbach, 2 = thermally assisted quantum tunnelling mechanism, 3 = Raman, 4 = quantum tunnelling mechanism. KD = Kramers' doublet. [20]

Once the properties have been measured and both energy barriers and blocking temperatures determined, consideration has to be given to the manner in which the magnetisation has relaxed. There are four defined mechanisms by which this can occur and these are graphically represented in Figure 1.8. The two most often discussed are the thermally dependent Orbach mechanism and the thermally independent quantum tunnelling mechanism (QTM), though thermally-activated (TA) QTM often occurs in tandem with thermally independent QTM. Raman

relaxation occurs *via* phonons, this is more commonly observed in complexes with ligands that display greater movement of ligand substituents as this provides a pathway for the phonons. [23]

The Orbach mechanism involves traversing the entire set of Kramers doublets. Thus for a $m_j = \pm 15/2$ for the magnetisation to relax to thermal equilibrium the magnetic moment has to travel over the energy barrier in a classical manner. Though a high energy barrier does not guarantee a high blocking temperature, as other relaxation mechanisms can occur, the most deleterious for hysteresis properties is QTM.[24]

This requirement to stabilise the ground-states has resulted in the dominance of π-conjugated, cyclic, anionic ligands in lanthanide organometallic SMMs. This is a result of the bonding in lanthanide complexes being almost entirely ionic in nature. Most common is the five-membered cyclopentadienyl (Cp) ligands, especially with oblate shaped charge densities such as with dysprosium. The eight-membered cyclooctatetraenyl (COT) finds much utilisation for prolate distributed charge densities, like those of erbium or holmium ions in the ground state.

1.4 Cyclopentadienyl Lanthanide SMMs

The prevalence of cyclopentadienyl (Cp) ligands in organometallic chemistry cannot be missed. There are, at the time of writing, over 63,000 entries in the Cambridge Crystallographic Data Centre (CCDC) of Cp-ligated metal complexes, with over 3000 4f element containing molecules, and there seems to be no slowing of pace of growth. Substitutions on the cyclopentadienyl ring are generally relatively simple to achieve, allowing for an extremely varied set of electronic and steric properties. This ability to tune to Cp ring means that the ring can be tailored to the unique chemical and physical properties of the desired metal.[20]

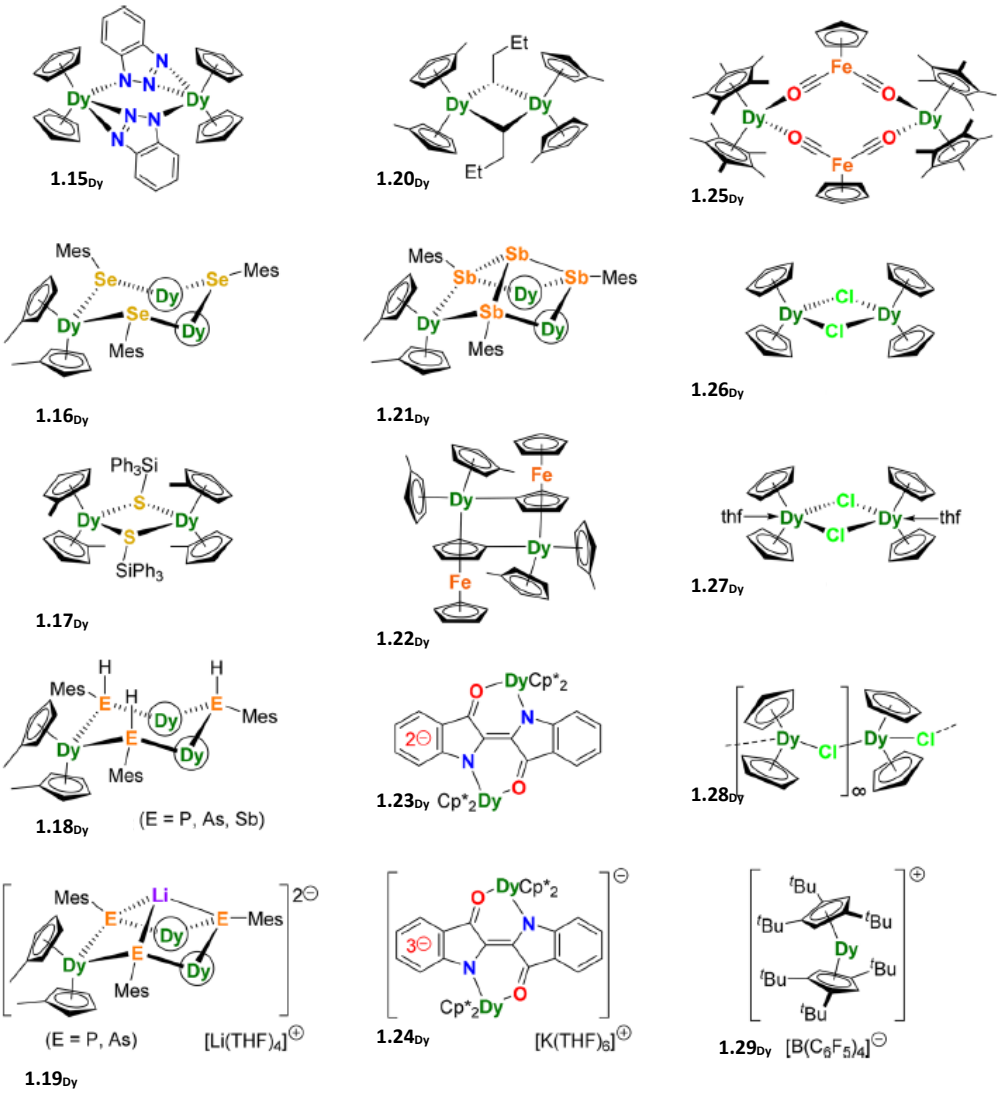

Figure 1.9: Examples of lanthanide organometallic SMMs of which all include the $[Cp^{R}_{2}Dy]^{+}$scaffold as a key feature. [25–34]

As **1.15$_{Dy}$** was the first organometallic SMM, it was also the first Cp-ligated SMM. [7] Since, there have been numerous additions this still growing family and a selection are presented in Figure 1.9.

For dysprosium based SMMs, it is not only required that the ligands be as axially positioned as attainable, but that the ligands be as close to the metal atom as is feasible. The closer the ligand gets, the greater the effect of stabilisation on the ground magnetic state occurs due to increased electron density.

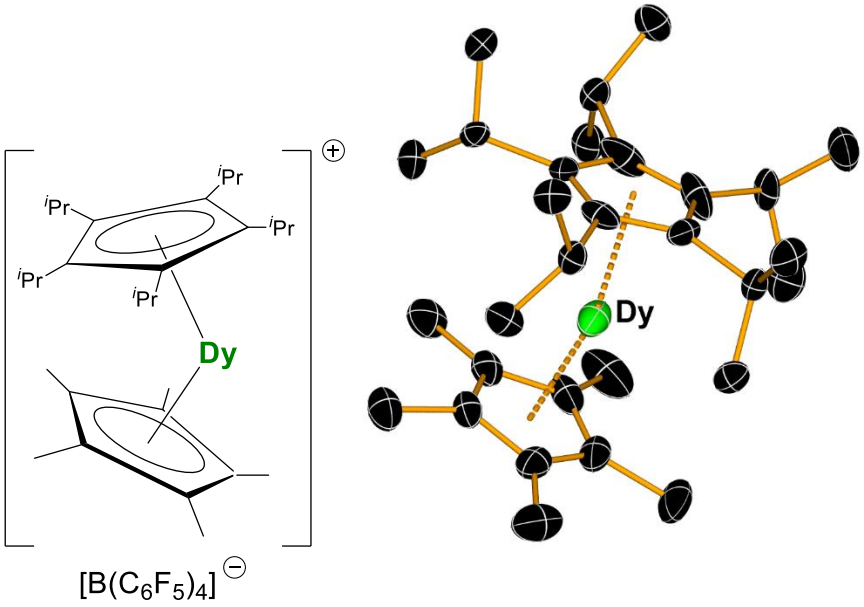

Figure 1.10: Structure (left) and thermal ellipsoid representation (right) of the cation of **1.29$_{Dy}$** (hydrogen atoms and anion omitted for clarity, displacement ellipsoids set at the 50 % probability level).[3]

This design criteria was successfully implemented in the synthesis of the current state-of-the-art SMM. This is the [Cp^{iPr5}DyCp*][BArF] (**1.29$_{Dy}$**, Cp^{iPr5} = penta-iso-propylcyclopentadienyl, Cp* = pentamethylcyclopentadienyl, BArF = B(C$_6$F$_5$)$_4$). The molecule displayed a blocking temperature of T_B = 80 K, scan rate 25 Oe s^{-1} and an effective energy barrier of U_{eff}/k_BT = 1541 cm^{-1}. The Cp$_{cent}$-Dy-Cp$_{cent}$ (cent = centroid) angle is 162.507(1) °, the Cp^{iPr5}-Dy and Cp*-Dy bond distances are 2.284(1) Å and 2.296(1) Å. This was a 9.7 ° wider bite angle, and an average shortening of 0.026 Å compared to the previous record holding SMM ([Cp$^{ttt}_2$Dy][BArF], Cp^{ttt} = tri-tert-butylcyclopentadienyl, U_{eff} = 1256(14) cm^{-1}, T_B = 60 K, scan rate 39 Oe s^{-1}). [3,35]

The success of **1.29$_{Dy}$** ([Cp^{iPr5}DyCp*][BArF]) was a culmination of years of work achieved by numerous research groups which have explored many alternative

avenues for SMM design. Prior to the publication of **1.29$_{Dy}$**, there had been great efforts made to synthesise and characterise a series of bridged SMMs. Bridging systems offers the ability to incorporate metal centres above one, thus increasing the total magnetic moment of the molecule.

Interestingly, though the general formula of [(Cp$_2$)Ln(μ-X)] (Cp = any cyclopentadienyl and all derivatives, X = any bridging unit) has been known for decades, **1.15$_{Dy}$** was the first SMM to fit this general formula.[2] All bridged systems are still plagued by the difficultly in aligning the anisotropy that was outlined earlier, however the potential to furthering our fundamental understanding of the field is both interesting and essential.

In the years following the reporting of **1.15$_{Dy}$**, many more examples of bridged organometallic SMMs have been added to the collection. Even seemingly simple molecules have furthered our understanding of the effects that exchange interactions can impart on magnetic properties of SMMs. An example of such is the chloride bridged complex [Cp$_2$Dy(μ-Cl)(THF)$_x$]$_n$ (**1.26$_{Dy}$** x = 0 n = 2, **1.27$_{Dy}$** x = 1 n = 2,and **1.28$_{Dy}$** x = 0, n = ∞,).[31]

The molecules **1.26$_{Dy}$** and **1.28$_{Dy}$** co-crystallised and separation was not achieved. Measurements of susceptibility under alternating current (ac) field showed two, independent, relaxation processes occurring with a 75% and 25% of χ. Further analysis showed that the dimer **1.26$_{Dy}$** had a relaxation time 500 times shorter than for **1.28$_{Dy}$** (τ = 0.15 ms and τ = 78.6 ms, for **1.26$_{Dy}$** and **1.28$_{Dy}$** respectively).[31] The longer relaxation for **1.28$_{Dy}$** coincides with a lower energy barrier of U_{eff}/k_BT = 26.3 cm^{-1} compared to U_{eff}/k_BT = 67.832 cm^{-1} for **1.26$_{Dy}$**. Application of a static direct

current (dc) field of 1 and 5 kOe successfully suppressed quantum tunnelling in **1.26$_{Dy}$** and maxima in the out-of-phase susceptibility measurements were seen at lower temperatures than with no external field.

The examples described demonstrate the versatility of the general formula of $[Cp^R_2Dy]^+[X]^-$ in the synthesis of molecular magnets. The wide range of substituted cyclopentadienyls coupled with the expanse of possible $[X]^-$ has allowed, and still allows, for a large chemical space in which the fundamental understanding of single-molecule magnetism can be expanded.

An offshoot has been the use of heteroatom substitution in the ring. Specifically, phosphorous atom rings, termed phospholyls, and arsenic containing rings, known as arsolyls (Figure 1.10).[36–38] However, for the f-block (lanthanides and actinides, Ln(III) and An(II-IV)), there are currently less than 100 examples of phospholyl and arsolyls reported in the CCDC. [39]

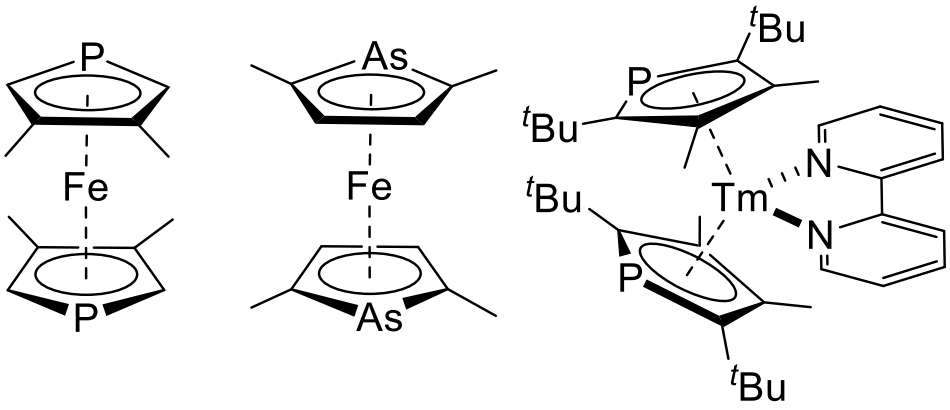

Figure 1.11: Examples of heterocyclopentadienyl organometallic complexes.[39–41]

Very few have been characterised magnetically. An example is the [(DSP)Er(η^8-COT)] reported in 2018 by Gao *et al.* (**1.30$_{Er}$**, DSP^- = 3,4-dimethyl-2,5-

bis(trimethylsilyl)phospholyl).[36] Comparisons to the previously reported [Cp*Er(η^8-COT)] (**1.31$_{Er}$**) with **1.30$_{Er}$** showed that replacement of the Cp* ring with DSP led to improved magnetic properties.[42] The energy barrier increased from 224.5 cm^{-1} for **1.31$_{Er}$** to 248.8 cm^{-1} for **1.30$_{Er}$**. Further, the blocking temperature (T_B) increased from 5 K to 9 K, with scan rates of 200 Oe s^{-1} and 9 Oe s^{-1}. The authors ascribed the improved magnetic properties to a weaker affinity of Er^{3+} toward DSP compared with Cp*, which in turn increases the affinity for the COT ligand. This shortens the bond distance so the COT ligand is even closer the equatorial plane of the Er^{3+}, thus stabilising the prolate charge density.

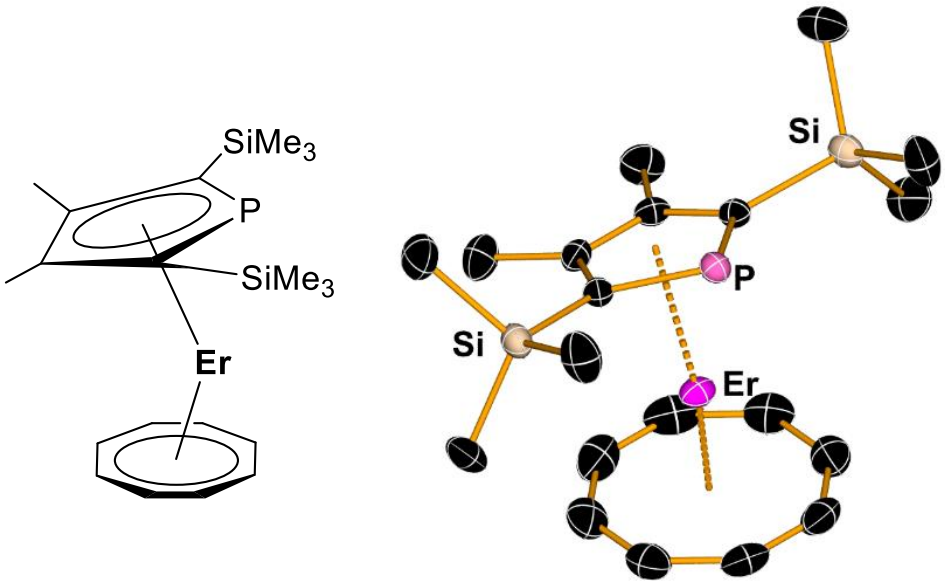

Figure 1.12: Structure and thermal ellipsoid representation of **1.30$_{Er}$** (hydrogen atoms omitted for clarity, displacement ellipsoids set at the 50 % probability level).[36]

The use of heterocyclopentadienyl ligands in SMM magnetochemistry has not had the same level of exploration devoted to it, but this will no doubt lead to interesting molecules and a greater understanding and control over the magnetic properties.

1.5 Cyclooctatetraenyl Lanthanide-SMMs

The 10π-8-memebered dianion cyclooctatetraenyl ($(C_8H_8)^{2-}$, $[COT]^{2-}$]) ligand is the second most commonly used in lanthanide organometallic chemistry. [20] As the trivalent lanthanides are large, relative to the rest of the periodic table, they easily bond in an η^8 manner to the $[COT]^{2-}$. As Cp ligands have been shown to generate strong axial crystal field beneficial to oblate-shaped electron densities, $[COT]^{2-}$ has demonstrated a clear use with prolate-shaped electron densities.[21]

An early example of a $[COT]^{2-}$ SMM is the [(η^8-COT)Er(Cp*)] (**1.31$_{Er}$**) from Gao *et al*.[42] The Er-COT_{cent} distance is 1.670(7) Å, much closer than the Er-Cp^*_{cent} at 2.279(4) Å. This SMM exhibited two distinct relaxation processes with energy barriers of U_{eff}/k_BT = 223.2 cm^{-1} and 136.1 cm^{-1}. The $[COT]^{2-}$ is large enough for its influence to be located in the equatorial plane, and this effect is of sufficient magnitude that the axial perturbation of the Cp* ligand does not completely inhibit SMM properties.

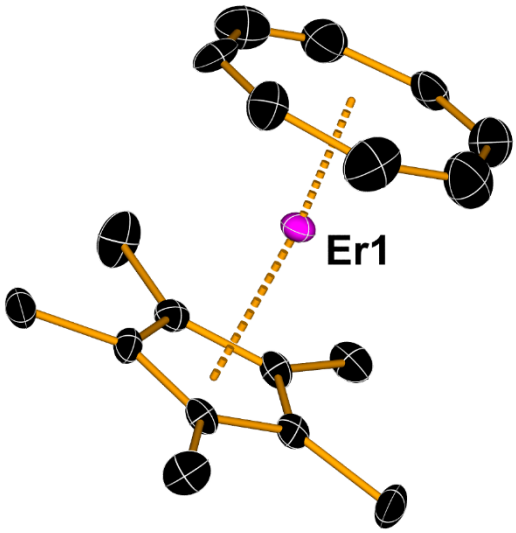

Figure 1.13: Thermal ellipsoid representation of a molecule of **1.31$_{Er}$** (hydrogen atoms omitted for clarity, displacement ellipsoids set at the 50 % probability level).[42]

Murugesu *et al*. utilised the 1,4-bis(trimethylsilyl)cyclooctatetraenyl dianion (COT'') to synthesis a sandwich complex of dysprosium **1.32$_{Dy}$** ([Dy(η^8-COT'')$_2$Li(THF)(DME)], Figure 1.14).[43] The centre of the lithiated COT'' ring shows a greater distance (1.925(9) Å) to the central dysprosium atom compared to the non-lithiated COT'' (1.8715(9) Å), a result of the withdrawal of electron density from the ring by the lithium. Analysis of the frequency dependent data in zero applied field resulted in a calculated energy barrier of U_{eff}/k_BT = 12.5 cm^{-1}. Application of a 600 Oe raised the energy barrier to U_{eff}/k_BT = 29.7 cm^{-1}, thereby validating the strong degree of QTM occurring at zero field. Even so, **1.32$_{Dy}$** exhibits markedly worse SMM properties compared to that of **1.31$_{Er}$**. Here, the equatorial plane crystal field of the COT'' ligands sufficiently lowers the SMM properties to result in a very low energy barrier.

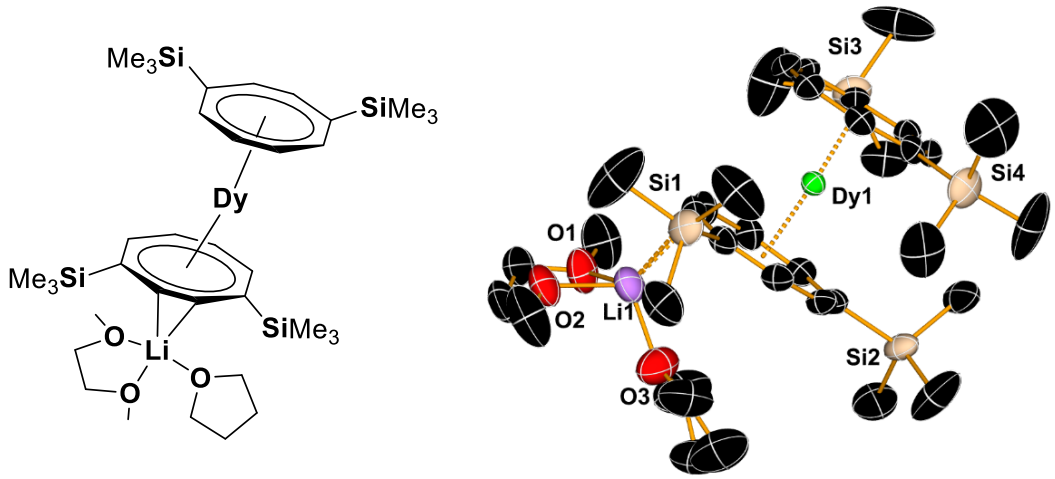

Figure 1.14: Structure and thermal ellipsoid representation of a molecule of **1.32$_{Dy}$** (hydrogen atoms omitted for clarity, displacement ellipsoids set at the 50 % probability level).[43]

The equatorial crystal field effects of [COT]$^{2-}$ were confirmed by Meihaus and Long, with the sandwich complex [K(18-c-6)][(η^8–COT)$_2$Er] (**1.33$_{Er}$**, Figure 1.15).[44] Here, the distances to the COT$_{cent}$ are 1.8835(3) Å and 1.8483(3) Å, a smaller difference than

seen in **1.32$_{Dy}$**. Analysis of the magnetic properties furnished an energy barrier of U_{eff}/k_BT = 147(1) cm^{-1}, between the two values reported for **1.31$_{Er}$**. This complex also exhibited relaxation times of 100 s at 10.1 K, which suggested hysteresis properties that were confirmed by the authors. A blocking temperature of 10 K was determined, however no scan rate was reported. This was the earliest erbium based SMM with hysteresis properties. As the first published bis-η^8-cyclooctatetraenyl erbium SMM, this work confirmed that carefully constructed crystal fields matched with appropriately shaped electron densities can lead to improved lanthanide SMMs as described by Rinehart and Long.[21]

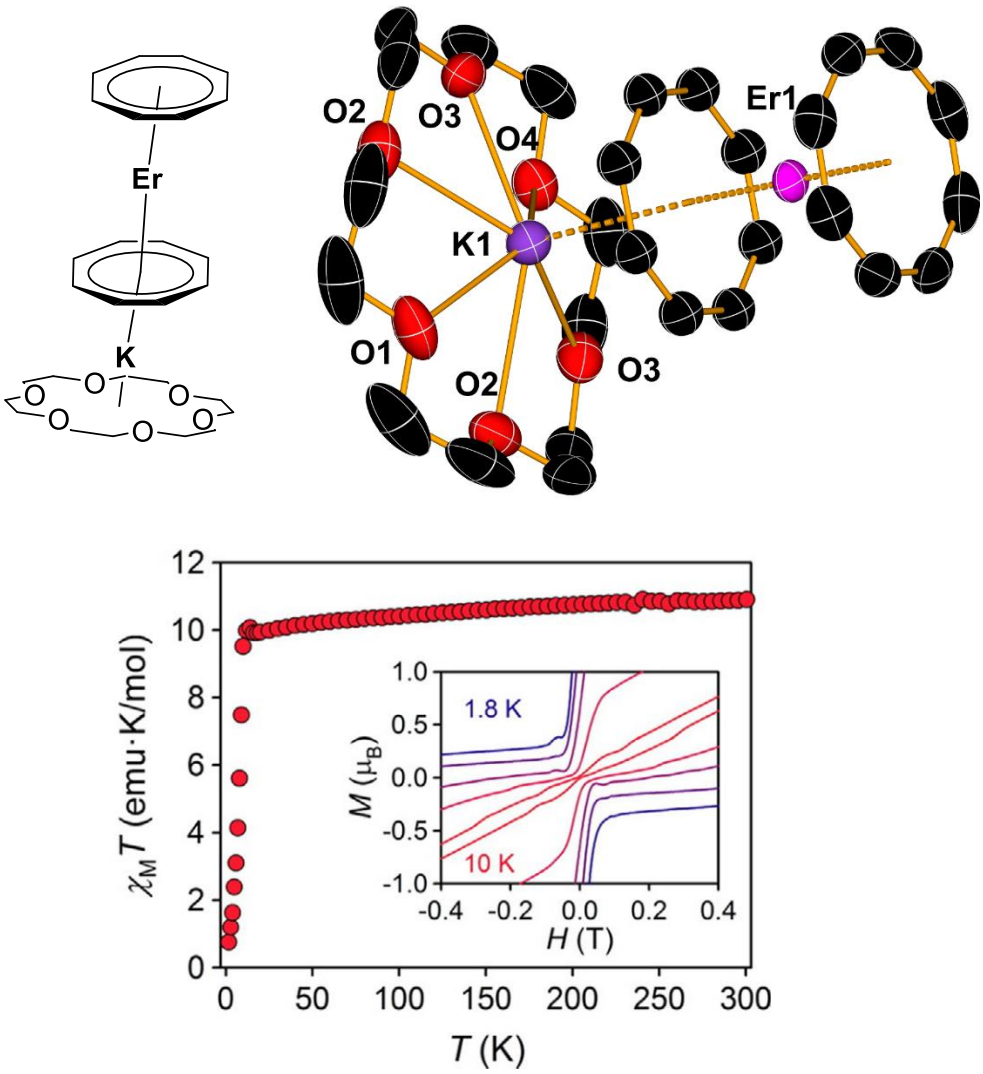

Figure 1.15: Structure and thermal ellipsoid representation of a molecule of **1.33$_{Er}$** (Top, hydrogen atoms omitted for clarity, displacement ellipsoids set at the 50 % probability level), temperature dependence of $\chi_M T$ and, inset, magnetisation (M) *vs.*field (H) hysteresis loops (bottom).[20,44]

Recent years has seen an increase in attempts to move away from sandwich complexes which use the same ligands, but throughout the $[COT]^{2-}$ ligand has been a mainstay of erbium-SMMs. Work published by Rinehart *et al.* demonstrated a 10^6 increase in relaxation time at 2 K by judicious choice of a phosphine-supporting ligand.[45] By synthesising a dimeric $[(\eta^8\text{-COT})Er(\mu\text{-I}]]_2(\mu\text{-dppm})$ (**1.34$_{Er}$**, dppm = (diphenylphosphino)methane Figure 1.16), the authors managed to increase the energy barrier from U_{eff}/k_BT = 75.6 cm^{-1} for $[(\eta^8\text{-COT})ErI(dmpe)]$ (dmpe =

bis(dimethylphosphino)methane up to U_{eff}/k_BT = 201.5 cm^{-1}. Their results illustrated how careful control of the direction and the magnitude of anisotropy can be utilised for the design and synthesis of SMMs.

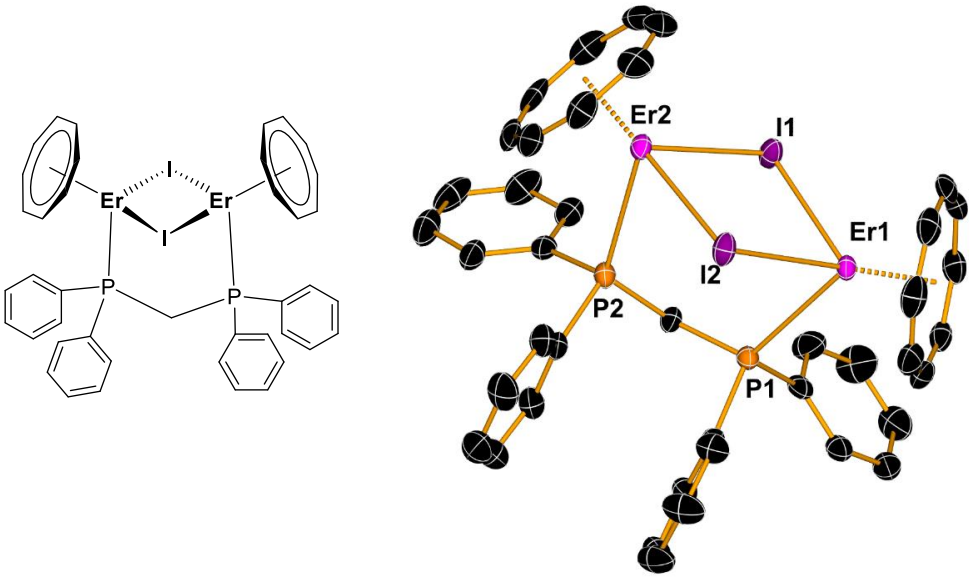

Figure 1.16: Structure and thermal ellipsoid representation of a molecule of **1.34$_{Er}$** (Top, hydrogen atoms omitted for clarity, displacement ellipsoids set at the 50 % probability level).[45]

More recently, Gao *et al.* have demonstrated how an axial field ligand can still be beneficial for the design of erbium-based SMMs when the donating ability of the ligand is weak, compared with the stronger field effects generated by the $[COT]^{2-}$.[46] By synthesising two half-sandwich complexes **1.35$_{Er}$** ([(LOMe)Er(η^8-COT)], LOMe = [CpCo{P(=O)(OMe)$_2$}$_3$]) and **1.36$_{Er}$** ([(THF)$_2$(OAr)Er(η^8-COT)], Ar = 2,6-(2,6-(diisopropylphenyl)$_2$)C_6H_3) comparisons between the weaker LOMe and stronger OAr donors could be elucidated.

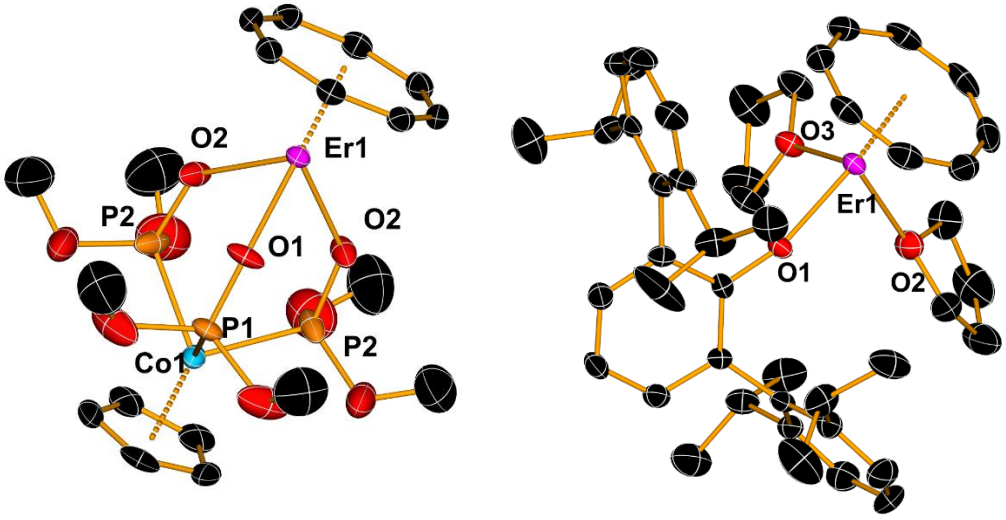

Figure 1.17: Thermal ellipsoid representation of a molecule of **1.35**$_{Er}$ and **1.36**$_{Er}$ (left and right respectively, hydrogen atoms omitted for clarity, displacement ellipsoids set at the 50 % probability level).[46]

For **1.35**$_{Er}$ U_{eff}/k_BT = 60.9 cm^{-1} and for **1.36**$_{Er}$ U_{eff}/k_BT = 44.1 cm^{-1}, though these are lower than **1.31**$_{Er}$ and **1.34**$_{Er}$, this work exemplifies the need to continue investigating all the different manners in which SMM properties can be tailored by rational design.

There have been great strides made in the development of SMMs – from d-block clusters moving to lanthanide organometallic complexes. Efforts to understand the effects of local geometry, soft *vs*. hard donor ligands, single-ion and multi-ion molecules, all have improved the chemist's ability to synthesise materials with more desirable properties. However, limitations still persist. That **1.29**$_{Dy}$ [Cp^{iPr5}DyCp*][BArF] is a salt would lead to increased difficultly in the manufacture of a device as well as the application of SMMs in other areas such as sensors . Therefore, further exploration of the potential solutions is required. The possible routes include bridged systems, solvato-mediated SMMs and investigating the number of metal centres in a molecule.

Chapter 2:

Heterobimetallic Lanthanide-Tungsten Isocarbonyl Complexes as Single-Molecule Magnets

2.1 Introduction

Isocarbonyl groups have found, and continue to find, application within both d-block and f-block chemistry, in areas such as the synthesis of interesting group VI metal complexes, furthering the understanding of f-block bimetallic systems and single-molecule magnetism.[28,47–56] The ability for CO stretching vibrations to be easily found within an IR spectrum gave a strong spectroscopic signal for the early years of f-block organometallic chemistry. Further, these signals allowed for comparisons to be drawn between the chemistry of the d-block and that of the f-block, such as the higher ionicity of bonds in f-block complexes. There are very few examples of direct, unsupported, bonds between metals of the d- and f- block (< 50 reported on the CCDC), due to the low stability of such a bond.[57–59] Isocarbonyl ligands offer a synthetic route to forming a bridge between these elements, thereby allowing the synthesis of heterobimetallic complexes, which can be investigated in lieu of directly bonded d-f complexes.[28,60,61] Heterometallic complexes are convenient as it allows for greater modulation of the overall characteristics, by altering the structural, electronic and magnetic properties of the building blocks. It has been suggested that the addition of a diamagnetic linker, such as W^0, has the effect of reducing the quantum-tunnelling of magnetisation within the system.[62]

There exist numerous pathways for the synthesis of heterobimetallic complexes, including the use of alkane elimination. Through careful choice of alkane generation, a clean reaction can be engendered such as the routes published by Sobaczynski *et*

al. in 2014.[63] An example of this is the simple elimination of $SiMe_4$ and YCp' that allowed for the facile synthesis of **2.1$_Y$**.

In 2016, Nippe's group published the first structurally characterised dysprosium isocarbonyl complex $[(THF)_5Dy((OC)W(CO)_2Cp)_3]\cdot thf$ (**2.2$_{Dy}$**) through an amine elimination reaction between $[Dy\{N(SiMe_3)_2\}_3]$ and $[HW(CO)_3Cp]$.[60] Magnetic dilution studies of **2.2$_{Y\text{-}Dy}$** (Y:Dy 12:1) were conducted, with the molecule synthesised through an elimination akin to **2.1$_Y$** albeit an amine is eliminated. This allowed for the extraction of the effective energy barrier, also known as the anisotropy barrier, at a value of U_{eff}/k_BT = 12.6 cm^{-1}. This is two orders of magnitude below the current record barrier height for the 5* complex (**1.27$_{Dy}$**, Chapter 1) with a barrier of U_{eff}/k_BT = 1,541 cm^{-1} but this is not surprising given the high coordination number of **2.2$_{Dy}$**, along with equatorially coordination of both isocarbonyl and THF molecules.

The ion yttrium(III) possesses a similar ionic radius to dysprosium(III) , and the comparison of **2.1$_Y$** and **2.2$_{Dy}$** clearly demonstrate the effect of steric crowding through the cyclopentadienyl ligand bound to the yttrium atom. It can be seen that **2.1$_Y$** has a more linear structure through the metals, with the isocarbonyl groups very much in the equatorial plane (where the Cp centroid defines the principal axis), this is described as a "transoid conformation" by Sobaczynski *et al*.[63] It could be suggested this coordination environment might be better suited to a lanthanide that displays a prolate magnetic-ground state, such as erbium, as these favour strong equatorial ligand coordination. [20]

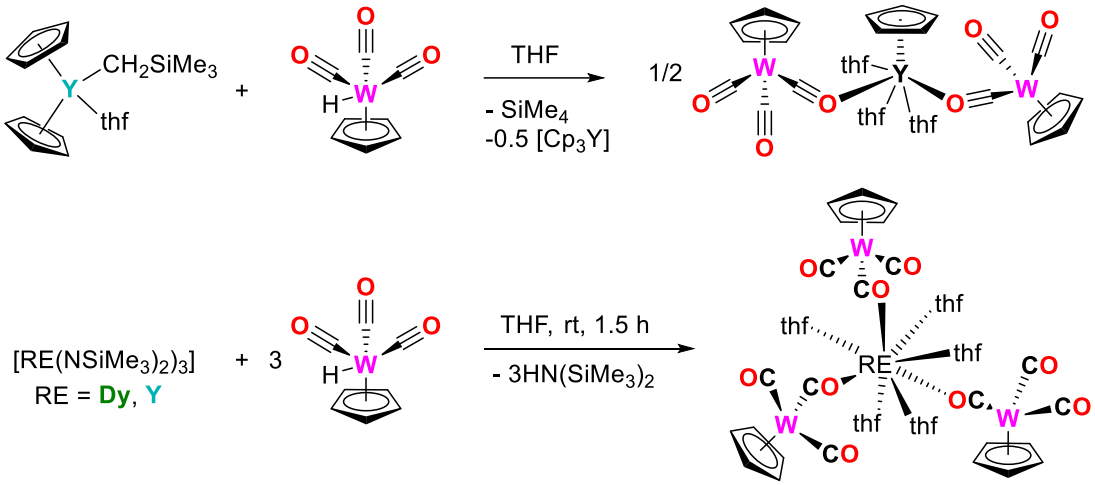

Scheme 2.1: Synthetic route to **2.1**$_{Y}$ and **2.2**$_{Y}$, **2.2**$_{Dy}$. [60,63]

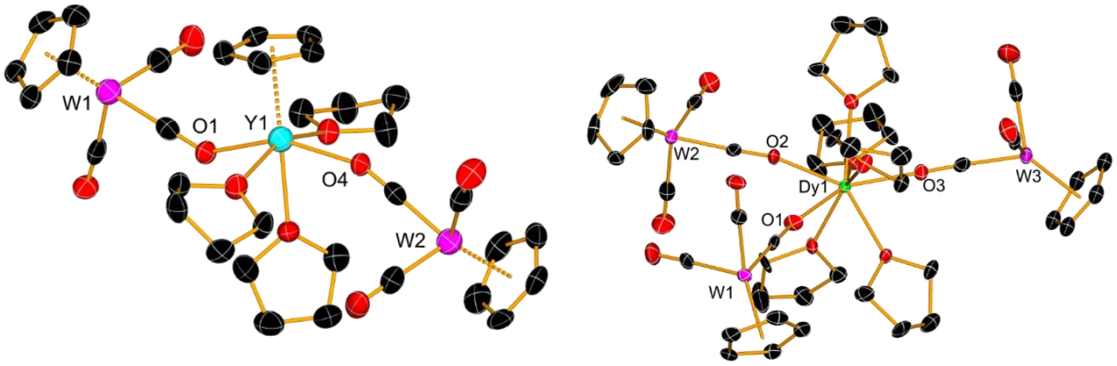

Figure 2.1:Thermal ellipsoid representation of **2.1**$_{Y}$ and **2.2**$_{Dy}$ (hydrogens omitted for clarity, ellipsoids set to 50% probability).[63]

Inspired by these pieces of work, tungsten carbonyl complexes were targeted to investigate the effects on the magnetic properties of an SMM of the strong back-bonding between the 5d metal and the carbonyl (CO) bond compared with similar systems such as **1.22**$_{Dy}$.

2.2 Previous Work and Research Aim

A pertinent example for SMMs of the application of carbonyl groups to form a bridge between a transition metal and a lanthanide is the dysprosium-iron carbonyl SMM synthesised in 2016 by the Layfield group.[28] This was the basis for the research on heterobimetallic SMMs. The complex, formed through a 1:1 salt metathesis between $[Cp^*_2Dy][BPh_4]$ and $K[CpFe(CO)_2]$, led to the isolation of the centrosymmetric dimer $[Cp^*_2Dy\{\mu\text{-}(OC)_2FeCp\}]_2$ (**2.3$_{Dy}$**).

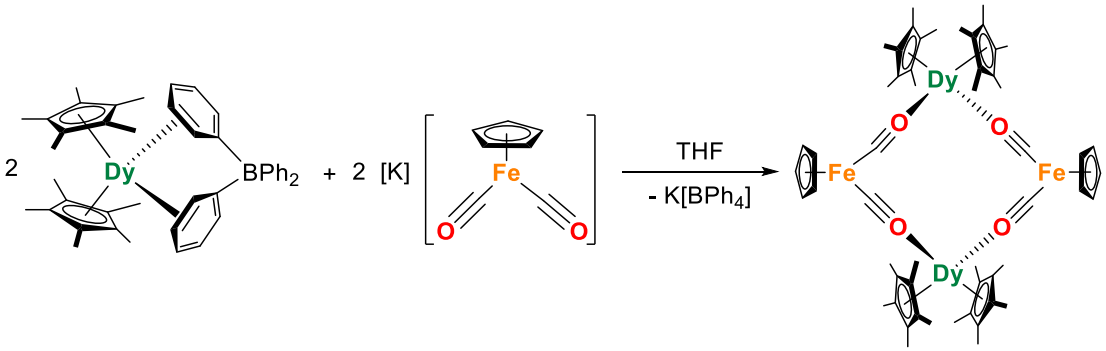

Scheme 2.2: Synthetic route to **2.3$_{Dy}$**.

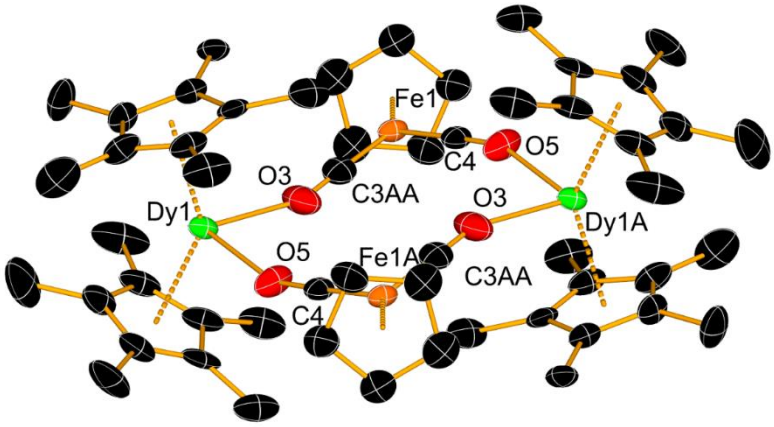

Figure 2.2: Thermal ellipsoid representation of **2.3$_{Dy}$** (hydrogens omitted for clarity, ellipsoids set to 50% probability).[28]

A heavy 5d-block metal could exhibit greater back bonding to the CO ligand than is seen with a 3d metal such as iron. This in turn would lead to a perturbed equatorial crystal field compared with reported, analogous complexes. [64] The ac (alternating current) magnetic susceptibility studies of **2.3$_{Dy}$** showed an anisotropy barrier of U_{eff}/k_BT = 662(2) cm^{-1}, remarkably high for a complex displaying such equatorial coordination of oxygen atoms from the isocarbonyl groups at the dysprosium metal centre. Moreover, as there are very few examples of carbonyl bridged d-/f-heterobimetallic complexes supported by the [CpM(CO)$_x$] motif, further studies of the magnetic properties of such complexes is warranted,[28,60] to expand our understanding of these particular systems and to see if any guiding ideas can be rationalised for further work in the field.

2.3 Results and Discussion

2.3.1 Synthesis and Solid-State Structure of $[Cp^*_2Ln(\mu\text{-}OC)_2CpW(CO)]_\infty$ and $[Cp^*_2Gd(THF)(\mu\text{-}OC)_2CpW(CO)]_\infty$

The complexes $[Cp^*_2Ln(\mu\text{-}OC)_2CpW(CO)]_\infty$ (**2.4$_Y$**, **2.4$_{Dy}$**) and $[Cp^*_2Gd(thf)(\mu\text{-}OC)_2CpW(CO)]_\infty$ (**2.4$_{Gd}$**) were synthesised *via* a salt metathesis reaction between $[Cp^*_2Ln][BPh_4]$ and $Na[CpW(CO)_3]$ in THF at 0 °C which was then allowed to warm to room temperature (Scheme 2.3).[28,65] Initial attempts at synthesising the transition metal precursor, $Na[CpW(CO)_3]$, were unsuccessful when directly following the published literature preparation.[65] Strict adherence to the published reaction time of one day led to a maximum of 40 % conversion and a mixture of NaCp, $Na[CpW(CO)_3]$ and $W(CO)_6$, which could not be separated.[65] Monitoring the reaction by ^{1}H NMR spectroscopy showed that the reaction time had to be extended to four days to achieve complete consumption of the reagents. Complexes **2.4$_Y$**, **2.4$_{Dy}$**, and **2.4$_{Gd}$** were isolated in yields of 43%, 39% and 35%, respectively.

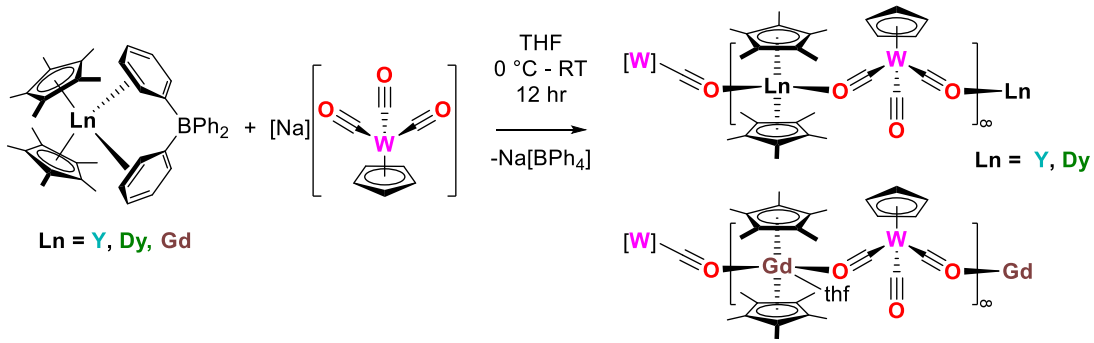

Scheme 2.3: Synthesis of **2.4$_{Ln}$**, showing a segment of polymeric structures.

All the complexes described herein are air and moisture sensitive, however in the solid-state visible decomposition was not observed after 30 minutes. This is presumably due to the polymeric nature of the solid-state structure.[66] The polymeric nature of the novel complexes described in this chapter were not expected. The analogous **1.22$_{Dy}$** adopts a dimeric structure and it was anticipated this would me emulated with the complexes **2.4$_{Y}$**, **2.4$_{Dy}$** and **2.4$_{Gd}$** though with potentially great deviation from the ideal shape as a result of the larger ionic radii of tungsten(I) *vs*. iron(I).

Crystals of **2.4$_{Y}$**, **2.4$_{Dy}$** and **2.4$_{Gd}$** suitable for solid-state studies by X-ray diffraction were grown either by layering hexanes onto a saturated THF solution or by vapour diffusion of hexanes into a saturated THF solution leading to the formation of yellow crystals for all complexes. The complexes **2.4$_{Y}$** and **2.4$_{Dy}$** are isostructural and crystallise in the monoclinic $P2_{1/n}$ space group, whereas **2.4$_{Gd}$** differs by a THF molecule coordinating to the gadolinium and crystallises in the monoclinic $P2_{1/c}$ space group. For both **2.4$_{Y}$** and **2.4$_{Dy}$**, the asymmetric unit contains one molecular unit differing again to **2.3$_{Gd}$** which has two molecular units of [Cp*$_2$Gd(THF)(μ-OC)$_2$CpW(CO)] per asymmetric unit. The solid-state structures can be seen in Figures 2.3 – 2.6 and a summary of relevant bond lengths and angles for the complexes **2.4$_{Y}$**, **2.4$_{Dy}$** and **2.4$_{Gd}$** are given below in Table 2.1.

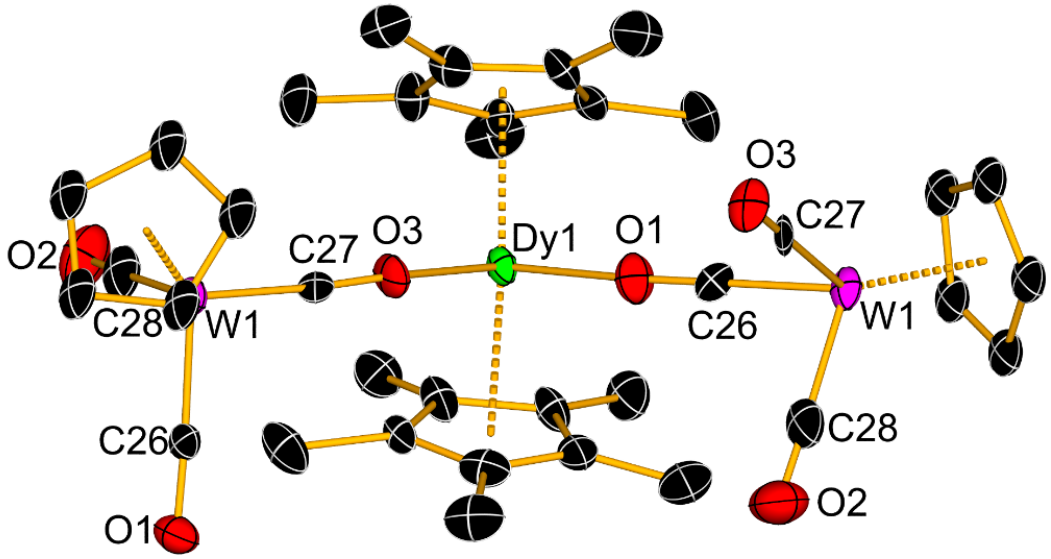

Figure 2.3: Thermal ellipsoid representation of the asymmetric unit in the polymeric structure of **2.4$_{Dy}$** (hydrogens omitted for clarity, ellipsoids set to 50% probability).

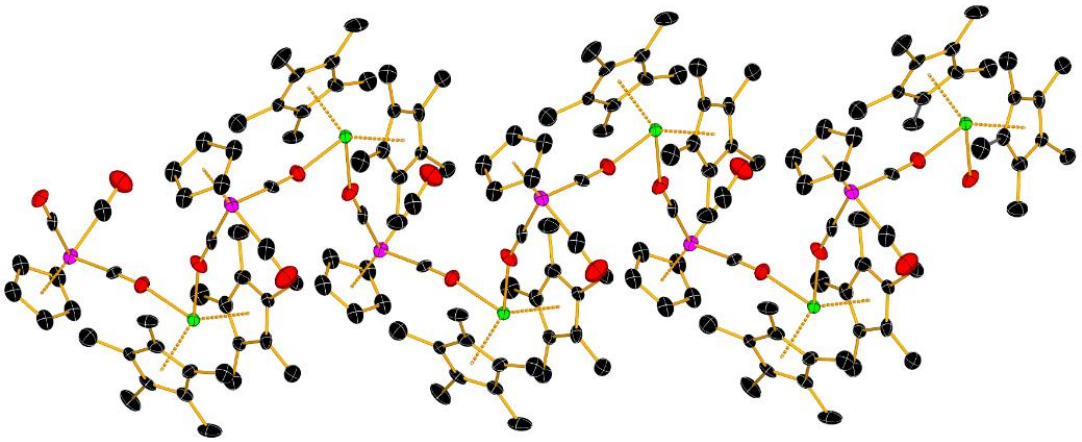

Figure 2.4: Thermal ellipsoid representation the expansion of **2.4$_{Dy}$** along the b-axis (dysprosium = green, tungsten = purple, carbon = black, oxygen = red, hydrogens omitted for clarity, ellipsoids set to 50% probability).

Table 2.1: Selected bond lengths and angles for **2.4$_{Y}$**, **2.4$_{Dy}$** and **2.4$_{Gd}$**.

	Bond / Å		**Angle / °**
Cp^*_{cent}-Y	2.341(18)-2.347(4)	Cp^*_{cent}-Y- Cp^*_{cent}	138.09(7)
Cp_{cent}-W	2.064(17)-2.065(16)	Cp^*_{cent}-Y-CO	77.90(15)-107.51(15)
μC-O	1.198(5)-1.199(6)	C-W-C	89.60(4)
C-O (terminal)	1.161(6)	O-Y-O	85.66(11)
Y···Y	7.9155(5)		
Cp^*_{cent}-Dy	2.346(4)-2.348(4)	Cp^*_{cent}-Dy-Cp^*_{cent}	138.74(16)
Cp_{cent}-W	2.009(5)	Cp^*_{cent}-Dy-CO	75.5(3)°-104.5(3)
μC-O	1.178(11)-1.204	C-W-C	90.22(17)
C-O (terminal)	1.167(3)	O-Dy-O	85.30(3)
Dy···Dy	7.9207(7)		
Cp^*_{cent}-Gd	2.421(3) - 2.463(6)	Cp^*_{cent}-Gd-Cp^*_{cent}	137.92-138.81(18)
Cp_{cent}-W	2.014(8)–2.044(12)	Cp^*_{cent}-Gd-CO	94.72-97.89
μC-O	1.187(8)– 1.206(9)	C-W-C	88.00(4)-92.75(4)
C-O (terminal)	1.165(19)–1.180(2)	O-Gd-O	146.02(18) – 147.04(17)

For the complex **2.4$_{Dy}$**, the Cp*-Ln-Cp* angle is 138.74(16)° which is slightly less obtuse than the those of the iron analogue **2.3$_{Dy}$** which shows an angle of 141.50(5)° and 141.50(2)°.[28] This deviates from the ideal, perfectly axial system that is desirable, though not essential, for dysprosium-based SMMs.[20] The complex **2.3$_{Y}$**, exhibits a ∠Cp*-Ln-Cp* bond angle of 138.09(7)°, which is again less obtuse than the iron

analogue **2.2$_{Y}$** which shows an angle of 141.50(5)°.[28] Complex **2.3$_{Gd}$** exhibits a Cp*-Ln-Cp* angles in the range 137.92-138.81(18)°, showing almost no significant chemical difference to the non-solvent containing complexes **2.3$_{Y}$** and **2.3$_{Y}$**, as the asymmetric unit differs due to the coordinating of a THF molecule to the gadolinium metal (Figure 2.4 and Figure 2.5). These suggest that the steric bulk provided by the Cp* ligands is of sufficient size to prevent solvent coordination for the smaller trivalent cations of yttrium and dysprosium metals but not for the larger gadolinium cation.

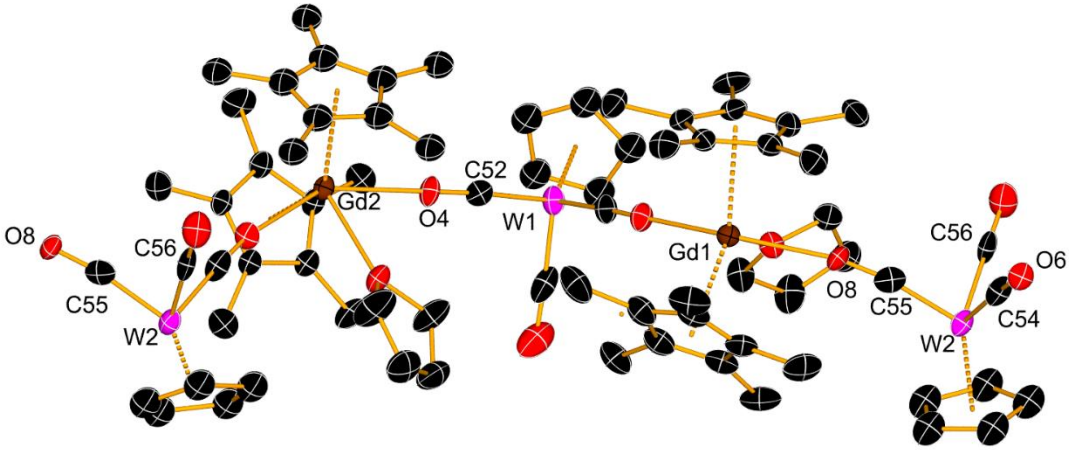

Figure 2.4: Thermal ellipsoid representation of the asymmetric unit in the polymeric structure of **2.4$_{Gd}$** (hydrogens omitted for clarity, ellipsoids set to 50% probability).

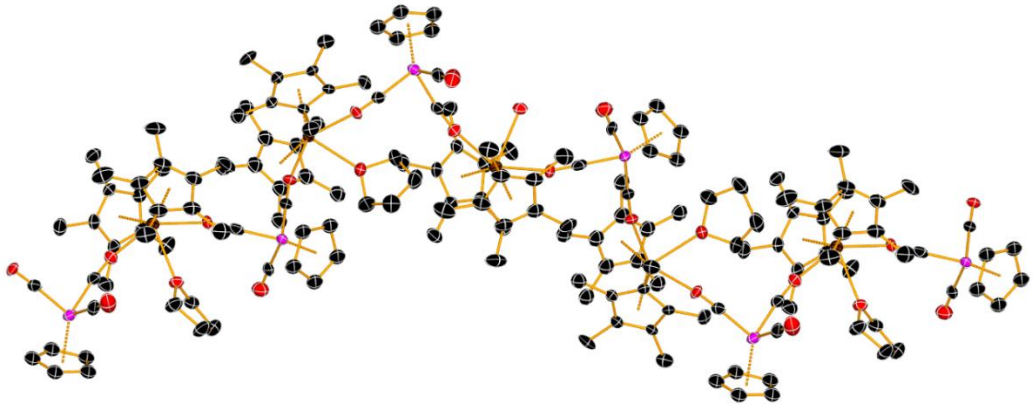

Figure 2.5: Thermal ellipsoid representation of **2.4$_{Gd}$** along the b-axis (gadolinium = brown, tungsten = purple, carbon = black, oxygen = red, hydrogens omitted for clarity, ellipsoids set to 50% probability).

The length of the axial ligand-metal distance has been shown to affect the magnetic properties of SMMs, where the closer the axial ligand is to the metal the greater the stabilisation of the ground m_J state and thus the greater the performance of the SMM if the relaxation is dominantly *via* the Orbach process.[1,3,20] In dysprosium metallocene SMMs, the Cp ligands are known to provide a dominant axial crystal field.[34] The Ln-Cp*$_{cent}$ (Ln = Y, Dy) bond lengths are 2.341(18)-2.347(4) Å for **2.4$_{Y}$** and 2.346(4)-2.348(4) Å for **2.4$_{Dy}$**. These are, chemically, significantly longer than the Dy-Cp*$_{cent}$ bond length of 2.296(1) Å for the record SMM **1.27$_{Dy}$**, but are similar to those of **2.3$_{Y}$** and **2.3$_{Dy}$** which shows distances of 2.332(16)-2.339(14) and 2.339(7)-2.344(7) Å, respectively. However, complex **2.4$_{Gd}$** exhibits an increased Ln-Cp*$_{cent}$ bond length to 2.421(3)-2.463(6) Å. This can tentatively be attributed to the THF molecule coordinated to the metal affecting the interactions between the Cp* ligands and the metal.

The relevance of the ligand field to SMM properties with respect to oblate lanthanides has been described earlier and thus, the equatorial component of the crystal field must be considered. In the complexes **2.4$_{Y}$** and **2.4$_{Dy}$**, the ∠O-Ln-O bonding angles are 85.66(11)° and 85.30(3)°, respectively. This is similar to the values of 87.40(1)° and 87.50(4)° reported for **2.3$_{Y}$** and **2.3$_{Dy}$**.[28] The corresponding angles for **2.4$_{Gd}$** are 146.02(18)-147.07(17)°, a widening of almost 60° compared with the yttrium and dysprosium analogues, which is attributed to the THF ligand. In the cases of Kempe's **2.1$_{Y}$** and Nippe's **2.2$_{Dy}$** the analogous angle is 154.3(2)° and 141.8(2)°,

respectively.[60,63] However, these complexes possess one (**2.1$_{Y}$**) or no (**2.2$_{Dy}$**) solvato ligands on the lanthanide, allowing solvent molecules to enter the coordination sphere resulting in the structural differences noted in this Section.

The ligands occupying the equatorial field of the dysprosium in a Dy-SMM can greatly perturb the g_Z component (the *g*-tensor in the *z* direction) of the electron density leading to diminished SMM properties (Chapter 1).[20] Thus, the distances between the oxygen atoms of the isocarbonyl ligands and the lanthanides is critical to understanding the magnetic properties of these complexes. The Ln-O distances for **2.4$_{Y}$** are in the range 2.288(4)-2.291(3) Å and for **2.4$_{Dy}$** are 2.304(6)-2.309(4) Å. The comparable lengths in the complexes **2.3$_{Y}$** and **2.3$_{Dy}$** are 2.264(19)-2.270(3) Å and 2.287(12)-2.293(9) Å, respectively. It can be seen that the isocarbonyl ligands are at a greater distance from the lanthanide in the lanthanide-tungsten complexes **2.4$_{Y}$**, **2.4$_{Dy}$**, and **2.4$_{Gd}$** presented here than in the iron analogue **2.3$_{Dy}$**.[28] They are also larger than the Ln-O lengths of 2.262(7)-2.285(7) Å exhibited by **2.1$_{Y}$** , but are chemically similar to those in **2.2$_{Dy}$** - 2.270(6)-2.320(6) Å. [60,67] For **2.4$_{Gd}$**, the Ln-O distances are 2.397(5)-2.428(5) Å, which is much longer than for the non-solvated complexes, as well as the iron analogues (**2.3$_{Dy}$**) and other complexes containing the {CpW(CO)$_3$} fragment (**2.1$_{Y}$**, **2.2$_{Dy}$**, **2.3$_{Y}$**, **2.3$_{Dy}$**).[28,60,67]

A key difference between the structures of **2.4$_{Ln}$** and the iron-based complexes **2.3$_{Y}$** and **2.3$_{Dy}$** is the lack of a terminal carbonyl in the latter. The C-O bond length of the terminal CO ligand in **2.4$_{Y}$** and **2.4$_{Dy}$** are 1.161(6) Å and 1.167(3) Å, respectively. For **2.4$_{Gd}$** the terminal C-O bond lengths are between 1.165(19) Å and 1.180(2) Å, the large variation seen here is reflected in the asymmetry of the molecular fragment.

For **2.1$_{Y}$** and **2.2$_{Dy}$**, the terminal C-O bond lengths are 1.155(14) Å, 1.200(14) Å and 1.156(10), 1.176(11) Å, respectively.[60,67]. The crystal structure of Na[CpW(CO)$_3$)] has not been reported and attempts to grow crystals mirroring suitable for solid-state studies were not successful, therefore comparisons cannot be made. The methods attempted were those that were successful for other complexes in this thesis alongside those reported for analogous complexes in the literature.

Each of the complexes, **2.4$_{Y}$**, **2.4$_{Dy}$**, and **2.4$_{Gd}$**, for chains which extend along the *b*-axis but display no obvious intermolecular bonding interactions such as hydrogen bonding. The nearest intermolecular metal-metal distance for **2.4$_{Y}$** is 9.3929(7) Å, for **2.4$_{Dy}$** the distance is 9.3599(5) Å, and for **2.4$_{Gd}$** the distance between metal centres is 9.2740(7) Å. It is apparent that though the coordination of THF to the Gd metal altering the structure of **2.4$_{Gd}$** relative to either **2.4$_{Y}$** and **2.4$_{Dy}$**, it has not had a significant effect on the packing of the molecules. The molecules are at such distances that inter chain interactions would be at best only weak interactions.[68]

Overall, the novel lanthanide-tungsten complexes **2.4$_{Y}$**, **2.4$_{Dy}$**, and **2.4$_{Gd}$** show structural features in line with their closest analogues, **2.1$_{Dy}$** and **2.2$_{Dy}$**. These exhibit the greatest similarities when compared parameter by parameter.[28] The principal, and most obvious, difference is the polymeric nature of the new complexes described herein and the dimeric structures previously published (Figures 2.1, 2.3 – 2.6).[28]

2.3.2 Solution-State Analysis of $[Cp^*_2Y(\mu\text{-}OC)_2CpW(CO)]_\infty$ by NMR spectroscopy

The ^{1}H NMR spectrum in d_8-THF at 298 K of $[Cp^*_2Y(\mu\text{-}OC)_2CpW(CO)]_\infty$ (Appendix 1, Figure S2.3) shows two clear singlets at 5.29 ppm and 1.96 ppm, which correspond to the C*H* of the Cp ring and the methyl protons of the Cp* rings, respectively, integrating in the ratio 5:30. This spectrum agrees with the solid-state structure that there is one Cp to two Cp* rings, but retention of structure in solution cannot be established as this only confirms the empirical formula is the same. The $^{13}C\{^1H\}$ NMR spectrum (Figure S2.4) displays signals at 119.01 ppm (C_5Me_5), 87.13 ppm (C_5H_5) and 10.71 ppm (C_5Me_5). Both the ^{1} the $^{13}C\{^1H\}$ NMR spectra agree with reported shifts for **2.2$_Y$**, with downfield shifts for nuclei bound to tungsten.[28] Unfortunately, observation of the CO peak of the $[CpW(CO)_3]^-$ unit was not possible. This is consistent with the lack of a reported *C*O peak in the ^{13} $C\{^1H\}$ NMR of **2.2$_Y$**. [28] Unfortunately, ^{89}Y NMR experiments were not available on the spectrometers accessible.

2.3.3 Infrared Spectroscopy of $[Cp^*_2Ln(\mu\text{-}OC)_2CpW(CO)]_\infty$ (Ln = Y, Dy) and $[Cp^*_2Gd(thf)(\mu\text{-}OC)_2CpW(CO)]_\infty$

IR spectroscopic studies conducted on powdered single-crystal samples revealed clear evidence of the retention of the carbonyl groups in the bulk samples and so supplements the ^{13}C NMR spectrum. The CO stretching vibrations of the complexes **2.4$_{Y}$**, **2.4$_{Dy}$** and **2.4$_{Gd}$** display similar shifts across the series consistent with the formation of isocarbonyl linkages, see Table 2.2.[65]

The precursor $Na[CpW(CO)_3]$ exhibits dramatically different positions for the carbonyl groups (1873 cm^{-1} and 1701 cm^{-1}, Figure S2.5) compared with the spectra for **2.4$_{Y}$**, **2.4$_{Dy}$** and **2.4$_{Gd}$**. Further, the precursor $Na[CpW(CO)_3]$ only exhibits two bands in the IR spectrum whereas the lanthanide complexes **2.4$_{Ln}$** all show three bands. This correlates to a group theory treatment of the precursor *vs*. the lanthanide complexes as explained by Cotton *et al.*, where the lowering of the symmetry from C_{3v} to C_1 affects the available stretching modes.[69]

The terminal carbonyls for all of the lanthanide complexes described herein exhibit stretching frequencies that are shifted to higher wavenumbers relative to the precursor $Na[CpW(CO)_3]$ (Table 2.2) which implies a weakening of the C-O bond in **2.4$_{Ln}$**. The terminal carbonyl stretching frequency is shifted to higher wavenumbers due to a reduction in the back-bonding into the π orbital and, therefore, an increase of the strength of the bond. This is corroborated by the differing bonds lengths of the previously described.

The complex **2.3$_{Gd}$** shows an additional feature in the terminal CO stretching band at 1613 cm^{-1}, possessing a shoulder, which can due to the presence of two crystographically different gadolinium centres.

Table 2.2: Summary of carbonyl IR frequencies for Na[CpW(CO)$_3$] **2.3$_Y$**, **2.3$_{Dy}$**, **2.3$_{Gd}$** and **2.2$_{Dy}$**. [28]

	Na[CpW(CO)$_3$]	**2.4$_Y$**	**2.4$_{Dy}$**	**2.4$_{Gd}$**	**2.3$_{Dy}$**
		ν / cm^{-1}	**ν / cm^{-1}**	**ν / cm^{-1}**	**ν / cm^{-1}**
μ-CO		1734	1724	1754	1789
		1614	1633	1613	1721
$CO_{terminal}$	1872, 1701	1915	1916	1916	-

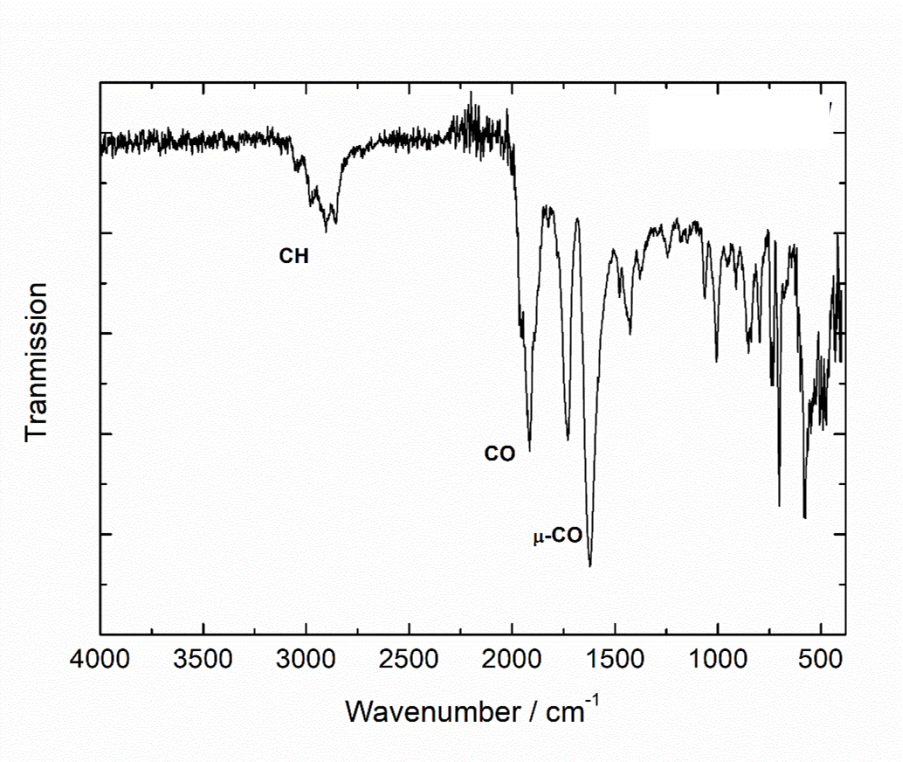

Figure 2.6 IR spectrum of **2.4$_Y$**.

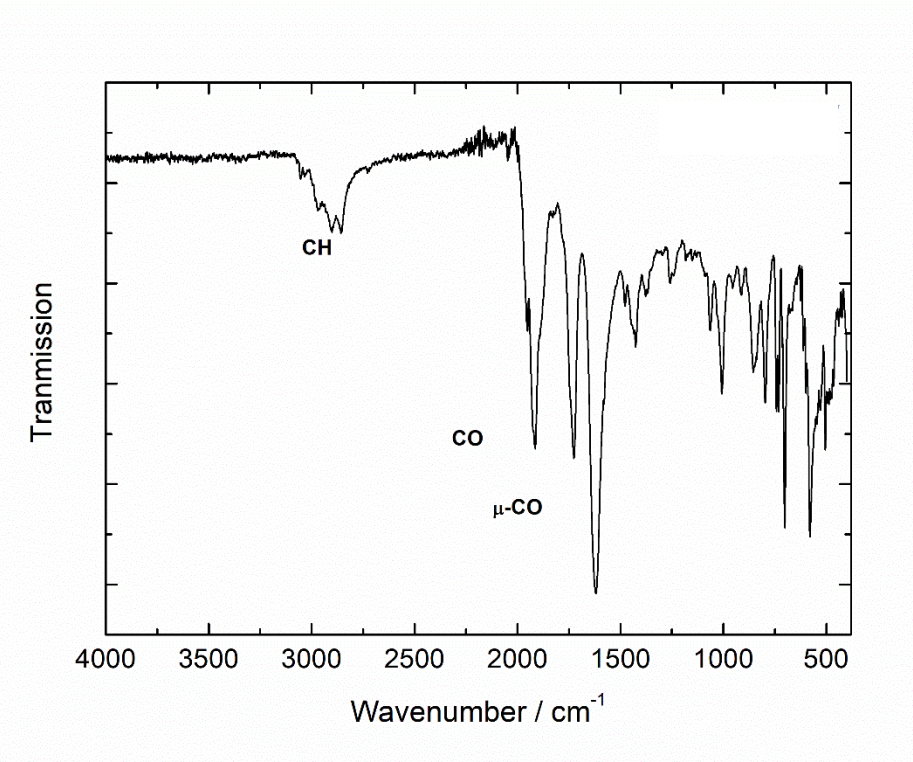

Figure 2.7: IR spectrum of **2.4**$_{Dy}$.

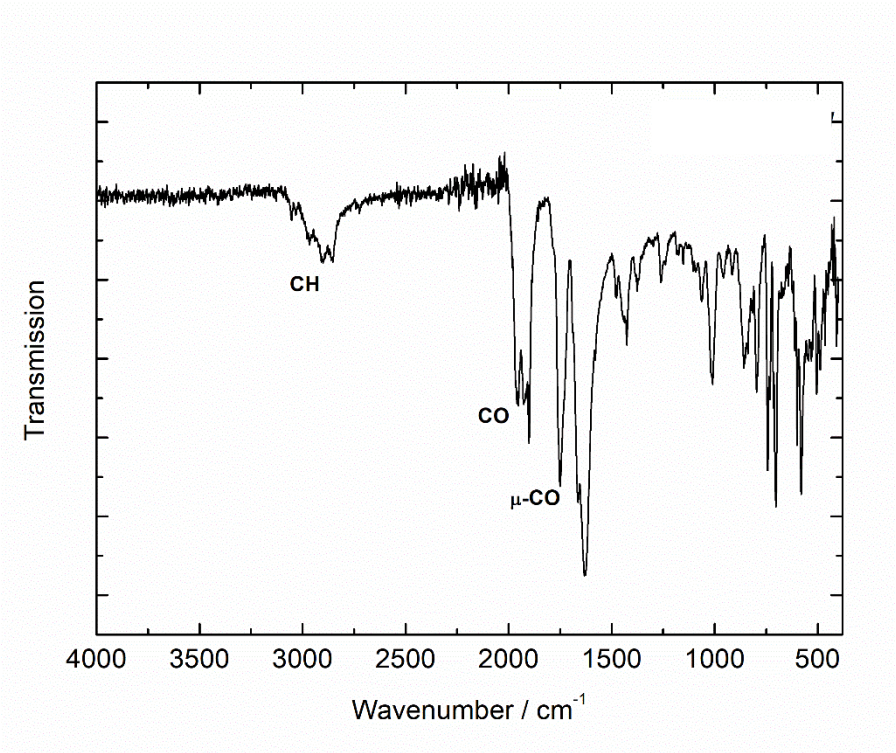

Figure 2.8: IR spectrum of **2.4**$_{Gd}$.

2.3.4 Magnetic Properties of $[Cp^*_2Dy(\mu\text{-}OC)_2CpW(CO)]_\infty$, $[Cp^*_2Dy_{0.1}Y_{0.9}(\mu\text{-}OC)_2CpW(CO)]_\infty$, and $[Cp^*_2Gd(thf)(\mu\text{-}OC)_2CpW(CO)]_\infty$

To determine if the complex $\mathbf{2.3_{Dy}}$ would display characteristic SMM behaviour, isothermal field dependence measurements of the magnetisation (*M*) *vs*. field/temperature (*B/T*) were conducted on a microcrystalline sample within the temperature range of 1.9-5.0 K. (Figure 2-12). The behaviour shows a non-superimposable nature thereby confirming that non-zero magnetic anisotropy.[70,71] The theoretical maximum value of *M* at saturation (M_{sat}) for a Dy^{3+} ion is 10.65 N_AB.[64,72,73] It can be seen that complex $\mathbf{2.3_{Dy}}$ reaches a maximum value of 5.04 N_AB. That $\mathbf{2.3_{Dy}}$ does not achieve this even at saturation and in a field of strength 7.0 T at 1.9 K is further evidence for the retention of anisotropy.[2] $\mathbf{2.3_{Gd}}$ displays a M_{sat} value of 6.65 N_AB which is close to the theoretical maximum of 7.00 N_AB. (Figure S2.6).

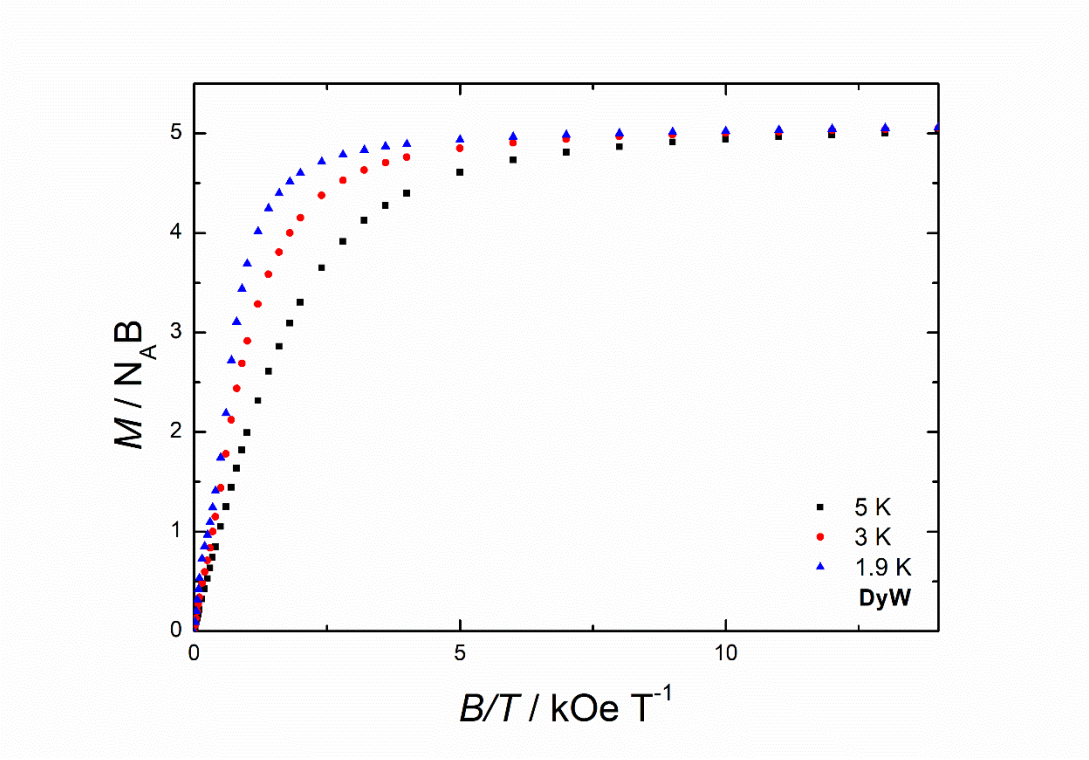

Figure 2.9: Magnetisation (*M*) *vs*. field/temperature (*B/T*) for **2.4**$_{Dy}$.

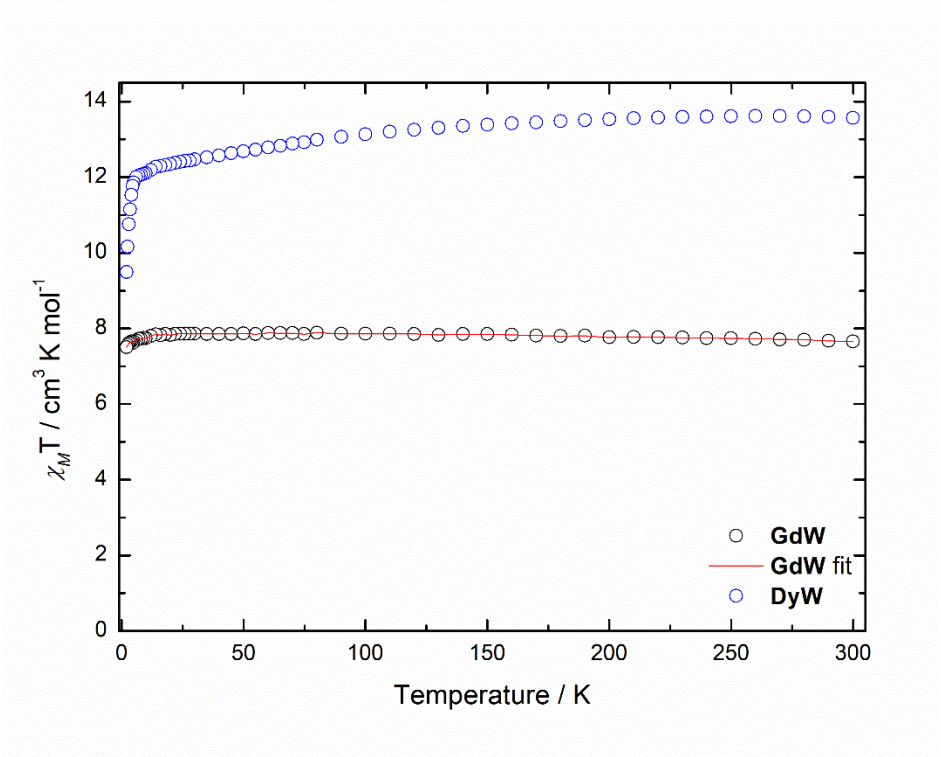

Figure 2.10: Plot of $\chi_M T$(T)in an applied field of 1000 Oe for **2.4**$_{Dy}$ and **2.4**$_{Gd}$. Solid line for **2.4**$_{Gd}$ represents the fit calculated using zJ = −0.001 cm^{-1}. [74]

The temperature dependence of the molar magnetic susceptibility, $\chi_M T$(T), for complexes **2.3$_{Dy}$** and **2.3$_{Gd}$**, was measured in a static dc field of 1000 Oe. At 300 K, $\chi_M T$ for **2.3$_{Dy}$** is 13.57 cm^3 K mol^{-1} and the value steadily lowers until 10 K where there is a sudden decrease to 9.49 cm^3 K mol^{-1} at 2 K. This indicates a thermal depopulation of the Dy^{3+} M_J states, possibly combined with a very weak anti-ferromagnetic exchange.[21,75–77] The susceptibility for **2.3$_{Gd}$** shows very little temperature dependence, decreasing from a value of 7.66 cm^3 K mol^{-1} at 300 K to reach 7.51 cm ^{3} K mol^{-1} at 2 K. This small decrease could be the result of a very weak anti-ferromagnetic interaction between chains. To confirm this, a fit of the data was conducted using *PHI* [74] (Figure 2.10) with the spin Hamiltonian shown below (Equation 2.1). Here, μ_B is the Bohr magneton, *B* is the magnetic induction, *S* is the total spin of the system, g_{Gd} is the Landé factor for gadolinium with a value of 1.99, and zJ = - 0.001 cm^{-1} representing an interchain exchange.

$$\hat{\mathcal{H}} = g_{Gd} \cdot \mu_B \cdot \vec{B} \cdot \vec{S} + zJ$$

Equation 2.1: Spin Hamiltonian used to fit **2.4$_{Gd}$**.

The SMM properties of complexes **2.4$_{Dy}$** were investigated through dynamic (ac) magnetic susceptibility measurements using an oscillating field of 3 Oe and zero applied dc field. The out-of-phase (imaginary component) of the ac susceptibility (χ'') was measured as a function of the ac frequency (ν) over the temperature range 1.9 – 52 K, showing clear maxima up to 42 K (Figure 2.11). Between 1.9 K and 22 K the

position of the maxima does not shift, which is a common sign of relaxation occurring through a quantum-tunnelling of the magnetisation (QTM).[78]

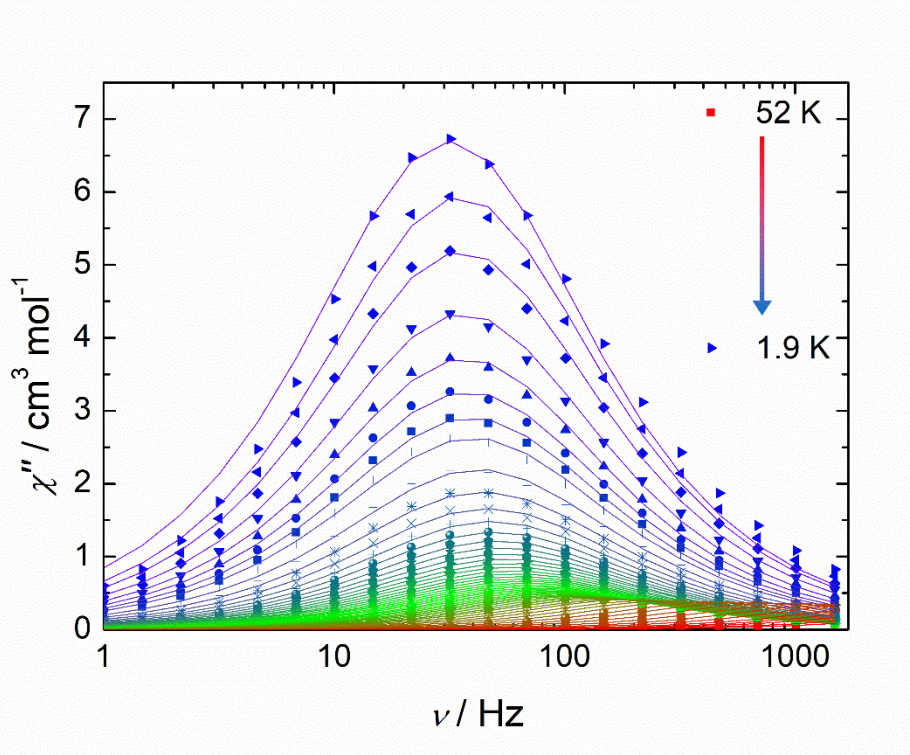

Figure 2.11: Frequency dependence of the out-of-phase (χ'') magnetic susceptibility for **2.4$_{Dy}$** in zero applied field.

From 22 K through to the maximum measured temperature of 52 K, the maxima χ'' shifts to higher frequencies due to the relaxation process becoming predominantly thermally-activated rather than just pure QTM. Plotting the in-phase (real) component of the ac susceptibility (χ') against the out-of-phase (imaginary) χ'' generates a Cole-Cole plot which exhibits purely parabola shaped curves (Figure 2.12). These were fitted with α = 0 – 0.148 which demonstrates a narrow range of relaxation times.

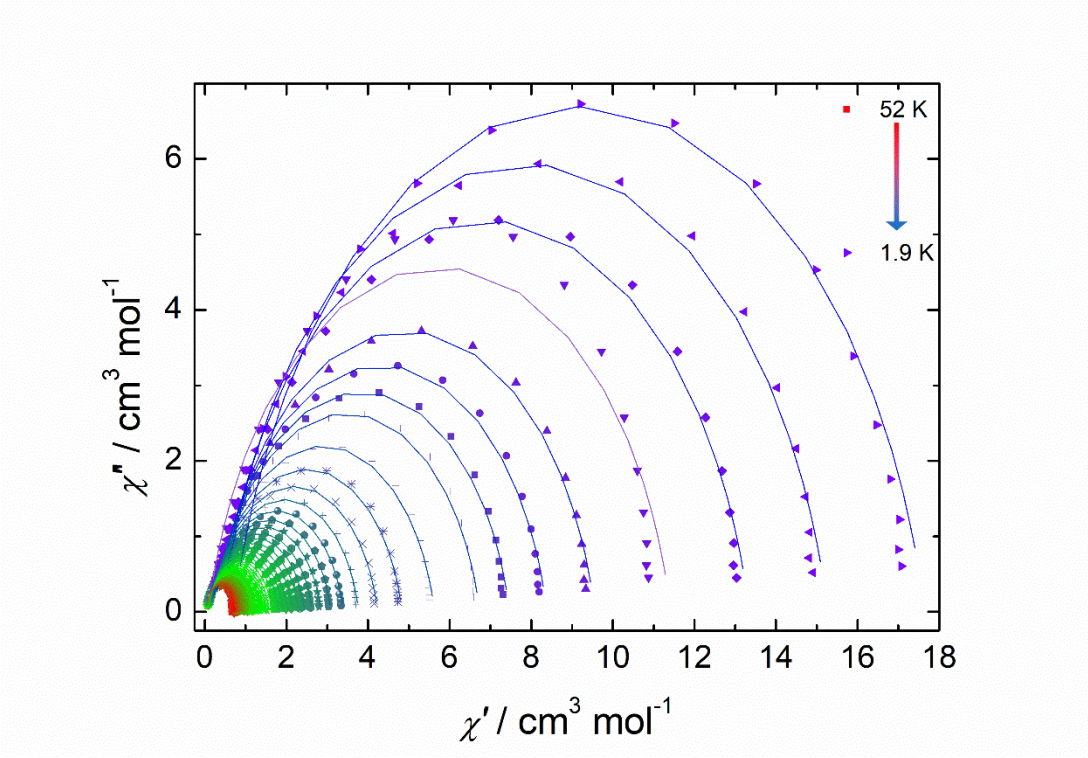

Figure 2.12: χ' vs. χ'' for **2.4$_{Dy}$** in zero applied field. The solid lines are fits to the experimental data with α = 0 – 0.148.

The value of τ, were extracted from the data obtained from the Cole-Cole plot. Next, a plot of the inverse (τ^{-1}) *vs.* temperature (Figure 2.13) was produced. A fit of this data was achieved using Equation 2.2, where τ_0 represents the pre-exponential factor, *C* is the Raman coefficient, *n* is the Raman exponent and τ_{QTM}^{-1} is the rate of QTM.[64]

$$\tau^{-1} = \tau_0^{-1} \cdot e^{-U_{eff}/k_BT} + CT^n + \tau_{QTM}^{-1}$$

Equation 2.2: Fitting equation used for **2.4$_{Dy}$**.

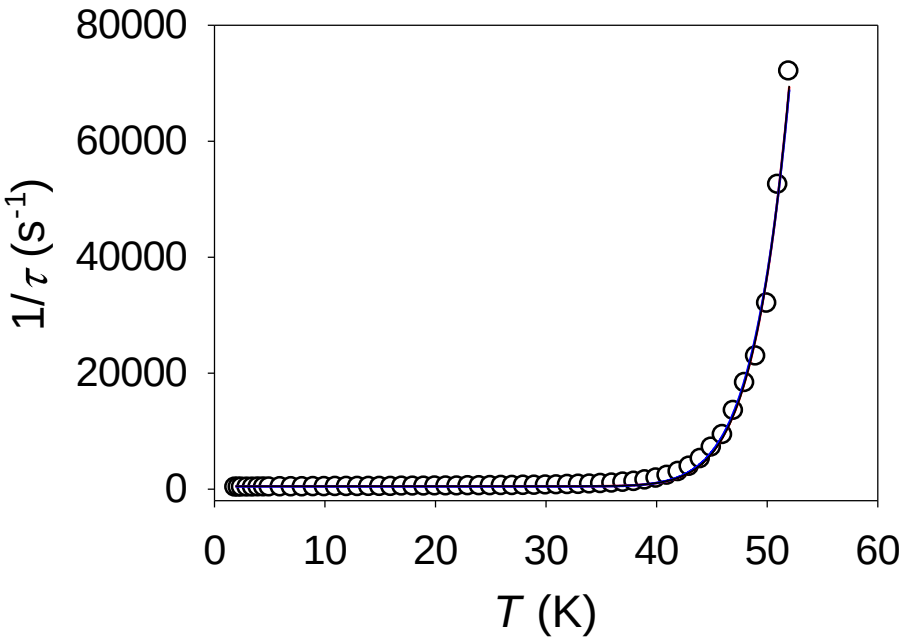

Figure 2.13: Temperature dependence of the inverse of the magnetization relaxation times (τ^{-1}) for **2.3$_{Dy}$**. U_{eff}/k_BT = 557(18) cm^{-1}, τ_o = 3 × 10^{-12} s, C = 1.34(6) × 10^{-9} s^{-1} K^{-n}, n = 3, τ_{QTM} = 3.71(8) ms.

The anisotropy barrier extracted from the data for **2.4$_{Dy}$**, using Equation 2.2, is reasonably large for an SMM at U_{eff}/k_BT = 557(18) cm^{-1}. It is much higher than the related SMM **2.2$_{Dy}$** (U_{eff}/k_BT = 12.6 cm^{-1}) [60] but smaller than that of **2.2$_{Dy}$** (U_{eff}/k_BT = 662 cm^{-1})[28] and drastically lower than the benchmark **1.27$_{Dy}$** (U_{eff}/k_BT = 1,541 cm^{-1}).That the barrier of **2.4$_{Dy}$** is smaller than **2.3$_{Dy}$** suggests that the isocarbonyl groups are imposing a greater effect for the former complex, as a result of the 5*d* metal.

The fast rate of QTM , τ_{QTM} = 3.71(8) ms, displayed by **2.4$_{Dy}$** suggests that it should show very little, if any, magnetic hysteresis properties which was confirmed through measurements of the magnetisation versus field loops (Figure 2.14). The study was conducted at 1.9 K with a sweep rate of 28 Oe s^{-1} and it is evident from the narrow,

S-shaped loop that **2.4$_{Dy}$** displays very weak hysteresis. It can be seen that there are step-like movements which is a further confirmation of strong QTM.

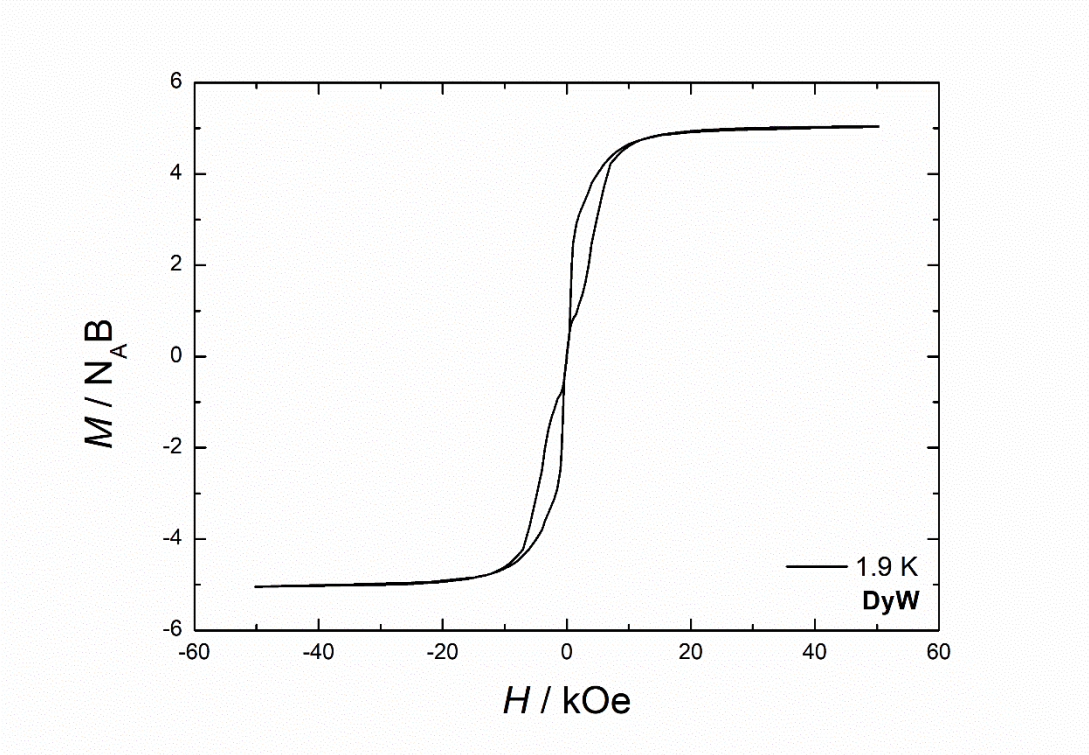

Figure 2.14: Magnetization (*M*) vs field (*H*) hysteresis loop for **2.3$_{Dy}$**, scan rate of 28 Oe s^{-1}.

As described in Section 2.3.1, the Ln-OC bond lengths are greater in the complexes **2.4$_{Y}$**, **2.4$_{Dy}$** and **2.4$_{Gd}$** than they are in the iron-analogues **2.3$_{Y}$** and **2.3$_{Dy}$**, by approximately 0.020(2) Å and 0.016(5) Å, respectively. The ∠O-Ln-O angles show no significant deviation between **2.4$_{Ln}$** and those in **2.3$_{Ln}$**. Thus, it followed that this may have led to an enhancement of the magnetic properties of the tungsten-carbonyl complexes as the effect of perturbation on the equatorial field should be diminished due to the longer bonds between the oxygen and the lanthanide.[20,21,79,80]

The magnetic properties displayed by **2.4$_{Dy}$** differ in many respects to those for the analogous complex **2.2$_{Dy}$**, but from considering the structural parameters of both complexes this seems to defy expectations of a better performing SMM.[20,21,28] Therefore the electronic properties of the ligand fields as a result of the back-bonding to the tungsten, which can be inferred through the infrared spectroscopy studies described in section 2.3.3, must be considered to rationalise the magnetic properties of the SMM **2.3$_{Dy}$**.

2.3.5 Computational Calculations of $[Cp^*_2Dy(\mu\text{-}OC)_2CpW(CO)]_n$

2.3.5.1 Declaration

The computational details, results and subsequent report in Section 2.3.5.2 were provided by Akseli Mansikkamäki of the Department of Chemistry, Nanoscience Centre, University of Jyväskylä, P. O. Box 35, FI-40014, Finland.

This Section can be found in work published by R. Collins, M. J. Heras Ojea, A. Mansikkamäki, J. Tang, R. Layfield, *Inorg. Chem.,* 2020, **59**, 1, 642-647. [64]

2.3.5.2 Results of CASSCF Calculations

Quantitative support for the analysis of the experimental susceptibility data was provided by an *ab-initio* computational study in which the geometry of **2.4$_{Dy}$** was extracted from the crystal structure and truncated for the multireference calculations, with one Cp^*_2Dy unit, two CpW units connected to dysprosium via the isocarbonyl ligands, and all CO ligands coordinated to the two tungsten atoms, *i.e.* $[Cp^*_2Dy\{(\mu\text{-}OC)W(Cp)(CO)_2\}_2]^-$ (**2.5$_{Dy}$**, Figure 2.15). The positions of hydrogen atoms were optimized using density functional theory and the electronic structure was modeled at the SA-CASSCF(9,7)//SO-RASSI level (see Appendix for full computational details).[81–87]

The energies and principal components of the *g*-tensors of the eight lowest Kramers doublets (KDs) arising from the crystal-field split $^6H_{15/2}$ ground multiplet for the Dy^{3+} ion are listed in Table 2.3. The *g*-tensor of the ground doublet is strongly axial (g_x = 0.0010, g_y = 0.0019, g_z = 19.5176), which should significantly reduce the rate of ground-state QTM. The principal magnetic axis of the ground KD is approximately oriented towards the centre of each Cp* ligand (Figure 2.15).

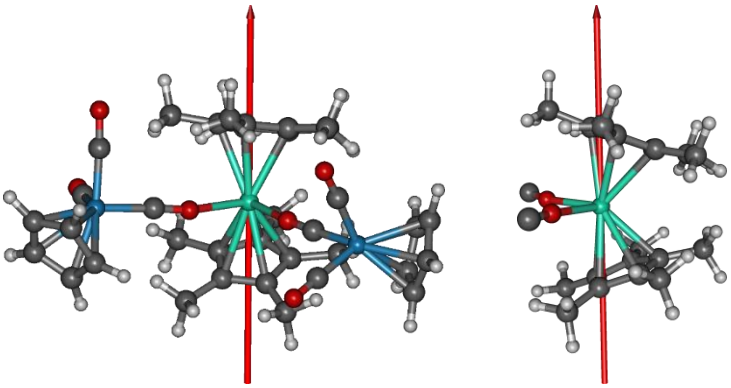

Figure 2.15: The principal magnetic axis of the ground Kramers doublet of **2.5$_{Dy}$** (left) and **2.6$_{Dy}$** (right).

Table 2.3: The energies and principal components of the g tensors of the eight lowest Kramers doublets (KDs) of **2.5$_{Dy}$** arising from the crystal-field split $^6H_{15/2}$ ground multiplet of the Dy(III) ion along with the angles (θ) between the principal magnetic axis of a given doublet and that of the ground doublet.

KD	E / cm^{-1}	g_x	g_y	g_z	θ
1	0	0.0010	0.0019	19.5176	0.0°
2	182	0.0134	0.0154	16.8468	4.4°
3	340	0.6487	0.9806	14.2336	7.1°
4	386	0.9205	1.8597	16.1142	84.4°
5	416	0.0930	2.4773	10.5826	24.0°
6	437	3.8030	6.7534	10.1946	74.3°
7	494	0.6148	1.1427	16.7089	86.3°
8	696	0.0180	0.0263	19.8289	89.6°

The axiality of the other *g*-tensors steadily decreases in the excited KDs as one moves to higher energies. The relatively large transverse components of the *g*-

tensors of the second-excited KD (g_x = 0.6487, g_y = 0.9806, g_z = 14.2336) should allow significant thermally-activated QTM. Furthermore, the principal axes of the three lowest doublets are roughly collinear, but the axis of the third excited doublet is almost perpendicular to the axis of the ground doublet. This feature of the electronic structure allows significant spin-phonon transitions and the barrier should be crossed at this point, resulting in an effective barrier of 386 cm^{-1} for the Orbach process. An approximate relaxation route was then constructed for **2.5$_{Dy}$** using previously established methodology, where the relaxation pathway is obtained by tracing the path set by largest transition moment matrix elements between the different electronic states.[88] The barrier is shown in Figure 2.16 and the numerical values of the transition magnetic moments and the squared projections of the states in the eight lowest KDs on the angular momentum states $|J_{M_J}\rangle$ with J = 15/2 are given in Table 5 and S2, respectively.

The calculation predicts relaxation via the third excited doublet, in agreement with the information obtained from the g-tensors. However, the barrier predicted by the multireference calculations is considerably lower than the value 583 cm^{-1} obtained experimentally. Whilst the sixth and seventh excited KDs at 494 cm^{-1} and 696 cm^{-1}, respectively, do encompass this barrier, the direction of the principal magnetic axes in these doublets are considerably skewed relative to the ground KD and the fifth-excited KD has a very strong transverse component to the g-tensor (g_x = 3.8030, g_y = 6.7534, g_z = 10.1946). Hence, it is extremely unlikely that the relaxation would take place via these higher excited states.

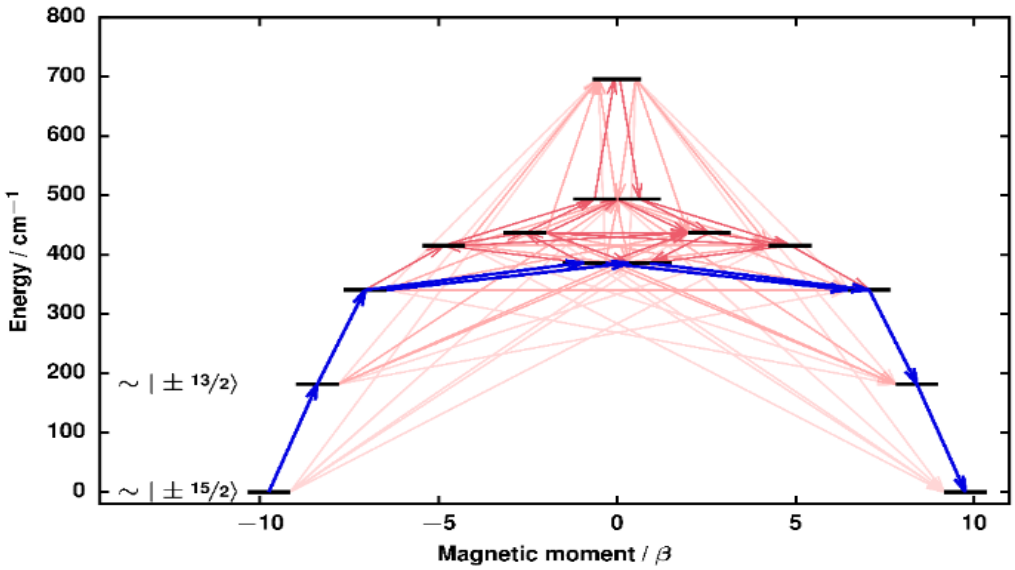

Figure 2.16: The *ab initio* blocking barrier constructed for **2.5**$_{Dy}$. The blue arrows indicate the most probable relaxation route. The stronger red colour in the other arrows indicates a stronger transition magnetic moment.

The discrepancy between experiment and theory most likely originates from neglecting electron correlation effects outside the 4*f* orbital space; more specifically, from an inaccurate description of the tungsten-to-carbonyl back donation. To confirm this, a Hartree–Fock (HF) calculation, which neglects all electron correlation effects, and a hybrid DFT calculation which accounts for electron correlation effects was carried by A. Mansikkamäki out on a closed-shell, 18-electron $[CpW(CO)_3]^-$ fragment. Effective atomic charges were then calculated for the atoms using the LoProp approach.[89] The effective charge of the tungsten atom changes slightly from 0.33 in the HF calculation to 0.34 in the hybrid DFT calculation, whereas the charges of the carbonyl carbon atoms change from 0.20, 0.20 and 0.22 to 0.10, 0.10 and 0.12 and the charges of the oxygen atoms change from –0.50, –0.51 and –0.47 to –0.41, –0.41 and –0.38. These values demonstrate that neglecting electron correlation in the W–CO interaction leads to overestimation of the charge polarization of the CO

ligand and to an excessively negative charge on the oxygen atoms. In turn, this leads to an overestimation of the equatorial component of the crystal field in **2.4$_{Dy}$**, which explains why the effective barrier height is underestimated in the calculations.

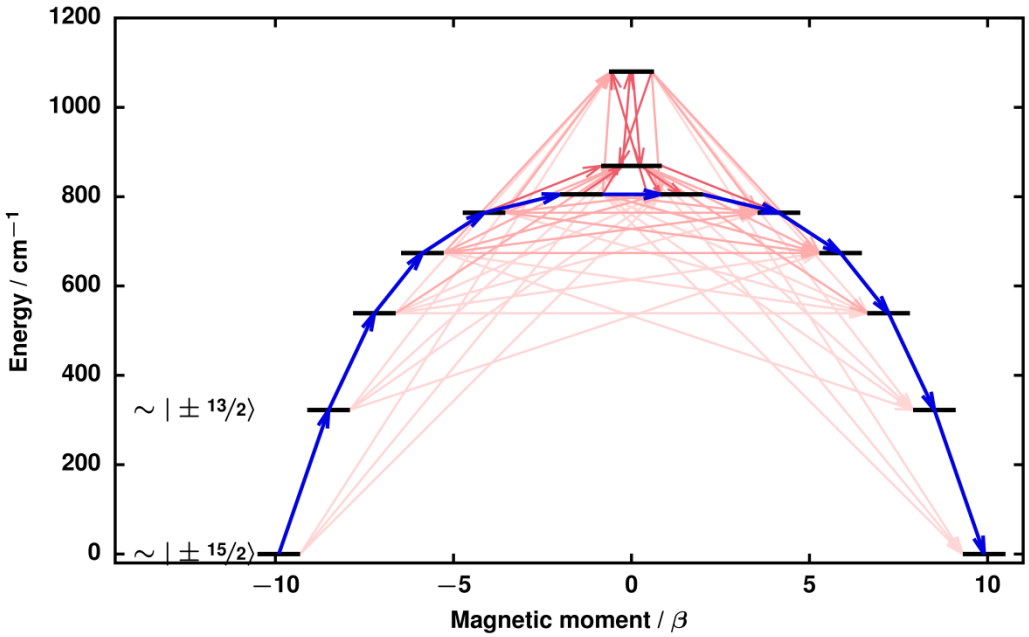

Figure 2.17: The *ab initio* blocking barrier constructed for **2.6$_{Dy}$**. The blue arrows indicate the most probable relaxation route. Stronger red colour in the other arrows indicates a stronger transition magnetic moment.

To provide further insight into the effects of tungsten-to-carbonyl back-donation on the magnetic properties of Dy^{3+}, the calculations performed on **2.5$_{Dy}$** were repeated on the simpler model system $[Cp^*_2Dy(OC)_2]^+$ (**2.6$_{Dy}$**) where the absence of tungsten atoms removes all back-donation effects. The energies and properties of the eight lowest KDs of **2.6$_{Dy}$** and the calculated *ab initio* crystal field parameters are listed in Tables S8 and S9. The principal magnetic axis of the ground KD in **2.6$_{Dy}$** is almost collinear with the corresponding axis in **2.5$_{Dy}$** (Figure 3). It is clear from the

principal components of the *g*-tensors that the crystal field around Dy^{3+} in **2.6$_{Dy}$** is more axial than in **2.5$_{Dy}$**. The transverse components of the *g*-tensors of the ground KD are an order of magnitude smaller in **2.6$_{Dy}$** than in **2.5$_{Dy}$** and the principal axes of the excited KDs have much smaller angles with respect to the axis of the ground doublet. A significant angle between the axes is not observed until the fourth excited doublet, compared to the third excited doublet in **2.5$_{Dy}$**. In contrast to **2.6$_{Dy}$**, the most probable relaxation route for **2.5$_{Dy}$** is predicted via the fifth excited doublet, giving a much larger effective barrier of U_{eff}/k_BT = 805 cm^{-1}. There is, however, moderately strong thermally assisted QTM also takes place at the third and fourth excited doublets, which implies that the relaxation may be faster than the barrier height suggests.

Finally, further computational evidence for the impact of tungsten-to-carbonyl back bonding on the magnetic axiality of the dysprosium metallocene unit was obtained from the calculated *ab initio* crystal field parameters in **2.5$_{Dy}$** and **2.6$_{Dy}$**.[90] The results reveal a much higher degree of axiality in **2.6$_{Dy}$** since the axial parameter B_{20} is 86% larger than in **2.5$_{Dy}$** and the B2±2 parameters are smaller (Tables S7 and S9).

2.3.5.3 Remarks on Computational Analysis

The large discrepancy between the experimental anisotropy barrier (U_{eff}/k_BT) values of **2.3$_{Dy}$**, **2.5$_{Dy}$** and **2.6$_{Dy}$** and those determined through CASSCF studies demonstrate the complexity encountered when modelling lanthanide SMMs and particularly those of a polymeric chain-like structure. A recent publication by Böhme and Plass [91]

discusses the limitations of the high computational requirements for complete *ab initio* quantum mechanical treatments of chain-like structures complexes.

This does not negate the qualitative description presented above, only it allows us to clarify the reasons for the large gaps between both calculated values and the experimentally derived value. What is clear from the SCF-CASSCF calculations is that the isocarbonyl-linkage has a markedly large influence on the crystal field of the Ln-metal centre, and thus, on the magnetic properties exhibited by **2.4$_{Dy}$**.

2.4 Conclusions

Building on the magnetic properties demonstrated by the isocarbonyl rare-earth metallocene complexes **2.3$_{Dy}$** ([Cp*$_2$Dy{μ-(OC)$_2$FeCp}]$_2$), an analogous reaction was undertaken to synthesise a tunsgten-carbonyl complex *via* a salt metathesis between [Cp*$_2$Ln][BPh$_4$] (Ln = Y, Gd, Dy) and Na[CpW(CO)$_3$]. The resulting complexes **2.4$_Y$**, **2.4$_{Gd}$**, and **2.4$_{Dy}$** have been characterised by X-ray diffraction studies, displaying polymeric arrangments. The complex **2.4$_{Dy}$** was shown to exhibit SMM properties including an anisotropty barrier of U_{eff}/k_BT = 557(18) cm^{-1} and a τ_{QTM} = 3.71(8) ms in a zero d.c. field. Interestingly, **2.4$_{Dy}$** showed no open magnetic hysteresis even at 1.9 K, a marked difference to the **2.3$_{Dy}$**, which showed open hystersis up to 6.2 K with a U_{eff}/k_BT = 662(2) cm^{-1}. The computational studies, emphasise the effect that the isocarbonyl linkage and its back-bonding on to the tungsten, has on the magnetic properties of the SMM. These findings indicate that traditional bonding motifs of organometallic chemistry can be applied to the design of new SMMs to tailor the rate of QTM, which has implications in the deisgn of molecular spin qubits.

Chapter 3:

Monometallic Lanthanide Cyclooctatetrene Complexes as Building Blocks to Inverse-Sandwich SMMs

3.1 Introduction

Routes to half-sandwich complexes with the general formula [(η^8-COT)LnI] as shown in Scheme 3.1 have been reported by Mashima *et al*[92,93] in 1994 (COT = cyclooctatetraene, Ln = La, Ce, Pr, Nd, Sm) and more recently by Münzfeld *et al*[94] in 2019 (Ln = Nd, Sm, Dy, Er). Both groups used lanthanide metals, iodine and neutral cyclooctatetraene in refluxing THF, though for dysprosium and erbium it was necessary to activate the lanthanide metals by *in situ* amalgamation to facilitate synthesis. The COT complexes of the earlier lanthanides have one more THF ligand coordinated than the later lanthanides, consistent with the lanthanide contraction. The magnetic properties of these complexes were not reported.

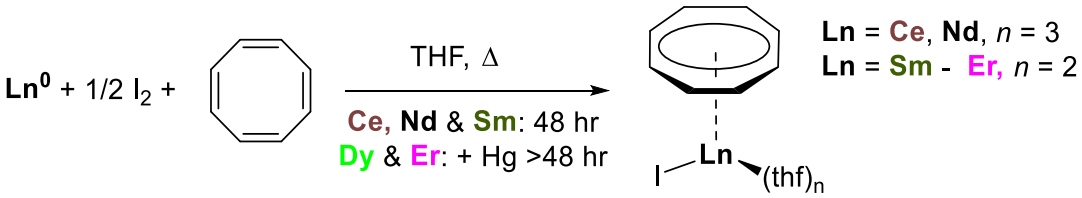

Scheme 3.1: Synthetic route to [(η^8-COT)LnI]complexes. [93,94]

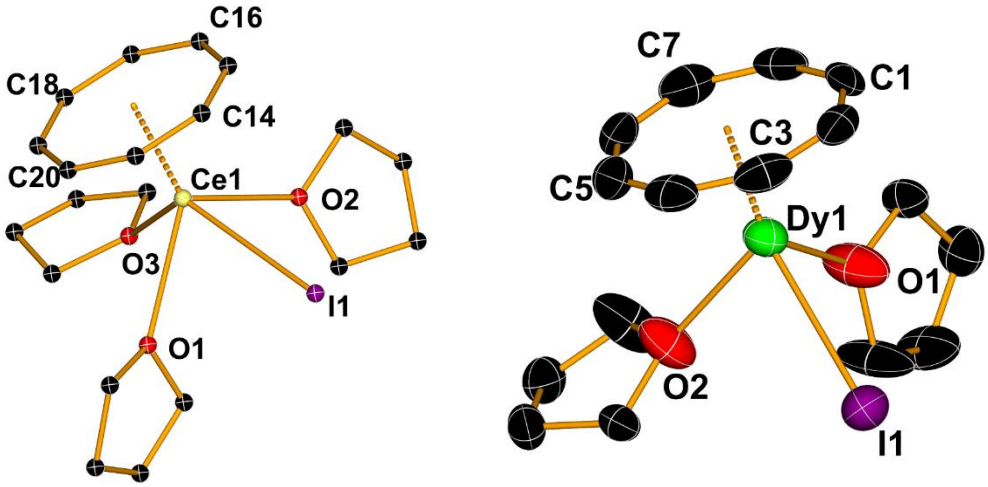

Figure 3.1: Thermal ellipsoid representations of the molecular structures of **3.1**$_{Ce}$ and **3.1**$_{Dy}$ (hydrogen atoms omitted for clarity, displacement ellipsoids set at the 50 % probability level). [92,94]

Lanthanide trisborohydride complexes [Ln$(BH_4)_3(THF)_n$] have been employed as precursors to more intricate organometallic complexes for decades and are recently finding greater application in the field of SMMs due to the easy handling and purification compared to the halide salts.[95–97] An example of a cyclooctatetraene lanthanide borohydride complexes is shown below (Figure 3.2). The structure shows the bridging ability of the borohydride unit, exhibiting $(\mu_3\text{-H})_2B(\mu_2\text{-H})_2$ coordination to the neodymium.

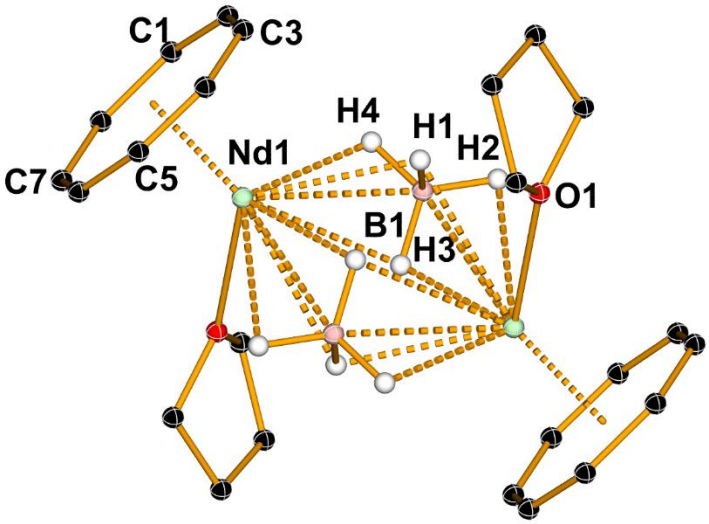

Figure 3.2: Thermal ellipsoid representation of **3.1$_{Nd}$** (hydrogen atoms except for BH_4^- omitted for clarity, displacement ellipsoids set at the 50 % probability level). [95]

A particularly interesting ligand, pioneered by Cloke *et al.*, is the 10π aromatic pentalenyl dianion, an example of such a ligand is shown in Figure 3.3. This ligand is typically used as a bulky silyl derivative such as Pn^{TIPS} = $[1,4\text{-}\{Si^iPr_3\}_2C_8H_4]^{2-}$ an example of this ligand can be seen in Figure 3.3. This ligand has allowed access to a number of interesting f-element organometallic complexes. In particular, the most relevant being the inverse-sandwich $[(Cp^*Ln)_2Pn^{TIPS}]$ complexes, where the lanthanide is divalent samarium, europium or ytterbium (**3.2$_{Sm}$** Figure 3.3).[98] An inverse-sandwich, sometimes referred to as a double metallocene, are where the ligand is sandwiched between two metals. This is a particularly interesting system on which magnetic studies were conducted where the *M vs. H* properties showed retention of anisotropy, a key feature for a successful SMM. Since the lanthanides in **3.2$_{Ln}$** are present in the divalent form, scope remains to employ pentalene ligands with trivalent lanthanides with the aim of developing new SMMs.

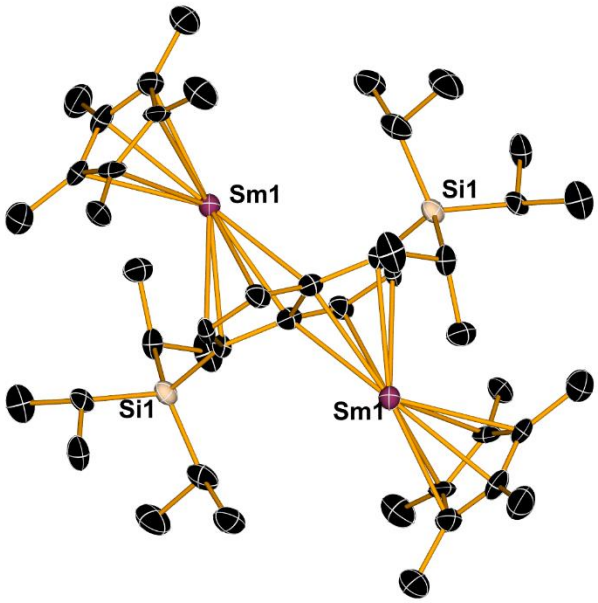

Figure 3.3: Thermal ellipsoid representation of **3.2**$_{Sm}$ (hydrogen atoms omitted for clarity, displacement ellipsoids set at the 50 % probability level).

3.2 Aims

The successful synthesis and measurements of complexes with the formula [(η^8-COTLn)$_2$Pn], from [(η^8-COT)Ln(BH_4)(THF)$_2$] where Ln = dysprosium, erbium, and yttrium, would give a holistic understanding to how double metallocene structures could be utilised in SMMs. Magnetic characterisation of both the desired final complexes and the precursors will further clarify the effects that the aromatic pentalene ligand has on SMM properties.

3.3 Results and Discussion

3.3.1 Synthesis and Structure of $[(\eta^8\text{-COT})Ln(BH_4)(THF)_2]$ ($\mathbf{3.3_{Ln}}$)

Formation of KBH_4 salts as a by-product is a common and reliable route to f-element complexes as a result of the low solubility of KBH_4 in THF.[97,99] Thus, the complexes $[(\eta^8\text{-COT})Ln(BH_4)(THF)_2]$ (**3.3$_{Ln}$**, Ln = Y, Gd, Dy, Er) were all synthesised through a salt metathesis reaction between $Ln(BH_4)_3(thf)_3$ and K_2COT in THF (20 mL) at −78 °C (Scheme 3.2). Optimisation of the reactions were attempted by altering the starting temperature, as well as reaction times, but it was found that both led to lower yields and higher quantities of unidentifiable impurities.

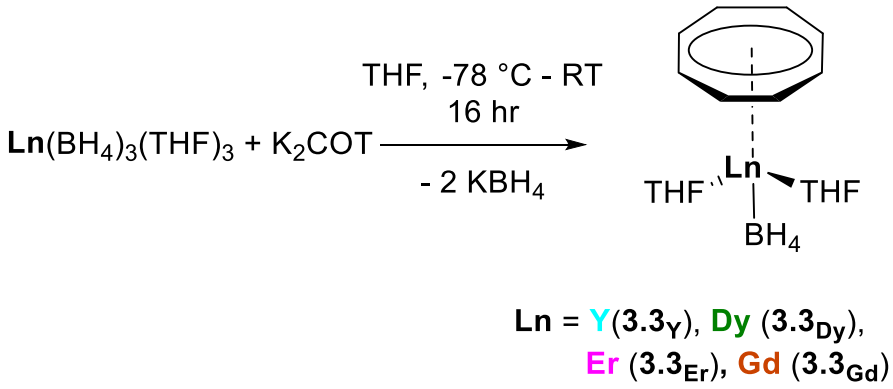

Scheme 3.2: Synthetic route to **3.3$_{Ln}$**.

Following work-up and purification, the complexes **3.3$_Y$**, **3.3$_{Dy}$**, **3.3$_{Gd}$** and **3.3$_{Er}$** were isolated as with yields of 69 %, 52%, 64% and 74%, respectively. Crystals suitable for solid-state studies were grown from saturated THF solutions stored at −35 °C for three days. All complexes were extremely air and moisture sensitive in both the solution and solid state; however, they were stable under an argon atmosphere for at least six months at room temperature.

The series of [(η^8-COT)Ln(BH_4)($THF)_2$] complexes are isostructural (Figure 3.4). Each complex consists of one η^8-COT ligand, two THF ligands and a $[BH_4]^-$ ligand that exhibits both bridging and terminal hydride atoms. Assignment by standard refinement of hydrogen positions from X-ray diffraction data is known to underestimate the distances to adjacent atoms and therefore IR-spectroscopy was used to provide necessary evidence of the types of bonding exhibited by the $[BH_4]^-$ ligand (see below).

The complexes **3.3$_{Dy}$** and **3.3$_{Er}$** crystallised in the orthorhombic space groups *Pbc*2_1 and *Pca*2_1, respectively, whereas complexes **3.3$_{Y}$** and **3.3$_{Gd}$** crystallised in the monoclinic space group *P*2_1/*n* (see Table 6.2 for crystallographic details). The intermolecular Ln···Ln distances for the complexes are between 7.4714(6)-7.7515(7) Å. Relevant distances are summarised in Table 3.1.

Table 3-1: Relevant distances of **3.3$_{Ln}$** (Å).

	3.3$_{Y}$	**3.3$_{Dy}$**	**3.3$_{Er}$**	**3.3$_{Gd}$**
Ln-COT$_{cent}$	1.825(8)	1.835(5)	1.802(3)	1.873(3)
Ln-COT$_{avg}$	2.591	2.587	2.568	2.623
Ln···B	2.587(2)	2.617(12)	2.667(8)	2.639(7)
Ln-O1	2.4186(13)	2.416(6)	2.388(3)	2.465(4)
Ln-O2	2.3808(13)	2.393(7)	2.360(4)	2.426(4)
Ln···Ln[a]	7.7515(7)	7.4935(6)	7.4935(6)	7.4346(2)

[a] shortest intermolecular Ln Ln separation

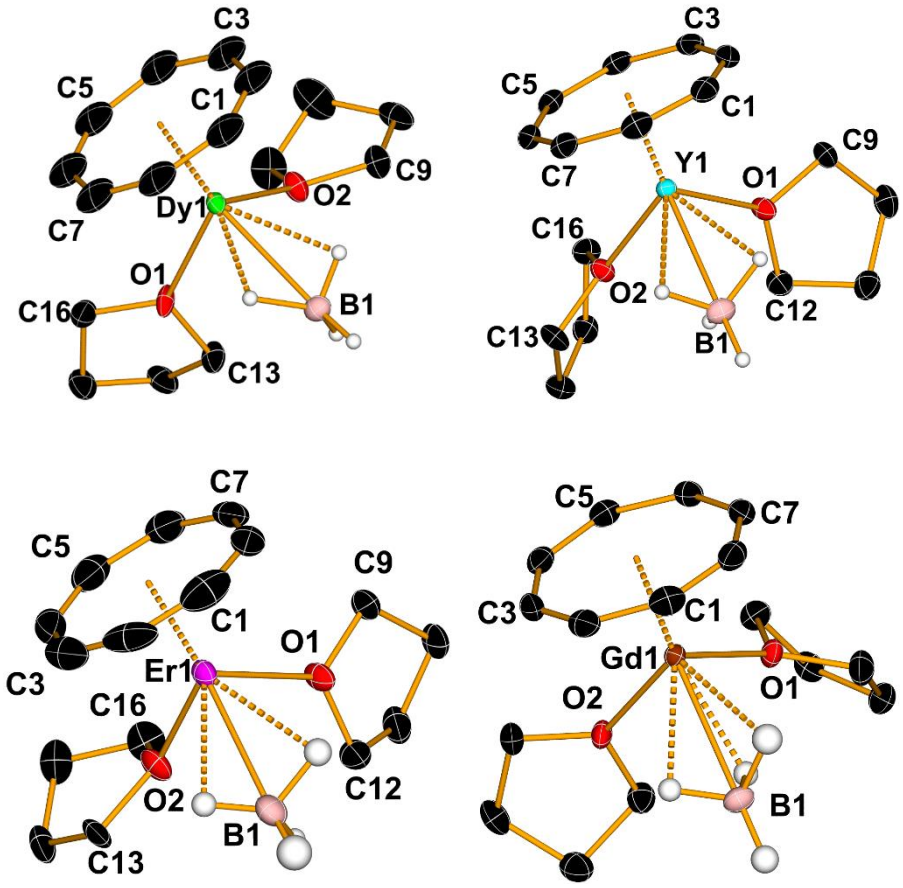

Figure 3.4: Thermal ellipsoid representation of **3.3$_{Ln}$** (hydrogen atoms except for $[BH_4]^-$ omitted for clarity, displacement ellipsoids set at the 50 % probability level).

For **3.3$_{Ln}$**, the distances from the metal atom to the centroid of the cyclo-octatetraene unit (COT_{cent}) are well within the expected values. They are 0.17-0.20 Å shorter than the analogous distance of 2.015(5) Å in **3.1$_{Ce}$**, which is again consistent with the lanthanide contraction.[92] This increase is greater than the approximately 0.1 Å difference between Ce^{3+} (1.010 Å) and the ionic radii of the later lanthanides (Gd^{3+} = 0.938 Å, Dy^{3+} = 0.912 Å, Er^{3+} = 0.890 Å).[19] This is likely a result of fewer THF molecules coordinating in **3.3$_{Ln}$** compared to **3.1$_{Ce}$**, which increased the electron density surrounding the latter complex weakening the interaction between cerium and COT.

The Ln···B distances in **3.3$_{Ln}$** are in the range 2.587(2)-2.667(8)Å. This is an average of 0.7 Å closer to the metal than the iodide in **3.1$_{Ce}$**, the Ln-I bond length is 3.299 Å.[92] This difference is greater than the reported values of the ionic radii of each ligand, where I^- is 2.11 Å and BH_4^- is 2.05 Å.[100] The smaller ionic radii of yttrium, dysprosium, gadolinium, and erbium compared to that of cerium is most likely the cause of the differing number of coordinated THF molecules.[18,19,101] The Ln-COT_{cent} bonds in the complexes **3.3$_{Ln}$** are in the range of 1.802(3)-1.873(3) Å, making them shorter than the analogous distances in **3.1$_{Nd}$** of 1.913 Å,[95] which is to be expected considering that the difference in ionic radii of Nd^{3+} and Dy^{3+} is close to 0.07 Å.[73]

A notable difference between the complexes **3.3$_{Ln}$** and their closest comparator in the literature is the monomeric nature of the new complexes compared to the dimeric nature of **3.1$_{Nd}$**. This most likely occurs due to the greater size in Nd^{3+} facilitating the bridging action of BH_4^- to bridge the metals, which cannot be achieved in **3.3$_{Ln}$**. [102,103] The Ln···B distances for **3.3$_{Ln}$** are in the range 2.587(3)-2.639(7) Å. Compared with **3.1$_{Nd}$**, where the Nd···B distances are in the range 2.875(6) – 2.941(6) Å[95], again the differences here are greater than that of the differences in ionic radii and can be tentatively attributed to the dimer possessing two BH_4^- units, notwithstanding that the ligands are bonded across the two metals. It is well known that X-ray crystallography often cannot accurately determine the positions of hydrogens in structures [102] therefore the bonds to hydrogen atoms are not described in this text. The bonding motifs of the BH_4^- ligands displayed in **3.3$_{Ln}$** are described in greater detail later (see below).

The Ln-O_{THF} bond lengths for **3.3$_{Ln}$** are in the range 2.360(4)–2.465(4) Å. These are very similar to those in the disolvated **3.1$_{Dy}$** (2.371 – 2.390 Å) and, unsurprisingly, shorter than those of the trisolvated **3.1$_{Ce}$** (2.555(7) – 2.640(7) Å).[92,94] Again, the corresponding bond length in **3.1$_{Nd}$** is greater than the ionic radii difference (Nd-O = 2.481(5) Å).[95,96]. The closer contacts between Ln-O in **3.3$_{Ln}$** can be ascribed to the higher Z_{eff} in these complexes as a result of the single borohydride unit per molecule compared with **3.1$_{Nd}$**, thus facilitating a shorter bond in **3.3$_{Ln}$**.

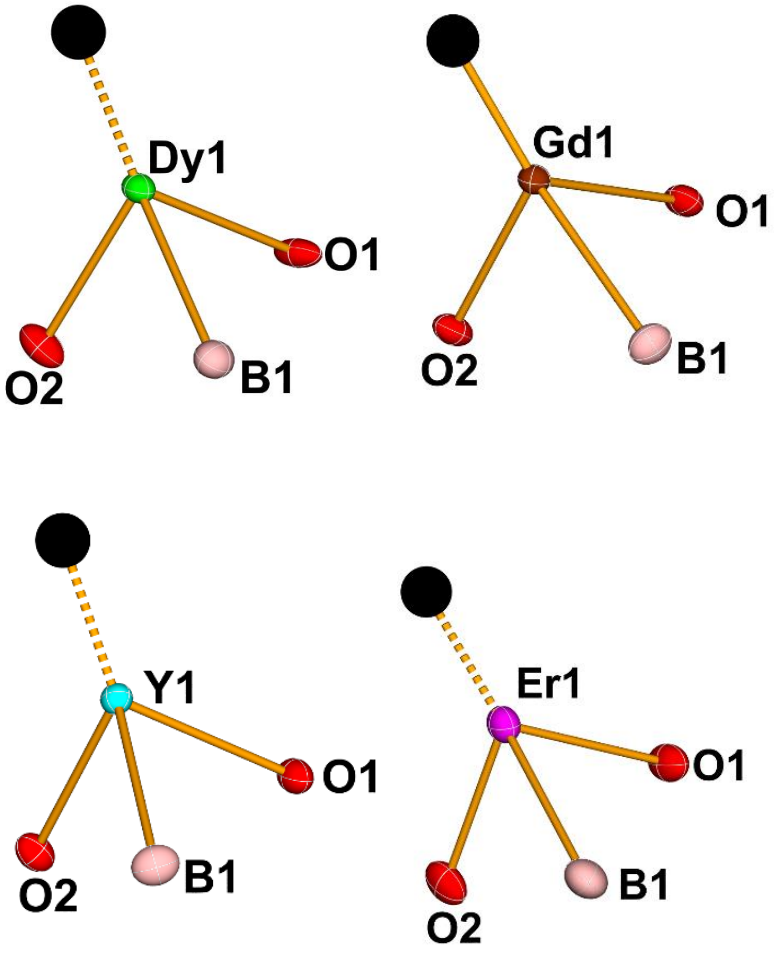

Figure 3.5: Simplified structures of **3.3$_{Ln}$** used for CShM analysis. (Black circles represent centroid coordination positions of the COT ligand, hydrogen atoms omitted for clarity, ellipsoids set to 50% probability level).[104]

For each of the **3.3$_{Ln}$** molecules, packing in the extended structures does not suggest any intermolecular interactions that would be of sufficient magnitude to affect either the magnetism.[105] The nearest atom-atom distance (carbons in the COT ring) for **3.3$_{Gd}$** is 6.121(9) Å, in **3.3$_{Er}$** the analogous distance is 5.300(2) Å, for **3.3$_{Dy}$** it is 5.682(9) Å, and for **3.3$_{Y}$** it is 5.986(6) Å. The closest metal-metal distances for **3.3$_{Er}$** is 7.493(1) Å, in **3.3$_{Dy}$** the analogous distance is 7.441(6) Å, for **3.3$_{Y}$** it is 7.351(9) Å, and for **3.3$_{Gd}$** it is 7.446(5) Å These distances are such that any magnetic interactions between metal centres would most likely be weak. [106,107]

It has been described earlier that the symmetry of a molecule can affect the magnetic properties (Chapter 1), therefore it is pertinent to evaluate these properties for the compounds **3.3$_{Ln}$**. This has been calculated here using the Continuous Shape Measures theory (CShM) implemented through the SHAPE 2.1 software package, which describes a distortion parameter, *S*, as the deviation from a series of ideal geometries.[104]

As the COT unit possesses local 8-fold symmetry and is a π-bonded ligand, it is suggested in the original publication to consider the centroid of the ligand and this is the method that is applied here.[104] The resulting "dummy" models for **3.3$_{Ln}$** are shown in Figure 3.5. CShM analysis shows that the simplified **3.3$_{Dy}$** molecule displays a distorted vacant trigonal bipyramidal (vTBPY-4) geometry with a value of *S* = 3.772 (*S* = 0 being no deviation from the ideal geometry). However, the next nearest geometry is tetrahedral with *S* = 3.92. The results are similar with *S* = 3.772 for **3.3$_{Er}$** *S* = 3.795 for **3.3$_{Gd}$**, and *S* = 3.760 for **3.3$_{Y}$**, both being a distorted vacant trigonal bipyramidal geometry. However, the calculated results for VTBPY-4 and T-4 are

extremely close, so the distinction between these geometries is difficult to state with confidence. The full results are given below in Table 3.2.

Table 3.2: Coordination geometries of simplified $\mathbf{3.3_{Ln}}$ structures, performed using SHAPE 2.1. [104]

[ML_4]	vTBPY-4	SS-4	T-4	SP-4
$\mathbf{3.3_{Dy}}$	3.772	7.026	3.930	34.086
$\mathbf{3.3_{Er}}$	3.837	7.009	4.183	34.734
$\mathbf{3.3_{Y}}$	3.760	7.184	3.850	33.193
$\mathbf{3.3_{Gd}}$	3.795	7.215	3.909	32.801

3.3.2 Synthesis and Structure of $[(\eta^8\text{-COTLn})_2Pn^{TIPS}]$ ($\mathbf{3.4_{Ln}}$)

The complexes $\mathbf{3.4_{Ln}}$ (Ln = Y, Dy, Er) were all synthesised through a salt metathesis reaction of $\mathbf{3.3_{Ln}}$ with K_2Pn^{TIPS} (K_2Pn^{TIPS} = $K_2[C_8H_4(1,4\text{-}Si^iPr_3)_2]$) in THF (20 mL) at – 78 °C (Scheme 3.3). Crude yields of 40 – 55 % were obtained, after purification yields significantly decreased to 9-12%. Low pure yields are due to the enhanced solubility afforded by the pendant silyl groups.

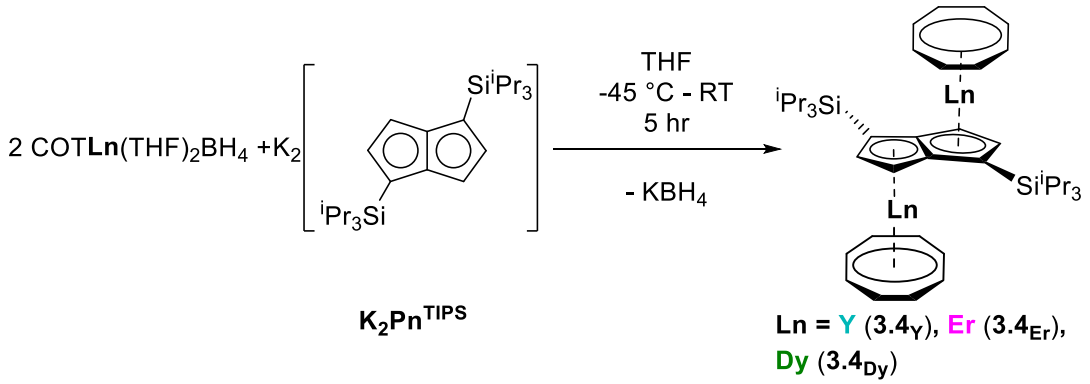

Scheme 3.3: Synthetic route to $\mathbf{3.4_{Ln}}$.

Crystals suitable for X-ray diffraction studies were grown from saturated toluene solutions stored at −35 °C for seven days. All complexes were air and moisture sensitive but stable at room temperature under an argon atmosphere. Compounds $\mathbf{3.4_{Ln}}$ are isostructural and all crystallised in the space group *P*-1, each asymmetric unit contains one-half of the molecule (see Table 6.3 for full crystallographic details). The full molecules are shown in Figure 3.6.

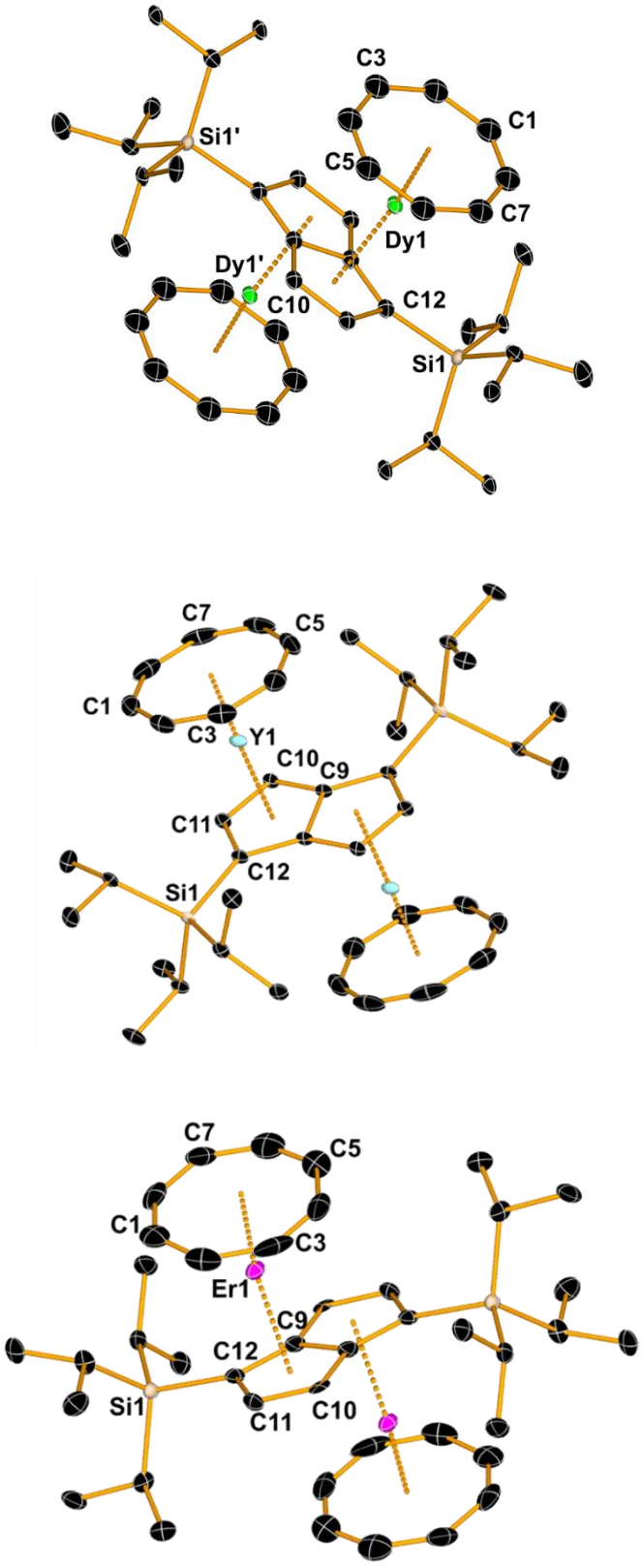

Figure 3.6: Thermal ellipsoid representation of **3.4**$_{Ln}$ (hydrogen atoms except for BH_4^- omitted for clarity, displacement ellipsoids set at the 50 % probability level).

The COT_{cent}-Ln-Pn_{cent} angle for **3.4$_{Dy}$** is 167.54(68) °, for **3.4$_{Er}$** it is 170.77(45) °, and for **3.4$_{Y}$** the angle is 169.39(13) °. The angle between the centroids of the COT and Cp/Pn ligands are somewhat more acute than in the COT_{cent}-Ln-Cp^*_{cent} complexes previously reported, which exhibit angles of COT_{cent}-Dy-Cp^*_{cent} = 171.96 °, COT_{cent}-Er-Cp^*_{cent} = 172.89 °, and COT_{cent}-Y-Cp^*_{cent} = 173.05 °.[42,108]

The COT_{cent}-Ln-Pn_{cent} angles are further still from linearity when compared to [(η^8-COT)Dy(η^9-C_9H_9)](∠ = 176.68 °).[94] The decrease in the bond angle for **3.4$_{Ln}$** compared to closely related compounds is most likely due to the Si^iPr_3 groups sterically crowding the local environment about the metal atom, alongside the increased proximity of the COT ligand and the metal further causing further crowding.

Table 3.3: Relevant distances of **4.5$_{Ln}$** (values in Å).

	3.4$_{Y}$	**3.4$_{Dy}$**	**3.4$_{Er}$**
Ln-COT_{cent}	1.7362(9)	1.746(1)	1.7421(7)
Ln-COT_{avg}	2.515	2.530	2.532
Ln-Pn_{cent}	2.3125(10)	2.320(12)	2.3262(8)
Ln-Pn_{avg}	2.599	2.612	2.617
Ln···Ln_{intra}	4.9986(18)	5.007(3)	5.0090(16)

The intra-metallic distance of an SMM may affect the magnetism through dipolar exchange coupling interactions, which generally become stronger with a decreasing M···M separation.[5,20,80] For complexes **3.4$_{Ln}$** the Ln···Ln distances are in the range 4.9986(18)-5.0090(16) Å. For the paramagnetic **3.4$_{Dy}$** and **3.4$_{Er}$** the intramolecular separation is small enough for magnetic exchange coupling to occur, which could also be facilitated by the pentalene ligand.

The COT_{cent}-Ln distances in **3.4$_{Ln}$** are in the range 1.7362(9)-1.746(10) Å. These values represent a shortening of approximately 0.06-0.10 Å across the three complexes

relative to **3.3$_{Ln}$**, and approximately 0.04 Å relative to the COT-Ln-Cp* complexes, and approximately 0.10 Å shorter than [(η^8-COT)Ln(η^9-C_9H_7)].[108] The Pn_{cent}-Ln distances in **3.4$_{Ln}$** are longer than those to the COT_{cent}, this is expected as the two metals affect the dianionic Pn^{TIPS} ligand such that each C5 ring acts as a monoanionic ligand to the metal atom akin to a cyclopentadienyl ligand. The Ln-$C5_{cent}$ of Pn^{TIPS} are slightly longer than those for the Ln-Cp^*_{cent} in [(η^8-COT)Ln(Cp*)] (2.290 – 2.300 Å), and shorter than those of **3.2$_{Ln}$** (2.389(6)-2.569(2) Å). [42,98,108]

Of the few pentalene-bridged structures available in the literature, only a handful are bimetallic. The remaining structurally characterised complexes are monometallic where the pentalene acting as a dianionic ligand towards the singular metal atom[109–111] with fold angles in the range 24-43 °.[109,110,112] There remains a dearth of bimetallic systems, the majority of which sandwich both metal atoms between two pentalene units. Only **3.2$_{Ln}$** displays an inverse-sandwich nature and heteroligation, comparable to that of **3.4$_{Ln}$**.[98] Both **3.4$_{Ln}$** and **3.2$_{Ln}$** show a planar pentalene unit with Ln-COT/Cp* on opposing faces and opposing C5 rings.

Thus, the new complexes reported here are only the second examples of inverse-sandwich lanthanide pentalene-bridged complexes and the first examples with trivalent lanthanides.

ChSM calculations were conducted on the complexes **3.4$_{Ln}$** to ensure consistent analysis, however due to the different two π-bonded ligands, COT and Pn, both centroids have been used as central points from which to conduct the analysis. The resulting “dummy” models for each complex is shown below (Figure 3.7). All three

complexes show the expected closest alignment with the linear geometry (L-2), with calculated deviations of *S* = 0.952 for **3.4**$_{Y}$, *S* = 1.052 for **3.4**$_{Dy}$, and *S* = 0.822 for **3.4**$_{Dy}$.

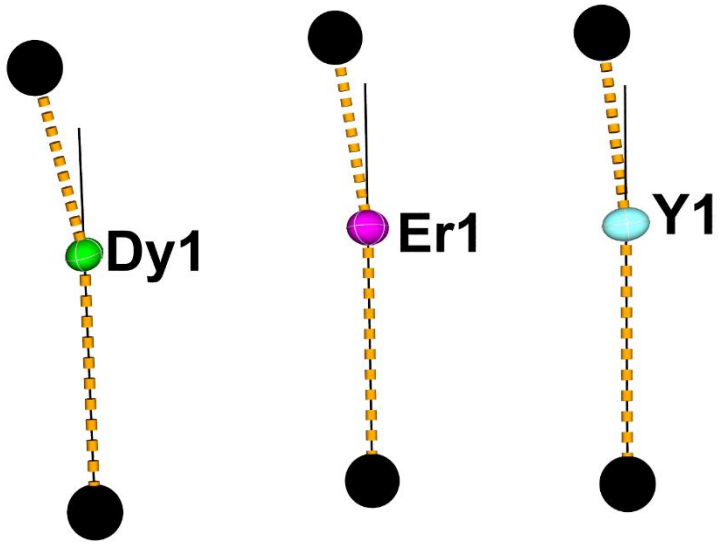

Figure 3.7: Simplified structures of **3.4**$_{Ln}$ used for CShM analysis, black line is a reference line.

Table 3.4: Coordination geometries of simplified COTLnBH4 structures calculated using SHAPE 2.1.

[ML_2]	vOC-2	vT-2	L-2
3.4$_{Y}$	20.973,	11.327	0.952
3.4$_{Dy}$	20.234	10.760	1.052
3.4$_{Er}$	21.482	11.698	0.822

3.3.3 Solution State Analysis of [(η^8-COT)Ln(BH_4)($THF)_2$] ($\mathbf{3.3_{Ln}}$)

To confirm the solid-state structural analysis, solution state studies were undertaken on the complexes described throughout this chapter. Thus, comprehensive NMR spectroscopic studies were undertaken on the complexes $\mathbf{3.3_{Ln}}$. The paramagnetic complexes, $\mathbf{3.3_{Dy}}$, $\mathbf{3.3_{Er}}$ and $\mathbf{3.3_{Gd}}$, were also subjected to ^{1} NMR spectroscopic studies. However, due to extensive line broadening inherent to paramagnetic complexes, the information imparted by these are more of a qualitative nature as the shape and number of the signals mimic that of the yttrium analogue.[19,101,113]

The complexes $\mathbf{3.3_{Ln}}$ are structurally analogous in the solid state and the ^{1}H NMR spectrum for $\mathbf{3.3_{Y}}$ in d_5-pyridine (Figure 3.8) is, therefore, the archetype of this family. The resulting spectrum displays signals within the expected diamagnetic range of 8 ppm to −2 ppm. There is a strong singlet at 6.29 ppm, integrating to 8 H which corresponds to the protons of C_8H_8. Initially, due to the ^{1}H NMR spectrum being collected in d_8-THF, the bound protio-THF molecules overlap slightly with that of the d_8-THF and so integration proved challenging but not impossible and sensible integrations can be achieved of the signals at 3.68 ppm and 1.64 ppm. Both signals integrate to 8 H each, representing the O-CH_2CH_2 for the former and the O-CH_2CH_2 of the THF molecules. Finally, there is a quartet centred at -0.50 ppm, integrating to 4 H atoms. Both the upfield shift and the integration confirm this as the BH_4^- ligand.[95,99,114,115] The J_{BH} coupling constant is 80 Hz, which is expected for a borohydride in a diamagnetic complex.[40,116,117]

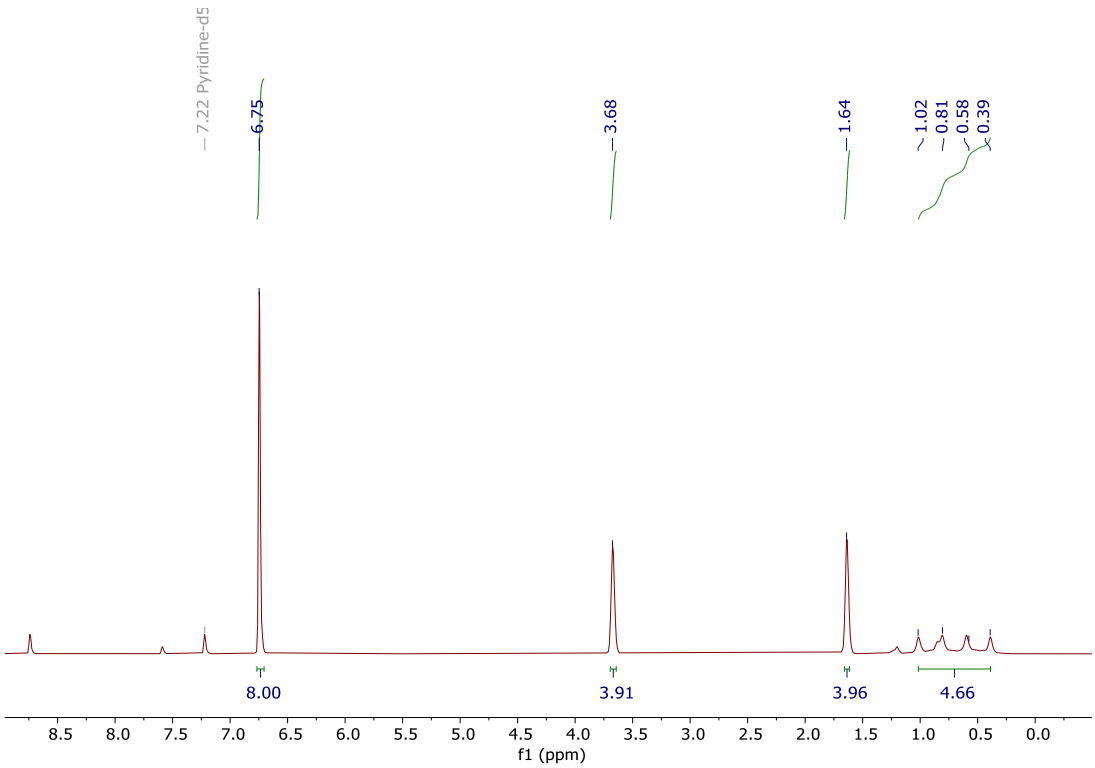

Figure 3.8: ^{1}H NMR spectrum of **3.3$_{Y}$** (d_5-pyridine, 400 MHz, 303 K).

The ^{1}H NMR spectroscopic studies of the paramagnetic molecules preclude quantitative analysis of the complexes **3.3$_{Dy}$**,**3.3$_{Er}$** and **3.3$_{Gd}$**. Spectra were recorded in d_5-pyridine and can be found in the Appendix 2. In complex **3.3$_{Er}$**, the protons of the COT ligand are shifted upfield to −15.18 ppm and the THF peaks shifted downfield to 28.04 ppm and 26.13 ppm. The upfield shift of the COT ligand is similar to that, though of a smaller magnitude, exhibited by [(η^8-COT)ErCp*] (−37 ppm).[118] The difference in the degree of the shift can be rationalised as the effects of the two solvent THF molecules and the BH_4^- in complex **3.3$_{Er}$** compared to Cp* in COTErCp*, where the Cp* imparts a lower degree of electron donation towards the metal centre. For **3.3$_{Gd}$**, the COT signal is 5.61 ppm, and the two THF signals appear at 3.70 ppm and 1.66 ppm. This minor shift of the signals is a result of the isotropic nature

of Gd^{3+} compared to the anisotropic Dy^{3+} and Er^{3+}, which both display greater shifts of the signals.[21,73]

The $^{13}C\{^{1}H\}$ NMR spectrum of **3.3$_{Y}$** (Figure 3.9) displays a signal at 94.03 ppm, corresponding to the C_8H_8 carbons of the COT ligand. The peaks at 68.39 ppm and 25.37 ppm correspond to the O<u>*C*</u>H_2CH_2 and OCH_2<u>*C*</u>H_2, respectively. The $^{13}C\{^{1}H\}$ NMR spectra of **3.3$_{Dy}$** and **3.3$_{Er}$** showed no discernible peaks due to their paramagnetism.

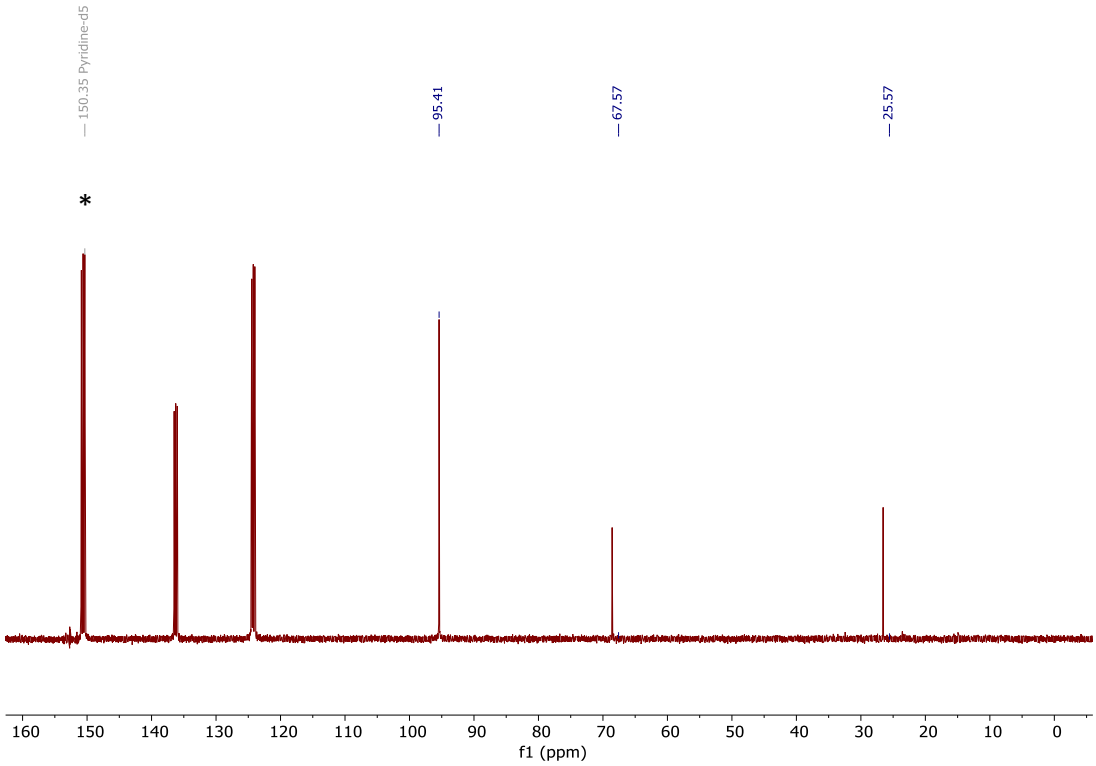

Figure 3.9: $^{13}C\{^{1}H\}$ NMR spectrum of **3.3$_{Y}$** (d_5-pyridine, denoted by *, 100 MHz, 303 K).

The $^{11}B\{^{1}H\}$ NMR spectrum of **3.3$_{Y}$** (Figure 3.10) displays only one single peak at −31.86 ppm, confirming that there is only one boron environment. Again, the $^{11}B\{^{1}H\}$ NMR spectra of **3.3$_{Dy}$** and **3.3$_{Er}$** showed no discernible peaks due to their paramagnetism.

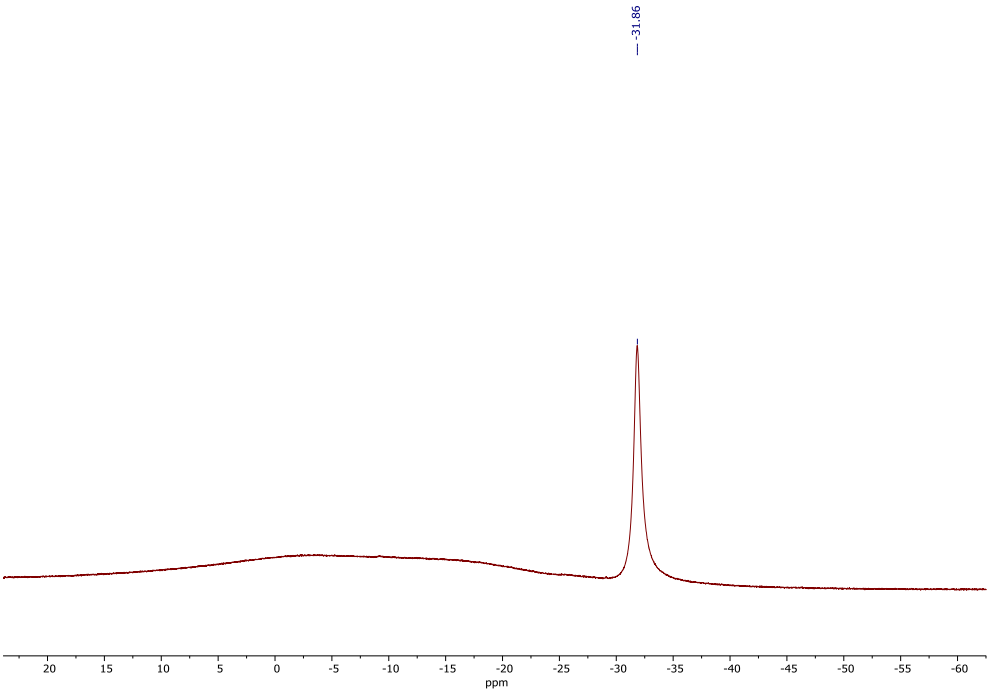

Figure 3.10: $^{11}B\{^{1}H\}$ NMR spectrum of **3.3Y** (d_5-pyridine, 128 MHz, 303 K).

3.3.4 Infrared Spectroscopy of $[(\eta^8\text{-COT})Ln(BH_4)(THF)_2$ ($\mathbf{3.3_{Ln}}$) and $[(\eta^8\text{-COTLn})_2Pn^{TIPS}]$

The borohydride ligands in $\mathbf{3.3_{Ln}}$ displays strong peaks between 2600-2100 cm^{-1}, which confirms the coordination of the ligand. This proves especially useful for the paramagnetic complexes $\mathbf{3.3_{Dy}}$ and $\mathbf{3.3_{Er}}$ as the BH_4^- is not visible in the ^1H or $^{11}B\{^1H\}$ NMR spectra (see above). All the spectra were collected in the solid state on an FT-IR spectrometer in an argon filled glovebox.

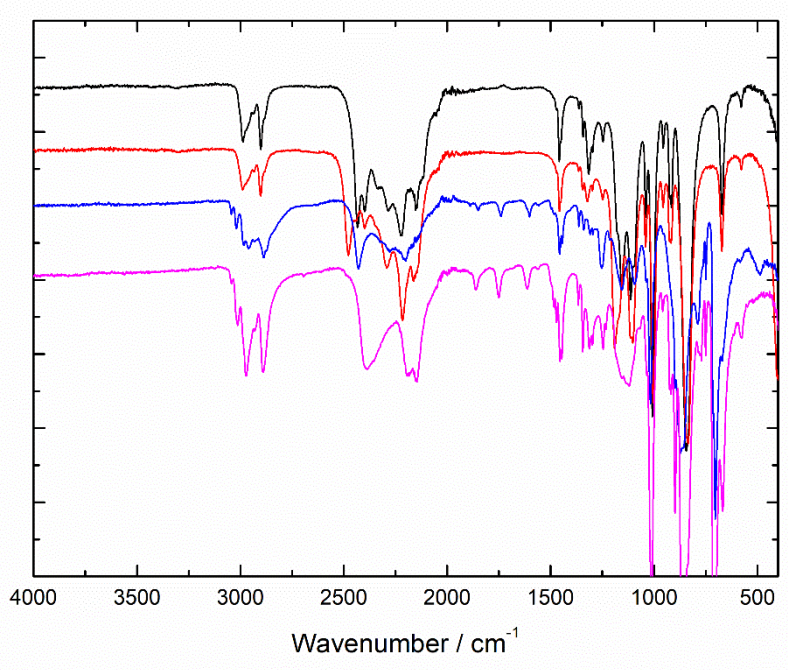

Figure 3.11: Stacked FT-IR spectra of $\mathbf{3.3_{Ln}}$ (black = $\mathbf{3.3_{Gd}}$, red = $\mathbf{3.3_{Y}}$, blue = $\mathbf{3.3_{Dy}}$, purple = $\mathbf{3.3_{Er}}$, transmission values are normalised before stacking).

Moreover, IR spectroscopy both confirms the ligands presence and can be utilised to determine the bonding mode exhibited by BH_4^-.[103,119,120] This compliments and confirms the SC-XRD structures already described (see above). As the complexes are

isostructural, **3.3$_{Er}$** is discussed in detail and the IR spectra are shown above (Figure 3.11).

In **3.3$_{Er}$** the peaks from 3010-2875 cm^{-1} are the CH stretches corresponding to the COT ligand as well as the THF molecules. For **3.3$_{Y}$** the values are 2970-2880 cm^{-1}, for **3.3$_{Gd}$** they are 2981-2901 cm^{-1} and for **3.3$_{Dy}$** they are 3024-2894 cm^{-1}. The peak at 2417 cm^{-1} represents a terminal B-H stretch, those at 2280-2180 cm^{-1} belong to the bridging B-H bonds. In the complex **3.3$_{Dy}$** the respective values are 2423 cm^{-1} and 2304-2199 cm^{-1}, for **3.3$_{Gd}$** they are 2438 cm^{-1} and 2343-2215 cm^{-1} for complex **3.3$_{Y}$** they are 2400 cm^{-1} and 2298-2192 cm^{-1}. These values are similar to those of the published Cb-Dy-BH_4 complex published by Durrant *et al.*, which also displayed both terminal and bridging B-H bonds. [103]

The IR spectra for **3.4$_{Dy}$**, **3.4$_{Er}$** and **3.4$_{Y}$** are shown below (Figure 3.12). The spectra each display peaks between 2970 – 2840 cm^{-1}, corresponding to C-H stretches arising from both the COT and Pn^{TIPS} ligands. It is clear that there are no peaks between 2750 – 1750 cm^{-1}, as this is the expected range for borohydride peaks there should be no peaks.

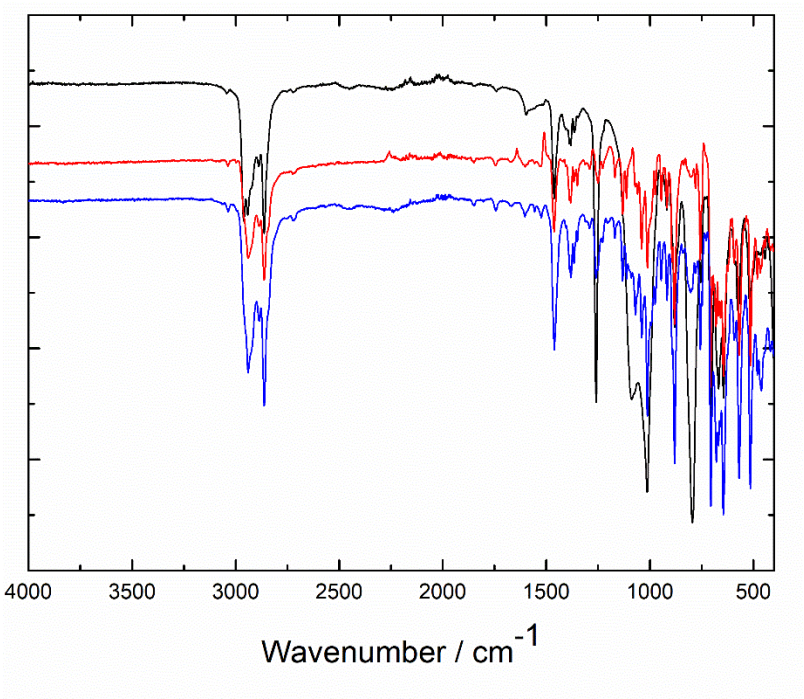

Figure 3.12: Stacked FT-IR spectra of **3.4**$_{Ln}$ (black = **3.4**$_{Dy}$, red = **3.4**$_{Er}$, blue = **3.4**$_{Y}$ transmission values are normalised before stacking).

3.3.5 Magnetic Characterisation of [(η^8-COT)Ln(BH_4)($THF)_2$] ($\mathbf{3.3_{Ln}}$)

Isothermal magnetisation (*M*) *vs*. field/temperature (*B/T*) were conducted on microcrystalline samples of $\mathbf{3.3_{Ln}}$ within the temperature range of 1.9-5.0 K (Figure 3.13 and Figure 3.14). Both $\mathbf{3.3_{Dy}}$ and $\mathbf{3.3_{Er}}$ display non-superimposable curves confirming the presence of magnetic anisotropy. [121,122] At 70 kOe the value of *M* for $\mathbf{3.3_{Dy}}$ is 5.55 N_AB, for $\mathbf{3.3_{Er}}$ *M* = 4.57 N_AB. Both values are half of the expected theoretical maximum, Dy^{3+} = 10.60 N_AB and Er^{3+} = 9.58 N_AB [101] However this is typical of the reported values within the literature and generally ascribed to significant anisotropy.[3,64,123,124]That $\mathbf{3.3_{Dy}}$ does not achieve saturation, as evidenced by the persistence of a sloped line, further demonstrates the anisotropy within the system.[2,80] This is similar to the complex $\mathbf{3.3_{Er}}$, which does not achieve saturation. This difference of behaviour is expected and could be ascribed to the oblate/prolate differences between the ground states of Dy^{3+}/Er^{3+} respectively.[21]

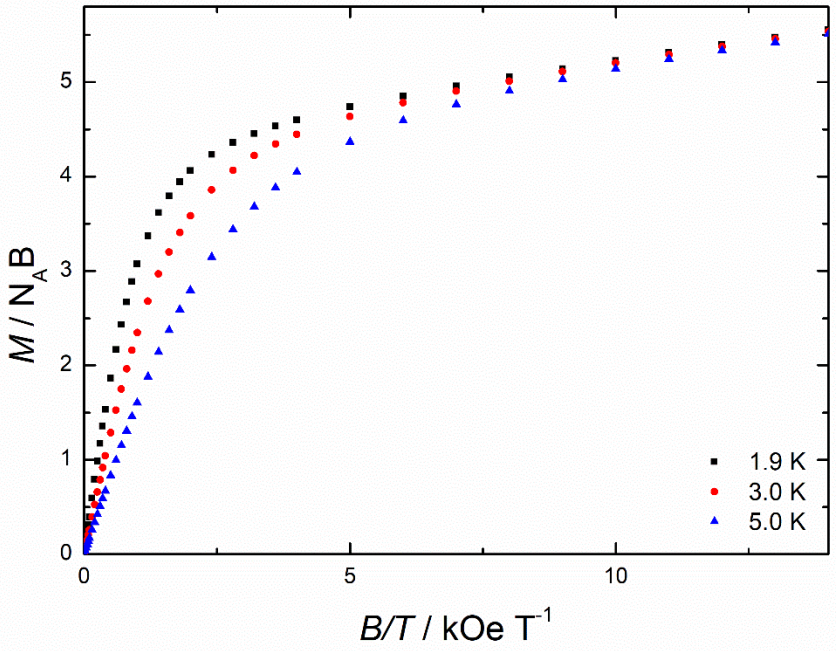

Figure 3.13: Magnetisation (*M*) vs. field/temperature (*B/T*) for **3.3**$_{Dy}$.

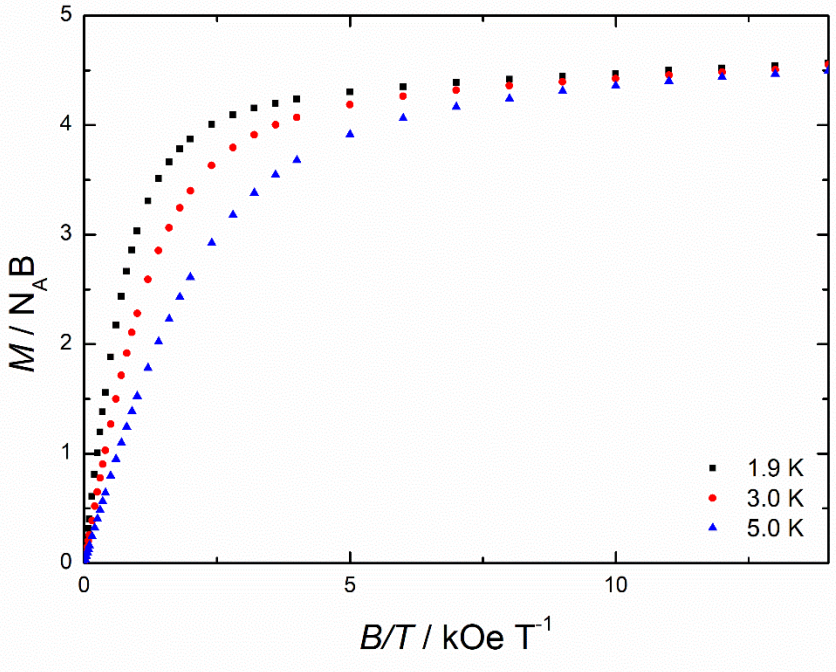

Figure 3.14: Magnetisation (*M*) vs. field/temperature (*B/T*) for **3.3**$_{Er}$.

Direct-current (dc) magnetic susceptibility measurements were carried out in the temperature range 2-300 K. The $\chi_M T$ value for **3.3$_{Dy}$** is 14.07 cm^3 K mol^{-1} and for **3.3$_{Er}$** the value of $\chi_M T$ is 10.93 cm^3 K mol^{-1}, these values are close to the expected values of 14.17 cm^3 K mol^{-1} and 11.48 cm^3 K mol^{-1} for Dy^{3+} and Er^{3+}, respectively.[125,126] Upon lowering the temperature, the $\chi_M T$ value for **3.3$_{Er}$** decreases slowly up to 25 K before decreasing at a faster rate to a value of 8.61 cm^3 K mol^{-1}. This gradual decrease is likely due a depopulation of the excited crystal field levels opposed to an onset of magnetic blocking. For **3.3$_{Dy}$**, the $\chi_M T$ value remains constant until 100 K then decreases sharply through to a final value of 8.60 cm^3 K mol^{-1}, again due to depopulation of excited crystal field levels.[3]

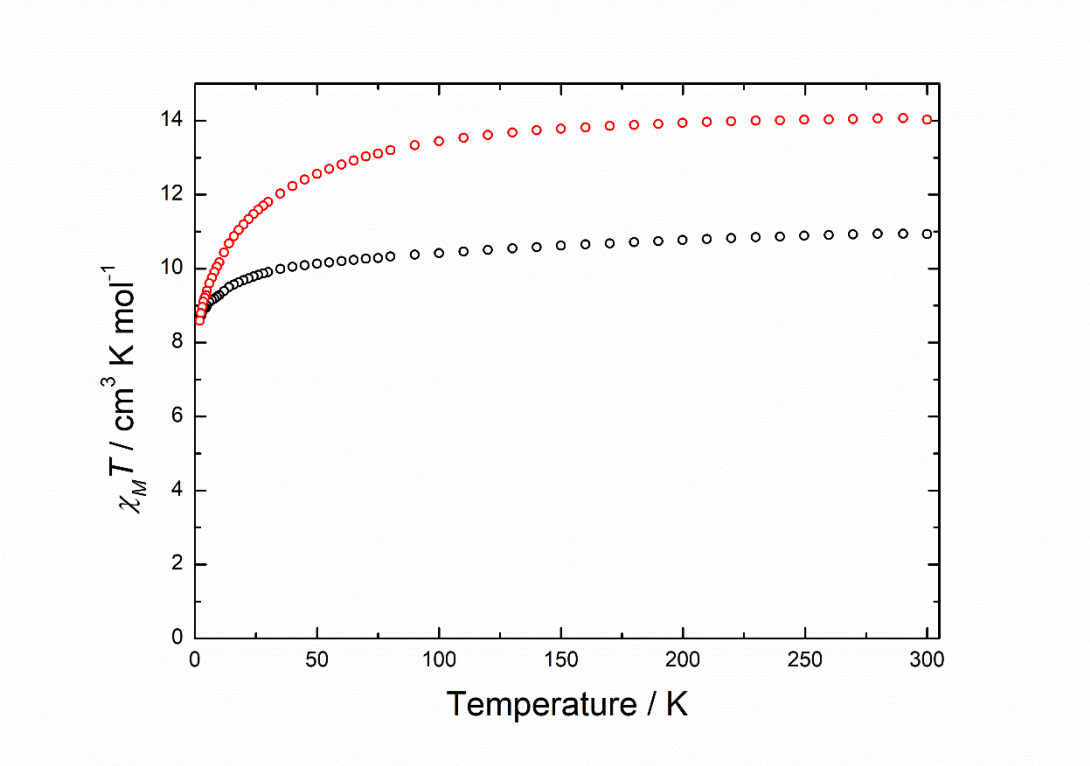

Figure 3.15: Plot of $\chi_M T$(T)in an applied field of 0.1 T for **3.3$_{Dy}$** (red) and **3.3$_{Er}$** (black).

The frequency dependencies of the magnetic susceptibility of **3.3$_{Dy}$** nor of **3.3$_{Ln}$** furnished sufficient clear maxima to allow the anisotropic energy barrier to be extracted. For the out-of-phase susceptibility of **3.3$_{Dy}$** (Figure 3.16) between 1.9 – 5.0 K shows a movement of the peak out of the frequency window as the temperature is raised. Low temperature values do not present enough clear peaks for further analysis. The out-of-phase measurement of **3.3$_{Er}$** (Figure 3.21) has no peaks at any temperature or frequency, values of χ'' increase dramatically at the upper limit of achievable frequency but with no clear peaks. The lack of discernible SMM properties through the in-phase and out-of-phase susceptibilities (Figure 3.19, Figure 3.20) could be due a combination of effects from the BH_4^- ligand which imparts a high degree of perturbation of the ligand field, resulting in extremely severe QTM effects This behaviour is similar to that exhibited by the 60 K precursor molecule $[(Cp^{ttt})_2DyCl]$. [123].

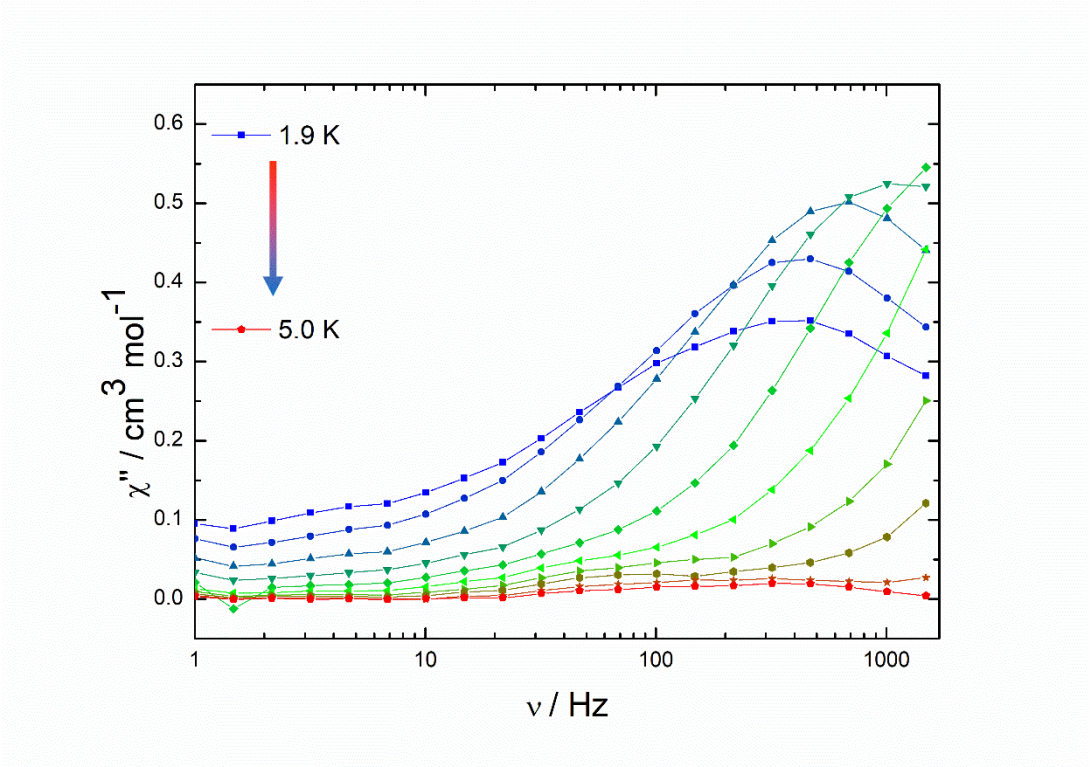

Figure 3.16: Frequency dependence of the out-of-phase (χ'') magnetic susceptibility for **3.3$_{Dy}$** in a 1 kOe applied field. Lines are guide to the eye and do not represent fits.

Magnetic hysteresis measurements were conducted on both dysprosium and erbium complexes (Figure 3.17 , Figure 3.18, respectively). For the dysprosium complex, there is no opening of the hysteresis loops at any field strength. This is expected from the ac data as well as the knowledge that the $[COT]^{2-}$ ligand extends provides an equatorial crystal field, where Dy^{3+} requires a strong axial crystal field, along with the strong effects of the BH_4^- ligand along with the two THF molecules. The situation for the erbium complex is similar, though it can be seen that at lower fields there exists a slight opening of the hysteresis loops with a scan rate of 23 Oe s^{-1}. Again, this is expected behaviour from the complex, as, contrary to Dy^{3+}, Er^{3+} requires a strong equatorial crystal field effects to furnish favourable SMM properties. The weakness of these properties must be ascribed to the deleterious effects of both the BH_4^- ligand and the two THF molecules, generating a crystal field lacking anisotropy.

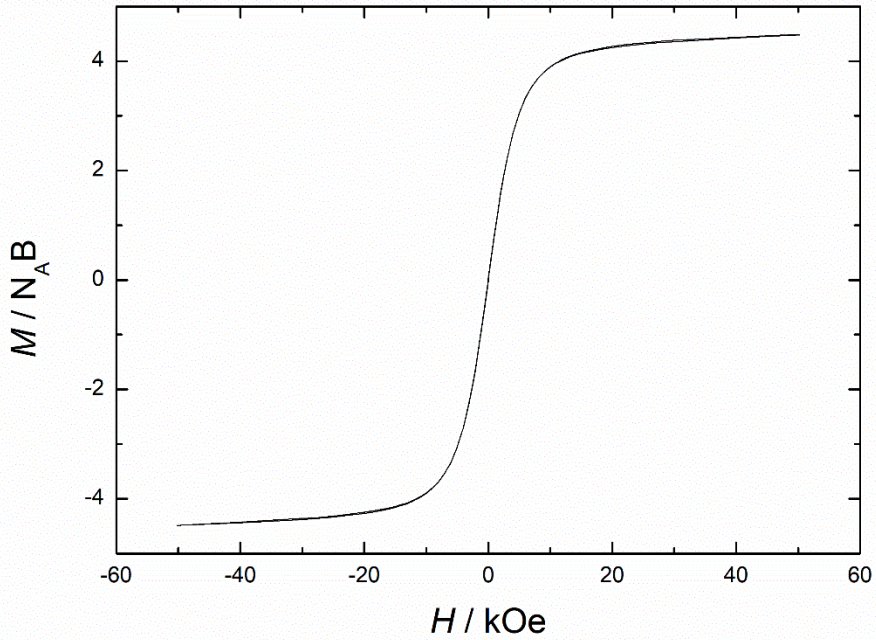

Figure 3.17: Magnetization (*M*) vs. field (*H*) hysteresis loop for **3.3$_{Dy}$,** scan rate of 23 Oe s^{-1}.

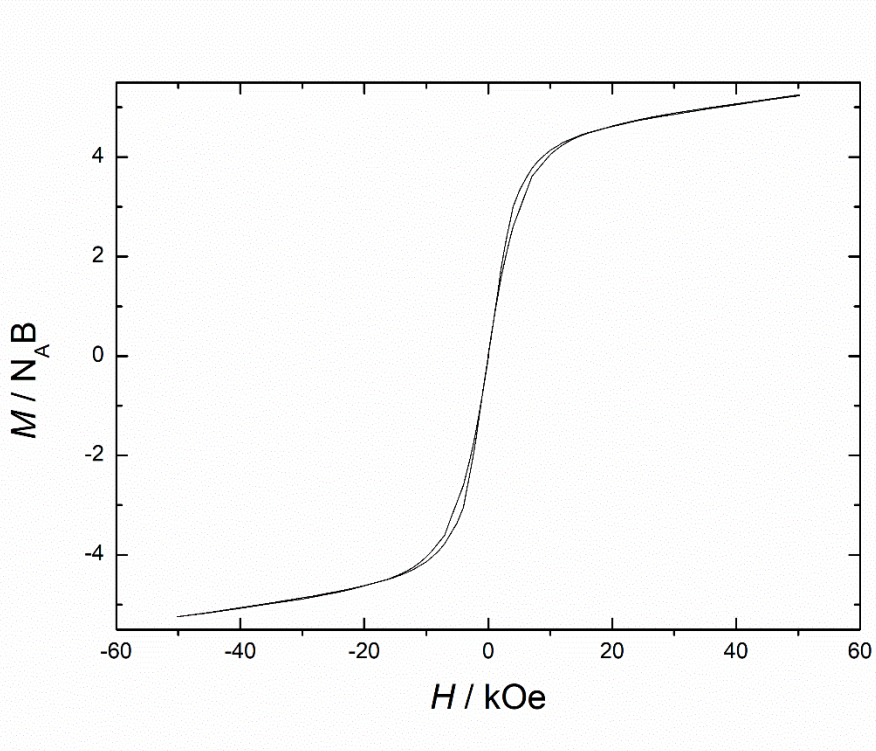

Figure 3.18: Magnetization (*M*) vs. field (*H*) hysteresis loop for **3.3$_{Er}$,** scan rate of 23 Oe s^{-1}.

The ChSM analysis of the complexes treat the π-bonded ligands as single points based on the centroids of the ligands. However, as a result of the effective diameter of the COT ligand the crystal-field effects are closer to the equatorial planes of the central metal atoms.[44,127] Therefore, the described magnetic properties can be understood to be a result of the perturbation crystal field in the equatorial plane. Additionally, the borohydride ligand imparts an electronic effect upon the ligand field, as a result of a high charge density, which will further increase the degree of QTM occurring.

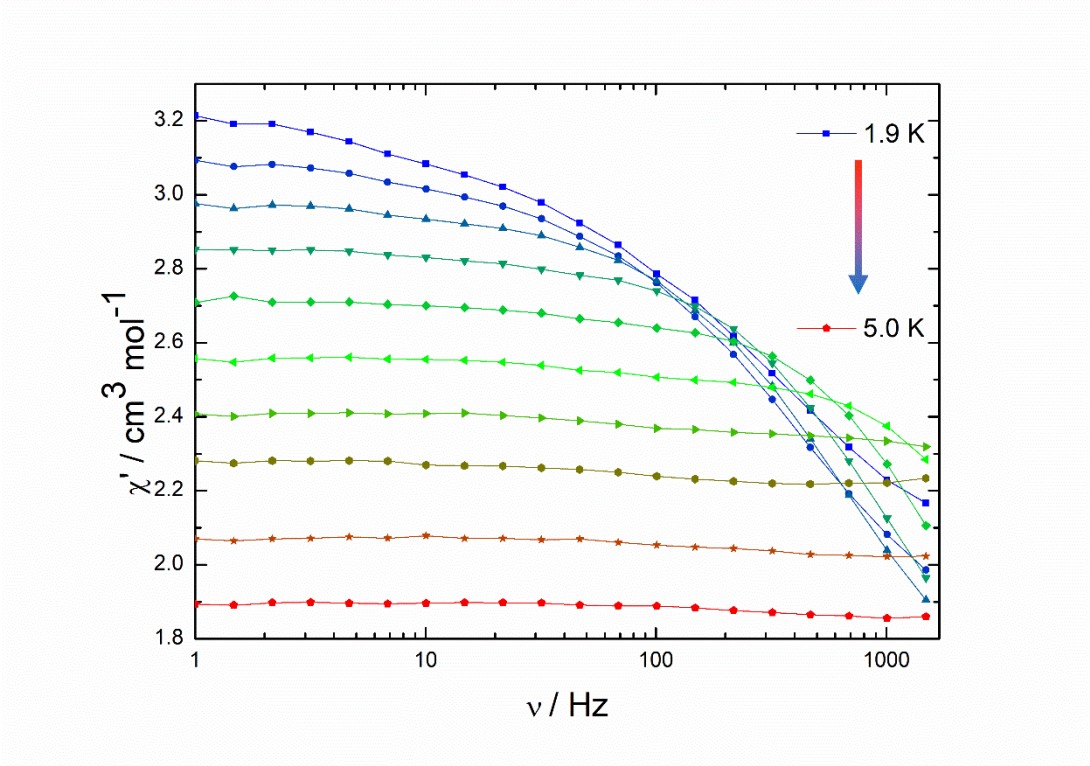

Figure 3.19: Frequency dependence of the in-phase (χ') magnetic susceptibility for **3.3$_{Dy}$** in a 0.7 T applied field. Lines are guide to the eye and do not represent fits.

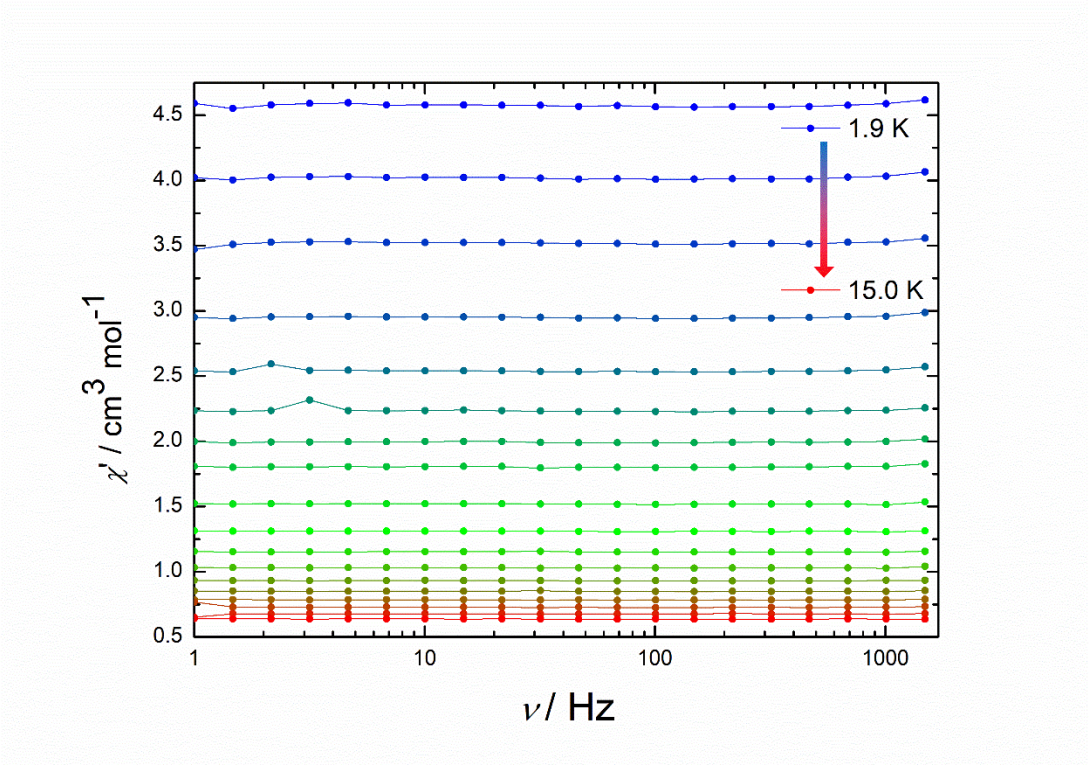

Figure 3.20: Frequency dependence of the in-phase (χ') magnetic susceptibility for **3.3**$_{Er}$ in a 0.7 T applied field. Lines are guide to the eye and do not represent fits.

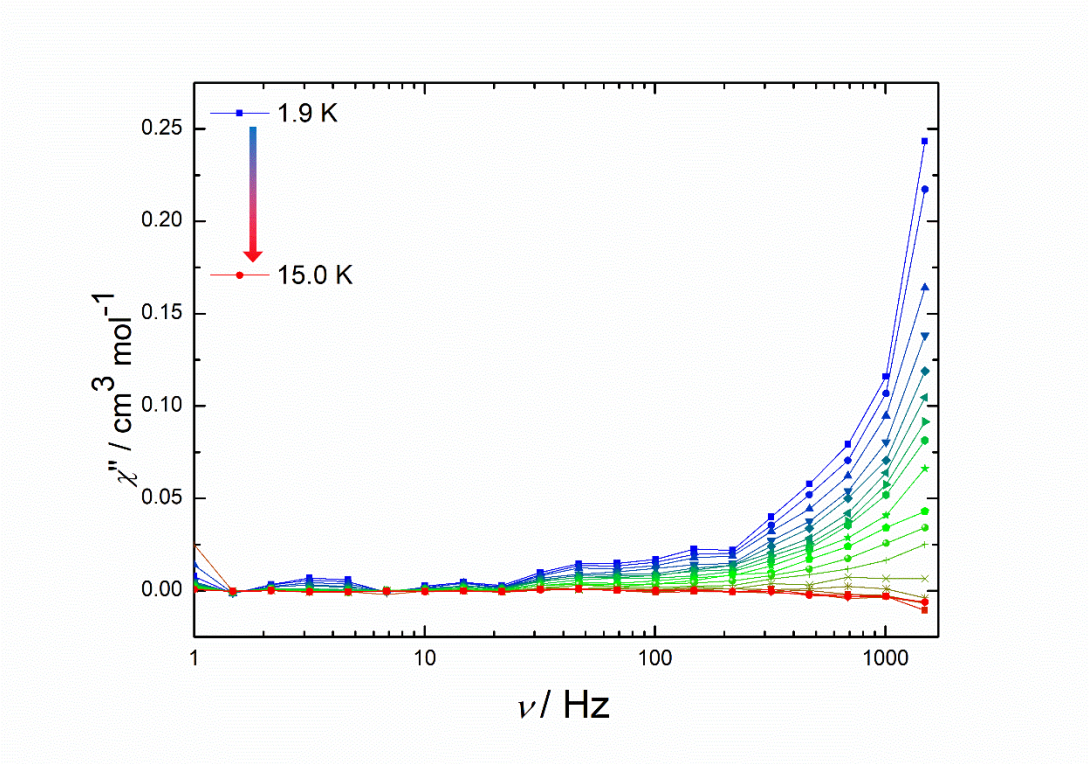

Figure 3.21: Frequency dependence of the out-of-phase (χ'') magnetic susceptibility for **3.3**$_{Er}$ in a 0.7 T applied field. Lines are guides to the eye and do not represent fits.

3.3.6 Computational Studies of $[(\eta^8\text{-COT})Dy(BH_4)(THF)_2]$ ($\mathbf{3.3_{Dy}}$) and $[(\eta^8\text{-COTDy})_2Pn^{TIPS}]$ ($\mathbf{3.4_{Dy}}$)

To further elucidate the experimental magnetic properties of the complexes described in this chapter, qualitative support was provided by basic theoretical calculations utilising the MAGELLAN program.[128] The software package assumes that the ground state of dysprosium exhibits a doublet along the principal anisotropy axis with an angular momentum quantum number of $|M_J| = \pm 15/2$ and implements an electrostatic methodology which predicts the magnetic anisotropy. The geometries of complexes were extracted from the crystal structures and then ran through MAGELLAN. Hydrogen atoms are excluded from these calculations. The results are generated as the red line which symbolises the principal magnetic easy axes, however no energy values or components of the *g*-tensors of the Kramers doublets (KD) are calculated.

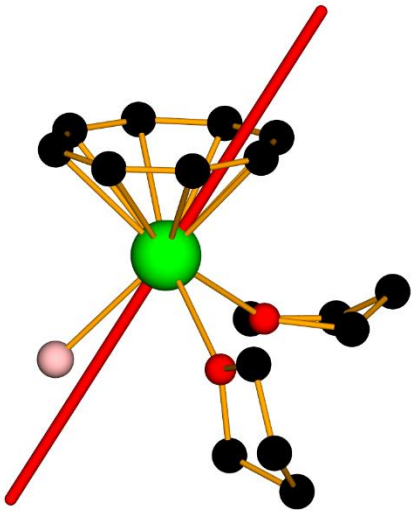

Figure 3.22: Calculated principal axes of the ground Kramers doublet of $\mathbf{3.3_{Dy}}$.

Thus, with these limitations the calculations were performed for both **3.3$_{Dy}$** and for **3.4$_{Dy}$**. For the complex **3.3$_{Dy}$**, Figure 3.22, the angle between COT_{cent}-Dy-axis is 31.59°. It can be seen that the principal axis is toward the boron atom of the BH_4^- ligand as well as close to the opposing edge of the COT ligand. Therefore, the borohydride ligand is greatly perturbing the equatorial crystal field of the complex.

The calculated principal axis, when compared with the experimental results, substantiate the suggestion that the borohydride ligand exerts a high degree of distortion upon the ligand field. That strong QTM effects that the **3.3$_{Dy}$** complex exhibits such can be understood based on this result.

For the complex **3.4$_{Dy}$** (Figure 3.23) the angle between COT_{cent}-Dy-axis is 7.03 ° and so much closer to the centroid of the COT and the Cp* ligands. This is a reasonable result as the high charge density of the BH_4^- is replaced with the lower charge density of the C5 ring of the pentalene unit. Further, it can be seen that the axes for each dysprosium atom is tending towards a parallel alignment which should engender favourable SMM properties. [129] Thus, the **3.3$_{Ln}$** complexes have the high possibility of being utilised as building blocks towards the inverse-sandwich trivalent lanthanide SMMs.

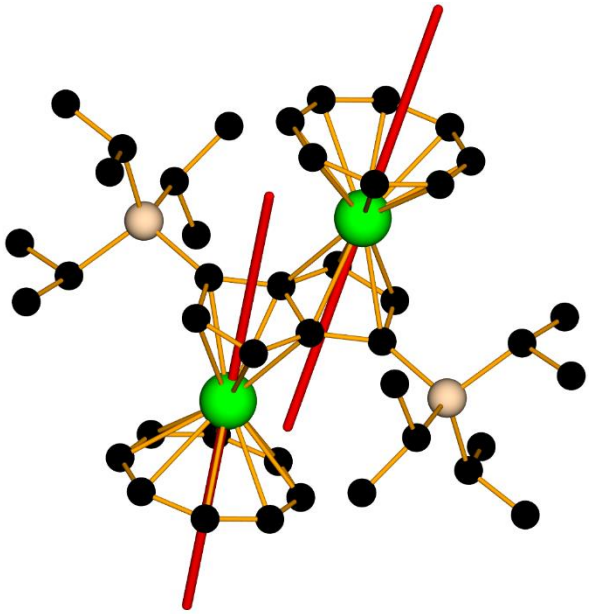

Figure 3.23: Calculated principal axes of the ground Kramers doublet of **3.4**$_{Dy}$.

3.4 Conclusion

This chapter describes the successful synthesis and solid-state characterisation of seven new lanthanide organometallic complexes (**3.3$_{Ln}$** and **3.4$_{Ln}$**). Magnetic studies were conducted on the monomeric **3.3$_{Ln}$** complexes and displayed a strong degree of QTM that was anticipated. Neither **3.3$_{Dy}$** nor **3.3$_{Er}$** furnished energy barriers to magnetic reversal as a result of the strong QTM. The same complexes also displayed no magnetic hysteresis at 1.9 K, though the erbium analogue **3.3$_{Er}$** had properties that were slightly improved compared with the dysprosium.

The computational studies conducted emphasise the deleterious effects that the borohydride ligand imparts on the magnetic properties of the complexes. The same studies conducted on the structure of **3.4$_{Dy}$** shows much more favourable principal axes and when these complexes have their magnetic properties measured, they should display much more favourable SMM properties.

3.5 Further Work

To advance the work outlined in this Chapter, the primary focus would be to complete the characterisation of the **3.4$_{Ln}$** complexes. These interesting structures could exhibit very promising SMM properties, as suggested by both literature comparisons along with the calculation of the principal easy axis in **3.4$_{Dy}$**. Solution state analysis along with magnetic characterisation would advance the understanding of inverse-sandwich systems in lanthanide SMMs.

As the intramolecular Ln···Ln distances are approximately 5 Å, there is a high probability of magnetic exchange coupling occurring and therefore it would be pertinent to synthesise a gadolinium analogue to be able to probe this with a complex where the isotropic nature of the metal aids in fitting the resulting data. The precursor **3.3$_{Gd}$** has been described in this chapter and so there remains to submit this molecule to similar synthetic procedures as for **3.4$_{Ln}$**. Successful isolation and measurement of a gadolinium analogue would allow for exchange couplings to be investigated. Knowledge of exchange couplings would further develop the analysis of inverse-sandwich SMMs.

There is also potential to utilise the borohydride group in salt metathesis reactions. The supply of suitable reagents for salt metathesis are only limited by imagination.

Chapter 4:

Monometallic Cyclooctatetraene Tetraphenylborate Lanthanide Complexes as Single-Molecule Magnets

4.1 Introduction

The effects of solvent ligands on the magnetic properties of lanthanide organometallic SMMs has not yet been thoroughly investigated. There some are examples in the literature of how solvents can direct a synthesis, leading to the formation of different molecular magnets with different magnetic properties.[130,79]

A recent report by Zhang *et al.* investigated the effects of latticed-bound solvents and how the single-crystal to single-crystal transformation resulted in a switching of the magnetic properties of a set of Dy^{3+} SMMs (**4.1$_{Dy}$**).[131] However, different solvents led to different structures and so the change in guest solvent modified the structures (Figure 4.1). When the lattice solvent was methanol, the coordination environment around the Dy^{3+} ion displayed a greater deviation from the ideal triangular dodecahedron than when there is no solvent or when dioxane is in the lattice. The molecular magnet with dioxane in the lattice exhibited open hysteresis up to 5 K, whereas when methanol was the lattice solvent no openings were visible. It follows that the different magnetic properties exhibited by the molecular magnets is a result of this structural change, brought on by the solvent substitution, and not as a result of the solvent acting directly upon the metal atom.

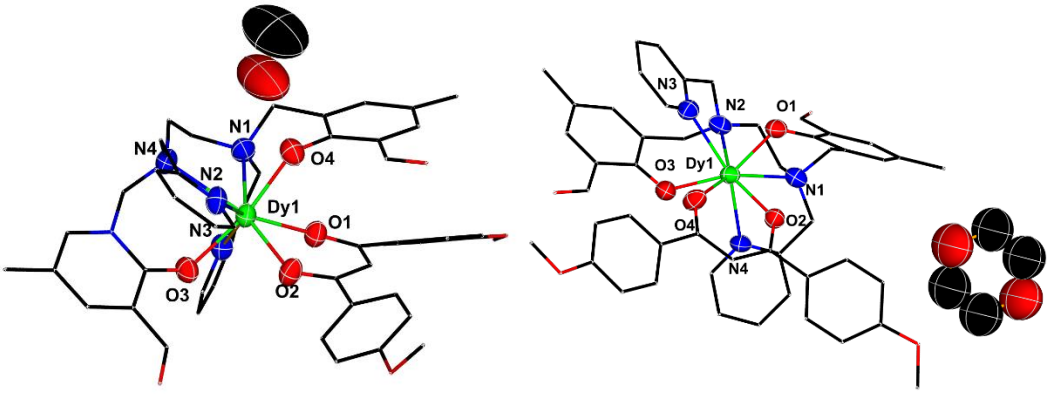

Figure 4.1: Structures of **4.1$_{Dy}$** ([Dy(L)(Bmpd)], Bmpd = 1,3-Bis(4-methoxyphenyl)-1,3-propanedione, L = methanol (left) and dioxane (right)) where single-crystals were soaked in appropriate solvent (hydrogen atoms omitted for clarity, displacement ellipsoids set at the 50 % probability level).

It is commonly stated that the ligand field surrounding the metal atom exerts a great influence over the resulting magnetic properties of a Ln-SMM.[132] Thus, by maintaining the ligand scaffold and the structure of the molecules, but altering the solvato ligands bound to the metal atom, the effects of changing solvato ligands on magnetism can be explored.

Previous work has shown that the type of counterion employed in Ln-SMM development can exert a structural effect which in turn affects the magnetic properties. For the family of $[Cp^R_2Dy]^+$, some of the most prevalent Ln-SMMs in the field, the choice of counterion is primarily whichever allows for the isolation of a pseudo-axial system.[34] These have ranged from the common tetraphenylborate anion to the more complex teflonate-type anions.[133,134] The $[Cp^*_2Dy(\mu\text{-}Ph_2BPh_2)]$ (**4.2$_{Dy}$**, Figure 4.2) molecule was subjected to magnetic studies by Demir *et al.* and displays an energy barrier to reversal of magnetisation of 331 cm^{-1}.[133] This is also impressive from the fact that the phenyl rings of the $[BPh_4]^-$ are close enough (Dy-C = 2.823(3) Å) to display agostic interactions, according to the authors. This interaction

contributes a negligible equatorial crystal field and so the magnetic properties are not significantly affected.

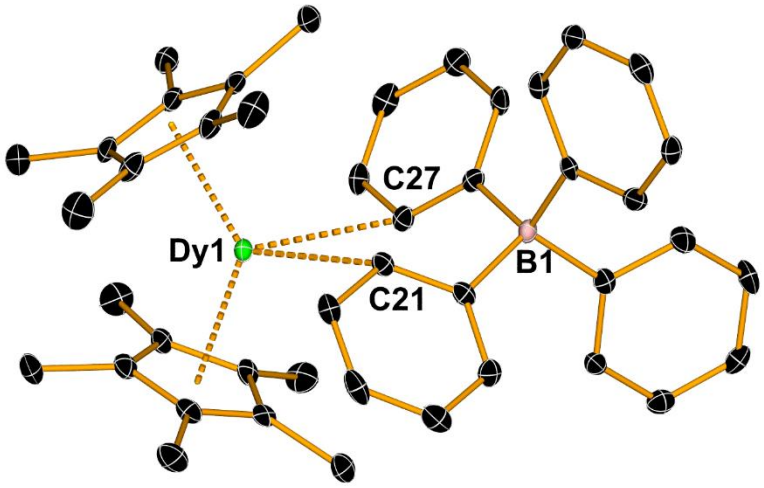

Figure 4.2: Thermal ellipsoid representation of **4.2$_{Dy}$** (hydrogen atoms omitted for clarity, displacement ellipsoids set at the 50 % probability level).[133]

A complex reported by Cendrowski-Guillaume *et al*, [(η^8-COT)Nd(THF)$_4$][BPh$_4$] (**4.3$_{Nd}$**, Figure 4.3), demonstrated the possibility of successfully synthesising a lanthanide-cyclo-octatetraene separated ion pair (SIP) along with the reactive versatility of the same compound.[95,96] This result creates an intriguing blueprint for the design of COT based SMMs. However, the magnetic properties of this compound were not reported. Neodymium-based SMMs are uncommon, as the lighter lanthanides (Pr, Nd, Sm) exhibit much lower magnetic moments and weaker spin-orbit coupling than the heavier lanthanides (Gd, Tb, Dy, Ho, Er, Tm and Yb). [135,136] Thus, for **4.3$_{Nd}$** it is highly likely that no SMM properties would be displayed.

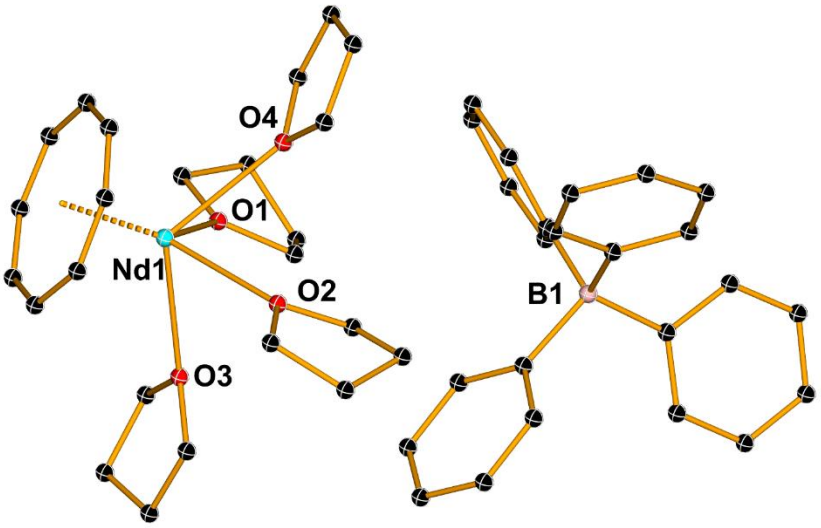

Figure 4.3: Thermal ellipsoid representation of **4.3$_{Nd}$** (hydrogen atoms omitted for clarity, displacement ellipsoids set at the 50 % probability level).[95]

4.2 Aims of the Chapter

This chapter aims to show how substitution of the solvato ligands could be utilised to modify the magnetic properties of lanthanide-cyclo-octatetraene SMMs. By synthesising a series of lanthanide organometallic complexes in which a substitution of one type of solvato ligand for another is straightforward, the effects on the magnetism should be then readily demonstrated. Comparisons of an oblate lanthanide ion (dysprosium) SMM and a prolate ion (erbium) will also allow for analysis of how the different ligand environments interaction with the respective spin-orbit coupled ground multiplets for each lanthanide.

4.3 Results and Discussion

4.3.1 Synthesis and Structure of $[(\eta^8\text{-COT})Ln(THF)_4][BPh_4]$ ($\mathbf{4.4_{Ln}}$)

Utilising the $[(\eta^8\text{-COT})Ln(BH_4)(THF)_2]$ complexes described in Chapter 3, efforts were made to abstract the borohydride anion through a protonolysis reaction with $[HNEt_3][BPh_4]$ (Scheme 4.1). Synthesis *via* this route furnished diborane, hydrogen and triethylamine as the side products, all of which are readily removed through washing and drying the product. The initial successful synthesis of the products $\mathbf{4.4_{Ln}}$ (Ln = Y, Dy, Er) was accomplished on a low millimolar scale in the glovebox, where vigorous effervescence could be seen soon after mixing the reactants. Shortly after this, crystalline material began to form. This material could be isolated simply by decanting the remaining reaction mixture and extensively washing the product with THF.

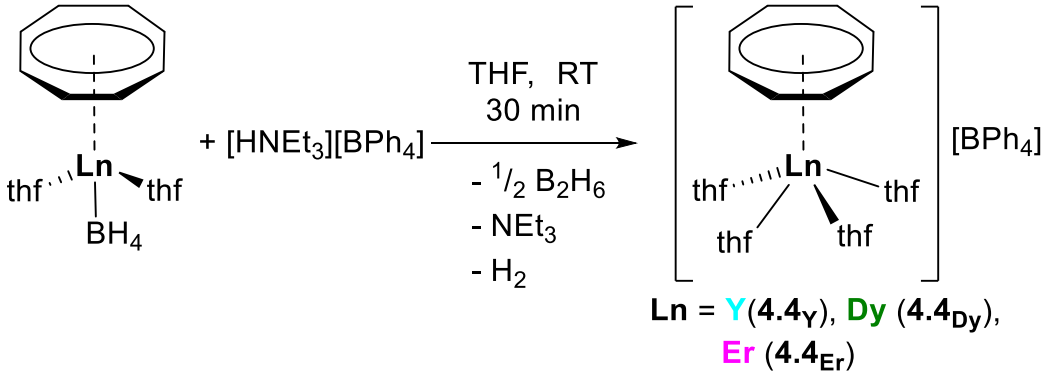

Scheme 4.1: Synthetic route to $\mathbf{4.4_{Ln}}$.

Unfortunately, though the crystalline materials would diffract X-rays, they were not of sufficient quality to allow for publication-quality data to be collected. To overcome

this, the reaction was repeated in the glovebox using smaller amounts of **3.1$_{Ln}$** (approximately 0.07 mmol) and a 20-fold excess of the acid [HNEt$_3$][BPh$_3$]. A large excess of acid was found to be optimal, as lower amounts did not lead to crystals, though this does not negate the possibility that the result was due to concentration effects. This method allowed for crystal growth and extremely high-quality crystals for diffraction studies, exemplified by an R_1 factor for 4**.4$_{Ln}$** between 2.31-2.59 %.

It was found that when scaling up the reaction (by a factor of 10) that new problems arose. If the reactions were stirred for longer 30 minutes, then a reduced yield and purity would result. This was noted primarily by ^{1}H NMR spectroscopy of **4.4$_{Ln}$** (see below) showing both precursor and product, irrespective of the number of washes conducted on the precipitated material. All reactions were conducted with an excess of [HNEt$_3$][BPh$_4$] as its high solubility allows for simple removal through washing and therefore allows for greater conversion. Conducting the reaction at low temperatures (−78 °C and 0 °C) did not improve either yield or purity. To obtain pure products, reaction times could not be longer than 10 minutes. Unfortunately, the side products could not be identified but are tentatively assigned as a degradation of the [HNEt$_3$][BPh$_4$] possibly catalysed by the lanthanide molecules. As determined by the numerous optimisation steps attempted, it can be suggested that **4.4$_{Ln}$** is a kinetic product with a small barrier to decomposition in a reaction mixture. The final yields are **4.4$_{Er}$** = 51 %, for **4.4$_{Dy}$** = 60 %, and for **4.4$_{Y}$** = 63 %.

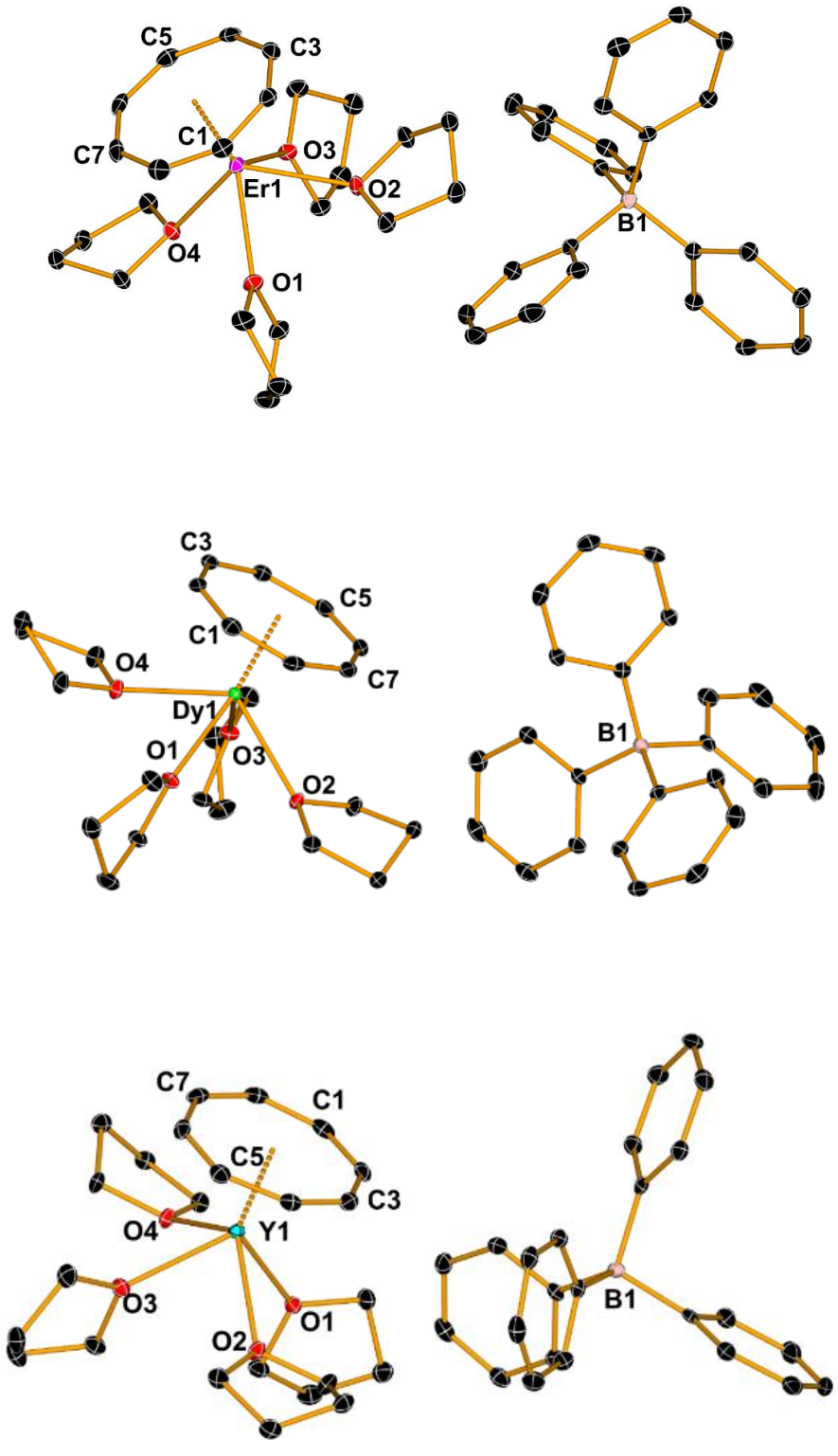

Figure 4.4 Thermal ellipsoid representation of **4.4**$_{Er}$ (top) **4.4**$_{Dy}$ (middle), **4.4**$_{Y}$ (bottom) (hydrogen atoms omitted for clarity, displacement ellipsoids set at the 50 % probability level).

The three **4.4$_{Ln}$** complexes are isostructural, crystallising in the space group *P*-1. The analogous neodymium complex (**4.3$_{Nd}$**) crystallised in the $P2_{1/n}$ space group.[95] The COT_{cent}-Ln distances are slightly elongated compared to the precursors; **4.4$_{Y}$** = 1.8602(7) Å, **4.4$_{Dy}$** = 1.8634(7) Å, and **4.4$_{Er}$** = 1.8422(8) Å. These are all well within the ranges reported for COT-Ln complexes.[42,44,108] Selected bond lengths for compounds **4.4$_{Ln}$** are summarised in Table 4.1.

Table 4.1: Relevant distances of **4.4$_{Ln}$** (values in Å).

	4.4$_{Y}$	**4.4$_{Dy}$**	**4.4$_{Er}$**
Ln-COT_{cent}	1.8602(7)	1.8634(7)	1.8422(8)
Ln-COT_{avg}	2.6131	2.6183	2.6039
Ln-O_{avg}	2.4291	2.4400	2.4201
Ln-B	7.786(2)	8.122(3)	8.513(3)
Ln-Ph_{cent}	5.9717(10)	6.8032(10)	6.541(10)
Ln-Ph_{close}	5.581(2)	6.055(3)	6.011(3)
Ln···Ln	8.1890(4)	8.1947(5)	8.1791(4)

The intermolecular Ln···Ln distances are important, as shorter distances can allow for dipolar exchange to occur, which can give rise to fast QTM pathways. Inspection of all three complexes confirms they each possess sufficiently long Ln···Ln distances as all three have separations > 8 Å.

In each of the complexes, the boron atom of the $[BPh_4]^-$ counter ion is at a distance great enough to consider the anion as non-coordinating, Ln···B = 8.122(3) Å, 8.514(3) Å, and 7.786(2) Å for **4.4$_{Dy}$**, **4.4$_{Er}$**, and **4.4$_{Y}$**, respectively..[137] This is a result of an electrophilic character of the Ln^{3+} cations below the threshold required to coordinate to the anion. Again, this is important to ensure that the crystal fields of the complexes are not perturbed by the anion. For the complexes **4.4$_{Ln}$** the distances from the metal to the nearest carbon on a phenyl ring (Ln···Ph_{close}) and to the centroid of the nearest

phenyl ring (Ln···Ph_{cent}), are all sufficiently large enough to be consistent with separated ion pairs (SIP) as all are above 5 Å. These distances are all much greater than in **4.2$_{Dy}$** (Dy···B = 4.475(3) Å, Dy···Ph_{cent} = 3.759 Å, Dy···Ph_{close} = 2.823(3) Å), which displayed a weak agostic interaction and is regarded as a contact ion pair.[133] The SIP nature of new complexes described is a result of the higher electron density in the solvent molecules compared to the phenyl ring of $[BPh_4]^-$ precluding any competition between the two groups.

The geometries of **4.4$_{Ln}$** were assessed by using CShM (Continuous Shape Measurements) calculations (see Section 3.3.1 for details). The simplified models used to perform the calculations for are shown below (Figure 4.5). All three complexes show closest alignment to a spherical square pyramidal (C_{4v}) structure, with calculated values of S = 3.181 for **4.4$_{Er}$**, S = 3.191 for **4.4$_{Dy}$** and S = 3.195 for **4.4$_{Y}$**.

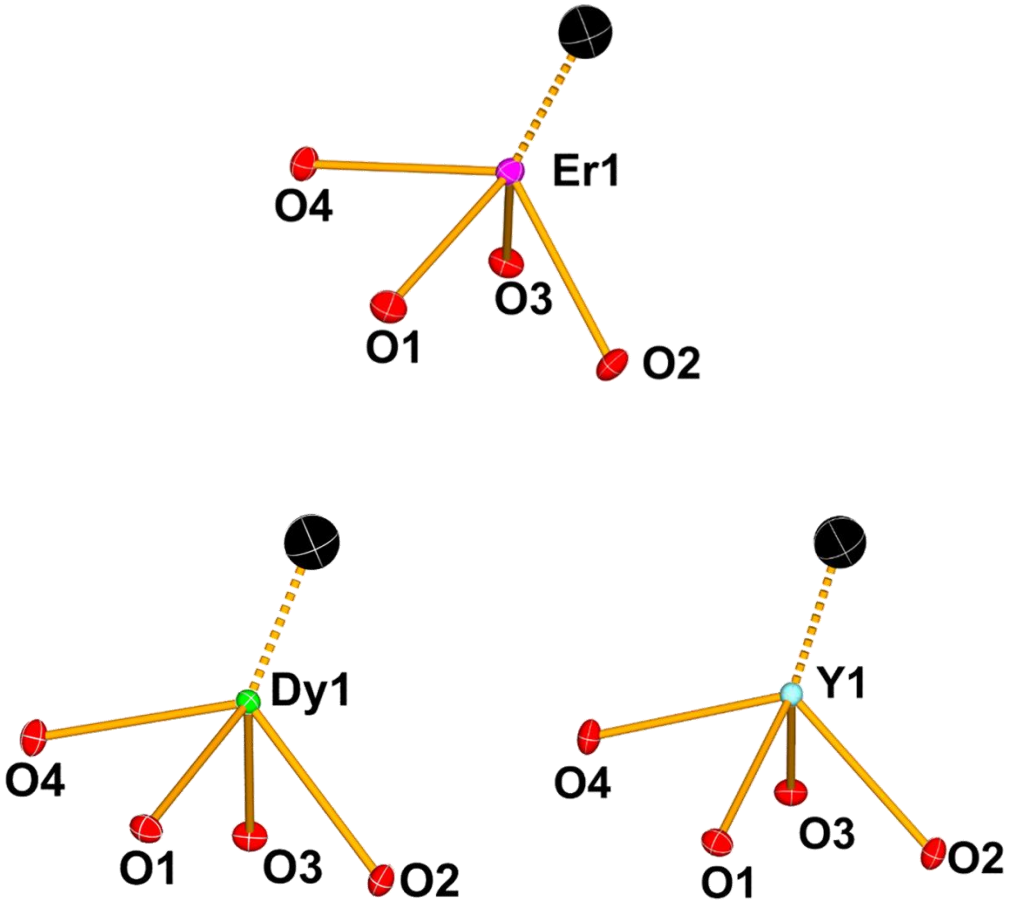

Figure 4.5: Diamond diagrams of the simplified structures of **4.4$_{Ln}$** used for CShM analysis (COT centroid represented in black, hydrogen atoms omitted for clarity, displacement ellipsoids set at the 50 % probability level).

These values show that each complex has a high degree of deviation from the ideal spherical square-based pyramid geometry. As $[COT]^{2-}$ is a 10π-aromatic 8-membered ligand, it should not reduce the symmetry of the molecule to an appreciable degree due to its inherent regularity. However, low symmetry complexes are not as ideal as molecules with high-order principal rotation axes, which had been targeted for their stronger SMM properties.[1,20]

Table 4.2: CShM analysis for **4.4$_{Ln}$**.

JTBPY-5	5	D_{3h}	Johnson trigonal bipyramid			JTBPY-5
SPY-5	4	C_{4v}	Spherical Square pyramid			SPY-5
TBPY-5	3	D_{3h}	Trigonal bipyramid			TBPY-5
vOC-5	2	C_{4v}	Vacant octahedron			vOC-5
PP-5	1	D_{5h}	Pentagon			PP-5
Structure	[ML5]	JTBPY-5	SPY-5	TBPY-5	vOC-5	PP-5
	4.4$_{Er}$	8.909	3.181	5.284	8.937	36.499
	4.4$_{Dy}$	8.981	3.191	5.299	8.966	36.506
	4.4$_{Y}$	8.930	3.195	5.276	8.967	36.45

4.3.2 Synthesis and Structure of $[(\eta^8\text{-COT})Ln(pyr)_4][BPh_4]$ ($\mathbf{4.5_{Ln}}$)

During the synthesis of $\mathbf{4.4_{Ln}}$, the initial attempts to grow crystals from crude material of publication-quality data were hampered by the insolubility of all the complexes in common solvents, including THF, toluene, benzene and diethyl ether even at reflux temperature. The investigations into solubility did, however, demonstrate the thermal stability of the complexes, as noted from ^{1}H NMR spectroscopy (see below). Application of the more polar pyridine, proved to be extremely successful, as it had previously shown potential in solubilising similar complexes (Scheme 4.2).[95] It was observed that dissolution in pyridine was accompanied by a drastic colour change , for $\mathbf{4.5_Y}$, from very pale yellow to a vibrant orange as a result of the original THF solvato ligands being substituted for pyridine. This colour change was similar for both dysprosium (yellow to light orange) and erbium (pink to deep orange). The subsequent solid-state study of $\mathbf{4.5_Y}$ showed that the colour change was a result of the complete substitution of the THF donor ligands by four pyridine ligands (Figure 4-6).

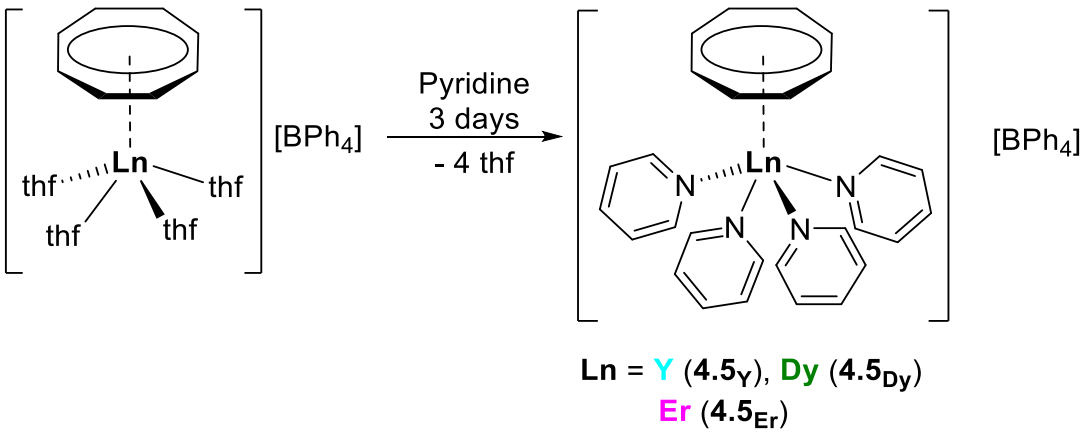

Scheme 4.2: Synthetic route to $\mathbf{4.5_{Ln}}$.

This result prompted further studies on the complexes **4.4$_{Dy}$** and **4.4$_{Er}$** to ascertain whether this was reproducible for the other lanthanides. This proved to be the case and solid-state structures were determined for both **4.5$_{Dy}$** and **4.5$_{Er}$** by X-ray diffraction studies. The molecular structures for **4.5$_{Ln}$** are isostructural, and crystallise in the space group *Pn* (Figure 4.6). Each of the complexes crystallised with a pyridine solvent within the lattice, however this is omitted from the images for clarity. It was also found by ^{1}H NMR spectroscopy that if crystals of **4.5$_{Ln}$** were washed excessively with THF, then the complexes **4.4$_{Ln}$** could be reformed though not as a complete reconversion. Thus, the coordination of the solvent molecules can be considered labile, however the incomplete reformation of **4.4$_{Ln}$** from **4.5$_{Ln}$** can be credited to the stronger donating ability of pyridine compared with that of THF.[138,139]

The molecular complexes **4.5$_{Ln}$** are structurally very similar to those described above for **4.4$_{Ln}$** (Table 4.2). The Ln-COT distance shows only a minor elongation upon solvent substitution. The Ln-solvent distance shows an increase due to the increased steric bulk and rigidity of pyridine. Selected bond lengths for compounds **4.5$_{Ln}$** are summarised in Table 4.3.

Table 4.3: Relevant distances of **4.5$_{Ln}$** (values in Å).

	4.5$_{Y}$	**4.5$_{Dy}$**	**4.5$_{Er}$**
Ln-COT$_{cent}$	1.8631(13)	1.8730(5)	1.8487(16)
Ln-COT$_{avg}$	2.6171	2.6141	2.6026
Ln-N$_{avg}$	2.5965	2.5785	2.4201
Ln-B	7.814(4)	7.665(1)	7.821(2)
Ln-Ph$_{cent}$	6.2794(15)	6.906(5)	6.3876(5)
Ln-Ph$_{close}$	5.5810(5)	5.7367(5)	5.947(12)
Ln···Ln	8.1890(4)	8.1947(5)	8.1791(4)

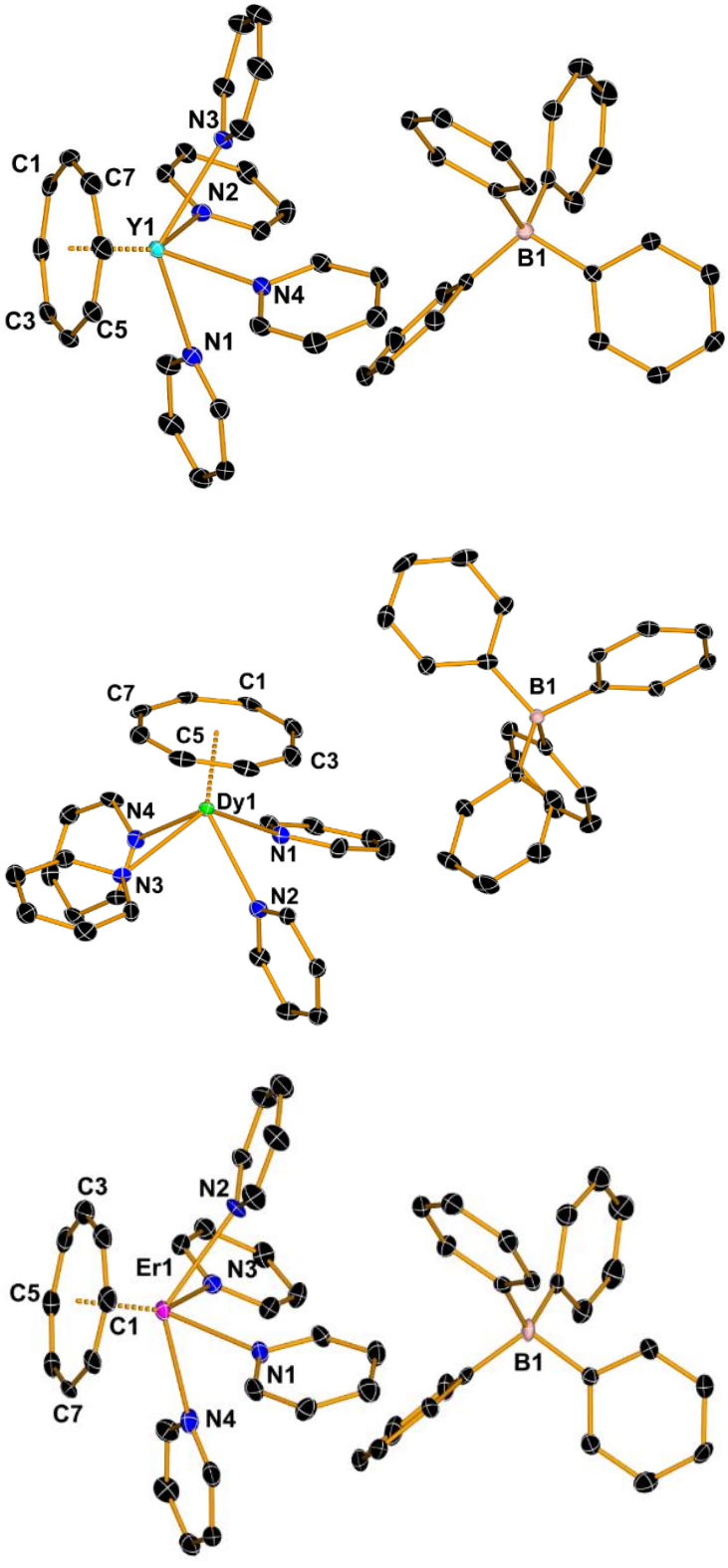

Figure 4.6: Thermal ellipsoid representations of **4.5**$_{Er}$ (top) **4.5**$_{Dy}$ (bottom left), **4.5**$_{Y}$ (bottom right) (hydrogen atoms omitted for clarity, displacement ellipsoids set at the 50 % probability level).

All distances between the metal atom and the $[BPh_4]^-$ counterion show no agostic interactions and are consistent with a separated ion pair. Whereas the distance to the COT ring centroid shows a variation across the family, with yttrium (1.8631(13) Å) and dysprosium (1.8730(5) Å) being similar and erbium (1.8487(16) Å) being closer to the centroid. The phenyl groups in the ^{1}H NMR spectrum of **4.5$_Y$** (see below) display the expected equivalency.

Finally, continuous shape measurement (CShM) calculations were undertaken on simplified models of the complexes **4.5$_{Ln}$**. The simplified models are shown below (Figure 4.7). Full details of the results are given in Table 4.4.

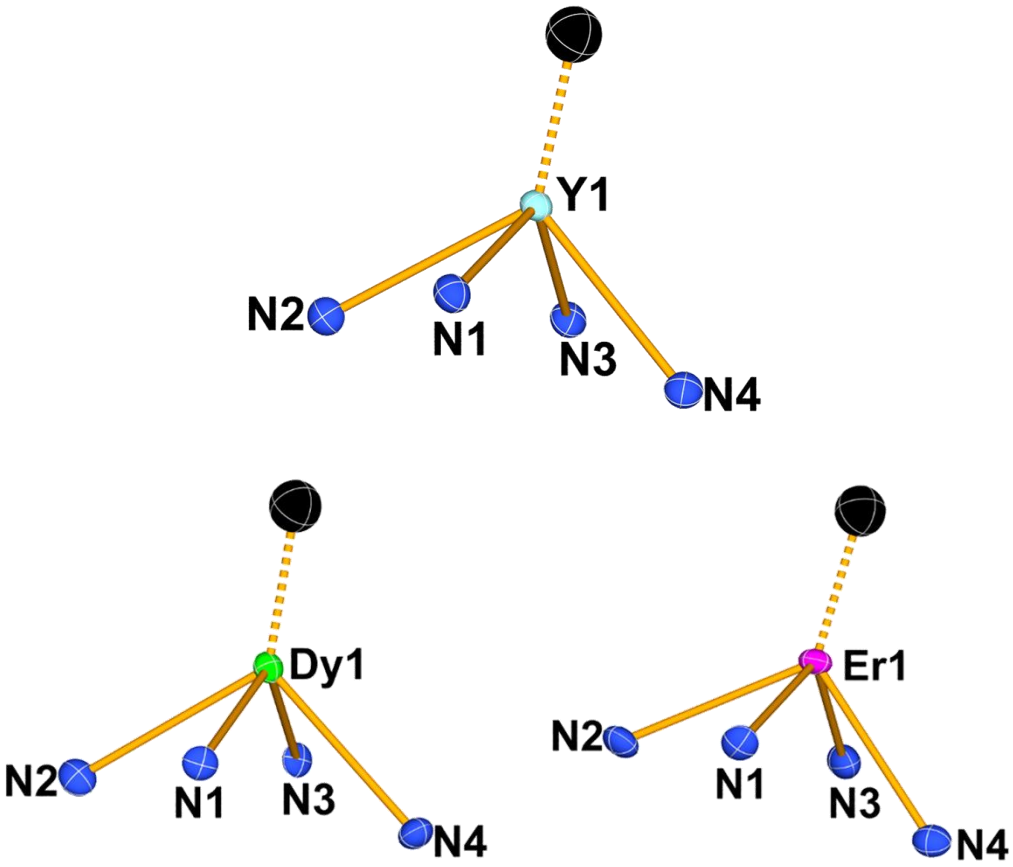

Figure 4.7: Models of the simplified molecular structures of **4.5$_{Ln}$** used for CShM analysis (COT centroid represented in black, hydrogen atoms omitted for clarity, displacement ellipsoids set at the 50 % probability level).

Considering the similarities between **4.4$_{Ln}$** and **4.5$_{Ln}$**, it is expected that all the complexes display a spherical square pyramid (C_{4v}) from the calculations. For **4.5$_{Y}$** S = 3.237, for **4.5$_{Dy}$** S = 3.333, and for **4.5$_{Er}$** S = 3.374. These complexes deviate slightly more so from the ideal geometry than those of **4.5$_{Ln}$**, however by an average S < 0.200. The increased planarity of pyridine, along with a slight increased steric bulk, results in this higher deviation for structurally very similar molecules.

Table 4.4: CShM analysis for **4.5$_{Ln}$**.

JTBPY-5	5	D_{3h}	Johnson trigonal bipyramid			JTBPY-5
SPY-5	4	C_{4v}	Spherical Square pyramid			SPY-5
TBPY-5	3	D_{3h}	Trigonal bipyramid			TBPY-5
vOC-5	2	C_{4v}	Vacant octahedron			vOC-5
PP-5	1	D_{5h}	Pentagon			PP-5
Structure	[ML5]	JTBPY-5	SPY-5	TBPY-5	vOC-5	PP-5
	4.5$_{Er}$	5.635	3.285	3.374,	8.058	35.614
	4.5$_{Dy}$	5.693	3.177	3.333	7.916	35.515
	4.5$_{Y}$	5.683	3.237	3.380,	8.002	35.562

4.3.4 Solution State Analysis of $[(\eta^8\text{-COT})Ln(THF)_4][BPh_4]$ ($\mathbf{4.4_{Ln}}$) and $[(\eta^8\text{-COT})Ln(pyr)_4][BPh_4]$ ($\mathbf{4.5_{Ln}}$)

Studies were undertaken on the complexes described throughout this chapter to investigate if the solid-state structure is retained in solution. To this effect, comprehensive NMR spectroscopic studies were undertaken on the complexes $\mathbf{4.4_Y}$ and $\mathbf{4.5_Y}$. The paramagnetic complexes $\mathbf{4.4_{Dy}}$, $\mathbf{4.5_{Dy}}$, $\mathbf{4.4_{Er}}$ and $\mathbf{4.5_{Er}}$, were also subjected to ^{1}H NMR spectroscopic studies. However, due to extensive line broadening inherent to complexes of these lanthanides as a result of their paramagnetic nature, the resulting information is more qualitative.[19,101,113]

The ^{1}H NMR spectrum of $\mathbf{4.4_Y}$ (Figure 4.8) in d_5-pyridine is shown below. The signals at 1.66 ppm and 3.69 ppm correspond to the $OCH_2C\underline{H}_2$ and the $OC\underline{H}_2CH_2$ protons of the THF ligands, respectively. Notably, the integrations show that there are only three molecules of THF, rather than the four seen in the solid-state structure (see above). This warranted further investigation to understand the discrepancy and so repeat reactions were conducted, with short (30 minutes), long (2 hours) and overnight (16 hours) reaction times. All showed the three THF molecules by integration (Appendix, Figure S7). This suggests that the THF is only weakly bound to the lanthanide metal and therefore is quite labile, probably subject to partial removal when the compound is dried using a dynamic vacuum.

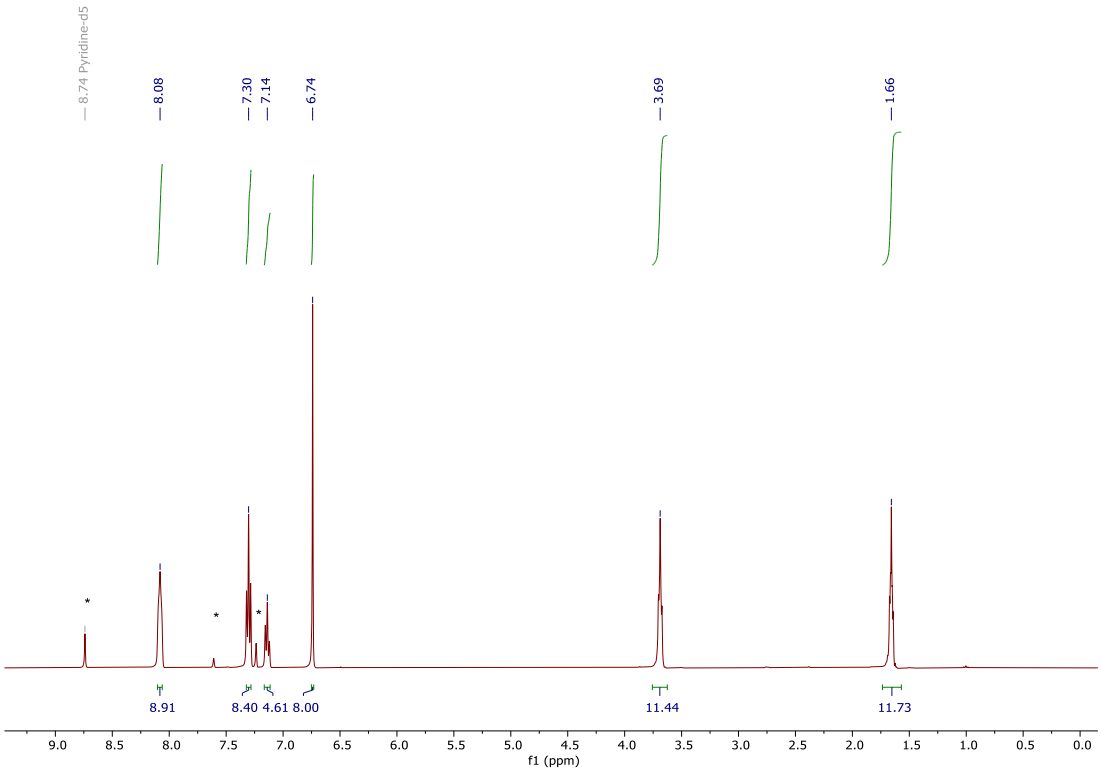

Figure 4.8: ^{1}H NMR spectrum of **4.4$_{Y}$** (d_5-pyridine, 400 MHz, 303 K, * represent deuterated solvent signals).

As discussed, longer reaction times led to lower purity of the final product, as seen by CHN and ^{1}H NMR spectroscopy. By integration, the impurities constituted 10 % of the products of the overnight reaction. Hence, final yields could not be improved through extended reaction times as this led to noticeable, visually and spectroscopically, impure final products. There was no evidence of residual $[BH_4]^-$ in the spectrum.

The $^{13}C\{^{1}H\}$ NMR spectrum of **4.4$_{Y}$** (see Appendix Figure S8) corroborates the ^{1}H NMR spectrum; the resonance at δ = 24.51 ppm corresponds to $OCH_2\underline{C}H_2$, 66.54 ppm corresponds to $O\underline{C}H_2CH_2$, 94.56 ppm is the $\underline{C}_8H_8$ carbon atoms in the COT ligand, 121.06 ppm is the *para*-carbon of the $[BPh_4]^-$, 124.89 ppm is the meta-carbon of the anion, 135.88 ppm is the *ortho*-carbon, and the quartet from 162.99 – 164.46 ppm is

the *ipso*-carbon of the phenyl rings in the $[BPh_4]^-$. The splitting of the *ipso*-carbon peak to a quartet is expected from the coupling of spins where I = 3/2 for ^{11}B and I = 1/2 for ^{13}C, with a coupling constant of 50 Hz.

Gratifyingly, the $^{11}B\{^1H\}$ NMR spectrum of **4.4$_Y$** shows only one peak at −5.42 ppm, a large enough shift to confirm that it is a different boron species to that of **3.3$_Y$** which had a single peak at −31.86 ppm. There are satellites visible in the $^{11}B\{^1H\}$ NMR spectrum, with a separation of 50 Hz, which can be attributed to the coupling to carbon atoms, however the low natural abundance of ^{13}C leads to a signal with very weak intensity, barely discernible above the baseline.

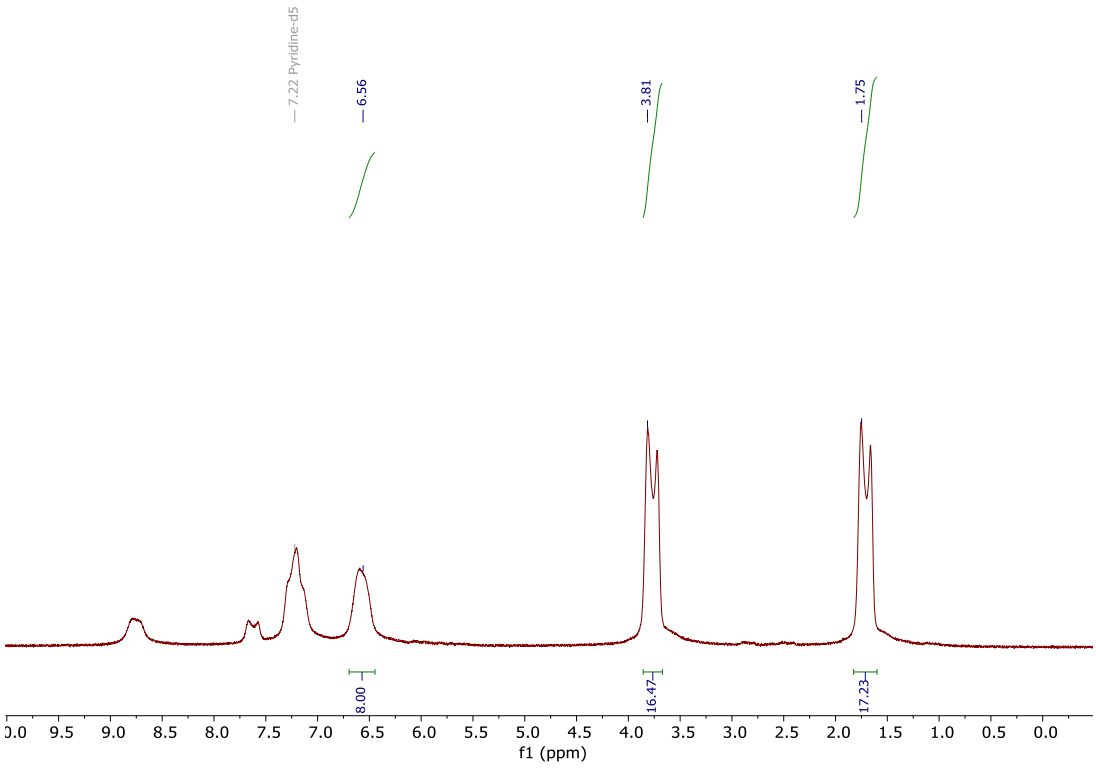

Figure 4.9: ^1H NMR spectrum of **4.4$_{Dy}$** (d_5-pyridine, 400 MHz, 303 K).

Though NMR spectroscopy of paramagnetic complexes can sometimes lead to spectra that are difficult, if not impossible, to assign, sometimes these spectra can be

informative. The ^{1}H NMR spectrum of **4.4$_{Dy}$** (Figure 4.9) is broadened compared with the diamagnetic **4.4$_{Y}$**, which is expected. However, signals corresponding to the THF can be assigned, thus the peak at 1.73 ppm is $OCH_2C\underline{\boldsymbol{H}}_2$ and that at 3.80 ppm is $OC\underline{\boldsymbol{H}}_2CH_2$. Further, the peak at 6.54 ppm can be assigned to the C_8H_8 protons of the COT ligand. Unfortunately, due to signal broadening it seems that the $[BPh_4]^-$ signals overlap with the d_5-pyridine signals. The low abundance of ^{13}C nuclei combined with the paramagnetic dysprosium leads to very faint signals, thus precluding collection of a ^{13}C{^{1}H} NMR spectrum. However, satisfyingly, a signal can be seen in the ^{11}B{^{1}H} NMR spectrum (see Appendix) at δ = −6.28 ppm.

The ^{1}H NMR spectra of **4.4$_{Er}$** and **4.5$_{Er}$** unfortunately displayed no assignable signals other than those belonging to the deuterated solvent. This contrast to the dysprosium analogues and may be due to the differences in the shape of the relevant electron densities in Er^{3+} when compared to Dy^{3+}. The COT ligand is large enough that it is considered to primarily act on, or be acted on, the equatorial ligand field. Thus, the COT ligand is affecting the prolate Er^{3+} to a higher degree which results in a T_1 relaxation which is too fast to allow for a signal to be observed.

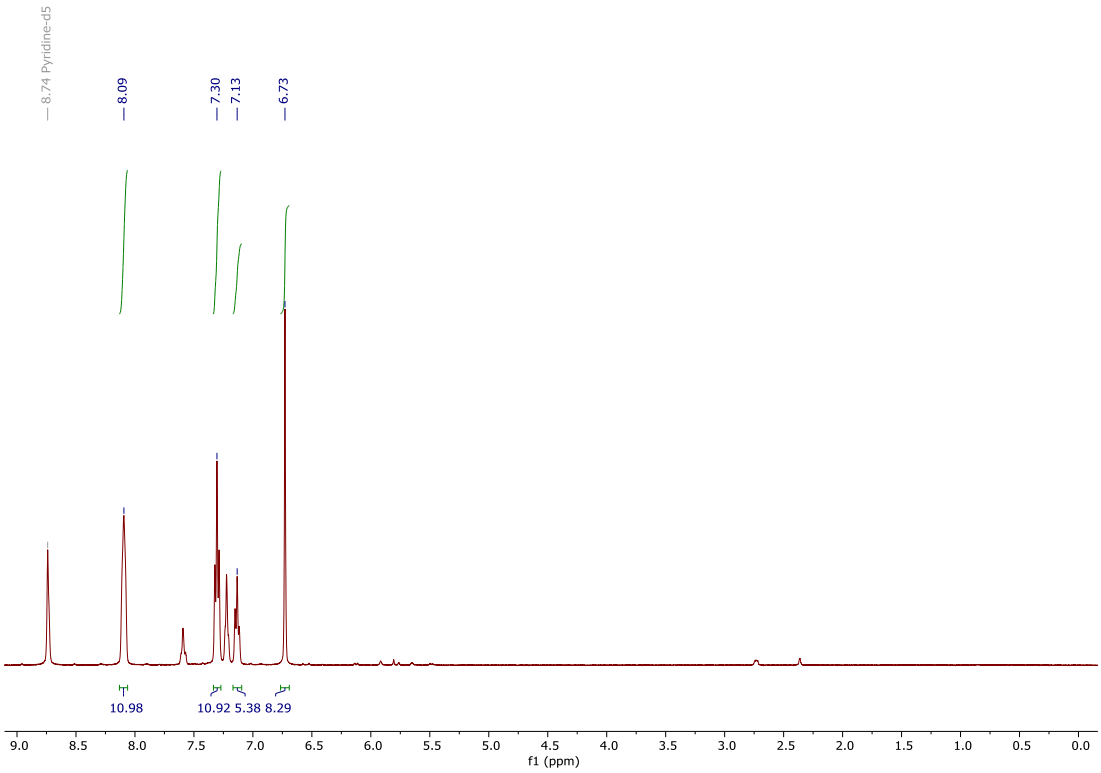

Figure 4.10: ^{1}H NMR spectrum of **4.5$_{Y}$** (d_5-pyridine, 400 MHz, 303 K).

Finally, the NMR spectra of **4.5$_{Y}$** confirm the complete substitution of THF molecules in **4.4$_{Y}$** to pyridine. The ^{1}H NMR spectrum of **4.5$_{Y}$** (Figure 4.10) shows no evidence of signals that would be associated with THF that are seen for **4.4$_{Y}$** (Figure 4.8). There is no shifting of the signals, therefore the assignments remain the same as for **4.4$_{Y}$**, which is to be expected as the only difference in these complexes is the solvation molecule. The difference in basicity of THF compared to pyridine is minimal, so the very minor/no variations in SC-XRD structures, calculated CShM geometries and NMR spectra are expected. The ^{13}C{^{1}H} and ^{11}B{^{1}H} NMR spectra (Appendix 2) for **4.5$_{Y}$** are analogous to those described for **4.4$_{Y}$**, showing the same shifts barring the expected lack of THF carbon signals in the ^{13}C{^{1}H} NMR spectrum.

4.3.5 Infrared Spectroscopy of $[(\eta^8\text{-COT})Ln(THF)_4][BPh_4]$ ($\mathbf{4.4_{Ln}}$) and $[(\eta^8\text{-COT})Ln(pyr)_4][BPh_4]$ ($\mathbf{4.5_{Ln}}$)

The FT-IR spectrum of $\mathbf{4.4_{Ln}}$ (Figure 4.11) shows quite clearly no peaks from 2750 - 1750 cm^{-1} for $\mathbf{4.4_{Er}}$, evidence for the removal of the BH_4^- ligand. The peaks at 3035-2892 cm^{-1} are those of the CH stretches for the COT ligand, the phenyl groups and THF molecules. For $\mathbf{4.4_{Dy}}$ the peaks are 3050 - 2881 cm^{-1}, and for $\mathbf{4.4_{Y}}$ 3056 - 2857 cm^{-1}. The peak at 1002 cm^{-1} visible in the spectrum of $\mathbf{4.4_{Er}}$ can be attributed to the C-O stretch belonging to the THF groups, as in the spectrum of $\mathbf{4.5_{Ln}}$ this peak disappears (see below). This peak in $\mathbf{4.4_{Dy}}$ is at 1001 cm^{-1} and in $\mathbf{4.4_{Y}}$ is at 1003 cm^{-1}.

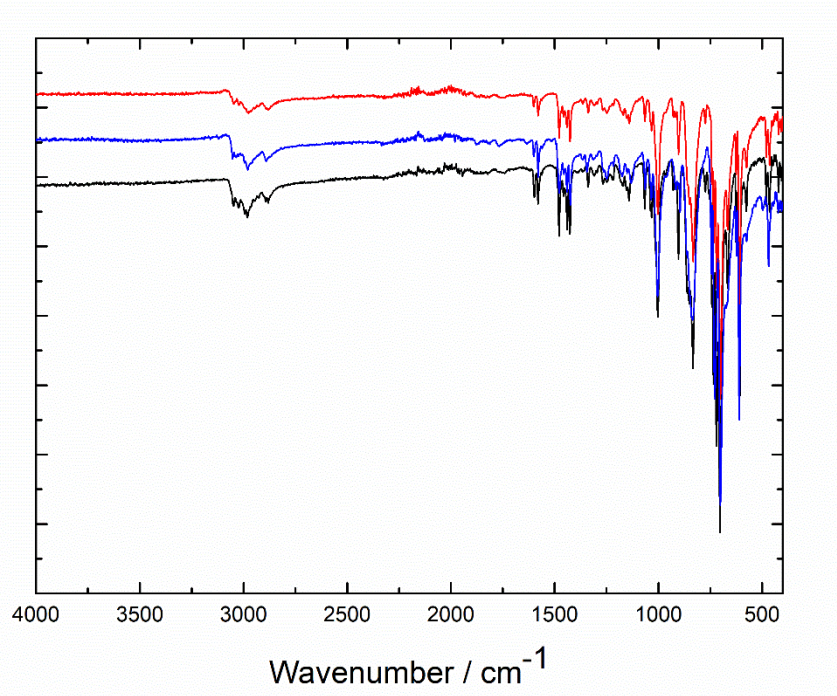

Figure 4.11: FT-IR spectrum of **4.4**$_{Ln}$, (red = **4.4**$_{Dy}$, blue = **4.4**$_{Er}$, black = **4.4**$_{Y}$,, transmission values are normalised before stacking).

The FT-IR spectra for **4.5**$_{Ln}$ (Figure 4.12) exhibit many similarities to those for **4.4**$_{Ln}$. This is expected as the only difference is the substitution of the solvation molecules and little difference in the geometry displayed by the complexes as elucidated by CShM analysis (see above).

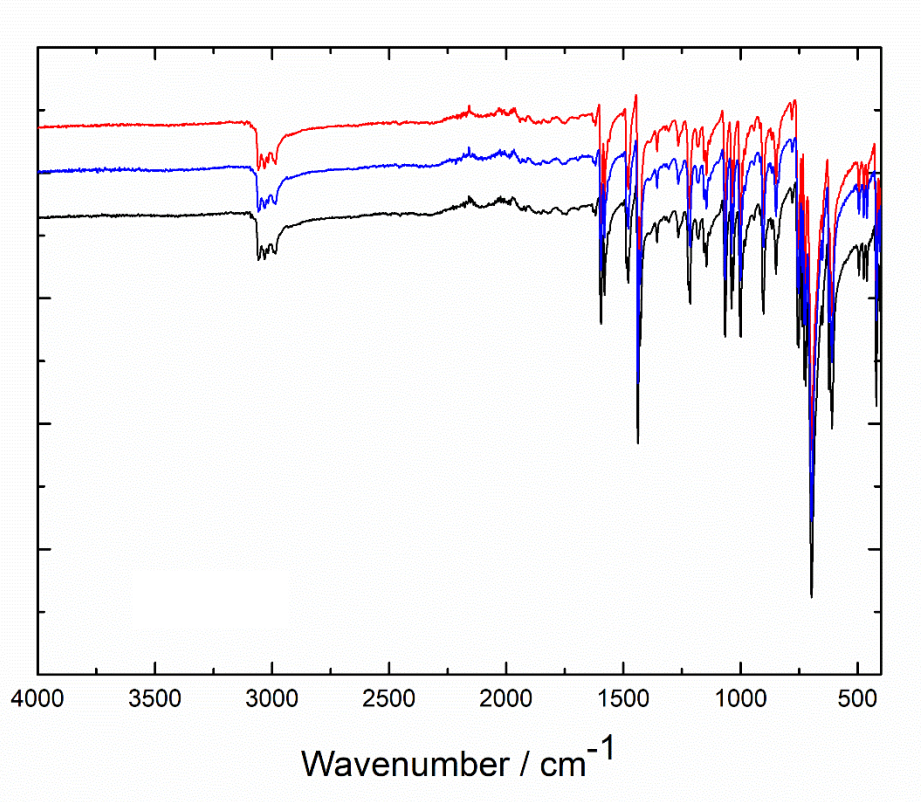

Figure 4.12: FT-IR spectrum of **4.5$_{Ln}$** (red = **4.5$_{Er}$**, blue = **4.5$_{Dy}$**, black = **4.5$_{Y}$**).

For all three complexes, the peak ascribed to the C-O in the THF molecules at approximately 1000 cm^{-1} is no longer present. In the spectrum of **4.5$_{Er}$**, a new, sharp peak at 1437 cm^{-1} is attributed to the C-N bonds present in the pyridine solvent molecules. For **4.5$_{Y}$** the same peak appears at 1439 cm^{-1} and for **4.5$_{Dy}$** the peak is at 1440 cm^{-1}.

4.3.6 Magnetic Characterisation of [(η^8-COT)Ln(THF)$_4$][BPh$_4$] (**4.4$_{Ln}$**) and [(η^8-COT)Ln(pyr)$_4$][BPh$_4$] (**4.5$_{Ln}$**)

For the complexes **4.4$_{Er}$** and **4.4$_{Dy}$**, measurements of the magnetisation (*M*) *vs*. field/temperature (*B/T*) were conducted at the temperatures of 1.9 K, 3.0 K and 5.0 K, and from zero external field to a maximum of 70 kOe. The non-superimposable nature of the curves at different temperatures confirmed the retention of magnetic anisotropy. The M_{sat} value for **4.4$_{Er}$** is 4.59 N_AB (Figure 4.13), roughly half that of the theoretical maximum of 9.00 N_AB for an isolated, free Er^{3+} ion in the $^4H_{15/2}$ ground state. Again, this confirms that the system remains anisotropic.[2] For the dysprosium complex, **4.4$_{Dy}$**, the value of *M* is 5.99 N_AB, a little over half of the theoretical maximum of 10.00 N_AB for a free Dy^{3+} ion in the $^6H_{15/2}$ ground state. It can be seen that the complex is not magnetically saturated, even at 70 kOe and 1.9 K (Figure 4.14). This is a further indication of significant magnetic anisotropy of the system.[140,141]

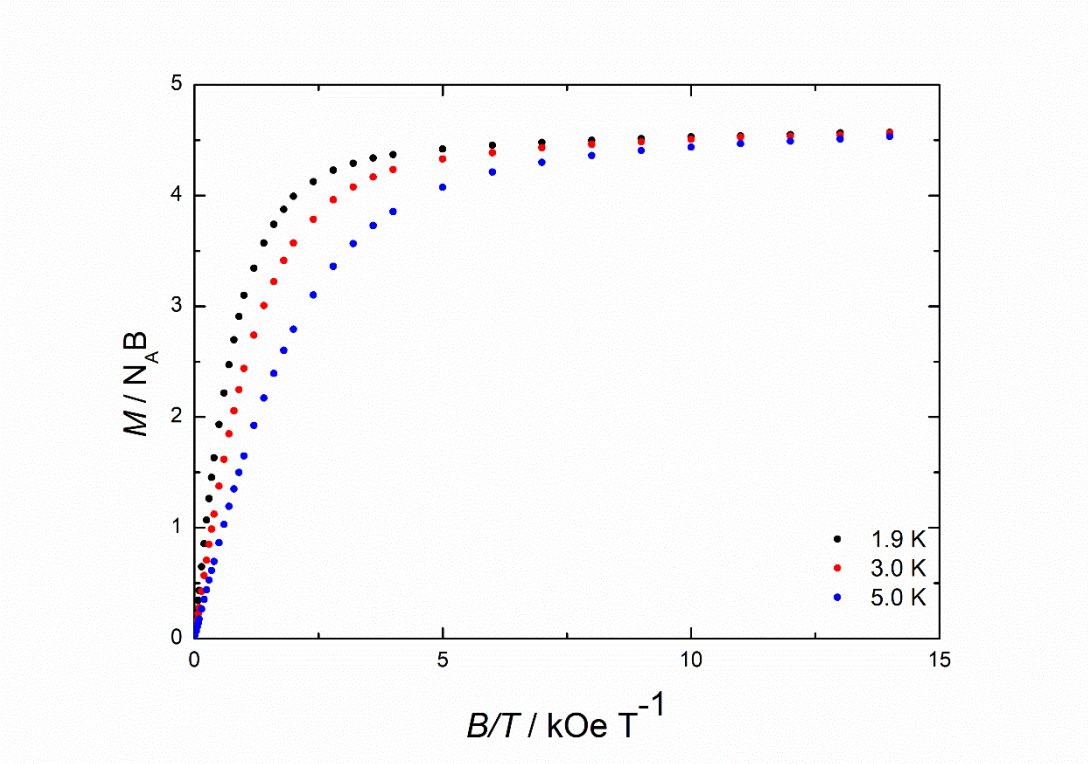

Figure 4.13: Magnetisation (*M*) *vs.* field/temperature (*B/T*) measurement of **4.4$_{Er}$.**

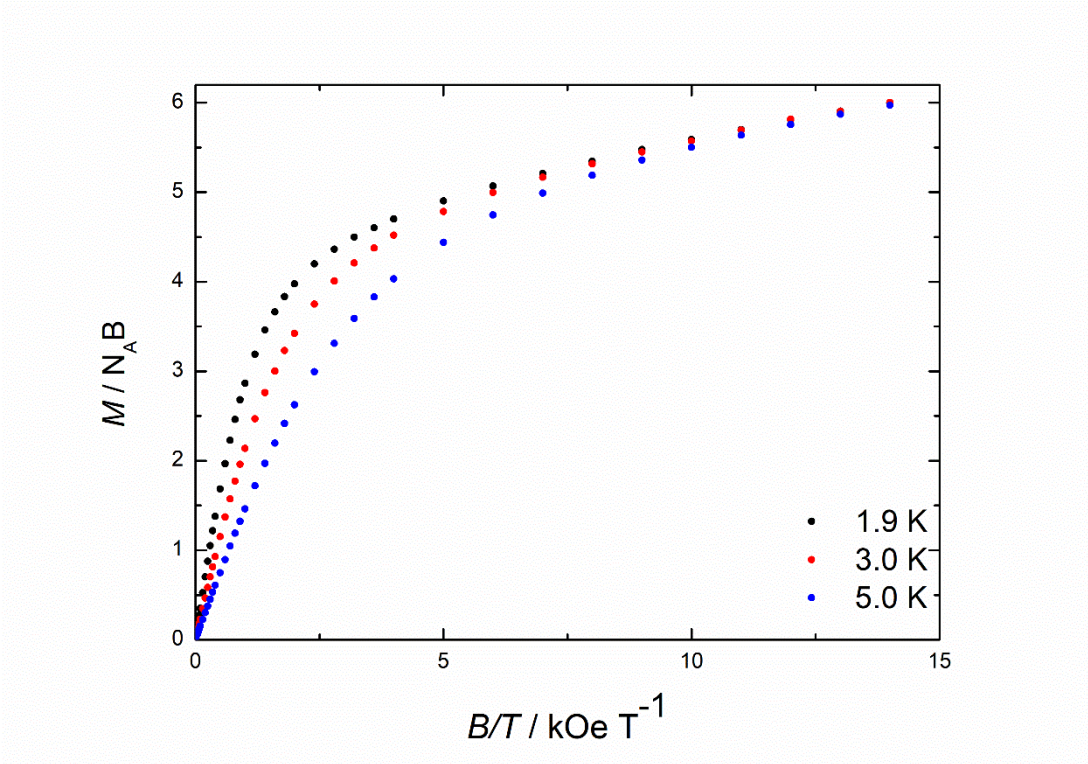

Figure 4.14: Magnetisation (*M*) *vs.* field/temperature (*B/T*) measurement of **4.4$_{Dy}$.**

Measurements of magnetisation *vs*. field at different temperatures were also conducted on the complex **4.5$_{Er}$** displaying similar non-superimposable curves as **4.4$_{Er}$** (Figure 4.15). Thus, magnetic anisotropy is retained upon substitution of THF for pyridine. The M_{sat} value is 4.91 N_AB, which is a little over half the theoretical maximum of 9.00 N_AB and this is again further evidence of retained magnetic anisotropy. However, it can be seen from the lack of plateauing, that even at the highest magnetic fields applicable, the magnetisation has not fully saturated. This could possibly be due to low-lying excited states that can be accessed even at low temperatures.

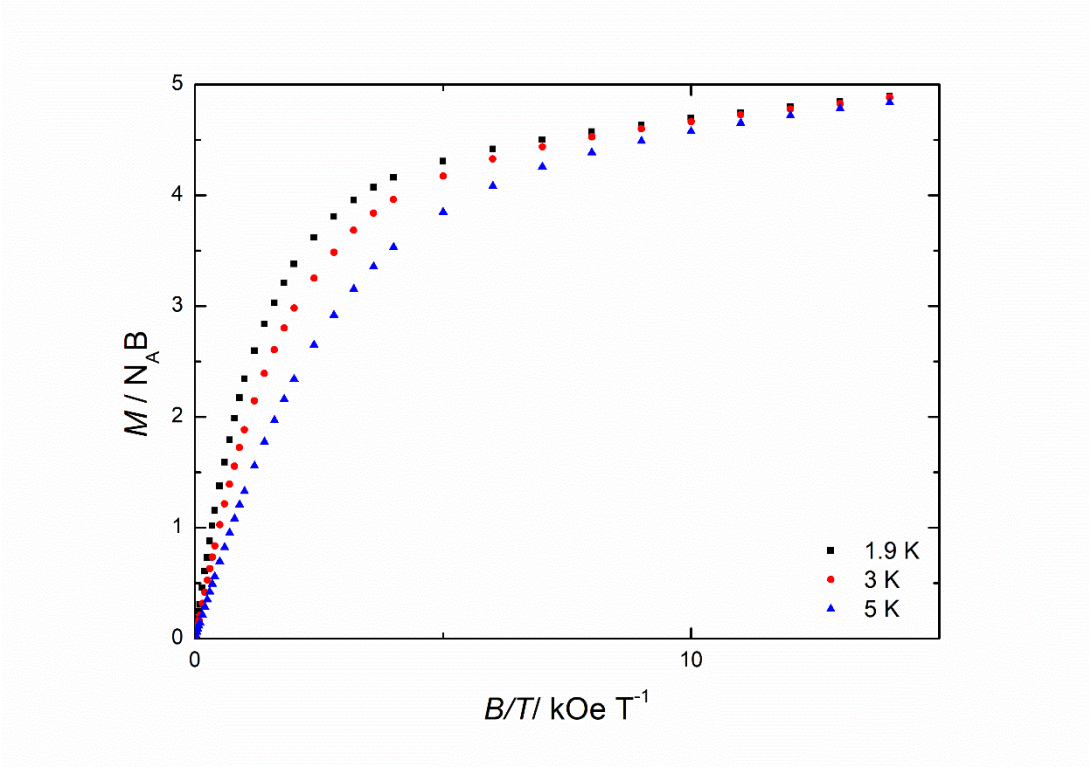

Figure 4.16: Magnetisation (*M*) vs. field/temperature (*B/T*) measurement of **4.5$_{Er}$**.

Measurements of the temperature dependent molar magnetic susceptibility, $\chi_M T$, was undertaken in a static field of 1 kOe for both **4.4$_{Dy}$** and **4.4$_{Er}$** The value of $\chi_M T$ at

300 K for **4.4$_{Dy}$** is 13.68 cm^3 K mol^{-1}, lower than the expected value of 14.17 cm^3 K mol^{-1}.[2,20,64,80] This is a possible consequence of crystal field splitting.[136] The value of $\chi_M T$ at 300 K for **4.4$_{Er}$** is 11.85 cm^{-3} K mol^{-1}, slightly higher than the theoretical maximum of 11.48 cm^3 K mol^{-1} for J = 15/2, where g_J = 1.20 .[94]

Complex **4.4$_{Dy}$** displays the expected behaviour of a monometallic Dy^{3+} SMM with a slow decrease in $\chi_M T$ until reaching a value of 12.57 cm^3 K mol^{-1} at 50 K. This is a result of depopulation of the excited crystal-field states.[134] Below this temperature, **4.4$_{Dy}$** experiences a sharp decline to finish at a value of 7.73 cm^{-1} K mol^{-1}, this behaviour is commonly associated with the onset of slow magnetisation dynamics.

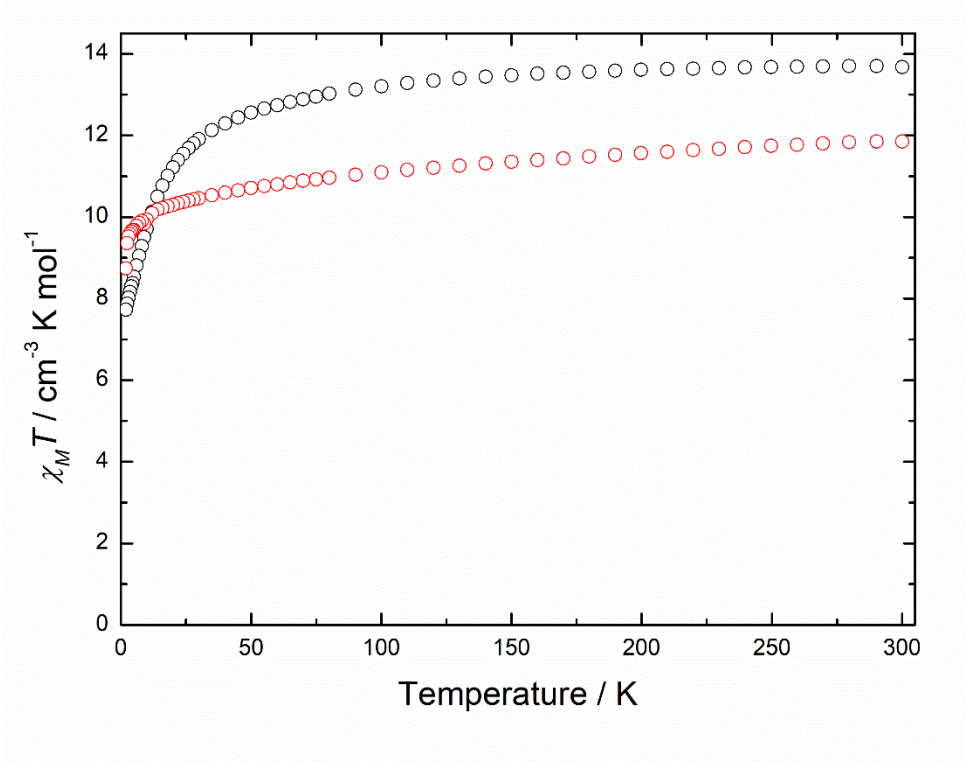

Figure 4.16: Plot of $\chi_M T$(T) in an applied field of 0.1 T for **4.4$_{Er}$** (red)and **4.4$_{Er}$** (black).

For the complex **4.4$_{Er}$** the value of $\chi_M T$ decreases monotonously to a value of 10.08 cm^{-3} K mol^{-1} at 13 K before a sharp decrease to a value of 8.74 cm^{-3} K mol^{-1}. This behaviour can be attributed similarly as with **4.4$_{Er}$**, where the initial decrease is a

result of the depopulation of the excited crystal-field states. The behaviour of both complexes is reminiscent of that displayed by the [(η^8-COT)LnCp*] family of complexes described by Gao *et al*., and markedly different to that of the **4.2$_{Dy}$**, the latter displaying a gradual and constant decrease of $\chi_M T$ down to 3.4 K whereupon the value plummets to < 4 cm^3 K mol^{-1}.[108,133]

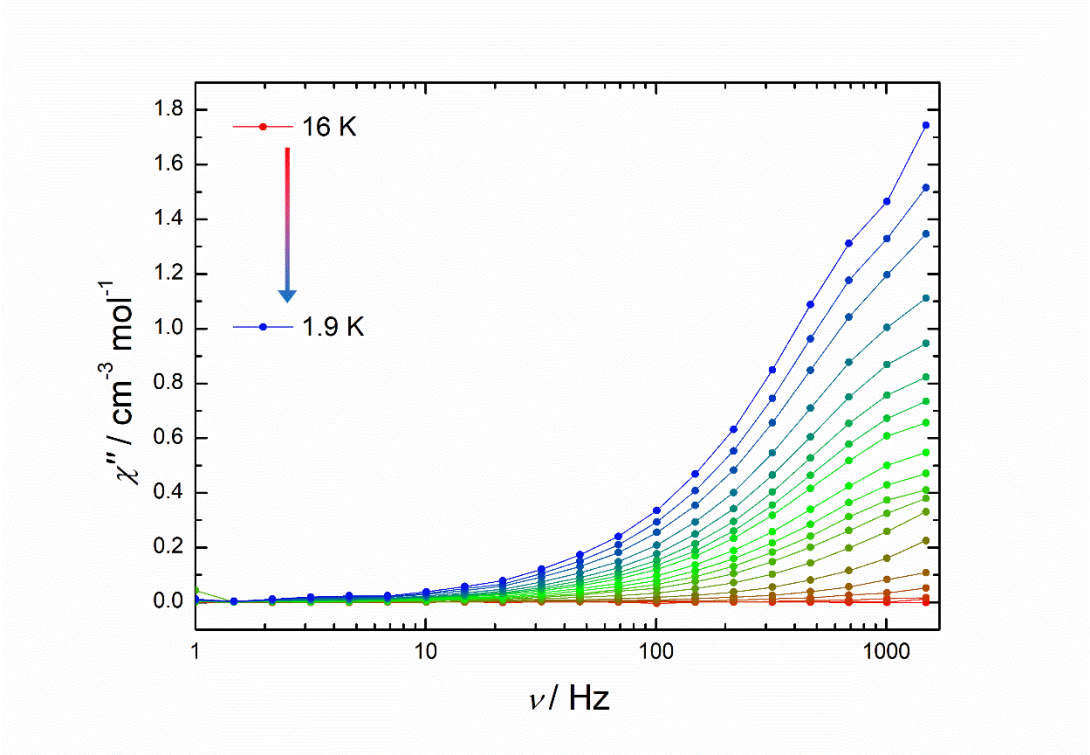

Figure 4.17: Frequency dependence of the out-of-phase (χ'') magnetic susceptibility for **4.4$_{Er}$** in zero applied field (lines are a guide for the eye).

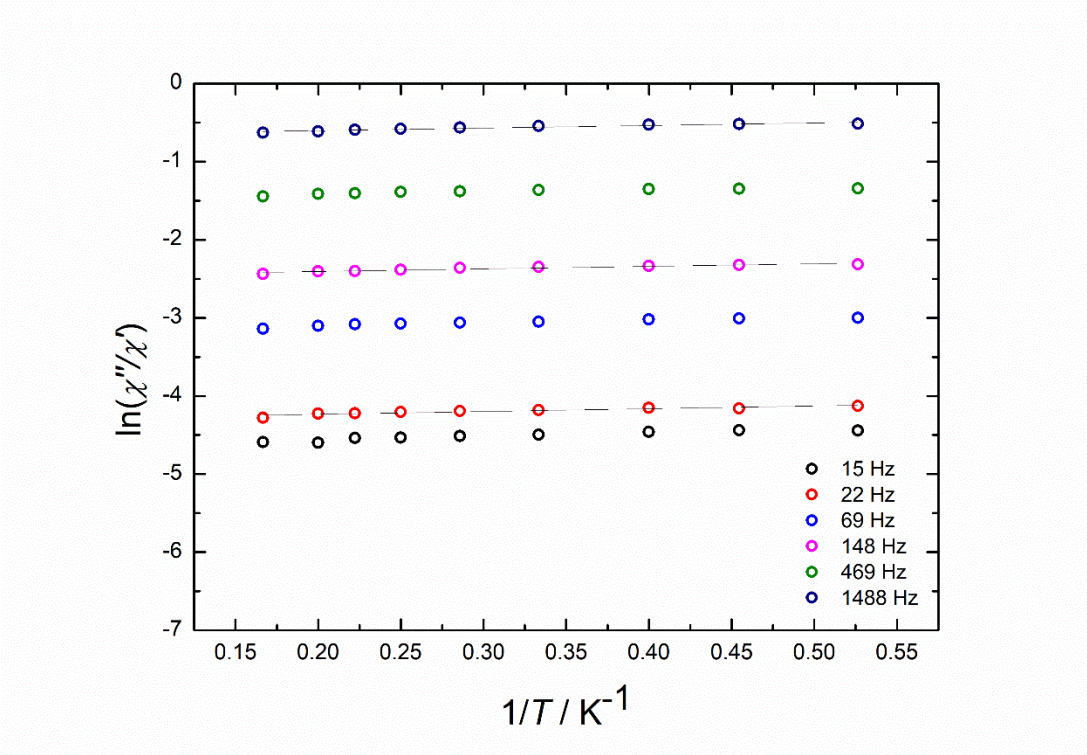

Figure 4.18: Plot of ln(χ''/χ') vs. T^{-1} for **4.4**$_{Er}$

For the complex **4.4**$_{Er}$, both the in-phase (χ') and out-of-phase (χ'') magnetic susceptibility measurements, no clear maximum peak is observed (Figure 4.17). This behaviour is attributed to a very strong degree of quantum tunnelling occurring in the complex.[142] Further, the lack of maxima in either measurement precluded the ability to fit the data using a Debye model.[66]

The magnetic hysteresis measurements were conducted at 1.9 K with a field sweep rate of 26 Oe s^{-1} (Figure 4.19). As expected from the previously described data, the measurement for **4.4**$_{Er}$ shows a commonly seen narrow, S-shape that is associated with weak hysteresis and no coercive field. Further, the abrupt step-like changes substantiate the occurrence of quantum tunnelling.[64] Consequently, it has been

demonstrated that the complex **4.4**$_{Er}$ displays no magnetic hysteresis properties as a result of high quantum tunnelling effects.

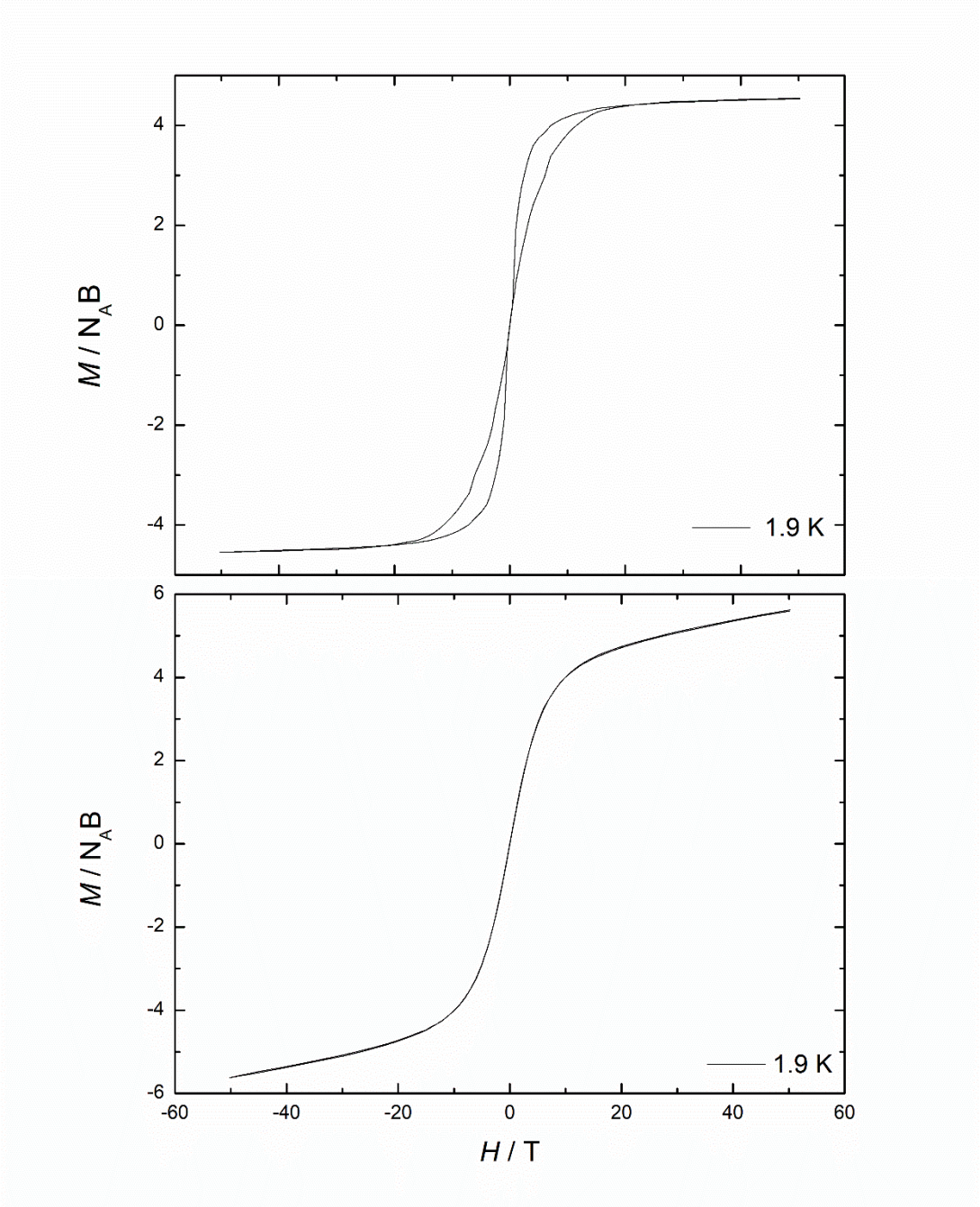

Figure 4.19: Magnetisation (*M*) *vs.* field (*H*) hysteresis loop for **4.4**$_{Er}$ (top) and **4.4**$_{Er}$ (bottom).

Hysteresis measurements were conducted for **4.4$_{Dy}$** and displayed no opening at any field strength. Therefore, the complex **4.4$_{Dy}$** possesses no magnetic hysteresis properties.

The lack of SMM properties displayed by **4.4$_{Dy}$** were anticipated, as the COT and the THF ligands are clearly closer to the equatorial plane than they are to the axial direction. This is in line with the oblate description of Dy^{3+} in its $^{6}H_{15/2}$ ground M_J state, which is perturbed through crystal field effects which have the impact of destroying the capability of the molecule from possessing any SMM properties.[21]

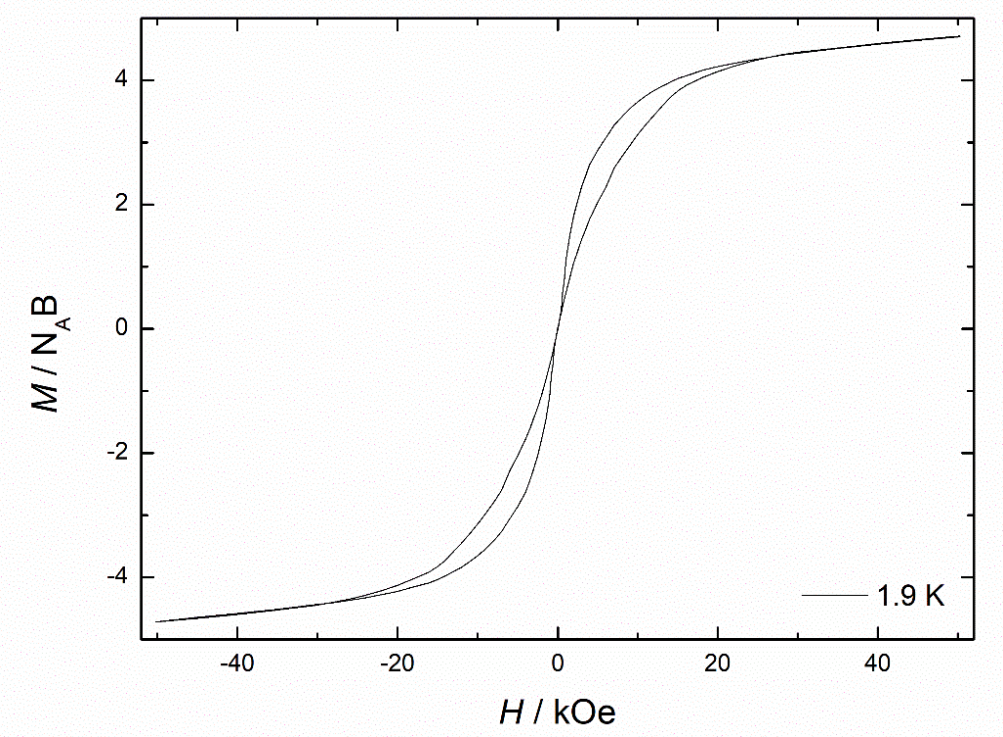

Figure 4.20: Magnetisation (M) vs. field (H) hysteresis loop for **4.5$_{Er}$.**

Magnetic hysteresis measurements of **4.5$_{Er}$** shows no open loop at 1.9 K (Figure 4.20), similar to that of **4.4$_{Er}$**. However, compared to the magnetic hysteresis of **4.4$_{Er}$**, the openings of the loops are slightly larger. Accordingly, the QTM effects seen here must be of a smaller magnitude than that of **4.4$_{Er}$**, albeit only slightly.

4.3.7 Computation Studies of $[(\eta^8\text{-COT})Dy(THF)_4][BPh_4]$ ($\mathbf{4.4_{Dy}}$), and $[(\eta^8\text{-COT})Dy(pyr)_4][BPh_4]$ ($\mathbf{4.5_{Dy}}$)

A deeper understanding of the experimental magnetic properties was sought and so the simple calculation program MAGELLAN was employed.[128]. The major restriction of this program is its inability to calculate any complexes other than those containing dysprosium atoms as the magnetic atom. To ensure any effects of the $[BPh_4]^-$ were not ignored, two models were subjected to the MAGELLAN program, once including the counterion and once without.

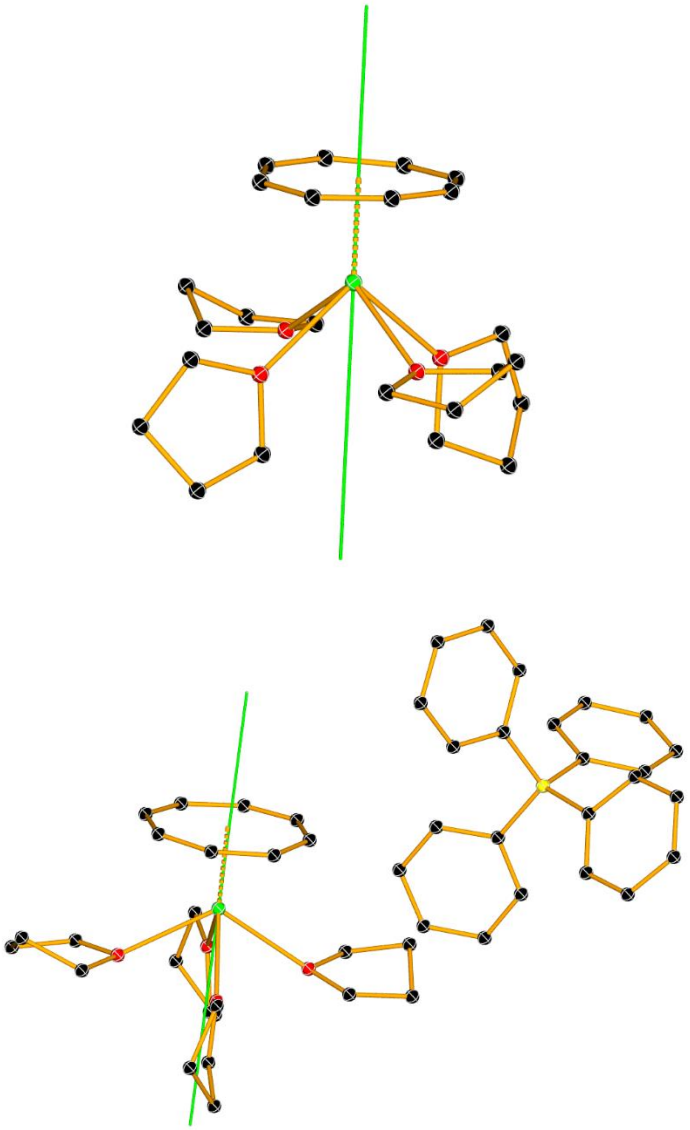

Figure 4.21: Calculated principal axes of the ground Kramers doublet of $\mathbf{4.4_{Dy}}$.

Starting with the THF-ligated complex (Figure 4.21), the principal magnetic axis lies almost exactly co-linear with the dysprosium-centroid axes. When the counterion is excluded, the deviation from co-linearity is 0.14 °. Due to the manner in which the calculations are performed, standard deviations are not reported. Once the counterion is included, this increases slightly to 1.12 °. This can be understood as the negative charge of the counterion is, for the purposes of the MAGELLAN calculations, treated as lying entirely on the boron atom. This results in a high charge density of the boron atom which has an appreciable effect upon the magnetic axis, drawing it closer to the counterion.

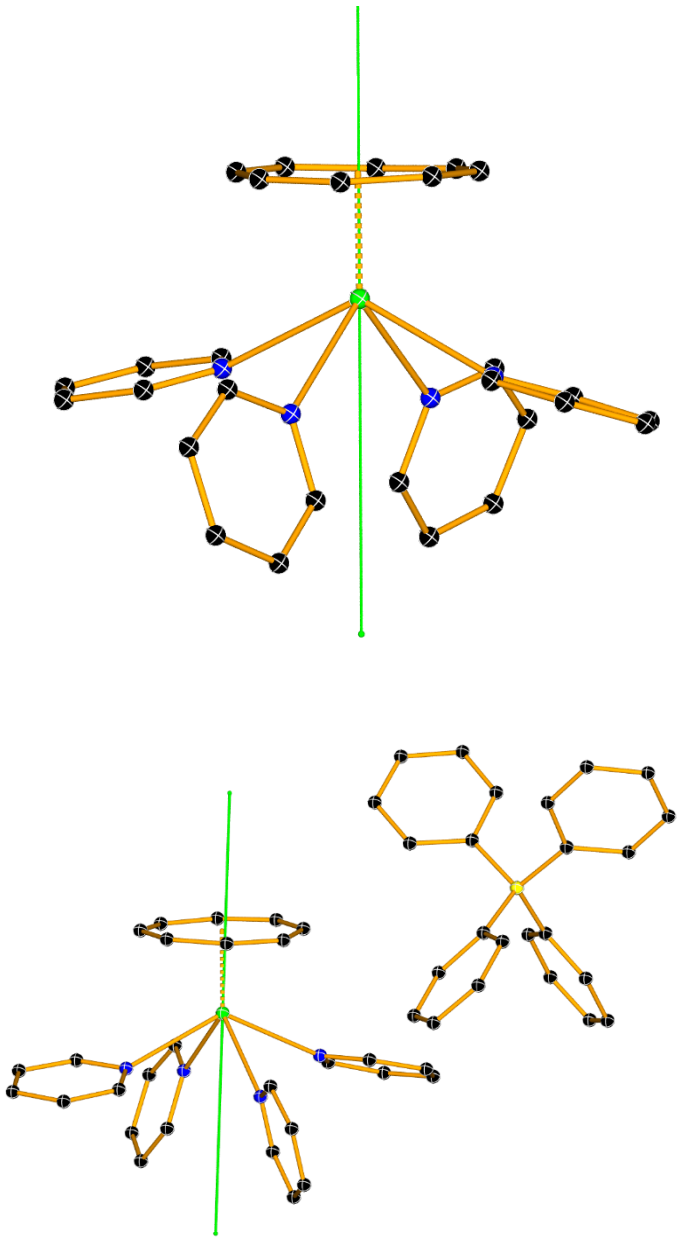

Figure 4.22: Calculated principal axes of the ground Kramers doublet of **4.5**$_{Dy}$.

The same procedure was applied to the pyridine-ligated molecules (Figure 4.22) and the calculated principal magnetic axis of the model without the counterion lies 0.50 ° away from the dysprosium-centroid axis. When the counterion is included, this increases to 2.32 °. This again can be understood to be a result of the boron atoms possessing a high charge density. That the effect is larger here than for the THF complexes presumably results from the greater distance between metal and boron

atom in **4.4$_{Dy}$** compared to the complex **4.5$_{Dy}$**. The difference in Dy···B of approximately 0.50 Å is sufficient to reduce the perturbation seen in the calculations.

The resulting information collected from these calculations explain the poor magnetic properties of both **4.4$_{Dy}$** and **4.5$_{Dy}$**. The COT ligand is large enough that the ligand field effects are closer to the equatorial plane than the axial, the exact opposite of the ideal situation for dysprosium based SMMs. That the principal magnetic axes for both complexes are so close to the dysprosium-centroid axes shows that COT, combined with equatorially coordinated solvent molecules, will not furnish strong SMM properties.

Caution must be taken when applying the information from the dysprosium complexes to that of the erbium analogues, but as they are isostructural the greater deviation of the principal magnetic axis in the pyridine molecules potentially clarifies the difference in magnetic properties between **4.4$_{Er}$** and **4.5$_{Er}$**.

4.4 Conclusion

This chapter describes the successful synthesis and solid-state characterisation of four new lanthanide organometallic complexes. All complexes were also characterised by NMR and infrared spectroscopy. Magnetic hysteresis measurements of all complexes show strong QTM effects as noted by the lack of open hysteresis at 1.9 K along with the step-like changes in the curves.

It can be concluded that minor alterations to a molecule's structure and electronics can have a dramatic effect on the magnetic properties. Substitution of THF molecules for more the more basic pyridine modified the geometries slightly, shown by ChSM, as well as the magnetic properties, seen in the differences between hysteresis. This knowledge could be applied in the development of solvent sensors based on the change in magnetic properties.

Though the described complexes do not display ground-breaking SMM properties, they do demonstrate establishment of a reliable route to $[(\eta^8\text{-COT})\text{Ln}]^+$ building blocks which could be utilised in the future.

4.5 Further Work

Further work is necessary to fully understand the behaviour of the complexes. This includes the full magnetic characterisation of **4.4$_{Dy}$**, **4.5$_{Dy}$** and**4.5$_{Er}$**. This would allow more detailed comparisons to be drawn and thus information learned could be applied to the construct of improved SMMs. As the structural characterisation is complete, there remains the possibility of utilising more intense computational studies, such as CASSCF, to further describe the properties of the complexes, especially the *g* tensors. Knowledge of the perturbation of the *g* tensors occurring could facilitate greater rational design in the next generation of lanthanide SMMs.

It would also be extremely beneficial if the counterion could successfully be substituted for another. A fluorinated analogue of BPh_4^- such as BArF ($B(C_6F_5)_4^-$) or $BArF_{24}$ ($B(C_6H_3(3,5\text{-}CF_3))$) could possess high enough local charge on the fluorine atoms to displace a solvato ligand and form a contact ion pair. Further, the fluorinated aluminium alkoxides ($Al\{OC(CF_3)_3\}_4$) have a different spatial requirement to the tetraphenyl borates, and so could impact on the SMM properties. Investigating the effects of counterion substitution would complement the solvent substitution studies described and allow for a deeper understanding of the innate features which drive Ln-SMM properties.

Another avenue worth pursuing would be utilising the complexes here as building blocks to other structures. As the tetraphenylborate counterion can readily be utilised in salt metathesis reactions, as shown with the work by Cendrowski-Guillaume *et al.*, to generate a plethora of new molecules. This should be limited only by the necessity of the reagent to be include an s-block metal, thankfully there is no

shortage of potential candidates. Ideally, heteroatom cyclopentadienyl ligands such as those described in Chapter 1 can be applied to generate mixed sandwich complexes.

Chapter 5:
Conclusion

5.1 Conclusion

To surmise, the aims of the project have been successfully fulfilled. A range of lanthanide organometallic single-molecule magnets were synthesised. The solid-state and magnetic properties were characterised. Diamagnetic structural analogues were also synthesised and their solid-state and solution-state properties were characterised.

The complex **2.4$_{Dy}$** ([Cp*$_2$Dy(μ-CO)W(CO)] exhibited an energy barrier to magnetic relaxation of U_{eff}/k_BT = 557(18) cm^{-1} and with τ_{QTM} = 3.71(8) ms. The complex did not display any magnetic hysteresis openings at any temperature above 1.9 K (the limit of the magnetometer). Computational studies elucidated the strong influence of the isocarbonyl linker in perturbing the crystal field, a result of a high degree of back-bonding occurring between the tungsten and the carbonyl. This work demonstrated the applicability of classic organometallic bonding motifs to the tailored design of SMMs and the resulting rate of QTM.

Complexes of the type [(η^8-COT)Ln(BH_4)(THF)$_2$] (**3.3$_{Ln}$** Ln = Y, Dy, Er) were synthesised and the magnetic properties of the dysprosium and erbium analogues were investigated. Both **3.3$_{Dy}$** and **3.3$_{Er}$** displayed high rates of QTM and did energy barriers could not be extracted. Synthesis of inverse-sandwich complexes **3.4$_{Ln}$** ([(η^8-COTDy)$_2$Pn^{TIPS}], Ln = Y, Dy, Er) was achieved by utilising **3.3$_{Ln}$**. The complexes **3.4$_{Ln}$** are the second example of inverse-sandwich complexes where the central ligand is of a pentalene scaffold and the metals from the f-block. Simple computational studies performed on **3.3$_{Dy}$** and **3.4$_{Dy}$** suggest a crystal field for **3.4$_{Ln}$** (Ln = Dy, Er) that would generate improved magnetic properties relative to **3.3$_{Ln}$** (Ln = Dy, Er). This shows the

utility of [(η^8-COT)Ln(BH_4)($THF)_2$] as a building-block to more structurally complex lanthanide organometallic complexes.

Finally, the complexes **4.4$_{Ln}$** ([(η^8-COT)Ln($THF)_4$][BPh_4], Ln = Y, Dy, Er) and **4.5$_{Ln}$** (Ln = Y, Dy, Er) and [(η^8-COT)Ln($pyr)_4$][BPh_4] were successfully synthesised and their solid-state and solution-state properties were characterised. The magnetic properties of **4.4$_{Ln}$** (Ln = Er, Dy) and **4.5$_{Ln}$** (Ln = Er, Dy) were investigated and it was shown that $[COT]^{2-}$solvated lanthanide complexes displayed magnetic properties that will inspire and inform future synthetic efforts towards better molecular magnets. Future work will be devoted to utilising these complexes to react with heteroatom cyclopentadienyl ligands to generate mixed sandwich complexes.

Chapter 6:

Experimental

6.1: General Methods and Materials

All reactions were carried out under a rigorously anaerobic and anhydrous atmosphere using standard Schlenk line techniques or in a glove-box under an atmosphere of pure argon or nitrogen (< 0.5ppm O_2). Solvents were dried by refluxing over molten potassium for 3 days, distilled and stored in ampoules with activated 4 Å molecular sieves and degassed with 3 freeze-thaw cycles. Glassware and cannulae were stored in an oven at 180 °C for 6 hr before use. X-ray diffraction data were collected on an Agilent Technologies SuperNova diffractometer using MoKα radiation, Rigaku FR-X diffractometer using MoKα radiation, or Agilent Gemini Ultra diffractometer using CuKα radiation (λ = 1.54184 Å) at 100 K. Structures were solved with SHELXS using direct methods and refined with SHELXL using least-squares minimization. NMR data was collected on; a Bruker 400 Ultrashield / Avance III 400 spectrometer operating at 400 MHz, Bruker 500 Ultrashield / 500 Avance III spectrometer operating at 500 MHz, Varian VNMR S400 spectrometer operating at 30 °C, unless otherwise stated, at frequencies of 400 MHz (^{1}H), 128 MHz (^{11}B), 100 MHz (^{13}C). ^{1}H and ^{13}C shifts were referenced internally to deuterated solvent resonances relative to TMS. FT-IR spectra were recorded on a Bruker Alpha spectrometer with a platinum-diamond ATR module. Elemental analyses, where performed, were carried out by Mr Stephen Boyer at London Metropolitan University, U.K, or MEDAC Ltd.

Magnetic susceptibility measurements were recorded on a Quantum Design MPMS-XL7 SQUID magnetometer equipped with a 7 T magnet. Direct current (dc) magnetic susceptibility measurements were performed on a polycrystalline samples in the

temperature range 1.9–300 K, in an applied field of 1000 Oe. The dynamics of the magnetization were investigated from the ac susceptibility measurements in the zero static fields and a 3.0 Oe ac oscillating field. Diamagnetic corrections were made with the Pascal's constants for all the constituent atoms as well as the contributions of the sample holder.

Cp*H (Cp* = $(C_5(CH_3)_5$-, KCp*, $[HNEt_3][BPh_4]$, NaCp (Cp = C_5H_5-, $Na[CpW(CO)_3]$, K_2COT, K_2Pn^{TIPS}, $Ln(BH_4)(THF)_n$ (Ln = Y, Gd, Er, Dy) were all prepared according to published literature procedures. $Na[CpW(CO)_3]$ was synthesised following literature with the modification of an extended reaction time (4 days) to achieve full conversion. All other materials were used as received.

6.2 Synthetic Procedure for Chapter 2: Heterobimetallic Lanthanide-Tungsten Isocarbonyl Complexes as Single-Molecule Magnets

*Analogous procedures were applied to all complexes in Chapter 2, only that for **DyW** is described herein, relevant differences in data are noted.*

6.2.1: $[Cp^*_2Dy(\mu\text{-}OC)_2CpW(CO)]_n$, 2.4_{Dy}

A Schlenk flask was charged with [Cp*2Dy][BPh_4] (0.286 g, 0.421 mmol) and Na[$CpW(CO)_3$] (0.317 g, 0.421 mmol) and THF (20 mL) was introduced at 0 °C. The reaction was allowed to warm to room temperature and stirred overnight. A precipitate formed, the yellow filtrate was isolated *via* cannula-filtration. The solvent removed from the filtrate *via* vacuo to give a yellow powdery solid. Crystals suitable for X-ray diffraction were grown over two weeks *via* a vapour diffusion of hexanes into a THF solution of the product and/or layering of hexanes onto a THF solution of the product. Yield; 0.129 g (39 %).FT-IR $\tilde{\nu}/cm^{-1}$;2970-2850 (br, CH), 1917 (s, terminal CO), 1726, 1615 (μ-CO). Anal. found (calcd. for $DyWO_3C_{28}H_{35}$) C 44.04 (43.89), H 4.71 (4.61) %. Crystal data; M = 765.91 g mol^{-1}, monoclinic, $P2_{1/n}$, a = 12.5341(5), b = 10.3160(3), c = 21.1831(6), α = 90.00, β = 106.362(3), γ = 90, V= 2628.09(15) $Å^3$, T = 150 K.

6.2.2: $[Cp^*_2Y(\mu\text{-}OC)_2CpW(CO)]_n$, 2.4$_Y$

Yield; 0.125 g (43%). ^{1}H NMR (500 MHz, d_8-THF, 298 K): δ_H 5.29 (5 H, s, C_5H_5), 1.96 (30 H, s, $C_5(CH_3)_5$). 13C{1H} NMR (d8-THF, 125.7 MHz, 298 K): δ_C 119.01 (s, Cp* *C*CH_3), 87.13 (s, Cp *C*), 10.71 (s, Cp* C*C*H3). FT-IR $\tilde{\nu}$/cm^{-1}; 2960-2850 (br, CH), 1920 (s, terminal CO), 1730, 1620 (bridging CO). Crystal data; M = 692.32 g mol^{-1}, monoclinic, $P2_{1/n}$, a = 12.5485(6), b = 10.3213(3), c = 21.2747(11), α = 90.00, β = 106.189(5), γ = 90, V= 2646.2(2) Å^3, T = 150 K.

6.2.3: $[Cp^*_2Gd(THF)(\mu\text{-}OC)_2CpW(CO)]_n$, 2.4$_{Gd}$

FT-IR $\tilde{\nu}$/cm^{-1}; 2940-2850 (br, CH), 1920 (s, terminal CO), 1748,1624 (s, bridging CO). Anal. found (calcd. for $GdWO_3C_{28}H_{35}(C_4H_8O)$) C 46.31 (46.13), H 5.07 (5.21) %. Crystal data; M = 832.42 g mol^{-1}, monoclinic, $P2_{1/c}$, a = 11.2617(3), b = 22.1933(3), c = 26.5611(5), α = 90.00, β = 95.052(17), γ = 90, V= 6612.70(2) Å^3, T = 150 K.

6.3 Synthetic Procedure for Chapter 3: Monometallic Lanthanide Cyclooctatetrene Complexes as Building Blocks to Inverse-Sandwich SMMs

6.3.1 [(η^8-COT)Ln(BH_4)(THF)$_2$]

[(η^8-COT)Y(BH_4)(THF)$_2$] 3.3$_Y$

A Schlenk flask was charged with $Y(BH_4)_3(THF)_3$ (0.500 g, 1.43 mmol) and THF (10 mL) was added, another flask was charged with K_2COT (0.261 g, 1.43 mmol) and THF (10 mL) was added. Both Schlenks were cooled to 0 °C and K_2COT was added dropwise *via* cannula to $Y(BH_4)_3(THF)_3$ over the course of 30 min. The mixture was allowed to warm to room temperature and stirred overnight. A precipitate was formed and the orange filtrate was isolated *via* cannula-filtration. The solvent was removed *via vacuo* to leave a light orange powder. Crystals suitable for X-ray diffraction were grown over two weeks from a saturated solution stored at -35 °C. Yield; 0.345 g (69 %). ^{1}H NMR (500 MHz, d_5-pyridine, 303 K): δ_H = 6.75 (8 H, s, C_8H_8), 3.68 (4 H, s, C_4H_8O), 1.64 (4 H, s, C_4H_8O), 1.02-0.39 (4 H, q, BH_4^-). ^{13}C{^{1}H} NMR (d_5-pyridine, 125.7 MHz, 303 K): δ_C = 95.41 (s, C_8H_8), 67.57 (s, C_4H_8O), 25.57 (s, C_4H_8O). ^{11}B{^{1}H} NMR (d_5-pyridine, 100.46 MHz, 303 K) δ_B = −30.82 (s, BH_4^-). FT-IR $\tilde{\nu}$/cm^{-1}; 2970-2880 (b, CH), 2400 (s, BH), 2343-2215 (b, BH). Anal. found (calcd. for $C_{16}H_{28}O_2BY$) C 53.85 (54.58), H 8.27 (8.01) %. Crystal data; M = 352.10 g mol^{-1}, monoclinic, $P2_{1/n}$, a = 7.4223(2), b = 23.9013(5), c = 9.5141(2), α = 90.00, β = 98.033(2), γ = 90.00, V= 1671.26(7) Å^3, T = 100 K.

[(η^8-COT)Dy(BH_4)(THF)$_2$] 3.3$_{Dy}$

Yield; 0.345 g (69 %). FT-IR $\tilde{\nu}$/cm^{-1}; 3024-2894 (b, CH), 2423 (s, BH), 2304-2199 (b, BH). Anal. found (calcd. for $C_{16}H_{28}O_2BDy$) C 45.14 (45.10), H 6.63 (7.20) %. FT-IR $\tilde{\nu}$/cm^{-1};

3023-2882 (b, CH), 2434 (s, BH), 2323-2182 (b, BH). Crystal data; M = 425.69 g mol^{-1}, orthorhombic, *Pbc*2_1, a = 8.17250(10), b = 19.9255(3), c = 10.3572(2), α = 90.00, β = 90.00, γ = 90.00, V= 1686.58(5) $Å^3$, T = 100 K

[(η^8-COT)Er(BH_4)($THF)_2$] 3.3$_{Er}$

Yield; 0.345 g (69 %). FT-IR $\tilde{\nu}/cm^{-1}$; 3010-2875 (b, CH), 2417 (s, BH), 2280-2180 (b, BH). Anal. found (calcd. for $C_{16}H_{28}O_2BEr$) C 44.25 (44.64), H 6.56 (7.13) %. Crystal data; M = 430.45 g mol^{-1}, orthorhombic, *Pbc*2_1, a = 19.8038(4), b = 8.13095(15), c = 10.3980(2), α = 90.00, β = 90.00, γ = 90.00, V= 1674.32(6) $Å^3$, T = 100 K

[(η^8-COT)Gd(BH_4)($THF)_2$] 3.3$_{Gd}$

Yield; 0.345 g (69 %). FT-IR $\tilde{\nu}/cm^{-1}$; 2981-2901 (b, CH), 2438 (s, BH), 2343-2215 (b, BH). Anal. found (calcd. for $C_{16}H_{28}O_2BY$) C 45.35 (45.71), H 7.06 (6.71) %. Crystal data; M = 420.44 g mol^{-1}, orthorhombic, *Pbc*2_1, a = 7.4346(2), b = 24.1607(7), c = 9.5191(3), α = 90.00, β = 90.00, γ = 90.00, V= 1693.27(9) $Å^3$, T = 100 K.

6.3.2 [(η^8COTLn)$_2$Pn^{TIPS}]

[(η^8-COTY)$_2$Pn^{TIPS}] 3.4$_Y$

A Schlenk flask was charged with [(η^8-COT)Y(BH_4)($THF)_2$] (0.100 g, 0.284 mmol) and THF (10 mL) was added, another flask was charged with K_2Pn^{TIPS} (0.070 g, 0.142 mmol) and THF (10 mL) was added. Both Schlenks were cooled to 0 °C and K_2Pn^{TIPS} was added dropwise *via* cannula to [(η^8-COT)Y(BH_4)($THF)_2$]over the course of 30 minutes. The mixture was allowed to warm to room temperature and stirred overnight. A precipitate was formed and the dark gold filtrate was isolated *via* cannula-filtration. The solvent was removed *via vacuo* to leave a dark brown coloured powder which was then extracted into toluene (20 mL). The filtrate was isolated *via* cannula-filtration and solvents removed *via vacuo* to give a dark golden solid. Crystals suitable for X-ray diffraction were grown over two weeks from a saturated toluene solution stored at -35 °C. Yield; 0.020 g (10 %). FT-IR $\tilde{\nu}$/cm^{-1}; 2970-2851 (b, CH). Crystal data; M = 800.91 g mol^{-1}, triclinic, *P*-1, a = 8.3069(4), b = 11.1360(8), c = 11.9454(9), α = 70.935(7), β = 79.715(5), γ = 68.730(5), V= 971.00(12) Å^3, T = 100 K.

[(η^8-COTDy)$_2$Pn^{TIPS}] 3.4$_{Dy}$

Yield; 0.014 g (9 %). FT-IR $\tilde{\nu}$/cm^{-1}; 2977-2843 (b, CH). Crystal data; M = 950.11 g mol^{-1}, triclinic, *P*-1, a = 8.3045(5), b = 11.1248(7), c = 11.9532(6), α = 70.813(5), β = 79.908(5), γ = 68.704(6), V= 969.79(11) Å^3, T = 100 K.

[(η^8-COTEr)$_2$Pn^{TIPS}] 3.4$_{Er}$

Yield; 0.013 g (12 %). FT-IR $\tilde{\nu}$/cm^{-1}; 2995-2834 (b, CH). Crystal data; M = 957.61 g mol^{-1}, triclinic, *P*-1, a = 19.8038(4), b = 8.13095(15), c = 10.3980(2), α = 70.735(7), β = 79.869(7), γ = 68.817(8), V= 967.82(15) Å^3, T = 100 K.

6.4 Synthetic procedure for Chapter 4: Monometallic Cyclooctatetraene Tetraphenylborate Lanthanide Complexes as Single-Molecule Magnets

Analogous procedures were applied to all ***[(η^8-COT)Ln(THF)$_4$][BPh$_4$]*** *and* ***[(η^8-COT)Ln(pyr)$_4$][BPh$_4$]*** *complexes (Ln = Y, Dy, Er) in Chapter 4, only that for* ***[(η^8-COT)Y(THF)$_4$][BPh$_4$]*** *and* ***[(η^8-COT)Y(pyr)$_4$][BPh$_4$]****, are described herein, details of spectroscopic and analytical data for dysprosium and erbium analogues are noted.*

6.4.1 [(η^8-COT)Ln(THF)$_4$][BPh$_4$]

[(η^8-COT)Y(THF)$_4$][BPh$_4$] (4.4$_Y$)

A Schlenk flask was charged with [(η^8-COT)Ln(BH$_4$)(THF)$_2$] (0.325 g, 0.923 mmol) and THF (10 mL) was added, another flask was charged with [HNEt$_3$][BPh$_4$] (0.389 g, 0.923 mmol) and THF (10 mL) was added. [(η^8-COT)Ln(BH$_4$)(THF)$_2$]was added dropwise at room temperature *via* cannula-filtration to [HNEt$_3$][BPh$_4$]over the course of 30 min. The mixture was allowed to warm to room temperature and stirred for 15 minutes. A crystalline precipitate was formed and the orange filtrate was isolated *via* cannula-filtration. The solvent was removed *via vacuo* to leave a light orange powder. Yield; 0.406 g (65 %). %). ^{1}H NMR (500 MHz, d_5-pyridine, 303 K): δ_H = 8.08 (8 H, s, *o*-H/BPh$_4$), 7.30 (8 H, s, *m*-H/BPh$_4$), 7.14 (4 H, t, *p*-H/BPh$_4$), 6.74 (8 H, s, C$_8$H$_8$), 3.69 (12 H, s, C$_4$H$_8$O), 1.66 (8 H, s, C$_4$H$_8$O). ^{13}C{^{1}H} NMR (d_5-pyridine, 125.7 MHz, 303 K): δ_C = 165.00 (*i*-C/BPh$_4$), 137.69 (*o*-C/BPh$_4$), 126.71 (*m*-C/BPh$_4$), 122.87 (*p*-C/BPh$_4$) 96.38 (s, C$_8$H$_8$), 68.35 (s, C$_4$H$_8$O), 26.32 (s, C$_4$H$_8$O). ^{11}B{^{1}H} NMR (d_5-pyridine, 100.46 MHz, 303 K) δ_B = -5.42 (s, [BPh$_4$]$^-$). %). FT-IR $\tilde{\nu}$/cm^{-1}; 3056-2857 (b, CH), 1003 (s, CO). Crystal data; M =

800.68 g mol^{-1}, triclinic, *P*-1, a = 9.7082(3), b = 13.0898(4), c = 16.1586(4), α = 85.809(2), β = 75.900(2), γ = 86.932(2), V= 1984.86(10) $Å^3$, T = 100 K.

[(η^8-COT)Dy(THF)$_4$][BPh$_4$] (4.4$_{Dy}$)

Yield;0.295 g (60 %). Anal. found (calcd. for $C_{48}H_{60}BO_4Dy$) C 65.65 (65.88), H 6.74 (6.53) %. FT-IR $\tilde{\nu}/cm^{-1}$; 3050-2881 (b, CH), 1001 (s, CO). Crystal data; M = 874.27 g mol^{-1}, triclinic, *P*-1, a = 9.7165(3), b = 13.1039(4), c = 16.1632(5), α = 85.855(2), β = 75.863(2), γ = 86.911(2), V= 1989.01(10) $Å^3$, T = 100 K.

[(η^8-COT)Er(THF)$_4$][BPh$_4$] (4.4$_{Er}$)

Yield; 0.188 g (51 %). Anal. found (calcd. for $C_{48}H_{60}BO_4Er$) C 65.38 (65.49), H 6.63 (6.54) %. FT-IR $\tilde{\nu}/cm^{-1}$; 3035-2892 (b, CH), 1002 (s, CO). Crystal data; M = 879.03 g mol^{-1}, triclinic, *P*-1, a = 9.7059(2), b = 13.0833(3), c = 16.1416(4), α = 85.751(2), β = 75.904(2), γ = 86.9426(19), V= 1981.23(9) $Å^3$, T = 100 K.

Generation of Crystals Suitable for X-ray Diffraction

To synthesise crystals of [(η^8-COT)Y(THF)$_4$][BPh$_4$] (Ln = Y, Dy, Er) suitable for X-ray diffraction, the reaction was performed with a ratio of 1:20 for [(η^8-COT)Ln(BH$_4$)(THF)$_2$] and [HNEt$_3$][BPh$_4$], respectively. This ensured slow nucleation of the product to allow for the growth of single crystals of sufficient quality to perform XRD studies.

6.4.2 [(η^8-COT)Ln(pyr)$_4$][BPh$_4$]

[(η^8-COT)Y(pyr)$_4$][BPh$_4$] (4.5$_Y$)

A vial was charged with [(η^8-COT)Y(pyr)$_4$][BPh$_4$] (0.100 g, 0.125 mmol) and pyridine (5 mL) was added. The orange solution was left to slowly evaporate, generating crystals suitable for X-ray diffraction studies. Yield; 0.090 g (90 %) Anal. found (calcd. for $C_{48}H_{60}BN_4Y$) C 73.00 (73.73), H 6.90 (7.63), N 7.64 (7.06) %. ^{1}H NMR (500 MHz, d_5-pyridine, 303 K): δ_H = 8.10 (8 H, s, *o*-H/BPh$_4$), 7.30 (8 H, s, *m*-H/BPh$_4$), 7.22 (4 H, t, *p*-H/BPh$_4$), 6.73 (8 H, s, C_8H_8). ^{13}C{^{1}H} NMR (d_5-pyridine, 125.7 MHz, 303 K): δ_C = 137.29 (*o*-C/BPh$_4$), 126.25 (*m*-C/BPh$_4$), 122.46 (*p*-C/BPh$_4$) 95.97 (s, C_8H_8). ^{11}B{^{1}H} NMR (d_5-pyridine, 100.46 MHz, 303 K) δ_B = -5.41 (s, [BPh$_4$]$^-$). %). FT-IR $\tilde{\nu}$/cm^{-1}; 3035-2892 (b, CH), 1439 (s, CN) Crystal data; M = 453.88 g mol^{-1}, triclinic, *P*-1, a = 9.49800(10), b = 14.08110(10), c = 17.55880(10), α = 90, β = 102.6100(10), γ =90, V= 2291.71(3) Å^3, T = 100 K.

[(η^8-COT)Dy(pyr)$_4$][BPh$_4$] (4.5$_{Dy}$)

Yield; 0.089 g (89 %). Anal. found (calcd. for $C_{52}H_{48}BN_4Dy$) C 69.33 (69.22), H 5.44 (5.36), N 6.07 (6.21) %. ^{1}H NMR (500 MHz, d_5-pyridine, 303 K): δ_H = 6.56 (8 H, s, C_8H_8). ^{11}B{^{1}H} NMR (d_5-pyridine, 100.46 MHz, 303 K) δ_B = −6.28 (s, [BPh$_4$]$^-$). %). FT-IR $\tilde{\nu}$/cm^{-1}; 3035-2892 (b, CH), 1440 (s, CN). Crystal data; M = 981.35 g mol^{-1}, triclinic, *P*-1, a = 9.49180(10), b = 14.0807(2), c = 17.5476(3), α = 90, β = 102.539(2), γ =90, V= 2289.32(6) Å^3, T = 100 K.

[(η^8-COT)Er(pyr)$_4$][BPh$_4$] (4.5$_{Er}$)

Yield; 0.090 g (90 %)Anal. found (calcd. for $C_{52}H_{48}BN_4Er$) C 67.38 (68.36), H 5.14 (5.33), N 6.25 (6.18) %. FT-IR $\tilde{\nu}$/cm^{-1}; 3035-2892 (b, CH), 1437 (s, CN). Crystal data; M = 500.76 g mol^{-1}, triclinic, *P*-1, a = 9.49403(10), b = 14.06490(13), c = 17.55510(14), α = 90, β = 102.6930(9), γ =90, V= 2286.89(4) Å^3, T = 100 K.

Crystallographic Data

Table 6.1: Crystal structure data for **2.4$_{Y}$**, **2.4$_{Dy}$** and **2.4$_{Gd}$**

	2.4$_{Y}$	**2.4$_{Dy}$**	**2.4$_{Gd}$**
Empirical formula	$C_{28}H_{35}YWO_3$	$C_{28}H_{35}DyWO_3$	$C_{28}H_{35}GdWO_3 \cdot (C_4H_8O)$
Formula weight	692.32	765.91	832.42
Crystal system	Monoclinic	Monoclinic	Monoclinic
Space group	$P2_1/n$	$P2_1/n$	$P2_1/c$
a / Å	12.5485(6)	12.5341(5)	11.2617(3)
b / Å	10.3213(3)	10.3160(3)	22.1933(3)
c / Å	21.2747(11)	21.1831(6)	26.5611(5)
α/ °	90.0	90.0	90.0
β / °	106.189(5)	106.362(3)	95.0524(17)
γ/ °	90.0	90.0	90.0
V/ Å^3	2646.2(2)	2628.09(15)	6612.7(2)
Z	4	4	4
T/ K	150	150	150
ρ_{calc} / g cm^{-3}	1.738	1.936	1.734
μ/ mm^{-1}	11.043	7.221	19.448
F(000)	1360.0	1468.0	3356.0
Radiation	CuKα (λ = 1.54184 Å)	MoKα (λ = 0.71073 Å)	CuKα (λ = 1.54184 Å)
2θ range for data collection/ °	7.406 to 148.944	3.414 to 52.744	5.198 to 148.992
Reflections collected	56222	15266	47330
Independent reflections	5326 [R_{int} = 0.0661, [R_{sigma} = 0.0224]	5347 [R_{int} = 0.1489, R_{sigma} = 0.1356]	13363 [R_{int} = 0.0652, R_{sigma} = 0.0660]
Data/restraints/parameters	5326/176/343	5347/60/336	13363/212/766
Goodness-of-fit on F^2	1.094	1.011	1.053
Final R indexes [$I>2\sigma(I)$]	R_1 = 0.0342, wR_2 = 0.0910	R_1 = 0.0607, wR_2 = 0.1427	R_1 = 0.0524, wR_2 = 0.1186
Final R indexes [all data]	R_1 = 0.0351, wR_2 = 0.0918	R_1 = 0.0745, wR_2 = 0.1528	R_1 = 0.0702, wR_2 = 0.1266
Largest diff. peak/hole / e Å^{-3}	1.77/-1.19	2.13/-2.75	0.89/-1.12

Table 6.2 Crystal and structure refinement data for **3.3$_{Ln}$**

	3.3$_{Y}$	**3.3$_{Dy}$**	**3.3$_{Er}$**	**3.3$_{Gd}$**
Empirical formula	$C_{16}H_{28}BYO_2$	$C_{16}H_{28}BDyO_2$	$C_{16}H_{28}BErO_2$	$C_{16}H_{28}BGdO_2$
Formula weight	352.10	425.69	430.45	420.44
Crystal system	Monoclinic	Orthorhombic	Orthorhombic	Monoclinic
Space group	$P2_1/_n$	$Pbc2_1$	$Pca2_1$	$P2_1/_n$
a / Å	7.4223(2)	8.17250(10)	19.8038(4)	7.4346(2)
b / Å	23.9013(5)	19.9255(3)	8.13095(15)	24.1607(7)
c / Å	9.5141(2)	10.3572(2)	10.3980(2)	9.5191(3)
α/ °	90.0	90.0	90	90.0
β / °	98.033(2)	90	90	97.990(3)
γ/ °	90.0	90.0	90	90.0
V/ Å^3	1671.26(7)	1686.58(5)	1674.32(6)	1693.27(9)
Z	4	4	4	4
T/ K	100.00	100.00	120.14	100.00
ρ_{calc} / g cm^{-3}	1.399	1.676	1.708	1.649
μ/ mm^{-1}	4.884	23.671	9.271	25.302
F(000)	736.0	844.0	852.0	836.0
Radiation	CuKα (λ = 1.54184 Å)	CuKα (λ = 1.54184 Å)	CuKα (λ = 1.54184 Å)	CuKα (λ = 1.54184 Å)
2θ range for data collection/ °	7.398 to 142.402	8.876 to 142.504	8.93 to 134.024	7.318 to 142.098
Reflections collected	9627	23406	19594	8799
Independent reflections	3198[R(int) = 0.0247] 224]	3209 [R_{int} = 0.0892, R_{sigma} = 0.0416]	2986 [R_{int} = 0.0672, R_{sigma} = 0.0300]	3224 [R_{int} = 0.0446, R_{sigma} = 0.0561]
Data/restraints/parameters	3198/0/229	3209/3/200	2986/1/197	3224/1/221
Goodness-of-fit on F^2	1.026	1.198	1.073	1.043
Final R indexes [$I>2\sigma(I)$]	R_1 = 0.0228, wR_2 = 0.0534	R_1 = 0.0472, wR_2 = 0.1285	R_1 = 0.0394, wR_2 = 0.1054	R_1 = 0.0371, wR_2 = 0.0847
Final R indexes [all data]	R_1 = 0.0272, wR_2 = 0.0549	R_1 = 0.0526, wR_2 = 0.1399	R_1 = 0.0397, wR_2 = 0.1060	R_1 = 0.0526, wR_2 = 0.0893
Largest diff. peak/hole / e Å^{-3}	0.37/-0.57	1.66/-1.55	2.30/-0.80	1.35/-0.78

Table 6.3: Crystal structure data for **4.4$_{Ln}$**

	4.4$_{Y}$	**4.4$_{Dy}$**	**4.4$_{Er}$**
Empirical formula	$C_{48}H_{60}BYO_4$	$C_{48}H_{60}BDyO_4$	$C_{48}H_{60}BErO_4$
Formula weight	800.68	874.27	879.03
Crystal system	Triclinic	Triclinic	Triclinic
Space group	*P-1*	*P-1*	*P-1*
a / Å	9.7082(3)	9.7165(3)	9.7059(2)
b / Å	13.0898(4)	13.1039(4)	13.0833(3)
c / Å	16.1586(4)	16.1632(5)	16.1416(4)
α/ °	85.809(2)	85.855(2)	85.751(2)
β / °	75.900(2)	75.863(2)	75.904(2)
γ/ °	86.932(2)	86.911(2)	86.9426(19)
V/ Å^3	1984.86(10)	1989.01(10)	1981.23(9)
Z	2	2	2
T/ K	100.00	100.00	100.00
ρ_{calc} / g cm^{-3}	1.340	1.460	1.473
μ/ mm^{-1}	2.409	10.388	4.271
F(000)	848.0	902.0	906.0
Radiation	CuKα (λ = 1.54184 Å)	CuKα (λ = 1.54184 Å)	CuKα (λ = 1.54184 Å)
2θ range for data collection	6.776 to 122.37	6.768 to 142.674	6.78 to 142.344
Reflections collected	25771	29632	29316
Independent reflections	5982 [R_{int} = 0.0357, R_{sigma} = 0.0291]	7611 [R_{int} = 0.0399, R_{sigma} = 0.0345]	7560 [R_{int} = 0.0464, R_{sigma} = 0.0413]
Data/restraints/parameters	5982/0/523	7611/0/519	7560/0/487
Goodness-of-fit on F^2	1.041	1.027	1.102
Final R indexes [$I>2\sigma(I)$]	R_1 = 0.0246, wR_2 = 0.0557	R_1 = 0.0231, wR_2 = 0.0558	R_1 = 0.0275, wR_2 = 0.0413
Final R indexes [all data]	R_1 = 0.0276, wR_2 = 0.0574	R_1 = 0.0253, wR_2 = 0.0570	R_1 = 0.0327, wR_2 = 0.0658
Largest diff. peak/hole / e Å^{-3}	0.27/−0.38	0.35/−0.66	0.76/−0.66

Table 6.4: Crystal structure data for **4.5$_{Ln}$**

	4.5$_{Y}$	**4.5$_{Dy}$**	**4.5$_{Er}$**
Empirical formula	$C_{28.5}H_{26.5}B_{0.5}N_{2.5}Y_{0.5}$	$C_{57}H_{53}BDyN_5$	$C_{29.08}H_{26.06}B_{0.5}Er_{0.5}N_{2.59}$
Formula weight	453.88	981.35	500.76
Crystal system	Monoclinic	Monoclinic	Monoclinic
Space group	P_n	P_n	P_n
a / Å	9.49800(10)	9.49180(10)	9.49403(10)
b / Å	14.08110(10)	14.0807(2)	14.06490(13)
c / Å	17.55880(10)	17.5476(3)	17.55510(14)
α/ °	90	90	90
β / °	102.6100(10)	102.539(2)	102.6930(9)
γ/ °	90	90	90
V/ Å^3	2291.71(3)	2289.32(6)	2286.89(4)
Z	4	2	4
T/ K	100.00	100.00	100.00
ρ_{calc} / g cm^{-3}	1.316	1.424	1.454
μ/ mm^{-1}	2.126	9.065	3.752
F(000)	948.0	1002.0	1021.0
Radiation	CuKα (λ = 1.54184 Å)	CuKα (λ = 1.54184 Å)	CuKα (λ = 1.54184 Å)
2θ range for data collection	8.128 to 142.444	8.128 to 122.252	8.134 to 142.538
Reflections collected	36016	35270	32499
Independent reflections	8423 [R_{int} = 0.0345, R_{sigma} = 0.0283]	6716 [R_{int} = 0.0486, R_{sigma} = 0.0.0336]	8309 [R_{int} = 0.0575, R_{sigma} = 0.0509]
Data/restraints/parameters	8423/2/789	6716/54/609	8309/2/582
Goodness-of-fit on F^2	1.019	1.109	1.071
Final R indexes [$I>2\sigma(I)$]	R_1 = 0.0219, wR_2 = 0.0536	R_1 = 0.0607, wR_2 = 0.1570	R_1 = 0.0562, wR_2 = 0.1515
Final R indexes [all data]	R_1 = 0.0228, wR_2 = 0.0542	R_1 = 0.0620, wR_2 = 0.1587	R_1 = 0.0660, wR_2 = 0.1740
Largest diff. peak/hole / e Å^{-3}	0.17/−0.26	1.70/−1.51	0.81/−1.13

Table 6.5: Crystal structure data for **4.5$_{Ln}$**

	3.4$_{Y}$	**3.4$_{Dy}$**	**3.4$_{Er}$**
Empirical formula	$C_{42}H_{64}Y_2Si_2$	$C_{42}H_{64}Dy_2Si_2$	$C_{42}H_{64}Er_2Si_2$
Formula weight	800.91	950.11	957.61
Crystal system	Triclinic	Triclinic	Triclinic
Space group	*P-1*	*P-1*	*P-1*
a / Å	8.3069(4)	8.3045(5)	19.8038(4)
b / Å	11.1360(8)	11.1248(7)	8.13095(15)
c / Å	11.9454(9)	11.9532(6)	10.3980(2)
α/ °	70.935(7)	70.813(5)	70.735(7)
β / °	79.715(5)	79.908(5)	79.869(7)
γ/ °	68.730(5)	68.704(6)	68.817(8)
V/ Å^3	971.00(12)	969.79(11)	967.82(15)
Z	1	1	1
T/ K	100.00	100.00	100.00
ρ_{calc} / g cm^{-3}	1.370	1.627	1.643
μ/ mm^{-1}	4.774	21.155	8.592
F(000)	420.0	476.0	478.0
Radiation	CuKα (λ = 1.54184 Å)	CuKα (λ = 1.54184 Å)	CuKα (λ = 1.54184 Å)
2θ range for data collection	7.848 to 142.084	7.848 to 143.41	7.842 to 143.808
Reflections collected	4624	6145	6070
Independent reflections	3332 [R_{int} = 0.1013, R_{sigma} = 0.0957]	3675 [R_{int} = 0.0297, R_{sigma} = 0.0420]	3677 [R_{int} = 0.1058, R_{sigma} = 0.1536]
Data/restraints/parameters	3332/0/155	3675/0/221	3677/0/235
Goodness-of-fit on F^2	1.540	1.040	1.160
Final R indexes [$I>2\sigma(I)$]	R_1 = 0.1044, wR_2 = 0.3083	R_1 = 0.0288, wR_2 = 0.0726	R_1 = 0.0710, wR_2 = 0.1915
Final R indexes [all data]	R_1 = 0.1412, wR_2 = 0.3673	R_1 = 0.0296, wR_2 = 0.0732	R_1 = 0.0959, wR_2 = 0.2015
Largest diff. peak/hole / e Å^{-3}	2.81/-2.96	1.02/-1.24	1.79/-1.95

References

1 F. S. Guo, A. K. Bar and R. A. Layfield, *Chem. Rev.*, 2019, **119**, 8479–8505.

2 R. A. Layfield, *Organometallics*, 2014, **33**, 1084–1099.

3 F. S. Guo, B. M. Day, Y. C. Chen, M. L. Tong, A. Mansikkamäki and R. A. Layfield, *Science (80).*, 2018, **362**, 1400–1403.

4 R. Sessoli, D. Gatteschi, A. Caneschi and M. A. Novak, *Nature*, 1993, **365**, 141–143.

5 E. Coronado, *Nat. Rev. Mater.*, 2020, **5**, 87–104.

6 N. Ishikawa, M. Sugita, T. Ishikawa, S. Y. Koshihara and Y. Kaizu, *J. Am. Chem. Soc.*, 2003, **125**, 8694–8695.

7 R. A. Layfield, J. J. W. McDouall, S. A. Sulway, F. Tuna, D. Collison and R. E. P. Winpenny, *Chem. – A Eur. J.*, 2010, **16**, 4442–4446.

8 G. A. Craig and M. Murrie, *Chem. Soc. Rev.*, 2015, **44**, 2135–2147.

9 O. Waldmann, *Inorg. Chem.*, 2007, **46**, 10035–10037.

10 F. Neese and D. A. Pantazis, *Faraday Discuss.*, 2011, **148**, 229–238.

11 G. Aromí and E. K. Brechin, in *Single-Molecule Magnets and Related Phenomena*, ed. R. Winpenny, Springer Berlin Heidelberg, Berlin, Heidelberg, 2006, pp. 1–67.

12 A. J. Tasiopoulos, A. Vinslava, W. Wernsdorfer, K. A. Abboud and G. Christou, *Angew. Chem. Int. Ed.*, 2004, **43**, 2117–2121.

13 D. Gatteschi, R. Sessoli and A. Cornia, *Chem. Commun.*, 2000, 725–732.

14 A. L. Barra, A. Caneschi, A. Cornia, F. Fabrizi de Biani, D. Gatteschi, C. Sangregorio, R. Sessoli and L. Sorace, *J. Am. Chem. Soc.*, 1999, **121**, 5302–5310.

15 M. Murrie, S. J. Teat, H. Stœckli-Evans and H. U. Güdel, *Angew. Chem. Int.*

Ed., 2003, **42**, 4653–4656.

16 S. Sanvito, *Chem Soc Rev*, 2011, **40**, 3336–3355.

17 S. T. Liddle and J. Van Slageren, *Chem. Soc. Rev.*, 2015, **44**, 6655–6669.

18 S. A. Cotton, in *Encyclopedia of Inorganic Chemistry*, John Wiley & Sons, Ltd, 2006.

19 S. Cotton, *Lanthanide and Actinide Chemistry*, John Wiley & Sons, 2006.

20 R. Collins, J. P. Durrant, M. He and R. A. Layfield, in *Handbook on the Physics and Chemistry of Rare Earths*, eds. J.-C. G. Bünzli and V. K. B. T.-H. on the P. and C. of R. E. Pecharsky, Elsevier, 2019, vol. 55, pp. 89–121.

21 J. D. Rinehart and J. R. Long, *Chem. Sci.*, 2011, **2**, 2078–2085.

22 J. Sievers, *Zeitschrift für Phys. B Condens. Matter*, 1982, **45**, 289–296.

23 A. Castro-Alvarez, Y. Gil, L. Llanos and D. Aravena, *Inorg. Chem. Front.*, 2020, **7**, 2478–2486.

24 K. Bernot, *Molecular Magnetism of Lanthanides Complexes and Networks*, MDPI - Multidisciplinary Digital Publishing Institute, Basel, 2017, vol. 3.

25 F. Tuna, C. A. Smith, M. Bodensteiner, L. Ungur, L. F. Chibotaru, E. J. L. L. McInnes, R. E. P. P. Winpenny, D. Collison and R. A. Layfield, *Angew. Chem. Int. Ed.*, 2012, **51**, 6976–6980.

26 T. Pugh, F. Tuna, L. Ungur, D. Collison, E. J. L. McInnes, L. F. Chibotaru and R. A. Layfield, *Nat. Commun.*, 2015, **6**, 7492.

27 T. Pugh, V. Vieru, L. F. Chibotaru and R. A. Layfield, *Chem. Sci.*, 2016, **7**, 2128–2137.

28 T. Pugh, N. F. Chilton and R. A. Layfield, *Angew. Chem. Int. Ed.*, 2016, **55**, 11082–11085.

29 T. Pugh, N. F. Chilton and R. A. Layfield, *Chem. Sci.*, 2017, **8**, 2073–2080.

30 F. S. Guo and R. A. Layfield, *Chem. Commun.*, 2017, **53**, 3130–3133.

31 S. A. Sulway, R. A. Layfield, F. Tuna, W. Wernsdorfer and R. E. P. Winpenny, *Chem. Commun.*, 2012, **48**, 1508–1510.

32 F. Tuna, C. A. Smith, M. Bodensteiner, L. Ungur, L. F. Chibotaru, E. J. L. McInnes, R. E. P. Winpenny, D. Collison and R. A. Layfield, *Angew. Chem. Int. Ed.*, 2012, **51**, 6976–6980.

33 D. N. Woodruff, F. Tuna, M. Bodensteiner, R. E. P. Winpenny and R. A. Layfield, *Organometallics*, 2013, **32**, 1224–1229.

34 B. M. Day, F.-S. Guo and R. A. Layfield, *Acc. Chem. Res.*, 2018, **51**, 1880–1889.

35 F.-S. Guo, B. M. Day, Y.-C. Chen, M.-L. Tong, A. Mansikkamäki and R. A. Layfield, *Angew. Chem. Int. Ed.*, 2017, **56**, 11445–11449.

36 S. M. Chen, J. Xiong, Y. Q. Zhang, Q. Yuan, B. W. Wang and S. Gao, *Chem. Sci.*, 2018, **9**, 7540–7545.

37 L. Jacquot, M. Xémard, C. Clavaguéra and G. Nocton, *Organometallics*, 2014, **33**, 4100–4106.

38 A. J. Ashe, J. W. Kampf, S. Pilotek and R. Rousseau, *Organometallics*, 1994, **13**, 4067–4071.

39 D. P. Mills and P. Evans, *Chem. - A Eur. J.*, 2021, **27**, 6645–6665.

40 J. Liu, L. E. Nodaraki, P. J. Cobb, M. J. Giansiracusa, F. Ortu, F. Tuna and D. P. Mills, *Dalt. Trans.*, 2020, **49**, 6504–6511.

41 F. Nief and L. Ricard, *Organometallics*, 2001, **20**, 3884–3890.

42 S. Da Jiang, B. W. Wang, H. L. Sun, Z. M. Wang and S. Gao, *J. Am. Chem. Soc.*, 2011, **133**, 4730–4733.

43 M. Jeletic, P. H. Lin, J. J. Le Roy, I. Korobkov, S. I. Gorelsky and M. Murugesu, *J. Am. Chem. Soc.*, 2011, **133**, 19286–19289.

44 K. R. Meihaus and J. R. Long, *J. Am. Chem. Soc.*, 2013, **135**, 17952–17957.

45 J. D. Hilgar, M. G. Bernbeck and J. D. Rinehart, *J. Am. Chem. Soc.*, 2019, **141**,

1913–1917.

46 Y. S. Meng, M. W. Yang, L. Xu, J. Xiong, J. Y. Hu, T. Liu, B. W. Wang and S. Gao, *Dalt. Trans.*, 2019, **48**, 10407–10411.

47 T. D. Tilley and R. A. Andersen, *J. Chem. Soc. Chem. Commun.*, 1981, 985–986.

48 K. Müller-Buschbaum, G. B. Deacon and C. M. Forsyth, *Eur. J. Inorg. Chem.*, 2002, **2002**, 3172–3177.

49 M. M. Deegan and J. C. Peters, *Chem. Commun.*, 2019, **55**, 9531–9534.

50 J. E. Ellis, R. A. Faltynek and S. G. Hentges, *J. Organomet. Chem.*, 1976, **120**, 389–396.

51 B. J. Aucott, A. K. Duhme-Klair, B. E. Moulton, I. P. Clark, I. V. Sazanovich, M. Towrie, L. A. Hammarback, I. J. S. Fairlamb and J. M. Lynam, *Organometallics*, 2019, **38**, 2391–2410.

52 R. E. Cramer, K. T. Higa, S. L. Pruskin and J. W. Gilje, *J. Am. Chem. Soc.*, 1983, **105**, 6749–6750.

53 N. N. GREENWOOD and A. B. T.-C. of the E. (Second E. EARNSHAW, Eds., Butterworth-Heinemann, Oxford, 1997, pp. 1296–1299.

54 T. Nasr Allah, S. Savourey, J. C. Berthet, E. Nicolas and T. Cantat, *Angew. Chem. Int. Ed.*, 2019, **58**, 10884–10887.

55 R. Rund, G. Balázs, M. Bodensteiner and M. Scheer, *Angew. Chem. Int. Ed.*, 2019, **58**, 16092–16096.

56 J. Bohnenberger, M. Schmitt, W. Feuerstein, I. Krummenacher, B. Butschke, J. Czajka, P. J. Malinowski, F. Breher and I. Krossing, *Chem. Sci.*, 2020, **11**, 3592–3603.

57 M. P. Blake, N. Kaltsoyannis and P. Mountford, *J. Am. Chem. Soc.*, 2011, **133**, 15358–15361.

58 P. L. Arnold, J. McMaster and S. T. Liddle, *Chem. Commun.*, 2009, 818–820.

59 G. Cavigliasso and N. Kaltsoyannis, *Inorg. Chem.*, 2006, **45**, 6828–6839.

60 C. M. Dickie and M. Nippe, *Inorg. Chem. Front.*, 2016, **3**, 97–103.

61 G. B. Deacon and C. M. Forsyth, *Chem. Commun.*, 2002, **8**, 2522–2523.

62 R. Modak, B. Mondal, Y. Sikdar, J. Banerjee, E. Colacio, I. Oyarzabal, J. Cano and S. Goswami, *Dalt. Trans.*, 2020, **49**, 6328–6340.

63 A. P. Sobaczynski, J. Obenauf and R. Kempe, *Eur. J. Inorg. Chem.*, 2014, 1211–1217.

64 R. Collins, M. J. M. J. Heras Ojea, A. Mansikkamäki, J. Tang and R. A. Layfield, *Inorg. Chem.*, 2020, **59**, 642–647.

65 A. E. Crease and P. Legzdins, *J. Chem. Soc. Dalt. Trans.*, 1973, 1501–1507.

66 J. Moutet, J. Schleinitz, L. La Droitte, M. Tricoire, F. Pointillart, F. Gendron, T. Simler, C. Clavaguéra, B. Le Guennic, O. Cador and G. Nocton, *Angew. Chem. Int. Ed.*, 2021, **60**, 6042–6046.

67 D. M. Lyubov, C. Doring, S. Y. Ketkov, R. Kempe and A. A. Trifonov, *Chemistry (Easton).*, 2011, **17**, 3824–3826.

68 C. Jin, X.-L. Li, Z. Liu, A. Mansikkamäki and J. Tang, *Dalt. Trans.*, 2020, **49**, 10477–10485.

69 F. A. Cotton, A. D. Liehr and G. Wilkinson, *J. Inorg. Nucl. Chem.*, 1955, **1**, 175–186.

70 Y. Fang, X. Q. Ji, J. Xiong, G. Li, F. Ma, H. L. Sun, Y. Q. Zhang and S. Gao, *Dalt. Trans.*, 2018, **47**, 11636–11644.

71 D. I. Alexandropoulos, L. Cunha-Silva, J. Tang and T. C. Stamatatos, *Dalt. Trans.*, 2018, **47**, 11934–11941.

72 F. A. Hart and F. P. Laming, *J. Inorg. Nucl. Chem.*, 1965, **27**, 1605–1610.

73 P. W. Atkins and D. F. Shriver, *Shriver & Atkins' Inorganic chemistry 5th ed.*, Oxford University Press, Oxford, 5th ed., 2010.

74 N. F. Chilton, R. P. Anderson, L. D. Turner, A. Soncini and K. S. Murray, *J. Comput. Chem.*, 2013, **34**, 1164–1175.

75 H. Li, J. Sun, M. Yang, Z. Sun, J. Tang, Y. Ma and L. Li, *Inorg. Chem.*, 2018, **57**, 9757–9765.

76 S. Biswas, L. Mandal, Y. Shen and M. Yamashita, *Dalt. Trans.*, 2019, **48**, 14096–14102.

77 S. Bala, G. Z. Huang, Z. Y. Ruan, S. G. Wu, Y. Liu, L. F. Wang, J. L. Liu and M. L. Tong, *Chem. Commun.*, 2019, **55**, 9939–9942.

78 M. Hołyńska, *Single-Molecule Magnets*, 2018, 1–39.

79 Y. S. Ding, N. F. Chilton, R. E. P. Winpenny and Y. Z. Zheng, *Angew. Chem. Int. Ed.*, 2016, **55**, 16071–16074.

80 D. N. Woodruff, R. E. Winpenny and R. A. Layfield, *Chem. Rev.*, 2013, **113**, 5110–5148.

81 B. O. Roos, in *Advances in Chemical Physics: Ab Initio Methods in Quantum Chemistry II, Vol. 69*, ed. K. P. Lawley, Wiley, New York, NY, USA, 1987, pp. 399–455.

82 P. Siegbahn, A. Heiberg, B. Roos and B. Levy, *Phys. Scr.*, 1980, **21**, 323–327.

83 B. O. Roos, P. R. Taylor and P. E. M. Sigbahn, *Chem. Phys.*, 1980, **48**, 157–173.

84 P. E. M. Siegbahn, J. Almlöf, A. Heiberg and B. O. Roos, *J. Chem. Phys.*, 1981, **74**, 2384–2396.

85 B. O. Roos, R. Lindh, P. Å. Malmqvist, V. Veryazov and P.-O. Widmark, *Multiconfigurational Quantum Chemistry*, Wiley, Hoboken, NJ, USA, 2016.

86 P. Å. Malmqvist, B. O. Roos and B. Schimmelpfennig, *Chem. Phys. Lett.*, 2002, **357**, 230–240.

87 L. Ungur and L. F. Chibotaru, *Chem. - A Eur. J.*, 2017, **23**, 3708–3718.

88 L. Ungur and L. F. Chibotaru, *Chem. - A Eur. J.*, 2017, **23**, 3708–3718.

89 L. Gagliardi, R. Lindh and G. Karlström, *J. Chem. Phys.*, 2004, **121**, 4494–4500.

90 N. Iwahara, L. Ungur and L. F. Chibotaru, *Phys. Rev. B*, 2018, **98**, 54436.

91 M. Böhme and W. Plass, *Chem. Sci.*, 2019, **10**, 9189–9202.

92 K. Mashima and H. Takaya, *Tetrahedron Lett.*, 1989, **30**, 3697–3700.

93 K. Mashima, Y. Nakayama, A. Nakamura, N. Kanehisa, Y. Kai and H. Takaya, *J. Organomet. Chem.*, 1994, **473**, 85–91.

94 L. Münzfeld, C. Schoo, S. Bestgen, E. Moreno-Pineda, R. Köppe, M. Ruben and P. W. Roesky, *Nat. Commun.*, 2019, **10**, 3135.

95 S. M. Cendrowski-Guillaume, M. Nierlich, M. Lance and M. Ephritikhine, *Organometallics*, 1998, **17**, 786–788.

96 S. M. Cendrowski-Guillaume, G. Le Gland, M. Nierlich and M. Ephritikhine, *Organometallics*, 2000, **19**, 5654–5660.

97 T. Arliguie, L. Belkhiri, S.-E. Bouaoud, P. Thuéry, C. Villiers, A. Boucekkine and M. Ephritikhine, *Inorg. Chem.*, 2009, **48**, 221–230.

98 A. F. R. Kilpatrick and F. G. N. Cloke, *Dalt. Trans.*, 2017, **46**, 5587–5597.

99 K. X. Yu, Y. S. Ding, Y. Q. Zhai, T. Han and Y. Z. Zheng, *Dalt. Trans.*, 2020, **49**, 3222–3227.

100 H. Maekawa, M. Matsuo, H. Takamura, M. Ando, Y. Noda, T. Karahashi and S. Orimo, *J. Am. Chem. Soc.*, 2009, **131**, 894–895.

101 N. Kaltsoyannis and P. Scott, *The f Elements*, Oxford University Press, Oxford, 1999.

102 T. J. Marks and J. R. Kolb, *Chem. Rev.*, 1977, **77**, 263–293.

103 J. P. Durrant, J. Tang, A. Mansikkamäki and R. A. Layfield, *Chem. Commun.*, 2020, **56**, 4708–4711.

104 J. Cirera, E. Ruiz and S. Alvarez, *Organometallics*, 2005, **24**, 1556–1562.

105 P. Atkins, J. de Paula and J. Keeler, *Physical Chemistry*, OUP Oxford, Oxford,

10th edn., 2013.

106 K. R. Vignesh, D. I. Alexandropoulos, B. S. Dolinar and K. R. Dunbar, *Dalt. Trans.*, 2019, **48**, 2872–2876.

107 J. Y. Shi, P. Y. Chen, M. Z. Wu, L. Tian and Z. Y. Liu, *Dalt. Trans.*, 2019, **48**, 9187–9193.

108 S. Da Jiang, S. S. Liu, L. N. Zhou, B. W. Wang, Z. M. Wang and S. Gao, *Inorg. Chem.*, 2012, **51**, 3079–3087.

109 F. G. N. Cloke, P. B. Hitchcock, M. C. Kuchta and N. A. Morley-Smith, *Polyhedron*, 2004, **23**, 2625–2630.

110 F. G. N. Cloke and P. B. Hitchcock, *J. Am. Chem. Soc.*, 2002, **124**, 9352–9353.

111 N. Tsoureas, L. Maron, A. F. R. Kilpatrick, R. A. Layfield and F. G. N. Cloke, *J. Am. Chem. Soc.*, 2020, **142**, 89–92.

112 K. Jonas, B. Gabor, R. Mynott, K. Angermund, O. Heinemann and C. Krüger, *Angew. Chem. Int. Ed. English*, 1997, **36**, 1712–1714.

113 H. C. Aspinall, *Chemistry of the f-block elements* , Gordon & Breach, Amsterdam, 2001.

114 J. T. Boronski, L. R. Doyle, J. A. Seed, A. J. Wooles and S. T. Liddle, *Angew. Chem. Int. Ed.*, 2020, **59**, 295–299.

115 J. B. Grinderslev, K. T. Møller, M. Bremholm and T. R. Jensen, *Inorg. Chem.*, 2019, **58**, 5503–5517.

116 V. D. Makhaev, A. P. Borisov, G. N. Boiko and B. P. Tarasov, *Bull. Acad. Sci. USSR, Div. Chem. Sci.*, 1990, **39**, 1081–1087.

117 M. J. Saly, J. Li, M. J. Heeg and C. H. Winter, *Inorg. Chem.*, 2011, **50**, 7385–7387.

118 H. Schumann, R. D. Koehn, F. W. Reier, A. Dietrich and J. Pickardt, *Organometallics*, 1989, **8**, 1388–1392.

119 R. D'Cunha, V. N. P. Kaimal and V. B. Kartha, *Spectrochim. Acta Part A Mol. Spectrosc.*, 1980, **36**, 907–913.

120 R. T. Paine, R. W. Light and M. Nelson, *Spectrochim. Acta Part A Mol. Spectrosc.*, 1979, **35**, 213–216.

121 J. Xi, X. Ma, P. Cen, Y. Wu, Y. Q. Zhang, Y. Guo, J. Yang, L. Chen and X. Liu, *Dalt. Trans.*, 2021, **50**, 2102–2111.

122 J. Mayans and A. Escuer, *Chem. Commun.*, 2021, **57**, 721–724.

123 F. S. Guo, B. M. Day, Y. C. Chen, M. L. Tong, A. Mansikkamäki and R. A. Layfield, *Angew. Chem. Int. Ed.*, 2017, **56**, 11445–11449.

124 S. Zhang, J. Tang, J. Zhang, F. Xu, S. Chen, D. Hu, B. Yin and J. Zhang, *Inorg. Chem.*, 2021, **60**, 816–830.

125 C. A. Gould, K. R. McClain, J. M. Yu, T. J. Groshens, F. Furche, B. G. Harvey and J. R. Long, *J. Am. Chem. Soc.*, 2019, **141**, 12967–12973.

126 J. D. Hilgar, B. S. Flores and J. D. Rinehart, *Chem. Commun.*, 2017, **53**, 7322–7324.

127 S. K. Singh, C. J. Cramer and L. Gagliardi, *Inorg. Chem.*, 2020, **59**, 6815–6825.

128 N. F. Chilton, D. Collison, E. J. L. McInnes, R. E. P. Winpenny and A. Soncini, *Nat. Commun.*, 2013, **4**, 2551.

129 H. Ke, Y. Yang, W. Wei, Y. Jiang, Y.-Q. Zhang, G. Xie and S. Chen, *Dalt. Trans.*, 2020, **49**, 10594–10602.

130 Y. X. Wang, Q. Xu, P. Ren, W. Shi and P. Cheng, *Dalt. Trans.*, 2019, **48**, 2228–2233.

131 S. Zhang, N. Shen, J. Zhang, F. Xu, J. Zhang, J. Tang, D. Hu, B. Yin and S. Chen, *Dalt. Trans.*, 2021, **50**, 624–637.

132 D. Parker, E. A. Suturina, I. Kuprov and N. F. Chilton, *Acc. Chem. Res.*, 2020, **53**, 1520–1534.

133 S. Demir, J. M. Zadrozny and J. R. Long, *Chem. – A Eur. J.*, 2014, **20**, 9524–9529.

134 P. Evans, D. Reta, C. A. P. Goodwin, F. Ortu, N. F. Chilton and D. P. Mills, *Chem. Commun.*, 2020, **56**, 5677–5680.

135 E. Bartolomé, A. Arauzo, J. Luzón, S. Melnic, S. Shova, D. Prodius, I. C. Nlebedim, F. Bartolomé and J. Bartolomé, *Dalt. Trans.*, 2019, **48**, 15386–15396.

136 Y. C. Chen, X. S. Huang, J. L. Liu and M. L. Tong, *Inorg. Chem.*, 2018, **57**, 11782–11787.

137 I. Krossing and I. Raabe, *Angew. Chem. Int. Ed.*, 2004, **43**, 2066–2090.

138 C. Goonesinghe, H. Roshandel, C. Diaz, H. J. Jung, K. Nyamayaro, M. Ezhova and P. Mehrkhodavandi, *Chem. Sci.*, 2020, **11**, 6485–6491.

139 M. Sandström, I. Persson and P. Persson, *Acta Chem. Scand*, 1990, **44**, 653–675.

140 A. M. Ako, V. Mereacre, R. Clérac, W. Wernsdorfer, I. J. Hewitt, C. E. Anson and A. K. Powell, *Chem. Commun.*, 2009, 544–546.

141 L. B. L. Escobar, G. P. Guedes, S. Soriano, N. L. Speziali, A. K. Jordão, A. C. Cunha, V. F. Ferreira, C. Maxim, M. A. Novak, M. Andruh and M. G. F. Vaz, *Inorg. Chem.*, 2014, **53**, 7508–7517.

142 E. Echenique-Errandonea, A. Zabala-Lekuona, J. Cepeda, A. Rodríguez-Diéguez, J. M. Seco, I. Oyarzabal and E. Colacio, *Dalt. Trans.*, 2019, **48**, 190–201.

143 M. J. Frisch, G. W. Trucks, H. B. Schlegel, G. E. Scuseria, M. A. Robb, J. R. Cheeseman, G. Scalmani, V. Barone, B. Mennucci, G. A. Petersson, H. Nakatsuji, M. Caricato, X. Li, H. P. Hratchian, A. F. Izmaylov, J. Bloino, G. Zheng, J. L. Sonnenberg, M. Hada, M. Ehara, K. Toyota, R. Fukuda, J. Hasegawa, M. Ishida, T. Nakajima, Y. Honda, O. Kitao, H. Nakai, T. Vreven, J. A. Montgomery Jr., J. E. Peralta, F. Ogliaro, M. Bearpark, J. J. Heyd, E.

Brothers, K. N. Kudin, V. N. Staroverov, R. Kobayashi, J. Normand, K. Raghavachari, A. Rendell, J. C. Burant, S. S. Iyengar, J. Tomasi, M. Cossi, N. Rega, J. M. Millam, M. Klene, J. E. Knox, J. B. Cross, V. Bakken, C. Adamo, J. Jaramillo, R. Gomperts, R. E. Stratmann, O. Yazyev, A. J. Austin, R. Cammi, C. Pomelli, J. W. Ochterski, R. L. Martin, K. Morokuma, V. G. Zakrzewski, G. A. Voth, P. Salvador, J. J. Dannenberg, S. Dapprich, A. D. Daniels, Ö. Farkas, J. B. Foresman, J. V Ortiz, J. Cioslowski and D. J. Fox, 2009.

144 J. P. Perdew, K. Burke and M. Ernzerhof, *Phys. Rev. Lett.*, 1996, **77**, 3865–3868.

145 J. P. Perdew, K. Burke and M. Ernzerhof, *Phys. Rev. Lett.*, 1997, **78**, 1396.

146 C. Adamo and V. Barone, *J. Chem. Phys.*, 1999, **110**, 6158–6170.

147 M. Dolg, H. Stoll, A. Savin and H. Preuss, *Theor. Chim. Acta*, 1989, **75**, 173–194.

148 A. Schäfer, C. Huber and R. Ahlrichs, *J. Chem. Phys.*, 1994, **100**, 5829–5835.

149 F. Aquilante, J. Autschbach, R. K. Carlson, L. F. Chibotaru, M. G. Delcey, L. De Vico, I. Fdez. Galván, N. Ferré, L. M. Frutos, L. Gagliardi, M. Garavelli, A. Giussani, C. E. Hoyer, G. Li Manni, H. Lischka, D. Ma, P. Å. Malmqvist, T. Müller, A. Nenov, M. Olivucci, T. B. Pedersen, D. Peng, F. Plasser, B. Pritchard, M. Reiher, I. Rivalta, I. Schapiro, J. Segarra-Martí, M. Stenrup, D. G. Truhlar, L. Ungur, A. Valentini, S. Vancoillie, V. Veryazov, V. P. Vysotskiy, O. Weingart, F. Zapata and R. Lindh, *J. Comp. Chem.*, 2015, **37**, 506–541.

150 P.-O. Widmark, P.-Å. Malmqvist and B. O. Roos, *Theor. Chim. Acta*, 1990, **77**, 291–306.

151 B. O. Roos, R. Lindh, P.-Å. Malmqvist, V. Veryazov and and Per-Olof Widmark, *J. Phys. Chem. A*, 2004, **108**, 2851–2858.

152 B. O. Roos, R. Lindh, P.-Å. Malmqvist, V. Veryazov and P.-O. Widmark, *Chem. Phys. Lett.*, 2005, **409**, 295–299.

153 W. Kutzelnigg and W. Liu, *J. Chem. Phys.*, , DOI:10.1063/1.2137315.

154 M. Filatov, *J. Chem. Phys.*, , DOI:10.1063/1.2338033.

155 D. Peng and M. Reiher, *Theor. Chem. Acc.*, 2012, **131**, 1081.

156 O. Christiansen, J. Gauss and B. Schimmelpfennig, *Phys. Chem. Chem. Phys.*, 2000, **2**, 965–971.

157 B. A. H. C. M. Marian, U. Wahlgren and O. Gropen, *Chem. Phys. Lett.*, 1996, **251**, 365–371.

158 L. Ungur and L. F. Chibotaru, in *Lanthanides and Actinides in Molecular Magnetism*, eds. R. A. Layfield and M. Murugesu, Wiley-VHC, Weinheim, Germany, 2015, pp. 153–184.

159 L. F. Chibotaru and L. Ungur, *J. Chem. Phys.*, 2012, **137**, 64112.

160 N. Iwahara and L. F. Chibotaru, *Phys. Rev. B*, 2015, **91**, 174438.

Appendix

Appendix for Chapter 2: Heterobimetallic Lanthanide-Tungsten Carbonyl Complexes as Single-Molecule Magnets

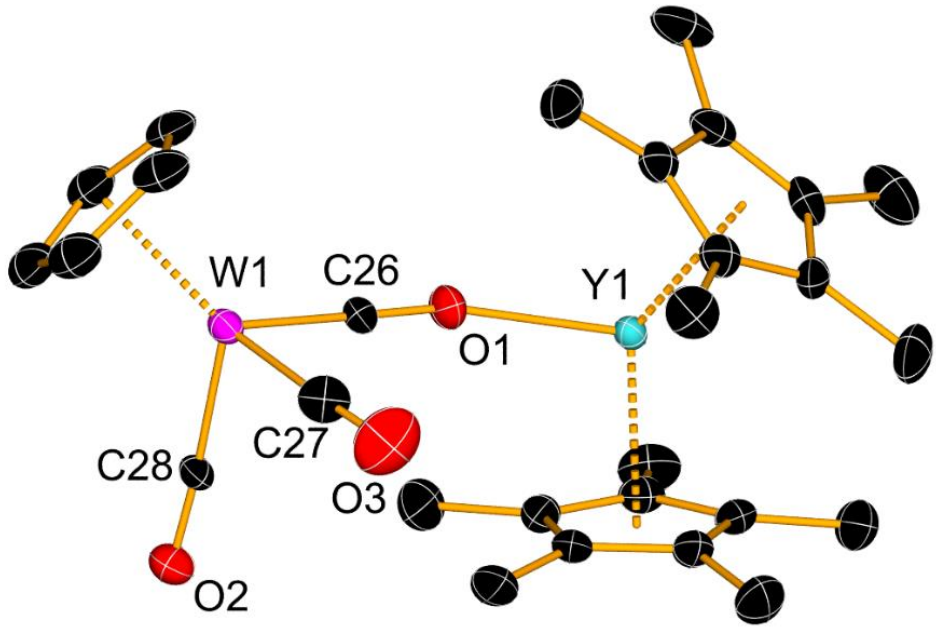

Figure S2.1: Diamond diagram of the molecular structure of **2.3$_Y$** (hydrogens omitted for clarity, ellipsoids set to 50% probability)

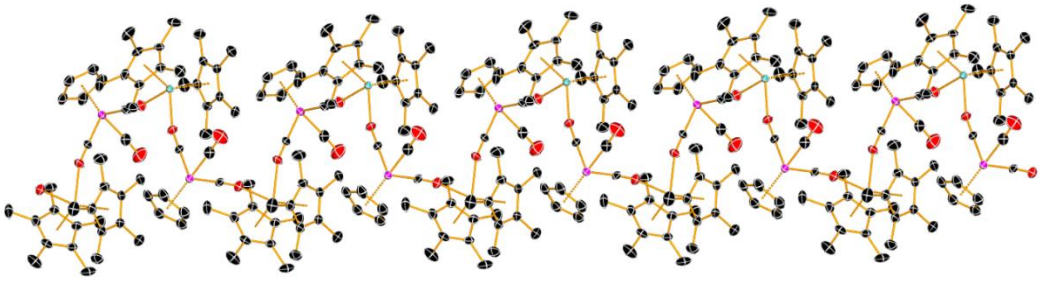

Figure S2.2: Diamond diagram of the expansion of **2.3$_Y$** along the *b*-axis (yttrium = blue, tungsten = purple, carbon = black, oxygen = red, hydrogens omitted for clarity, ellipsoids set to 50% probability).

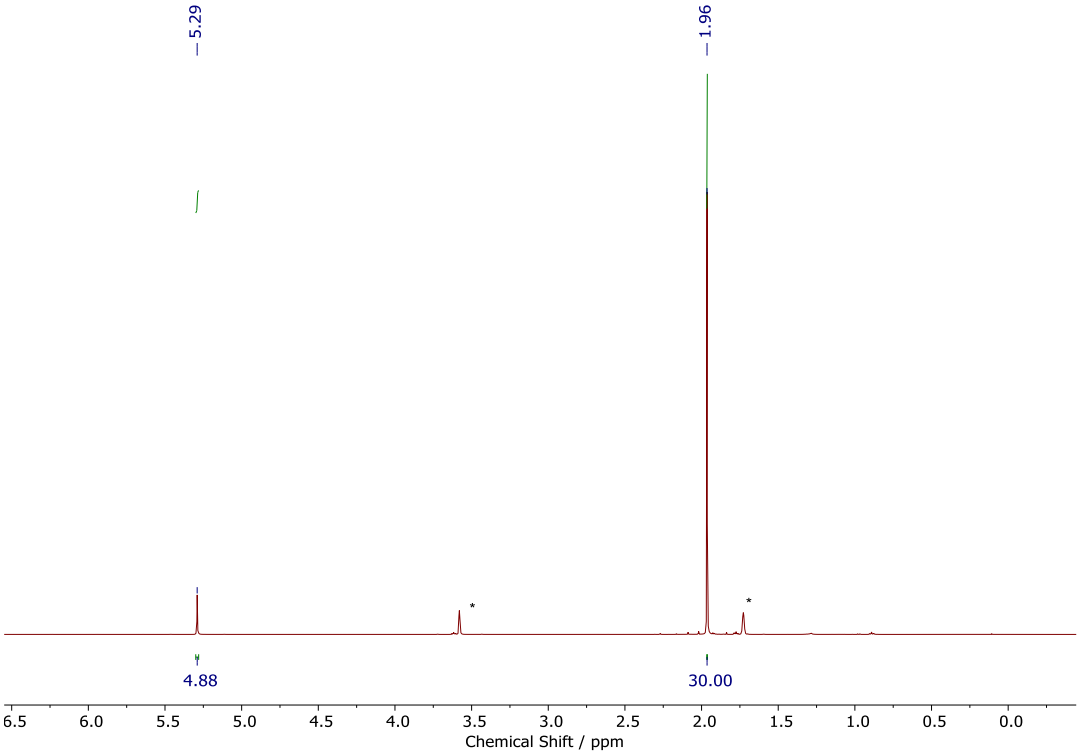

Figure S2.3: ^{1}H NMR spectrum in d_8-THF (*) at 298 K of $[Cp^*_2Y(\mu\text{-}OC)_2CpW(CO)] \infty$ **2.4$_Y$**.

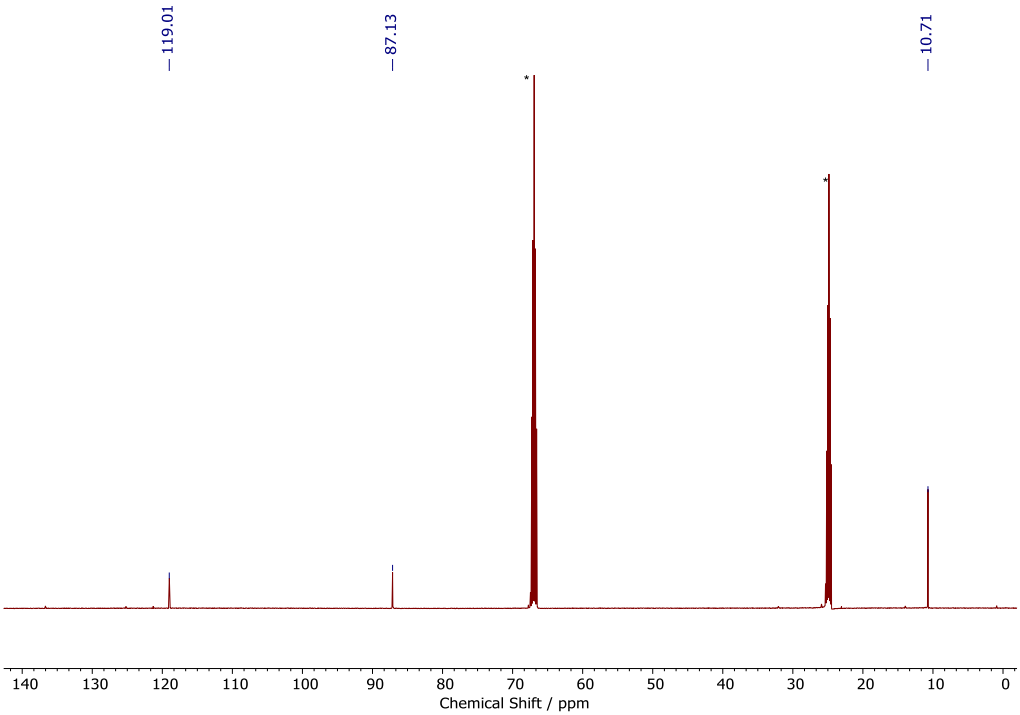

Figure S2.4: $^{13}C\{^{1}H\}$ NMR spectrum in d_8-THF (*) at 298 K of $[Cp^*_2Y(\mu\text{-}OC)_2CpW(CO)]_\infty$ **2.4Y**.

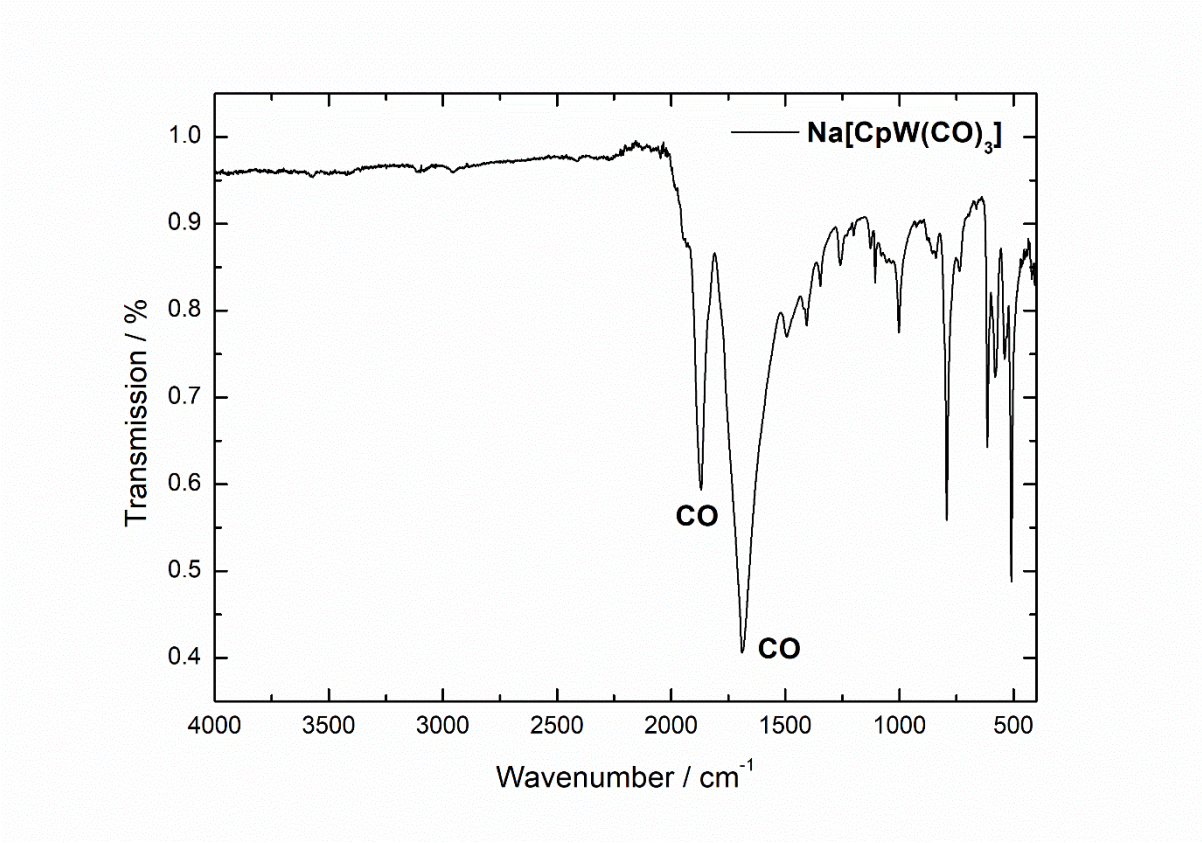

Figure S2.5: Solid-state IR of **Na[CpW(CO)$_3$].**

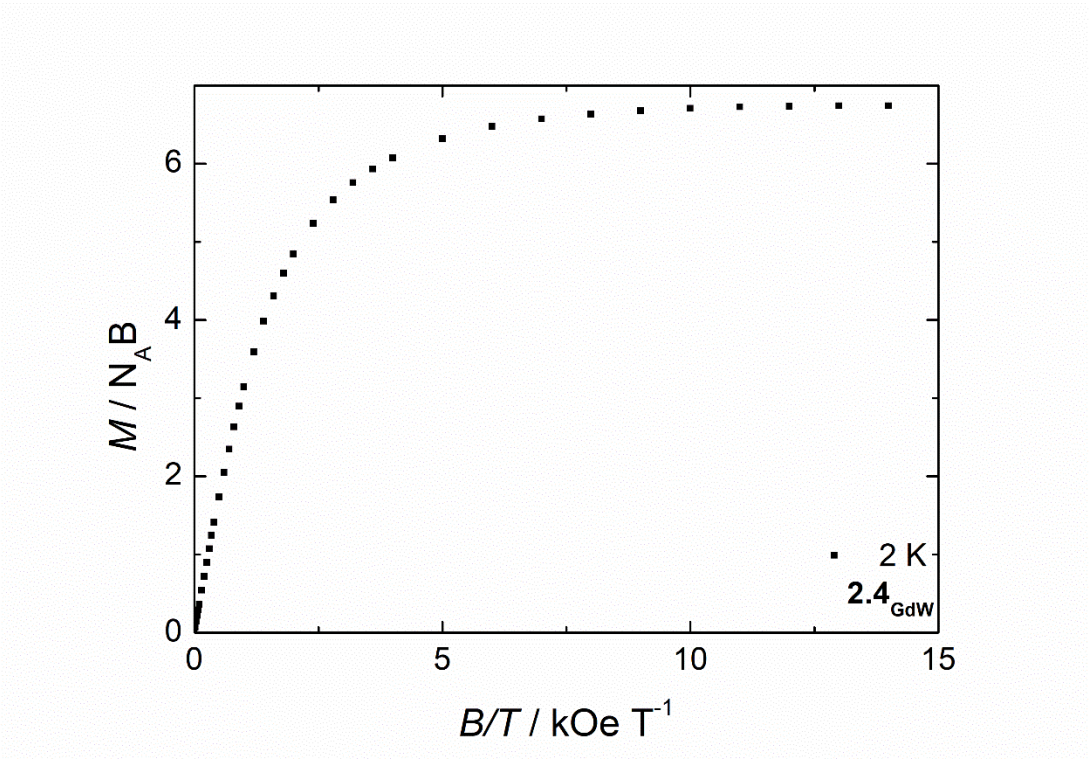

Figure S2.6: Magnetisation (*M*) *vs.* Field/Temperature (*H/T*) for **2.4$_{Gd}$.**

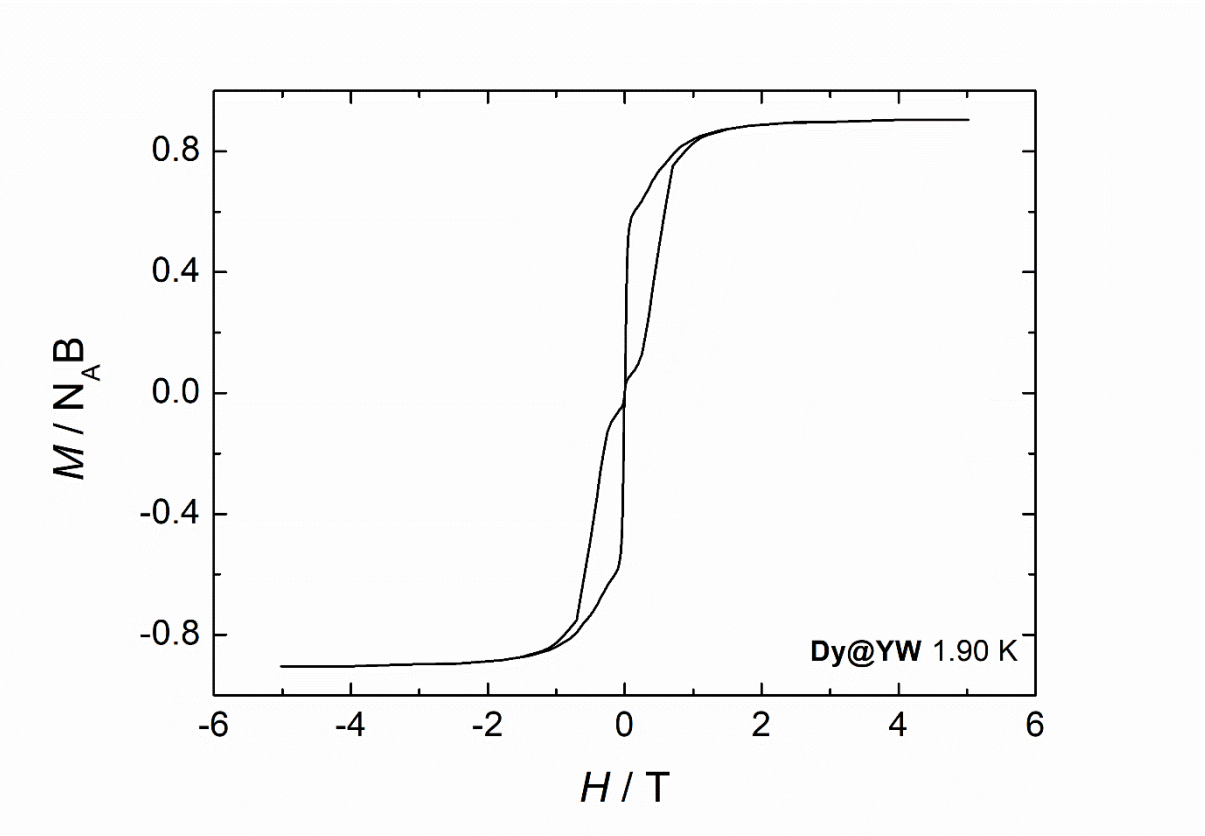

Figure S5: Magnetization (*M*) vs field (*T*) hysteresis loops for **2.4$_{Dy@Y}$**, scan rate of 28 Oe s^{-1}.

Computational details

The geometry used in the multireference *ab initio* calculations was extracted from the crystal structure. The positions of hydrogen atoms were optimized using density functional theory (DFT) while the positions of heavier atoms were kept frozen at their crystal structure coordinates. The DFT calculations were carried out using the Gaussian 09 software revision E.01[143] and the PBE0 hybrid exchange correlation functional.[144–146] A 4f-in-core 55 electron MWB55 pseudopotential was used for Dy and a 60 electron MWB60 pseudopotential was used for W along with corresponding valence basis sets.[147] Ahlrichs' older valence-polarized triple-ζ (TZVP) basis was used for the other atoms.[148] The accuracy of the integration grid was set to "UltraFine" and the accuracy of two-electron integrals to 10^{-12} atomic units.

The multireference *ab initio* calculation were carried out using the Molcas 8.2 quantum chemistry software.[149] Roos' relativistic atomic natural orbital basis sets (ANO-RCC) were used throughout. VQZP-quality basis was used for the Dy ion ([9s8p6d4f3g2h] contraction), VTZP-quality basis sets for the Cp carbon atoms, the CO ligand coordinated to the Dy ion and the W atom ([4s3p2d1f], [4s3p2d1f] and [8s7p5d3f2g1h] contractions for C, O and W, respectively), and VDZP-quality basis sets were used for other atoms ([2s1p], [3s2p1d] and [3s2p1d] contractions for H, C and O, respectively).[150–152] First, three separate state-averaged complete active space self-consistent field (SA-CASSCF) calculations[81–85] were carried out for sextet, quartet and doublet states. The active space consisted of the nine 4f electrons in the seven 4f orbitals. All 21 sextet, 224 quartet and 490 doublet roots were solved. Scalar relativistic effects were introduced using the scalar exact two-component (X2C)

transformation[153–155] as implemented in Molcas. The bielectronic integrals were stored using the Cholesky decomposition with a threshold of 10^{-8} atomic units. In a second step, spin-orbit coupling (SOC) was accounted using the restricted active space state-interaction approach;[86] The lowest 21 sextet, 128 quartet and 130 doublet roots corresponding to an energy cut-off of 50 000 cm^{-1} were mixed by SOC using the atomic mean-field integral (AMFI) formalism.[156,157] Static magnetic properties (*g*-tensors and the transition magnetic moments) and the ab initio crystal-field decomposition[87] were evaluated using the SINGLE_ANISO routine.[87,158,159] Effective atomic charges were calculated using the LoProp approach[89] as implemented in Molcas. The quoted numbers are the average charges of all 21 sextet states. The deviation of the charges between the different SA-CASSCF states is very small and arises only at the fourth decimal. HF and PBE0 DFT calculations on the $[CpW(CO)_3]^-$ fragment were carried out using Molcas and VTZP basis for W, C and O atoms and VDZP for H atoms. Both calculations were restricted closed-shell calculations with just one state considered.

To obtain more insight into the possible relaxation mechanisms, an approximate relaxation route was constructed using previously established methodology [3] where the relaxation pathway is obtained by tracing the path set by largest transition moment matrix elements between the different electronic states. The barrier and the numerical values of the transition magnetic moments are given in Figure 2 and Table 2, respectively. The shape of the barrier is very similar to that calculated for $[Cp^*_2Dy\{\mu\text{-}(OC)_2FeCp\}]_2$ [4] which has a very similar coordination environment

around the Dy ion. The calculation predicts relaxation via the third excited doublet, in agreement with the information obtained from the *g*-tensors.

The *ab initio* crystal-field (CF) parameters of **2.5$_{Dy}$** were calculated using a previously established methodology. The parameters are listed in Table S3 in the Iwahara–Chibotaru notation. This notation has the advantage that all matrix elements of the CF operators are of the order unity and the parameters between different ranks can be easily compared. The magnitudes of the parameters with opposite *q* are also equal ($|B_{kq}| = |B_{k-q}|$) which reduced the number of parameters one needs to consider when examining the strength of the CF. The strong axiality of the lower-energy doublets originates from the large value of the second rank axial parameter B_{20}. However, the off-diagonal second rank elements are of the same order of magnitude as the axial parameter leading to strong mixing of the pure angular momentum states. The axial component of the CF in **2.5$_{Dy}$** is much weaker and that the equatorial coordination of the CO bridges introduces significant off-diagonal, which lead to lower overall CF splitting and stronger mixing of the pure angular momentum states, respectively.

Using the calculated CF parameters, the electronic states belonging to the eight lowest KDs were decomposed to contributions from pure angular momentum states $|JM_J\rangle$ with *J* = 15/2. The decomposition is shown in Table S7. It is immediately clear that the states in the two lowest doublets have large (>0.96) squared projections on the states with M_J = ±15/2 and M_J = ±13/2, respectively. The states in the third

doublet still have squared projections of 0.92 on the M_J = ±11/2 states, but from the fourth doublet onwards the states become strongly mixed and cannot be assigned to specific M_J values in a meaningful way. This is again consistent with an Orbach mechanism taking place via the third excited doublet.

Table S1. Squared projections of the states in the eight lowest Kramers doublets (KDs) on the angular momentum states $|JM_J\rangle$ with J = 15/2 for **2.5$_{Dy}$**.

M_J	KD1		KD2		KD3		KD4	
15/2	0.965	0.000	0.020	0.000	0.004	0.252	0.004	0.041
13/2	0.010	0.000	0.965	0.000	0.009	0.083	0.096	0.014
11/2	0.259	0.000	0.071	0.000	0.017	0.917	0.033	0.174
9/2	0.030	0.000	0.247	0.001	0.026	0.133	0.267	0.044
7/2	0.006	0.000	0.044	0.002	0.012	0.172	0.193	0.134
5/2	0.002	0.001	0.027	0.001	0.022	0.066	0.313	0.182
3/2	0.008	0.000	0.007	0.002	0.029	0.147	0.154	0.498
1/2	0.003	0.001	0.021	0.007	0.115	0.011	0.640	0.128
–1/2	0.001	0.003	0.007	0.021	0.011	0.115	0.128	0.640
–3/2	0.000	0.008	0.002	0.007	0.147	0.029	0.498	0.154
–5/2	0.001	0.002	0.001	0.027	0.066	0.022	0.182	0.313
–7/2	0.000	0.006	0.002	0.044	0.172	0.012	0.134	0.193
–9/2	0.000	0.030	0.001	0.247	0.133	0.026	0.044	0.267
-11/2	0.000	0.259	0.000	0.071	0.917	0.017	0.174	0.033
–13/2	0.000	0.010	0.000	0.965	0.083	0.009	0.014	0.096
–15/2	0.000	0.965	0.000	0.020	0.252	0.004	0.041	0.004
M_J	KD5		KD6		KD7		KD8	
15/2	0.005	0.024	0.010	0.028	0.036	0.011	0.003	0.011
13/2	0.043	0.194	0.056	0.057	0.034	0.071	0.027	0.011
11/2	0.043	0.082	0.064	0.118	0.139	0.074	0.029	0.055
9/2	0.162	0.808	0.173	0.228	0.158	0.212	0.101	0.068
7/2	0.051	0.241	0.219	0.653	0.501	0.258	0.139	0.203
5/2	0.138	0.335	0.345	0.198	0.347	0.527	0.347	0.236
3/2	0.152	0.004	0.083	0.434	0.312	0.261	0.325	0.465
1/2	0.182	0.153	0.117	0.227	0.082	0.099	0.530	0.375
–1/2	0.153	0.182	0.227	0.117	0.099	0.082	0.375	0.530
–3/2	0.004	0.152	0.434	0.083	0.261	0.312	0.465	0.325
–5/2	0.335	0.138	0.198	0.345	0.527	0.347	0.236	0.347
–7/2	0.241	0.051	0.653	0.219	0.258	0.501	0.203	0.139
–9/2	0.808	0.162	0.228	0.173	0.212	0.158	0.068	0.101
-11/2	0.082	0.043	0.118	0.064	0.074	0.139	0.055	0.029
–13/2	0.194	0.043	0.057	0.056	0.071	0.034	0.011	0.027
–15/2	0.024	0.005	0.028	0.010	0.011	0.036	0.011	0.003

Table S2. Numerical values of the magnitudes of transition magnetic moments between different components of the eight lowest Kramers doublets in **2.5$_{Dy}$**.

Transition moments for transition on the same side of the barrier								
KD	1	2	3	4	5	6	7	8
1		1.82576	0.38226	0.07836	0.31257	0.15584	0.06519	0.02142
2	1.82576		2.30623	0.37865	0.40657	0.32968	0.16393	0.04750
3	0.38226	2.30623		1.29542	2.34756	0.75755	0.24029	0.04398
4	0.07836	0.37865	1.29542		1.62835	1.58369	0.65777	0.07121
5	0.31257	0.40657	2.34756	1.62835		2.80212	1.03955	0.12947
6	0.15584	0.32968	0.75755	1.58369	2.80212		1.86551	0.15225
7	0.06519	0.16393	0.24029	0.65777	1.03955	1.86551		1.74147
8	0.02142	0.04750	0.04398	0.07121	0.12947	0.15225	1.74147	
Transition moments for transition through the barrier								
KD	1	2	3	4	5	6	7	8
1	0.00047	0.00096	0.00928	0.09139	0.01539	0.04081	0.05490	0.01742
2	0.00096	0.00481	0.02960	0.28449	0.08460	0.11943	0.12464	0.05081
3	0.00928	0.02960	0.27243	1.07801	0.20990	0.31942	0.24115	0.03744
4	0.09139	0.28449	1.07801	1.76243	1.51943	1.20702	0.53477	0.08984
5	0.01539	0.08460	0.20990	1.51943	0.62392	1.10131	0.97438	0.19200
6	0.04081	0.11943	0.31942	1.20702	1.10131	2.49273	1.42774	0.16836
7	0.05490	0.12464	0.24115	0.53477	0.97438	1.42774	1.63462	0.46431
8	0.01742	0.05081	0.03744	0.08984	0.19200	0.16836	0.46431	0.44699

Table S3. Calculated crystal-field parameters of **2.5$_{Dy}$** for ranks up to k = 12 given in the Iwahara–Chibotaru notation[90,160] (rank k = 14 also has nonzero values but the numbers are so small that they cannot be distinguished from numerical noise).

k	$\|q\|$	Re(B_{kq})	Im(B_{kq})	$\|B_{kq}\|$
2	0	-304.037779	0.000000	304.037779
2	1	8.705454	-0.408061	8.715012
2	2	103.466247	-28.936519	107.436429
4	0	-41.856691	0.000000	41.856691
4	1	-1.329623	3.466475	3.712728
4	2	6.206129	-0.725208	6.248357
4	3	-3.120273	-2.422301	3.950145
4	4	29.141553	-23.907254	37.693327
6	0	0.501415	0.000000	0.501415
6	1	-2.682652	-5.737629	6.333799
6	2	27.522914	-9.290610	29.048687
6	3	-1.865433	-4.371149	4.752556
6	4	-2.084643	0.643903	2.181822
6	5	-0.726861	-1.285153	1.476464
6	6	1.426944	-3.174197	3.480186
8	0	0.301917	0.000000	0.301917
8	1	0.055022	0.078849	0.096149
8	2	-0.642959	0.190557	0.670603
8	3	0.090721	0.167700	0.190666
8	4	-0.049013	0.075232	0.089789
8	5	-0.016929	-0.006366	0.018087
8	6	-0.016558	0.020926	0.026685
8	7	0.003852	-0.001360	0.004085
8	8	0.002408	-0.007456	0.007835
10	0	0.008737	0.000000	0.008737
10	1	0.007701	0.017877	0.019465
10	2	-0.031556	0.014028	0.034534
10	3	0.001633	0.001007	0.001919
10	4	-0.001490	-0.001800	0.002336
10	5	0.004129	0.002834	0.005008
10	6	-0.000469	0.001022	0.001125
10	7	-0.003384	-0.001840	0.003852
10	8	-0.000610	-0.001989	0.002080
10	9	-0.002189	-0.000409	0.002227
10	10	-0.001249	-0.004121	0.004306
12	0	0.007760	0.000000	0.007760
12	1	0.000041	-0.003898	0.003898
12	2	-0.000585	-0.000683	0.000899
12	3	-0.000538	-0.000305	0.000618
12	4	0.001640	-0.001288	0.002085
12	5	-0.000384	-0.000401	0.000555
12	6	-0.000137	0.000078	0.000158
12	7	0.000134	0.000040	0.000140

12	8	-0.000015	0.000128	0.000129
12	9	0.000037	0.000007	0.000037
12	10	0.000008	0.000087	0.000087
12	11	-0.000020	0.000000	0.000020
12	12	-0.000026	-0.000029	0.000039

The parameters are listed only for $q \geq 0$; values for parameters with $q < 0$ are given by $B_{k-|q|} = (-1)^{k+|q|} B_{k|q|}{}^{*}$

Table S4. The energies and principal components of the **g** tensors of the eight lowest Kramers doublets (KDs) of the model system **2.6$_{Dy}$** arising from the crystal-field split $^{6}H_{15/2}$ ground multiplet of the Dy(III) ion along with the angles (θ) between the principal magnetic axis of a given doublet and that of the ground doublet

KD	E / cm^{-1}	g_x	g_y	g_z	θ
1	0	0.0001	0.0002	19.8085	0.0
2	323	0.0086	0.0090	17.0152	1.0
3	539	0.0471	0.0562	14.4524	2.4
4	674	0.6079	0.7274	11.7472	1.5
5	764	1.9959	2.7307	8.49013	13.3
6	805	8.8035	7.6515	2.81763	1.3
7	869	0.5026	1.6289	15.1008	89.7
8	1080	0.0211	0.0361	19.6012	89.8

Table S5. Calculated crystal-field parameters of the model system **2.6$_{Dy}$** for ranks up to k = 12 given in the Iwahara–Chibotaru notation (rank k = 14 also has nonzero values but the numbers are so small that they cannot be distinguished from numerical noise).

k	$\|q\|$	Re(B_{kq})	Im(B_{kq})	$\|B_{kq}\|$
2	0	-564.744294	0,000000	564,744294
2	1	1,611760	-6,311318	6,513870
2	2	-17,904107	-90,477978	92,232432
4	0	-47,706278	0,000000	47,706278
4	1	0,660893	1,546883	1,682149
4	2	1,879420	3,319518	3,814632
4	3	-0,300688	1,176187	1,214013
4	4	-24,386196	17,456937	29,990518
6	0	-12,092300	0,000000	12,092300
6	1	-1,219964	1,170298	1,690535
6	2	-6,686701	-23,195368	24,139948
6	3	-0,133416	1,778457	1,783455
6	4	-2,591788	2,455202	3,570068
6	5	2,135843	1,107975	2,406124
6	6	5,443981	3,465409	6,453371
8	0	0,530983	0,000000	0,530983
8	1	0,033041	-0,047016	0,057465
8	2	0,185990	0,912009	0,930781
8	3	0,000205	-0,055334	0,055334
8	4	0,067814	-0,106360	0,126140
8	5	-0,020557	-0,020024	0,028698
8	6	-0,019633	-0,024066	0,031058
8	7	0,003781	-0,005285	0,006498
8	8	0,000113	0,002730	0,002732
10	0	0,010328	0,000000	0,010328
10	1	0,002750	-0,001735	0,003252
10	2	0,017891	0,028793	0,033899
10	3	-0,001722	-0,003417	0,003826
10	4	0,012887	-0,004136	0,013534
10	5	-0,003006	0,000640	0,003073
10	6	-0,003752	-0,000795	0,003835
10	7	-0,000286	-0,001749	0,001772
10	8	0,001797	-0,006666	0,006904
10	9	-0,002043	0,000624	0,002136
10	10	-0,007103	0,000476	0,007119
12	0	0,006679	0,000000	0,006679
12	1	0,000170	-0,000804	0,000822
12	2	-0,001193	0,001892	0,002236
12	3	0,000098	0,000039	0,000106
12	4	-0,001139	0,001082	0,001571
12	5	0,000169	-0,000122	0,000208
12	6	0,000140	-0,000142	0,000200
12	7	0,000019	-0,000009	0,000021
12	8	-0,000059	0,000184	0,000193
12	9	-0,000019	0,000004	0,000020

12	10	0,000018	0,000013	0,000022
12	11	0,000031	0,000055	0,000063
12	12	0,000052	0,000110	0,000122

The parameters are listed only for $q \geq 0$; values for parameters with $q < 0$ are given by $B_{k-|q|} = (-1)^{k+|q|} B_{k|q|}{}^{*}$

Table S6. Squared projections of the states in the eight lowest Kramers doublets (KDs) on angular momentum states $|JM_J\rangle$ with J = 15/2

M_J	KD1		KD2		KD3		KD4	
15/2	0.965	0.000	0.020	0.000	0.004	0.252	0.004	0.041
13/2	0.010	0.000	0.965	0.000	0.009	0.083	0.096	0.014
11/2	0.259	0.000	0.071	0.000	0.017	0.917	0.033	0.174
9/2	0.030	0.000	0.247	0.001	0.026	0.133	0.267	0.044
7/2	0.006	0.000	0.044	0.002	0.012	0.172	0.193	0.134
5/2	0.002	0.001	0.027	0.001	0.022	0.066	0.313	0.182
3/2	0.008	0.000	0.007	0.002	0.029	0.147	0.154	0.498
1/2	0.003	0.001	0.021	0.007	0.115	0.011	0.640	0.128
–1/2	0.001	0.003	0.007	0.021	0.011	0.115	0.128	0.640
–3/2	0.000	0.008	0.002	0.007	0.147	0.029	0.498	0.154
–5/2	0.001	0.002	0.001	0.027	0.066	0.022	0.182	0.313
–7/2	0.000	0.006	0.002	0.044	0.172	0.012	0.134	0.193
–9/2	0.000	0.030	0.001	0.247	0.133	0.026	0.044	0.267
-11/2	0.000	0.259	0.000	0.071	0.917	0.017	0.174	0.033
–13/2	0.000	0.010	0.000	0.965	0.083	0.009	0.014	0.096
–15/2	0.000	0.965	0.000	0.020	0.252	0.004	0.041	0.004
M_J	KD5		KD6		KD7		KD8	
15/2	0.005	0.024	0.010	0.028	0.036	0.011	0.003	0.011
13/2	0.043	0.194	0.056	0.057	0.034	0.071	0.027	0.011
11/2	0.043	0.082	0.064	0.118	0.139	0.074	0.029	0.055
9/2	0.162	0.808	0.173	0.228	0.158	0.212	0.101	0.068
7/2	0.051	0.241	0.219	0.653	0.501	0.258	0.139	0.203
5/2	0.138	0.335	0.345	0.198	0.347	0.527	0.347	0.236
3/2	0.152	0.004	0.083	0.434	0.312	0.261	0.325	0.465
1/2	0.182	0.153	0.117	0.227	0.082	0.099	0.530	0.375
–1/2	0.153	0.182	0.227	0.117	0.099	0.082	0.375	0.530
–3/2	0.004	0.152	0.434	0.083	0.261	0.312	0.465	0.325
–5/2	0.335	0.138	0.198	0.345	0.527	0.347	0.236	0.347
–7/2	0.241	0.051	0.653	0.219	0.258	0.501	0.203	0.139
–9/2	0.808	0.162	0.228	0.173	0.212	0.158	0.068	0.101
-11/2	0.082	0.043	0.118	0.064	0.074	0.139	0.055	0.029
–13/2	0.194	0.043	0.057	0.056	0.071	0.034	0.011	0.027
–15/2	0.024	0.005	0.028	0.010	0.011	0.036	0.011	0.003

Appendix 2 – Chapter 4: Monometallic Cyclooctatetraene Tetraphenylborate Lanthanide Complexes as Single-Molecule Magnets

NMR Spectra

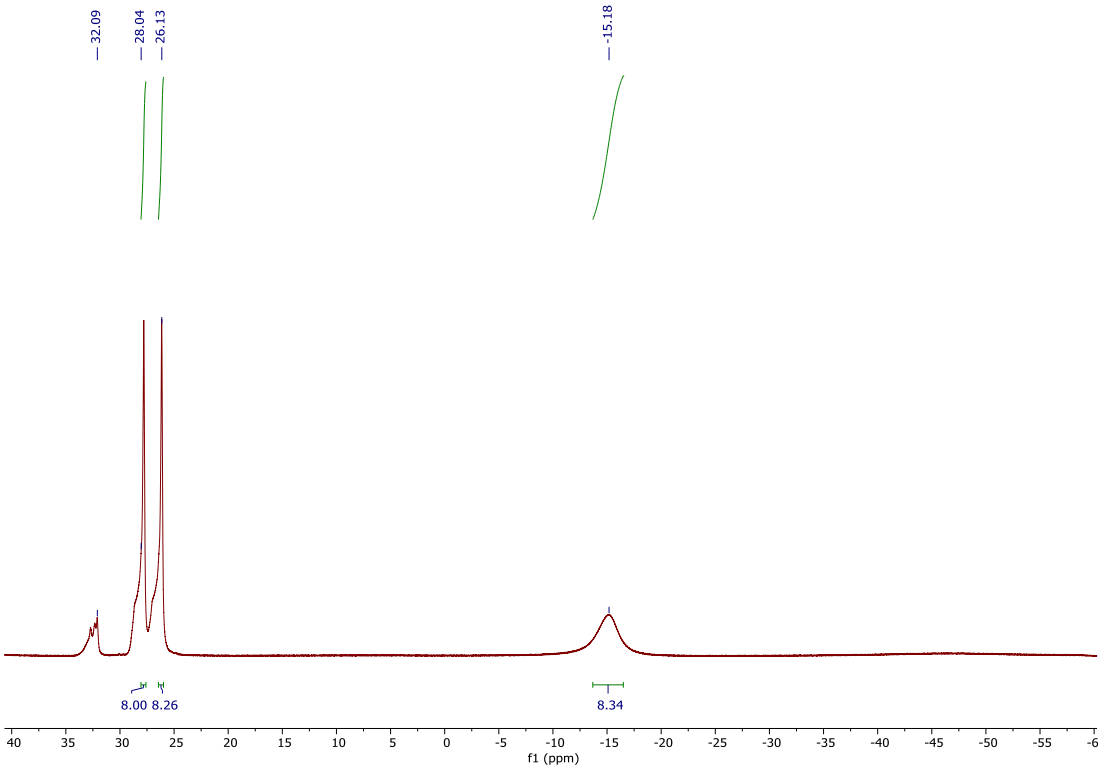

Figure S6: ^{1}H NMR spectrum of **4.4$_{Er}$** (d_5-pyridine, 400 MHz, 303 K).

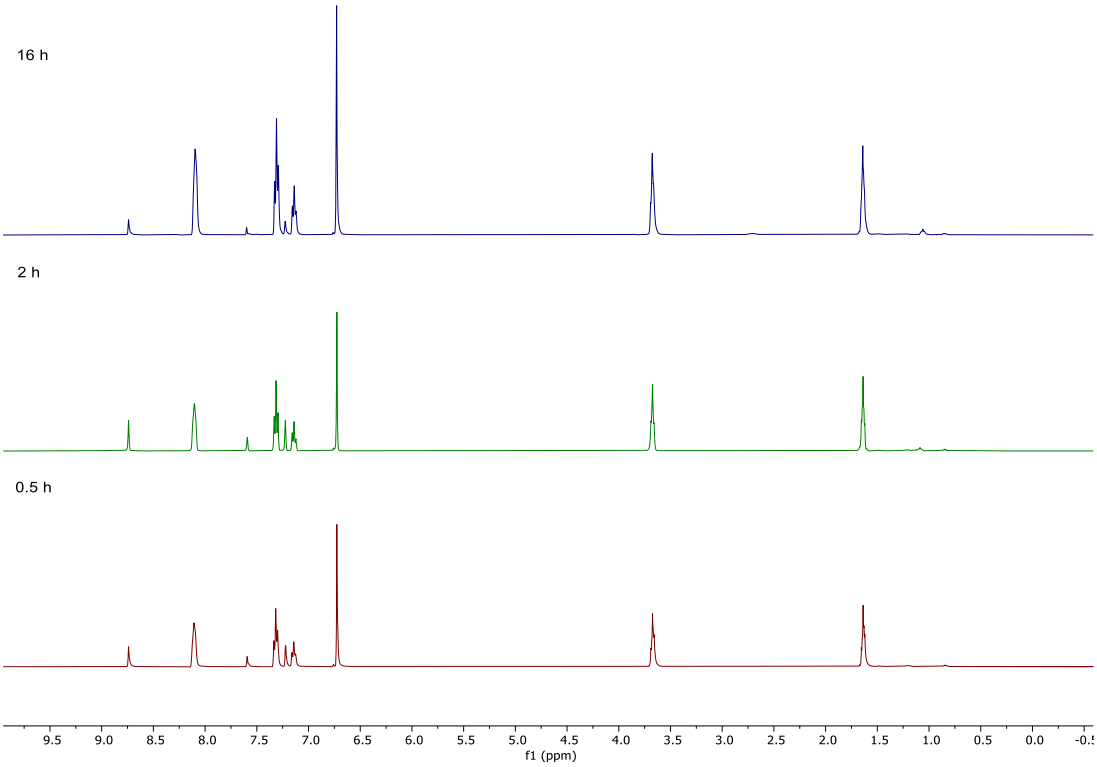

Figure S7: Stacked ^{1}H NMR spectra of **4.3$_{Y}$** reactions from different reaction times (d_5-pyridine, 400 MHz, 303 K).

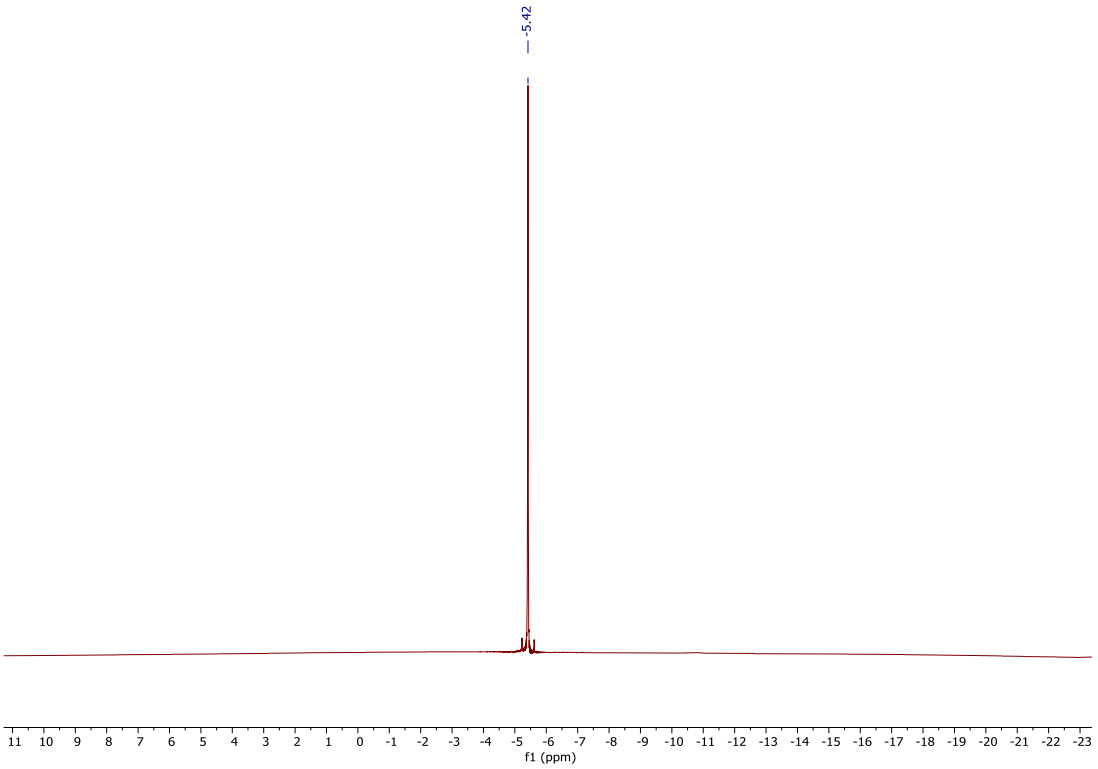

Figure S8: ^{11}B{^{1}H} NMR spectrum of **4.3$_{Y}$** (d_5-pyridine, 128 MHz, 303 K).

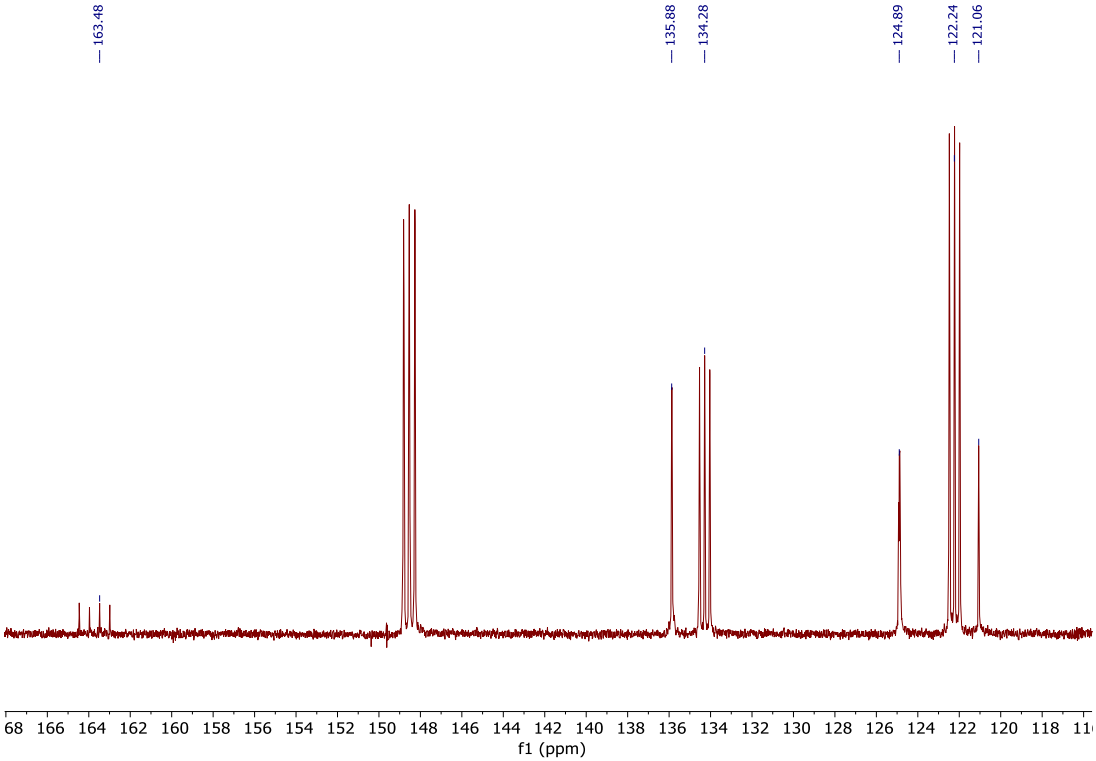

Figure S9: $^{13}C\{^{1}H\}$ NMR spectrum of **4.3$_{Ln}$** (d_5-pyridine, 128 MHz, 303 K).

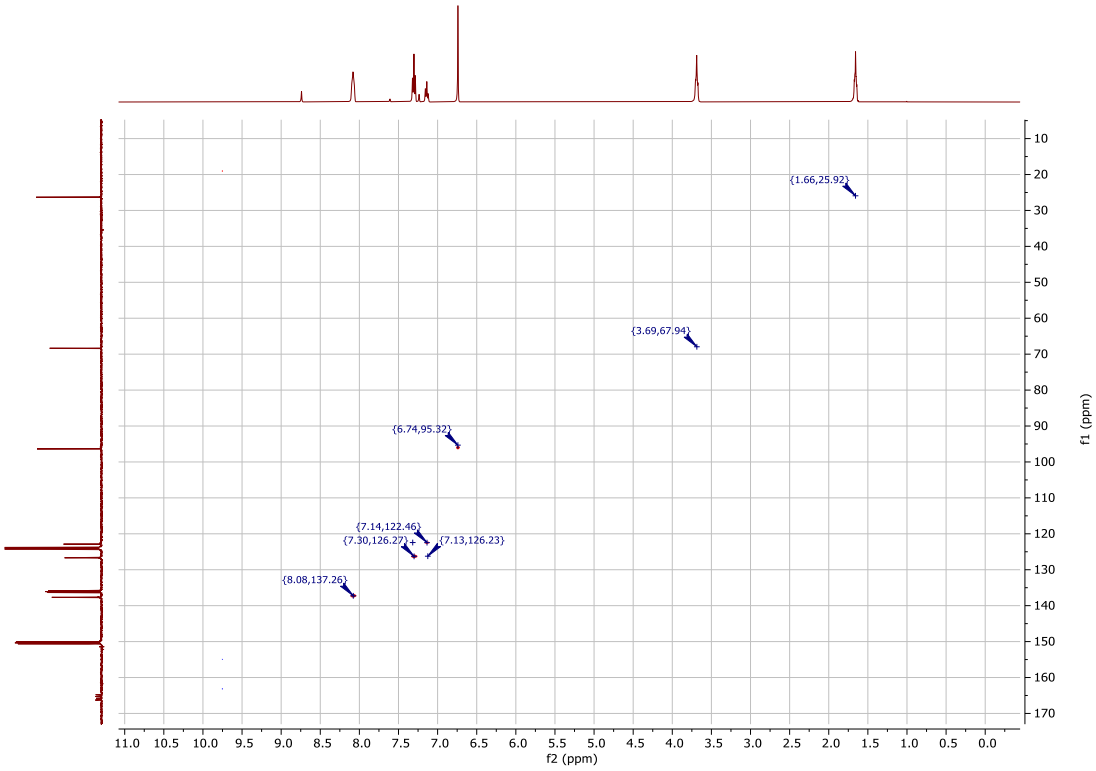

Figure S10: ^{1}H-^{13}C HSQC NMR spectrum of **4.3$_{Y}$** (d_5-pyridine, 303 K).

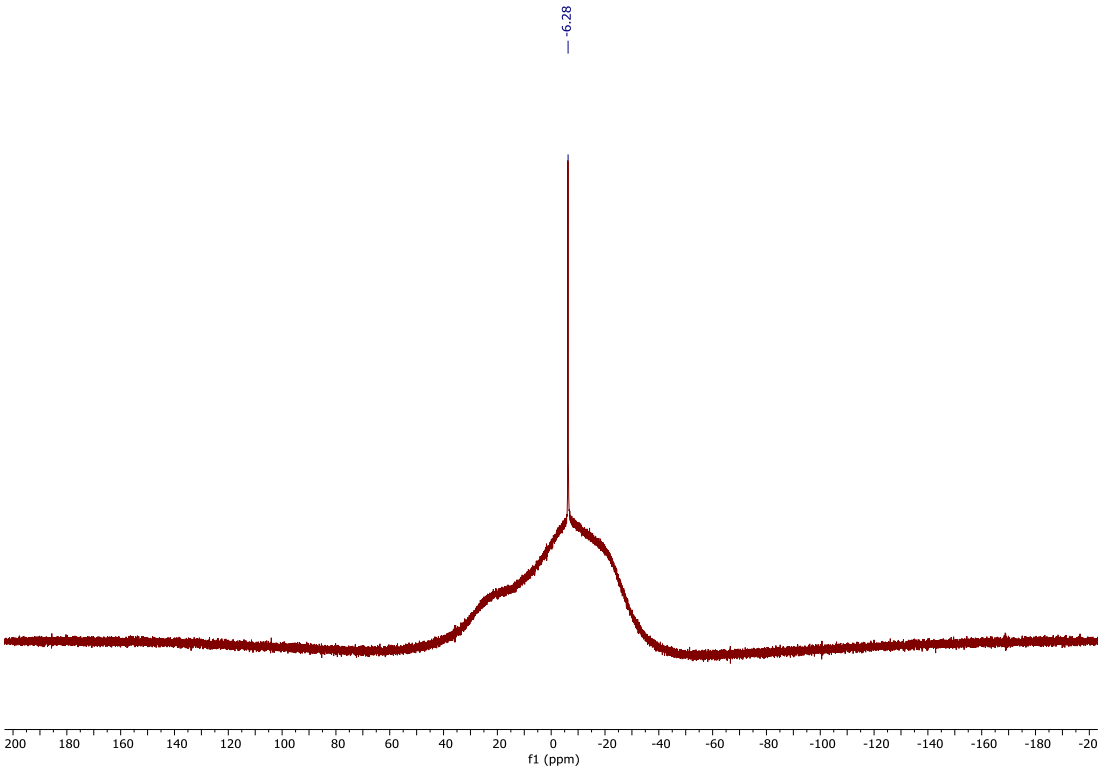

Figure S11: $^{11}B\{^{1}H\}$ NMR spectrum of **4.4$_{Dy}$** (d_5-pyridine, 400 MHz, 303 K).

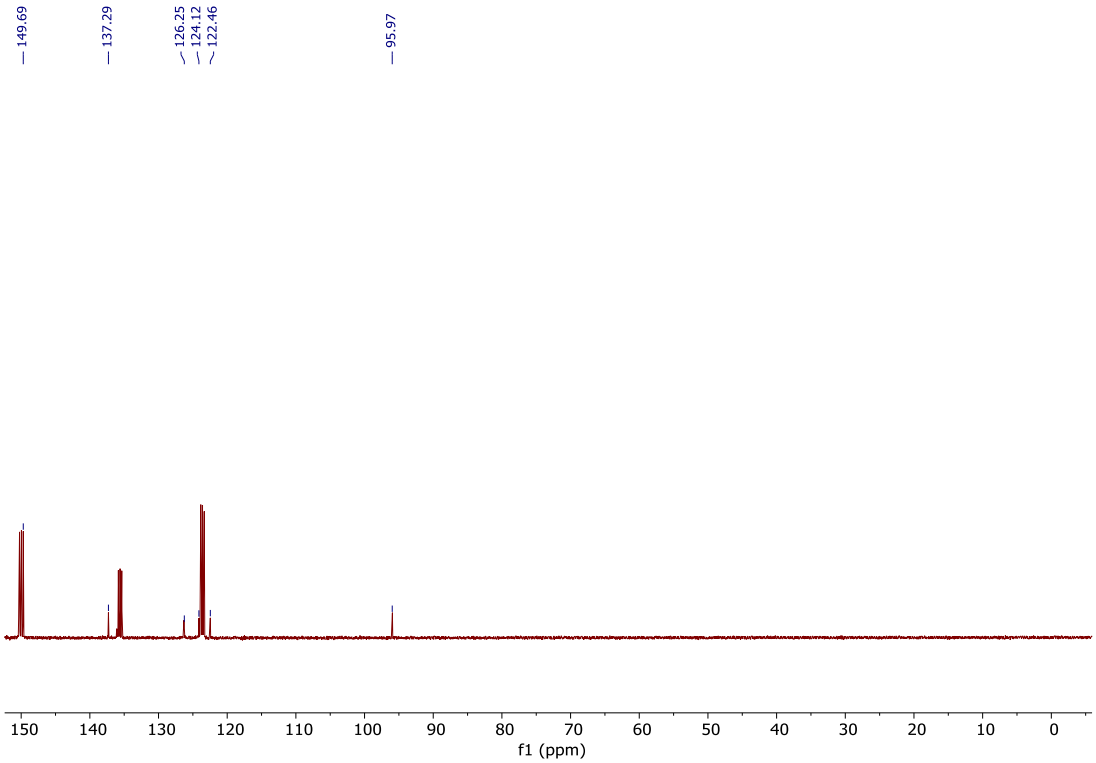

Figure S12: ^{1}H NMR spectrum of **4.5$_{Y}$** reactions from different reaction times (d_5-pyridine, 400 MHz, 303 K).

Magnetic Properties

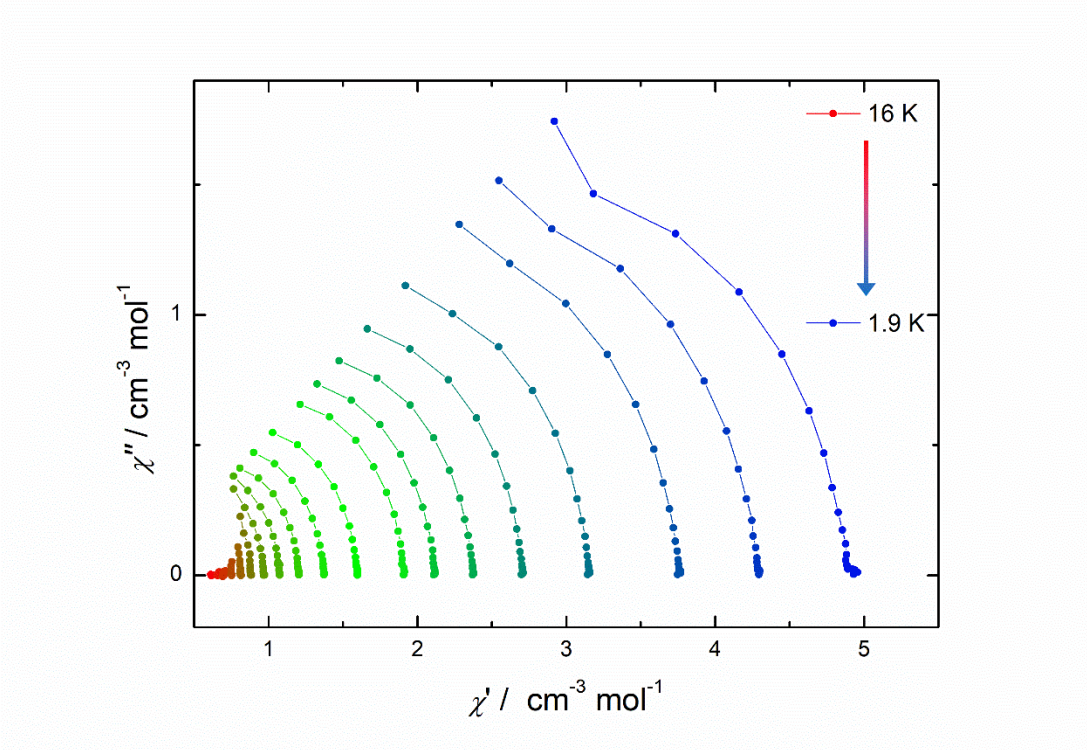

Figure S13: Cole-Cole of (χ'' *vs.* χ') for **4.5**$_{Er}$. No α parameter could be extracted due to no maxima in peaks.